VETENSKAP OCH KONST

KUNGL TEKNISKA HÖGSKOLAN

FLOW PROCESSES IN ROCKET ENGINE NOZZLES WITH FOCUS ON FLOW SEPARATION AND SIDE-LOADS

Jan Östlund

Licentiate Thesis

Stockholm, 2002

FLOW PROCESSES IN ROCKET ENGINE NOZZLES WITH FOCUS ON FLOW SEPARATION AND SIDE-LOADS
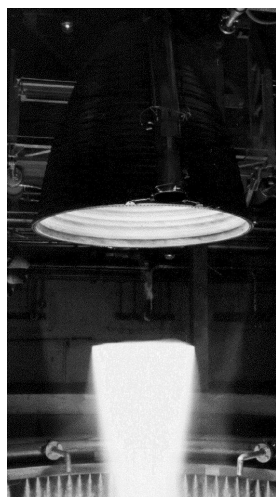
by

Jan Östlund
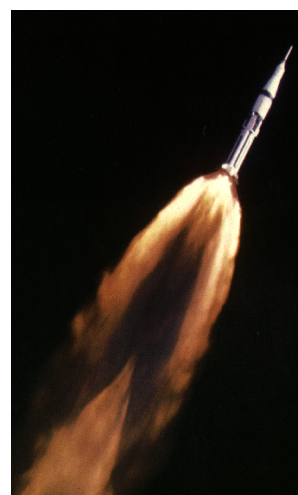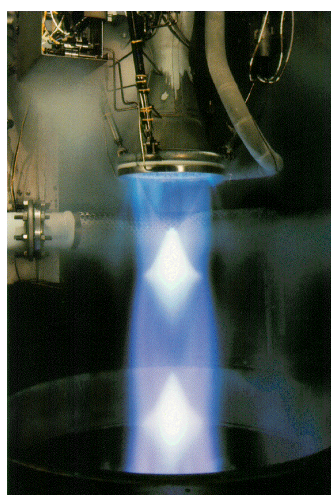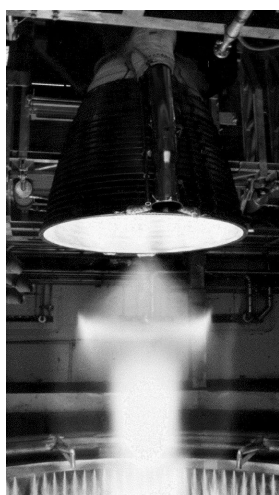
ABSTRACT

The increasing demand for higher performance in rocket launchers promotes the development of nozzles with higher performance, which is basically achieved by increasing the expansion ratio. However, this may lead to flow separation and ensuing unstationary, asymmetric forces, so-called side-loads, which may present life-limiting constraints on both the nozzle itself and other engine components. Substantial gains can be made in the engine performance if this problem can be overcome, and hence different methods of separation control have been suggested, however none has so far been implemented in full scale, due to the uncertainties involved in modelling and predicting the flow phenomena involved.

The present thesis presents a comprehensive, up-to-date review of supersonic flow separation and side-loads in internal nozzle flows with ensuing side-loads. In addition to results available in the literature, it also contains previously unpublished material based on this author's work, whose main contributions are
(i)   discovery the role of transition between different separation patterns for side-load generation,
(ii)   experimental verification of side-loads due to aeroelastic effects and
(iii) contributions to the analysis and scaling of side-loads.

A physical description of turbulent shock wave boundary layer interactions is given, based on theoretical concepts, computational results and experimental observation. This is followed by an in-depth discussion of different approaches for predicting the phenomena. This includes methods for predicting shock-induced separation, models for predicting side-load levels and aeroelastic coupling effects. Examples are presented to illustrate the status of various methods, and their advantages and shortcomings are discussed. The third part of the thesis focuses on how to design sub-scale models that are able to capture the relevant physics of the full-scale rocket engine nozzle. Scaling laws like those presented in here are indispensable for extracting side-load correlations from sub-scale tests and applying them to full-scale nozzles.

The present work was performed at VAC's Space Propulsion Division within the framework of European space cooperation.

Keywords: turbulent, boundary layer, shock wave, interaction, intermittent, overexpanded, rocket nozzle, flow separation, side-load, models, criteria, prediction, review.

TABLE OF CONTENTS

1 INTRODUCTION

The performance of rocket engines is highly dependent on the aerodynamic design of the expansion nozzle, the main design parameters being the contour shape and the area ratio. The optimal design of traditional bell-type nozzles for given operating conditions (i.e. chamber and ambient pressures) is already supported by accurate and validated tools. However, during operation at chamber pressures below design pressure, the flow will not be fully attached, but separated. The separation line will move towards the nozzle exit as the chamber pressure increases (during start-up) or when the ambient pressure decreases (during the vehicles ascent). Different kinds of dynamic loads occur in the nozzle when the flow is separated, the most well known of these being the so called side-load, that has attracted the attention of many researchers. This occurs during testing at sea level condition or during the first phase of the actual flight. The increasing demand for higher performance in rocket launchers promotes the development of nozzles with higher performance and hence larger area ratio, where the problem of flow separation and side-loads is present during a substantial part of the ascent.

One possible solution of the described problem is to adapt the nozzle contour during the flight to the changes of ambient and chamber pressure. Attempts in this direction, however, have not yet been successful due to weight and mechanical complexity of such adapting devices.

Another approach is to introduce so called Flow Separation Control Devices (FSCD), by which high area ratio nozzles can be operated at separated condition at high ambient sea level pressure without severe loads, thereby obtaining an improved overall performance. The feasibility of such devices is presently the objective of demonstration tests[R 6]. The main reason why such devices do not yet exist in full scale is that several basic questions regarding the nature of the flow separation phenomena and corresponding side-loads remain to be answered, which means that basic research is needed.

Building of knowledge regarding flow separation and side-loads has been a continuous process at Volvo Aero Corporation (VAC) since 1993, when the Flow Separation Control working (FSC) group was formed with CNES, Snecma and Astrium.

VAC performed focused studies on the topic within the GSTP/FSC program[R 5], 1996-1999, under a contract with the European Space Agency (ESA) and the Swedish National Space Board (SNSB). This included sub-scale testing of rocket nozzles at the modified hypersonic wind tunnel HYP500 at the Aeronautical Research Institute of Sweden (FFA)*, in order to investigate the aerodynamic and aeroelastic behaviour of a parabolic contour with and without FSCD inserts.

In the subsequent FSCD-program since 1998, under contract with Swedish National Space Board (SNSB) and Centre National d'Études Spatiales (CNES), flow separation and side-loads have been studied analytically and experimentally in sub scale test campaigns[R 6]. This work was performed in co-operation with FOI, CNES, Snecma, ONERA, LEA, DLR and Astrium[R 2-R 4, R 7, R 8, R 104, R 105, R 108, R 117, R 123, R 124, R 130, R 132, R 158- R 161].

Within the frame of the FSCD-program, VAC performed new sub-scale nozzle tests at FFA's test facility in Stockholm. In the FSCD program VAC has tested eight different nozzle concepts, which are listed in Table 1.

The present author has been actively involved in the VAC/FSCD activities since 1997, being in charge of the test design (including design of model contours), hardware set-up and instrumentation, as well as test logic and evaluation of test results. CFD-computations have been extensively used for designing the models. They are indispensable for a qualitative understanding of the physics and flow phenomena, and hence provide a necessary input for setting up model descriptions and making meaningful evaluations.

---

* is now a part of the Swedish Defence Research Agency (FOI)

This thesis presents a comprehensive, up-to-date review of turbulent shock wave boundary layer interactions in internal nozzle flows with ensuing side-loads, including results available in the literature as well as previously unpublished results. It gives a detailed physical description of the phenomena, based on theoretical concepts, computational results and experimental observation. This is followed by an in-depth review of different approaches for predicting the phenomena. This includes methods developed to predict shock-induced separation and models for prediction of side-load levels and aeroelastic coupling in rocket nozzles. Examples are presented to illustrate the status of various methods, and their advantages and shortcomings are discussed. The third part of the thesis focuses on the problems associated with designing sub-scale models that are able to capture the most relevant physics of the full-scale rocket nozzle. The presented scaling laws are indispensable for extracting side-load correlations from sub-scale tests and applying them to full-scale nozzles.

The main contributions of the author to the understanding and modelling of separation and side-loads concern
(i)   discovering the role of transition between different separation patterns for side-load generation,
(ii)   experimental verification of side-loads due to aeroelastic effects and
(iii)   contributions to the analysis and scaling of side-loads.

It was observed already in the early 1970's by Nave and Coffey[R 95] that a transition in separation pattern from the free-shock separation (FSS) to the restricted shock separation (RSS) and vice-versa might occur. However, it was not understood that these transitions are the origin of two distinct side-load peaks, until Östlund et al[R 5] presented the detailed analysis of the VOLVO S1 nozzle flow.

In highly aeroelastic cases a significant amplification of the side-loads can be obtained as the flow interacts with the mechanical structure. The study of aeroelastic effects in separated nozzle flows requires dynamic models of the mechanical nozzle-engine support system, the flow separation, as well as the coupling between these two. A simplified technique for handling these difficult coupling problems was proposed by Pekkari[R 102,R 103] in the early 1990's. Östlund[R 108] made this model applicable by improving the aerodynamic modelling, which were subsequently verified in experiments.

In order to translate measured data into engineering correlations, it is necessary to relate model tests to the real rocket engine nozzles. Here, the main challenge is to reproduce the behaviour of the chemical reacting hot propellants using air with totally different gas properties. Some basic ideas on scaling of separation and side-loads are presented in this thesis, and their relevance to real rocket nozzles is discussed on the basis of two different sub-scale designs for Vulcain.
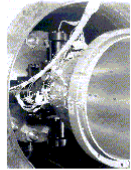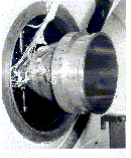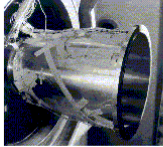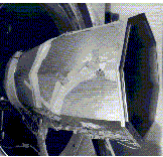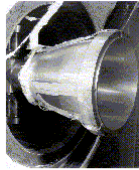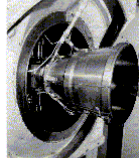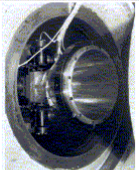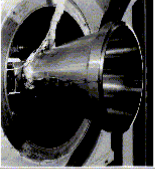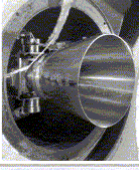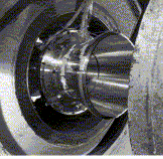
Nozzle	Base Contour	ε	Nozzle Picture	Description/Test objectives
VolvoS1	Parabolic contour	20		This nozzle was designed with the geometrical definition of the Vulcain nozzle as a model. The primary objectives were to investigate the separation and side-load behaviour in a Vulcain like nozzle. More specific objectives were to study the influence of different structural response of the nozzle on the side load magnitude and investigate the degree of aeroelastic coupling.
VolvoS2	Parabolic contour	20.8		S2 was dedicated to investigating the same h/w as S1 with an applied extension. The nozzle length was increased with approximately 25 %. The extension was made in such a way that the pressure gradient was relatively high in the extension. The chief objective was to study the impact on the end-effect side load peak.
VolvoS3	Parabolic contour	18.2		This nozzle is a more refined scaling of the Vulcain nozzle compared with S1. The idea was here not only to duplicate the nozzle wall geometry, pressure and Mach number profile, but also to imitate the internal flow-field. As the chemistry is completely different, hydrogen / oxygen vs. air, it is impossible to get identical flow patterns. The contour was however made to have the same wall pressure profiles and Mach number distribution and the internal shock as close as possible to the Vulcain.
VolvoS4	Parabolic Polygon	18.2		The Polygon nozzle is a patented Volvo invention. The aim of the Polygon nozzle is to have a design with a side load reduction relative to a normal axi-symmetric nozzle. The shape is three-dimensional, see the figure. This Polygon nozzle has an identical base-line contour as S3. The nozzle was made as an octagon with the polygonisation starting at the predicted position for the separation pattern transition. The objective was to evaluate the degree of side-load reduction with this concept.
VolvoS5	Parabolic contour (VolvoS3) + Positive pressure gradient on the second bell	18.2		S5 is a Dual-Bell nozzle, i.e. another FSC concept. This is a well-known nozzle type since several decades. Actual testing with separation has however been very limited and side load measurements were lacking when these test where performed. The contour of S5 is equal to S3 in the first upstream section. This constitutes the first bell. The dual-bell contour used for this nozzle is then designed according to the principle of positive pressure-gradient in the second bell. This means that the separation front in theory will travel directly from the start of the second bell out to the exit during the start transient.
VolvoS6	Truncated Ideal Contour (TIC)	20.7		S6 is a truncated ideal contoured nozzle, i.e. from a different family of contours compared with S1-S5. This type of nozzle has no internal shock why it only features free shock separation. The primary objectives were to investigate the separation and side-load behaviour in this type of nozzle.
VolvoS6 short	Truncated Ideal Contour (TIC), same contour as VolvoS6	13.9		This is a shorten S6 nozzle. The objective was to investigate the influence of changes in the geometry downstream of the separation on the separation location and corresponding side-load.
VolvoS7	High Pressure Gradient (HPG)	24.6		In nozzles with an internal shock it exist a driving mechanism for transition between two different separation patterns. However, the contour can be design such as this transition is suppressed. Hence, it will only be free shock separation in the nozzle. With the S7 nozzle this type of design was demonstrated.
VolvoS7 short	High Pressure Gradient (HPG)	20.3		This is a shorter version of the S7 nozzle. The objective was to investigate the influence of the downstream geometry on the separation and side-load.
VolvoS8	HPG with film injection	22.1		The S8 nozzle is a HPG contour with film injection. This nozzle was designed to have similar flow properties regarding mass flow rate and film injection pressure ratio as the film cooled Vulcain 2 and Vulcain 2+ nozzle. The objective was to study the impact of film injection on separation and side-loads.

Table 1. Sub scale nozzles tested by VAC at FFA's HYP500 facility.

The following papers are included in the Appendix:

Paper 1
R 5   Mattsson, J. (changed name to Östlund 1999), Högman, U., and Torngren, L., ''A Sub-Scale Test Programme on Investigation of Flow Separation and Side-Loads in Rocket Nozzles'', Proceedings of the 3rd European Symposium on Aerothermodynamics of Space Vehicles, ESA-ESTEC, Netherlands, November 24-26, 1998.

Paper 2
R 6   Östlund J., Bigert M., ''A Subscale Investigation on Side-Loads in Sea Level Rocket Nozzles'', AIAA 99-2759, June 1999.

Paper 3
R 104 Östlund J., Jaran M., ''Assessment of Turbulence Models in Overexpanded Rocket Nozzle Flow Simulations'', AIAA 99-2583, June 1999.

Paper 4
R 108 Östlund, J., Damgaard T., Frey M., "Side-Load Phenomena in Highly Overexpanded Rocket Nozzles", AIAA-2001-3684, July 2001.

The author has also contributed to the common FSCD group paper found in R 105, which have also been incorporated in parts in chapters 4 and 6.

In addition, the following work includes results reported by this author in numerous classified technical notes at VAC, ESA/ESTEC and CNES.

Results for which no references are given are previous unpublished results produced specifically for the purpose of the present report. They are mainly based on test results for the VOLVO S1, S3 and S6-S7 nozzles.

2   NOZZLE FUNDAMENTALS

The main system used for space propulsion is the rocket – a device that stores its own propellant mass and expels this mass at high velocity to provide force. This thrust is produced by the rocket engine, by accelerating the propellant mass particles to the desired velocity and direction, and the nozzle is that part of the rocket engine extending beyond the combustion chamber, see Figure 1. Typically, the combustion chamber is a constant diameter duct into which propellants are injected, mixed and burned. Its length is sufficient to allow complete combustion of the propellants before the nozzle accelerates the gas products. The nozzle is said to begin at the point where the chamber diameter begins to decrease. The flow area is first reduced giving a subsonic (Mach number < 1) acceleration of the gas. The area decreases until the minimum or throat area is reached. Here the gas velocity corresponds to a Mach number of one. Then the nozzle accelerates the flow supersonically (Mach number > 1) by providing a path of increasing flow area.

Simply stated, the nozzle uses the pressure generated in the combustion chamber, p_c, to increase thrust by accelerating the combustion gas to a high supersonic velocity. The nozzle exit velocity, v_e, that can be achieved is governed by the nozzle area ratio (i.e., the nozzle exit area , A_e, divided by the throat area , A_t) commonly called the expansion ratio, ε.
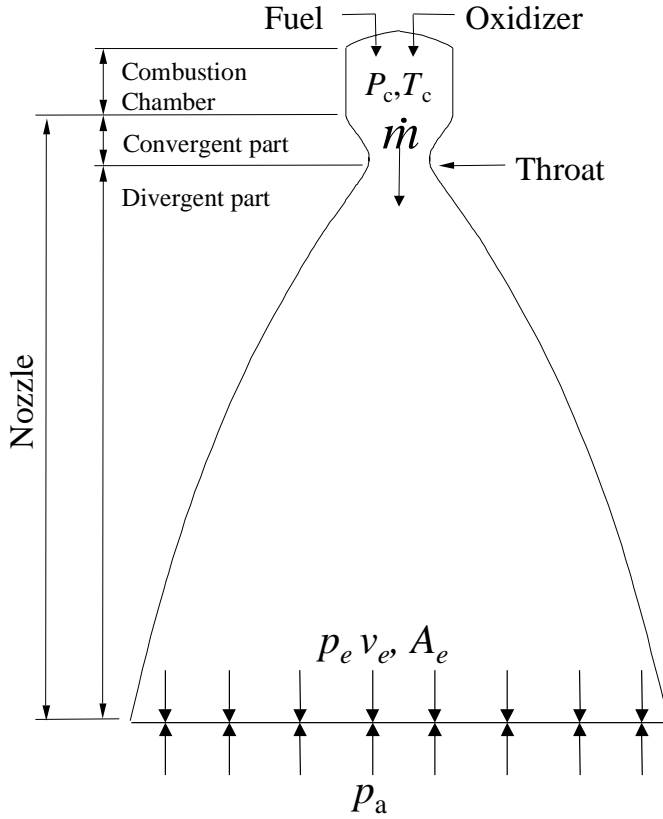
Figure 1. Definition of nozzle.

It can be shown that an ideal nozzle, i.e. the nozzle producing the maximum possible thrust, is a nozzle where the exit pressure is adapted to the ambient pressure. By definition an ideal nozzle expands the throat flow isentropically and produces a parallel uniform exit flow at a prescribed exit Mach number, M_e, or ε. The expansion ratio and the nozzle exit pressure, p_e, for such a nozzle are given by:

$$\varepsilon = \frac{A_e}{A_t} = \frac{1}{M_e} \sqrt{\left[\frac{2}{\gamma+1}\left(1+\frac{\gamma-1}{2}M_e^2\right)\right]^{\left(\frac{\gamma+1}{\gamma-1}\right)}} \qquad \text{Eq. 1}$$

$$p_e = p_c \left(1 + \frac{\gamma - 1}{2} M_e^2 \right)^{\left(\frac{\gamma}{1-\gamma} \right)}$$

<div align="right">Eq. 2</div>

Where γ is the ratio of specific heat capacities.

The thrust, F, produced by the nozzle can be expressed with some commonly used performance parameters in the propulsion community as:

$$F = \left(\dot{m} v_e + p_e A_e \right) - p_a A_e = C_F p_c A_t = \dot{m} I_{sp}$$

<div align="right">Eq. 3</div>

Where $\dot{m}$ is the engine mass flow rate, C_F is the thrust coefficient (dimensionless) and I_{sp} the specific impulse [m/s]. v_e and p_e are average values of the velocity and pressure over the nozzle exit area.

C_F gives the amplification of the thrust due to the gas expansion in the rocket nozzle compared to the thrust that would have been obtained if the chamber pressure only acted over the throat area only.

I_{sp} is a measure of how efficiently a given flow rate of propellant is turned into thrust.

Using the isentropic relations the ideal specific impulse can be written as:

$$I_{sp,ideal} = \frac{F}{\dot{m}} = v_e + A_e \frac{p_e - p_a}{\dot{m}} = \sqrt{\frac{2\gamma R T_c}{\gamma - 1} \left[1 - \left(\frac{p_e}{p_c} \right)^{\frac{\gamma-1}{\gamma}} \right]} + \sqrt{\frac{R T_c}{\gamma} \left[\frac{2}{\gamma+1} \right]^{\frac{\gamma+1}{1-\gamma}}} \cdot \varepsilon \frac{p_e - p_a}{p_c}$$

<div align="right">Eq. 4</div>

Here, T_c is the combustion chamber temperature and R is the gas constant.

Optimum performance is obtained with pressure matching (i.e. $p_e = p_a$) throughout the vehicle's ascent. Inspection of equation 1,2 and 4 indicates that this requires a variable ε i.e. an adaptable nozzle. However the required mechanism for such a nozzle is usually complex, heavy and difficult to cool and has therefore only been demonstrated in experimental rockets. Instead, a nozzle with a fixed expansion ratio is chosen as a compromise taking into consideration the performance requirement throughout the flight trajectory, see Figure 2.

Any off-design operation with either overexpanded or underexpanded exhaust flow induces performance losses. These inherent losses due to non-adapted flow condition for fixed geometry nozzles may rise up to 15%, compared to a continuously adapted exhaust flow.[R 9] In principle, a first- or main stage rocket nozzle could be designed for a high area ratio in order to achieve high vacuum performance, but the flow would then separate inside the nozzle during low altitude operation, with an ensuing risk for side-load generation. The requirement of stable nozzle operation on ground together with high vacuum performance lead to the design of a nozzle that is highly overexpanded, but operationally full flowing at sea level condition, but significantly underexpanded at high altitude operation ($p_a=0$), where the main part of the flight trajectory takes place, and hence gives a low overall performance. This is illustrated in Figure 2, which compares the performance (specific impulse) during flight of an adapted ideal nozzle with an ideal and a real rocket nozzle (i.e. losses are included), both with fixed area ratio, $\varepsilon=45$, as a function of altitude respectively. It can be seen that there is a great potential for performance increase if the negative effects associated with flow separation can be handled.
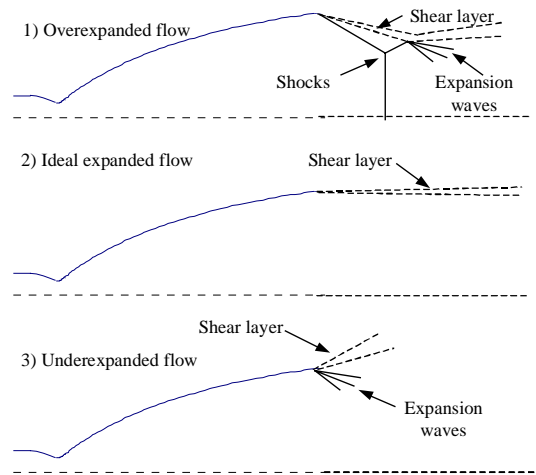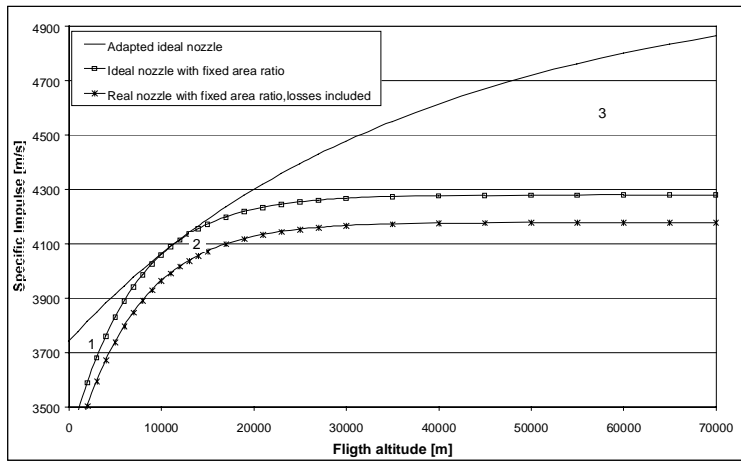
Figure 2. Performance and flow phenomena of a real nozzle versus altitude. (The model by Oates[R 10] has been used for modelling the decrease in atmospheric pressure with altitude.)

3   NOZZLE CONTOUR DESIGN AND FLOW FIELD

Different types of conventional convergent-divergent rocket nozzles exist, each producing their own specific internal flow field. Before analysing separation and side-loads in rocket nozzles, it is essential to understand the features of the different contour types, as the internal flow field determines the characteristics of the nozzle separation behaviour. Figure 3 shows examples of the Mach number distribution in some of the most common nozzle types. Methods to generate these nozzle contours will be discussed in the following.
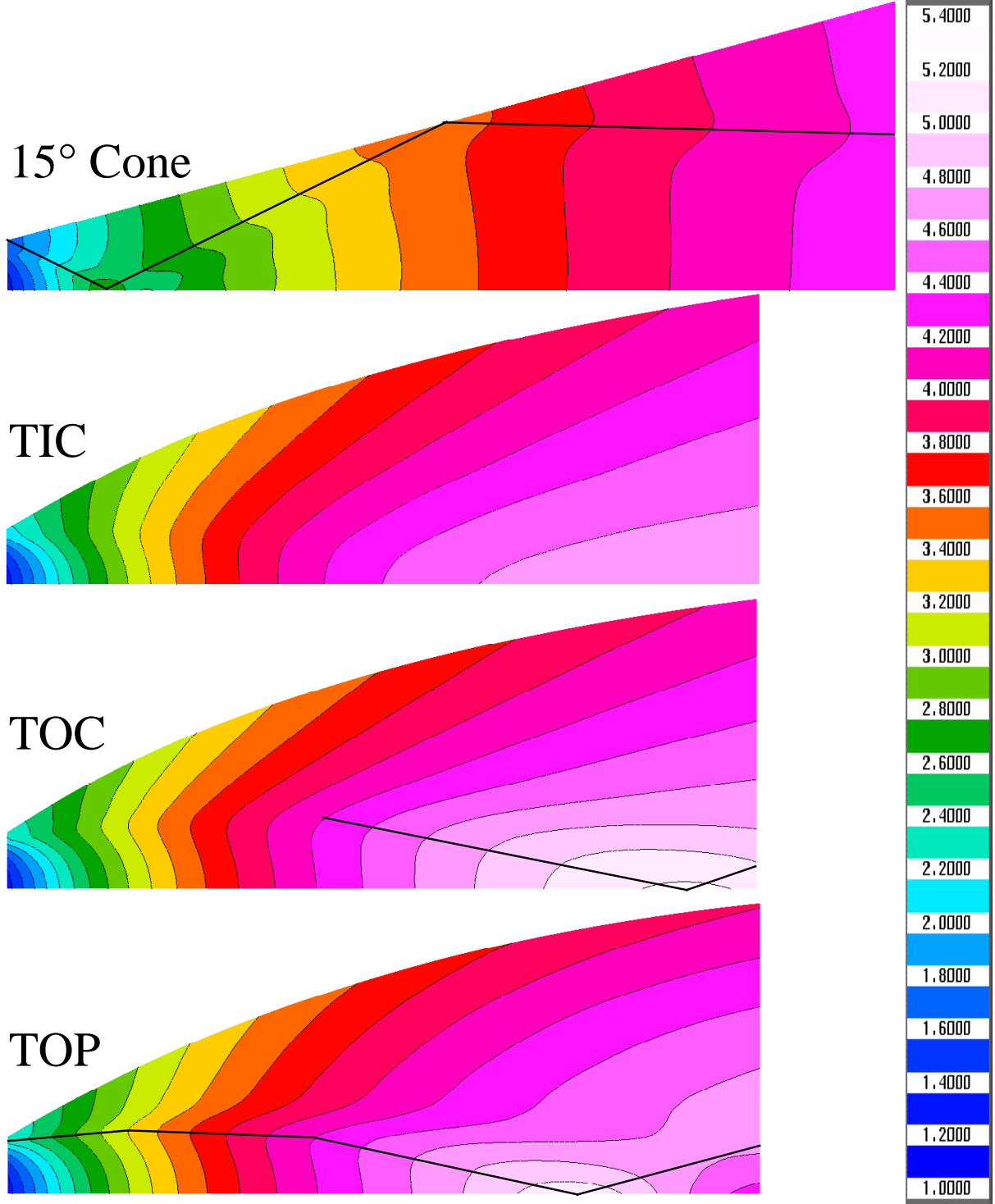
Figure 3. Mach number distribution in a 15° conical (ε=43.4, L=20.9), TIC (M_D=4.67, ε=43.4, L=17.7), TOC (ε=43.4, L=17.7) and TOP (ε=43.4, L=17.7) nozzle (From top to bottom). The thick line indicates the approximate position of the internal shock.

3.1 INTRODUCTORY REMARKS

3.1.1 Losses

A real rocket nozzle is subject to different losses. The loss mechanisms fall into three categories: 1) geometric or divergence losses, 2) viscous drag losses and 3) chemical kinetic losses. Geometrical losses arise when a portion of the nozzle exit flow is directed away from the nozzle axis, resulting in a radial component of momentum. By calculating the momentum of the actual nozzle exit flow and comparing it to the ideal, parallel and uniform flow condition, the geometric efficiency, η_{geo}, can be determined. This also includes profile losses due to a non-uniform velocity profile at the nozzle exit, e.g. caused by small recompression waves in the nozzle flow. By careful shaping of the nozzle wall contour, relatively high geometric efficiency can be obtained.

A drag force, produced by the viscous effects at the nozzle wall, acts opposite to the direction of the thrust, and therefore results in a decrease in nozzle efficiency. This viscous drag efficiency is defined as:

$$\eta_{drag} = 1 - \frac{\Delta C_{F,drag}}{C_{F,ideal}} \qquad \text{Eq. 5}$$

where C_F is the thrust coefficient and $\Delta C_{F,drag}$ is the difference in C_F due to viscosity The drag force is obtained by calculation of the momentum deficit in the wall boundary layer. The third nozzle loss mechanism is due to finite-rate chemical kinetics. Ideally, the engine exhaust gas reaches chemical equilibrium at any point in the nozzle flow field, instantaneously adjusting to each new temperature and pressure condition. In real terms, however, the rapidly accelerating nozzle flow does not permit time for the gas to reach full chemical equilibrium. The chemical kinetics efficiency is calculated by comparing the one-dimensional kinetics (ODK) solution to the one-dimensional equilibrium (ODE) solution, or:

$$\eta_{kin} = \frac{C_{F,ODK}}{C_{F,ODE}} \qquad \text{Eq. 6}$$

The combined effects of geometric loss, viscous drag and chemical kinetics then give the overall nozzle efficiency:

$$\eta_{noz} = \eta_{geo}\eta_{kin} - (1 - \eta_{drag}) \qquad \text{Eq. 7}$$

Which typically varies between 0.90-0.98.

The optimum nozzle contour is a design compromise that result in a maximum overall nozzle efficiency. Experience tells the nozzle designer that a long nozzle is needed to maximise the geometric efficiency; but at the same time, nozzle drag and nozzle weight is reduced if the nozzle is shortened. If chemical kinetics is an issue, then acceleration of exhaust gases at the nozzle throat should be slowed down by increasing the radius of curvature of the throat region, at the cost of an increased nozzle length.

3.1.2 Computational methods

In supersonic flow the Euler equations are hyperbolic i.e. the flow is only determined by the upstream conditions. In this case the method of characteristics (MOC) can be used to calculate the nozzle flow field. This method is the most commonly used in the rocket nozzle society for generating nozzle contours and determining loads and performances. This method is described in any basic book about compressible flow see e.g. the classical book by Shapiro[R 11]. This is e.g. the basic method used for wind tunnel design.

For the present work, Volvo in-house MOC codes for design of different types of nozzle contours is used.

For evaluation calculation, the Two-Dimensional Kinetics nozzle performance code (TDK) by Frey and Nickerson[R 12] is the most commonly used and validated MOC program in the west. TDK can perform a

complete two-dimensional nozzle performance calculation including boundary layer and non-equilibrium chemical reactions. Thus, losses due to divergency, viscous drag and chemical kinetics effects are included.

3.1.3   Initial expension region

In a nozzle the initial expansion occurs along contour TN, see Figure 4, and this determines the character of the downstream flow field. Choosing a corner expansion as the initial expansion TN yields a slightly shorter nozzle than the one obtained with a radius downstream of the throat for any given expansion ratio. However in rocket application a sharp corner downstream the throat are generally avoided due to chemical kinetics effects and a wall contour TN having a radius of curvature equal to 0.5 times the throat radius i.e. $r_{td}=0.5r_t$, are widely used. Using a transonic-flow analysis, a constant Mach-number line TO can be defined at the throat. Given the flow condition along TO and the solid boundary TN, a kernel flow field TNKO can be generated with the method of characteristics. The flow in the kernel is entirely determined by the throat conditions and constitutes the expansion zone. This kernel is the basis in all MOC design methods.
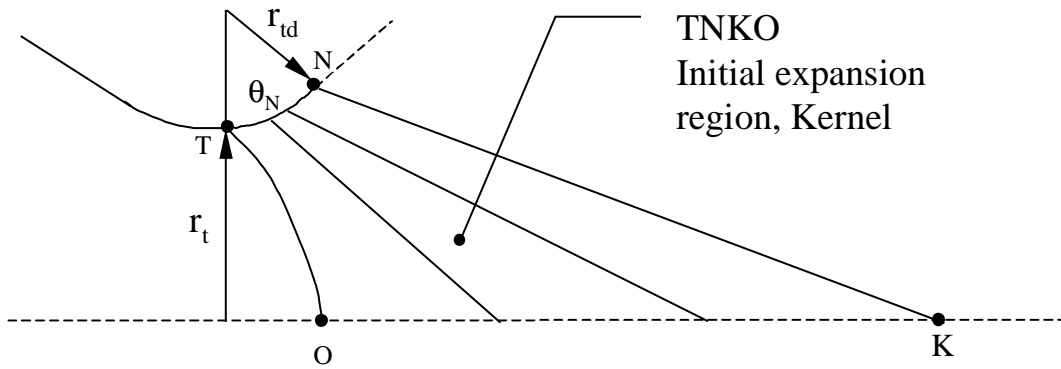
Figure 4. Initial expansion region, kernel.

3.2   CONICAL NOZZLES

The conical nozzle, Figure 3 and Figure 5, is historically the most common contour for rocket engines since it is simple and usually easy to fabricate. There is a record of extensive nozzle research in the subject by the German scientists at Peenemünde. For the low area ratio nozzles considered for the V-2 rocket no significant advantage of using more complicated contours was found, probably due to the manufacturing reasons.
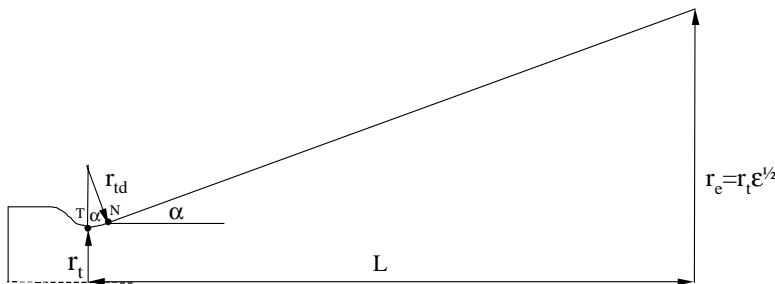
Figure 5. Definition of conical nozzle.

The exhaust velocity of a conical nozzle is essentially equal to the one-dimensional value corresponding to the expansion ratio, with the exception that the flow directions are not all axial. Hence, there is a performance loss due to the flow divergence. Assuming conical flow at the exit Malina[R 13] showed that the geometrical efficiency become:

$$\eta_{geo} = \frac{1+\cos\alpha}{2}$$

Eq. 8

Where α denotes the nozzle cone half angle.

The length of the conical nozzle can be expressed as:

$$L_{\alpha^\circ,cone} = \frac{r_t\left(\sqrt{\varepsilon}-1\right)+r_{td}\left(\sec\alpha-1\right)}{\tan\alpha} \qquad \text{Eq. 9}$$

Typically, cone half angles can range between 12° to 18°. A common compromise is a half angle of 15°. Due to its high divergence losses, the conical nozzle is nowadays mainly used for solid rocket boosters with small expansion ratios and small thrusters where simple fabrication methods are preferred. Nevertheless, a 15° conical nozzle is often used as a reference in comparing lengths and performance of other types of nozzles. A term used when designing bell nozzles is the "percent bell". The phrase refers to the length of the nozzle compared to a 15° half-angle conical nozzle with the same ε.

3.3   IDEAL NOZZLE

As mentioned above, the ideal nozzle is a nozzle that produces uniform exit flow conditions. The nozzle contour, which achieves this, can be designed with MOC. An outline of an ideal nozzle flow is shown in Figure 6.
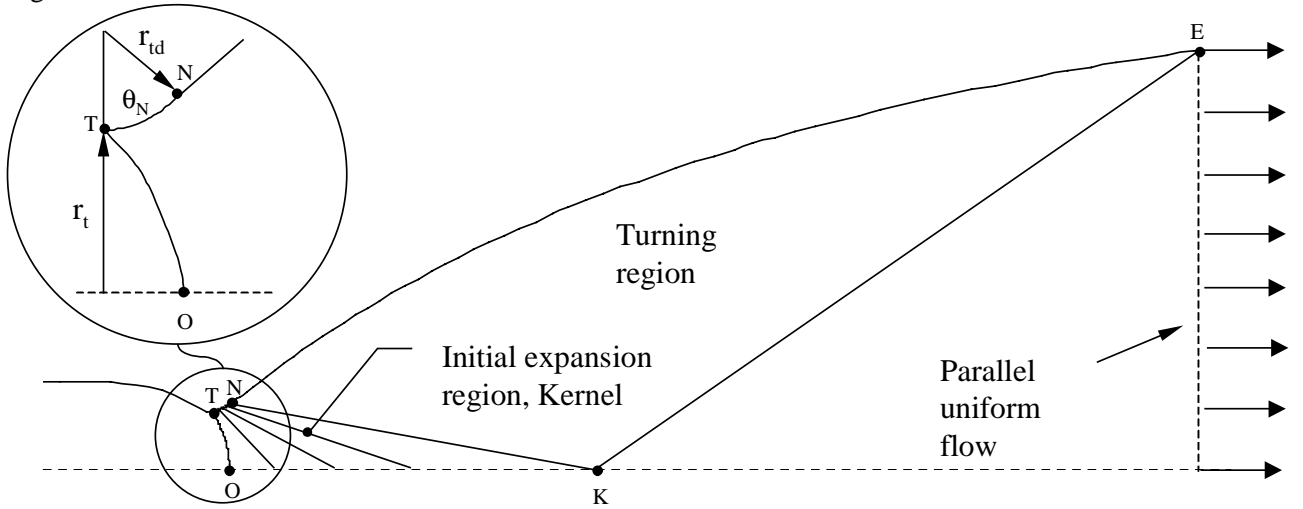
Figure 6. Basic flow structures in an ideal nozzle.

Contour TNE is the diverging portion of the nozzle. After the initial expansion TN, the contour NE turns the flow over to axial direction. TN also defines the Mach number at K, which is equal to the design Mach number obtained at the exit. With the Mach line NK defined it is possible to construct the streamline between N and E with the use of MOC which patches the flow to become uniform and parallel at the exit and thus complete the nozzle design. In Figure 7 the left and right running characteristics are shown for an ideal nozzle. The design Mach number is M=4.6 and the gas properties are γ=1,2 with a molecular mass =13.63 g/mole. The TDK program was used to generate the starting line TO.
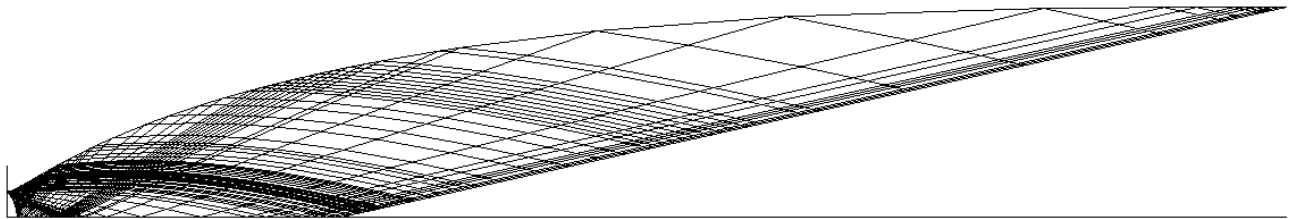
Figure 7. Left and right running characteristics for an ideal nozzle. M_{Design}=4.6, γ=1.2, $L\approx50r_t$.
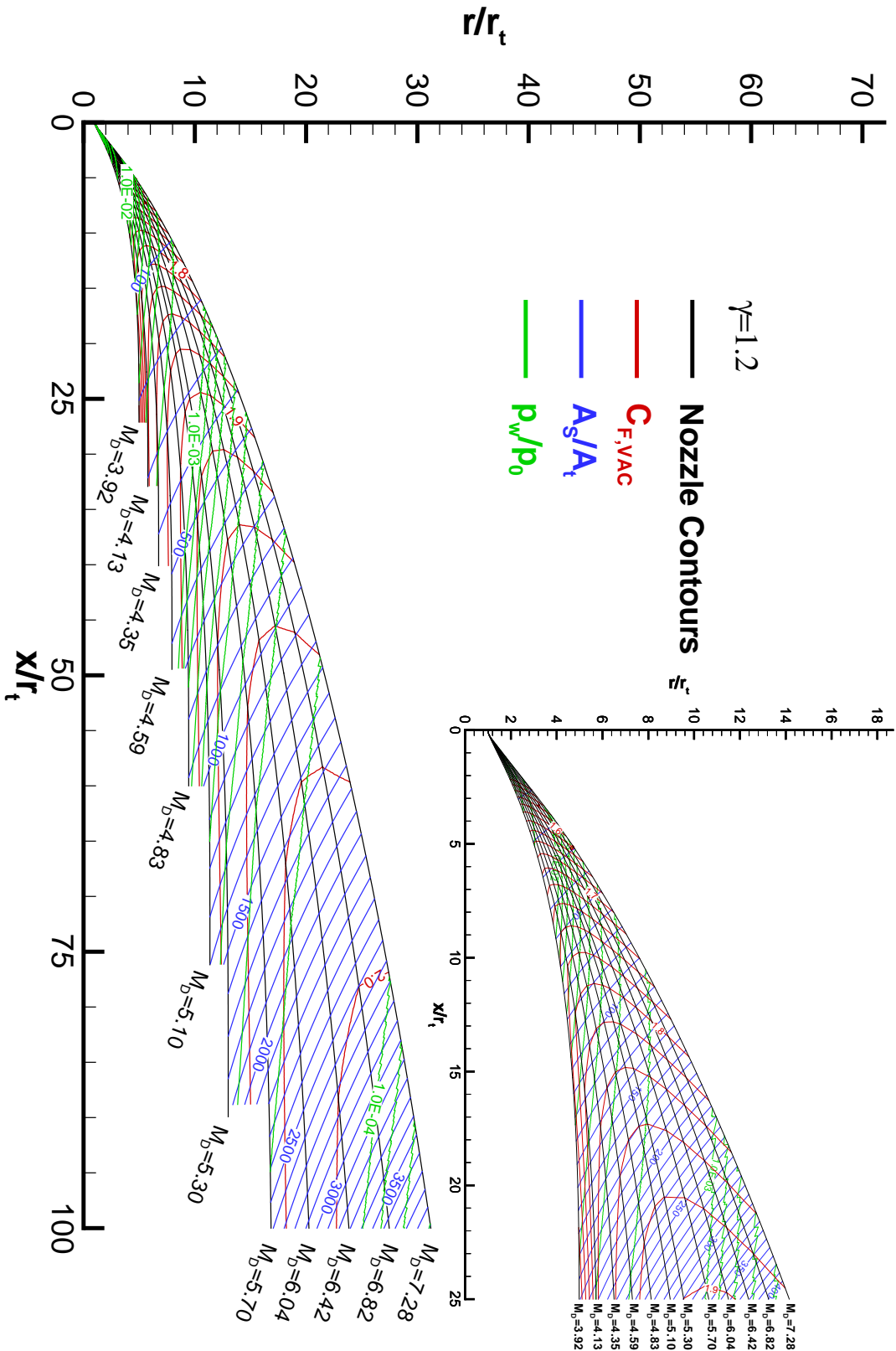
Figure 8. Ideal nozzle contours together with lines representing constant surface area, vacuum thrust coefficient and wall pressure respectively. (The 12 ideal contours have been generated with a Volvo in-house program and the performance have been calculated with TDK with boundary layer losses included)

3.3.1 Truncated Ideal Contoured nozzles (TIC)

The ideal nozzle is extremely long ($L \approx 50 r_t$ in the specific case shown in Figure 7), and consequently is not practically feasible for rocket applications. The huge length is necessary to produce a one-dimensional exhaust profile. However, the thrust contribution of the last part of the contour is negligible due to the small wall slopes. A feasibly rocket nozzle can be obtained by truncating the contour, such contours are called truncated ideal contours (TIC). Ahlberg et al[R 24] proposed a graphical technique for selecting optimum nozzle contours from a family of TIC nozzles. The LR-115, Viking and the RD-0120 nozzle are examples of TIC nozzles. The method can be outlined as follows, a complete set of ideal nozzle contours is synthesised in a plot together with lines representing constant surface area, exit diameter, length and vacuum thrust coefficient respectively, see Figure 8. Within a given constraint such as expansion ratio (or exit diameter), surface area, or length an optimisation process can then be used to determine where to truncate the full nozzle contour to obtain maximum performance. The optimisation is best visualised by considering an enlarged section of the typical plot described above, see Figure 9. Point A in the figure, which is the point where the thrust coefficient line is tangent to a line of constant radius, r/r_t, is the optima representing the exit point of a nozzle contour yielding maximum thrust for a given expansion ratio. Similarly, point B, the point which the thrust coefficient line is tangent to the constant surface area line, A_s/A_t, representing the optima for a given surface area. Nozzle of maximum performance for a given length is represented by point C. Point D in the figure represents the most thrust obtainable from any given nozzle contour. When the contour extends beyond this point, wall friction becomes greater than the pressure forces giving a negative thrust contribution, which decreases the total performance. These sets of nozzles are not of practical interest, since the set of nozzles represented by point A has the same thrust but are smaller, i.e. shorter and smaller expansion ratio. As an example, the right and left running characteristics of a truncated ideal nozzle are shown in Figure 10 and corresponding Mach number distribution is shown in Figure 3. For this case the nozzle was optimised versus minimum surface area.
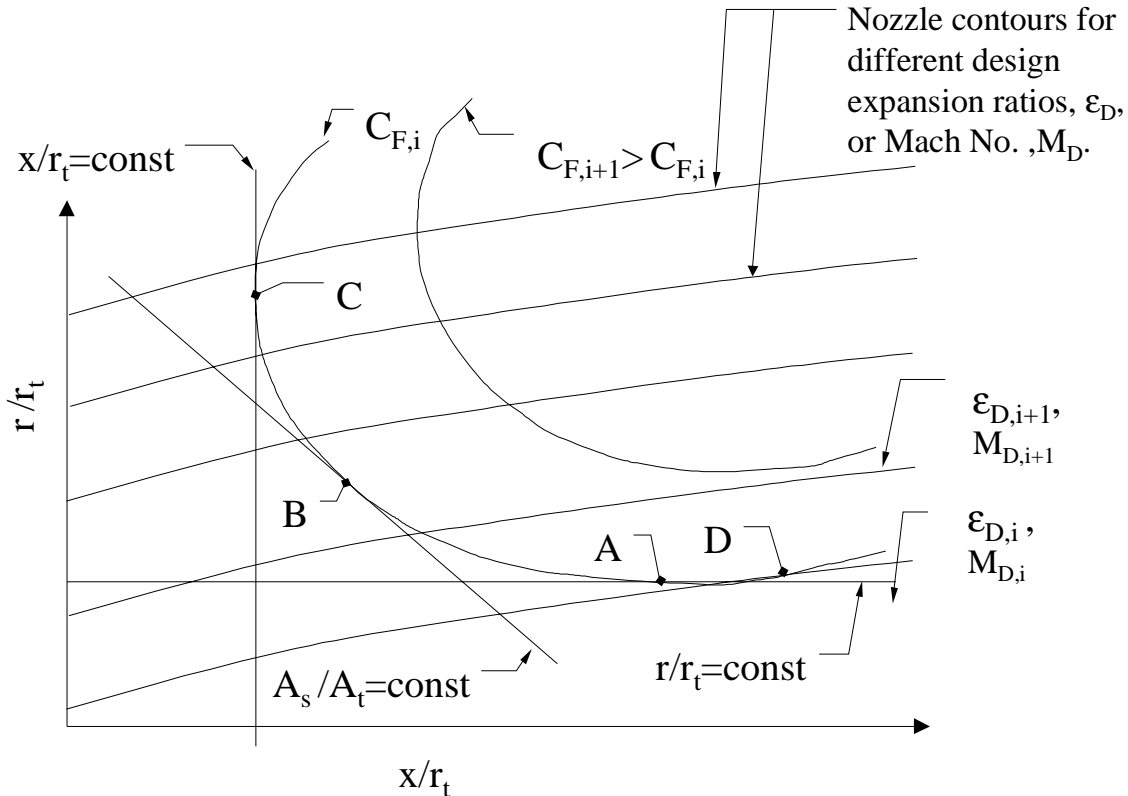
Figure 9. Illustration of optimum nozzle for given constraints.
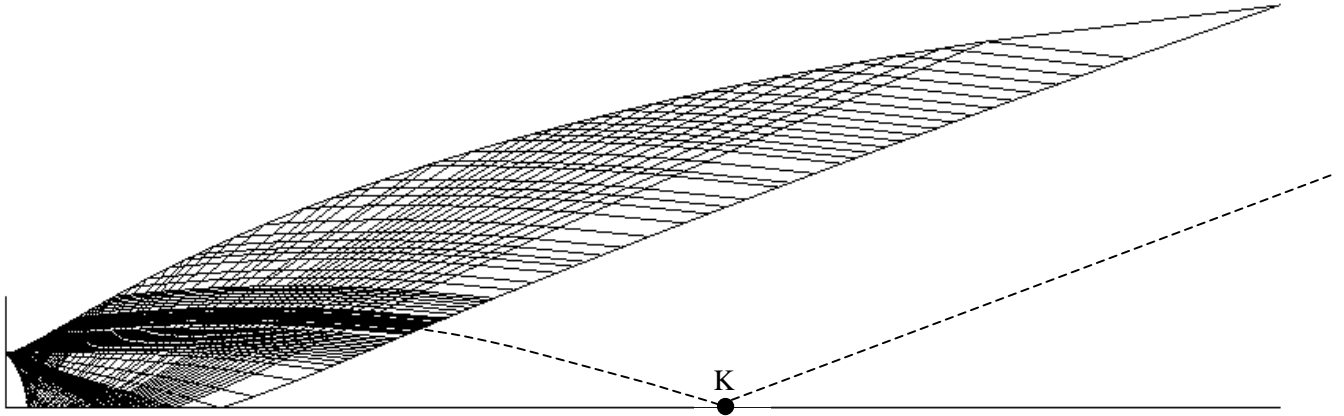
Figure 10. Left and right running characteristic lines in a truncated ideal contoured (TIC) nozzle. Obtained by truncating the ideal nozzle given in Figure 7 at $x/r_t \approx 18$.

3.3.2   Compressed Truncated Ideal Contoured nozzles (CTIC)

In 1966 Gogish[R 135] suggested a method to design extremely short nozzles. The basis of the method is to linearly compress a TIC nozzle. He suggested that such compressed truncated ideal contours (CTIC) or compressed truncated perfect contours (CTPC) as it is sometimes labelled, may have higher performance than a Rao nozzle (see next section) for the same envelope. A CTIC nozzle is obtained by linearly compressing of a TIC nozzle in the axial direction to obtain the desired nozzle length. A discontinuity in the nozzle slope produced in the above compression procedure is eliminated by a cubic equation which smoothly connects the linearly compressed curve with the initial circular curve. The above procedure yields a nozzle which has a more rapid initial expansion followed by a more severe turn back, as compared to the TIC nozzle. As a consequence, strong right-running compression waves will propagate from the compressed contour into the flow field. If the compression is strong enough, the characteristic lines will coalesce and form a right running oblique shock wave. The shock wave will increase the static pressure as the flow crosses the shock wave. If the shock wave lies near the nozzle wall, the pressure along the wall will be increased, thus increasing the nozzle thrust. This effect is the mechanism Gogish considered when he suggested that the compressed nozzle might yield higher performance than a Rao nozzle. However, as the study by Hoffman[R 136] showed, this is not the case. Hoffman found that the Rao nozzle is superior to the CTIC nozzle. For some designs, however, the difference in performance was quite small indicating that an optimum CTIC nozzle is certainly a good propulsive nozzle. As an example the LE7A is probably a CTIC nozzle.

3.4   THRUST OPTIMISED CONTOURED NOZZLES (TOC)

A direct and elegant approach of designing nozzle contours is the method of using the calculus of variations. Guderley and Hantsch[R 14-R 15] formulated the problem of finding the exit area and nozzle contour to produce the optimum thrust, for prescribed values of the nozzle length and the ambient pressure. However, the method was not widely adopted until the complicated solution method presented by Guderley and Hantsch was simplified significantly by Rao.[R 16] Therefore the obtained nozzle contour is often labeld a Rao nozzle in the west. In Russia this nozzle type is better known as a Shmyglevsky nozzle since Shmyglevsky independently formulated the same method in Russia.[R 17-R 20]. The basic idea behind the method of generating a Rao-Shmyglevsky nozzle or the thrust optimised contour (TOC) as it sometimes is called are outlined in Figure 11. First, a kernel flow is generated with MOC, for a variety of θ_N and a given throat curvature r_{td}. For given design parameters (such as ε and M_E or ε and L) the points P and N can now be found by satisfying the following conditions concurrently:

1. Mass flow across PE equals the mass flow across NP.
2. The resulting nozzle gives maximum thrust.

By using the calculus of variations, these conditions are formulated as specific relations that must be fulfilled along PE and NP see e.g. reference R 16.
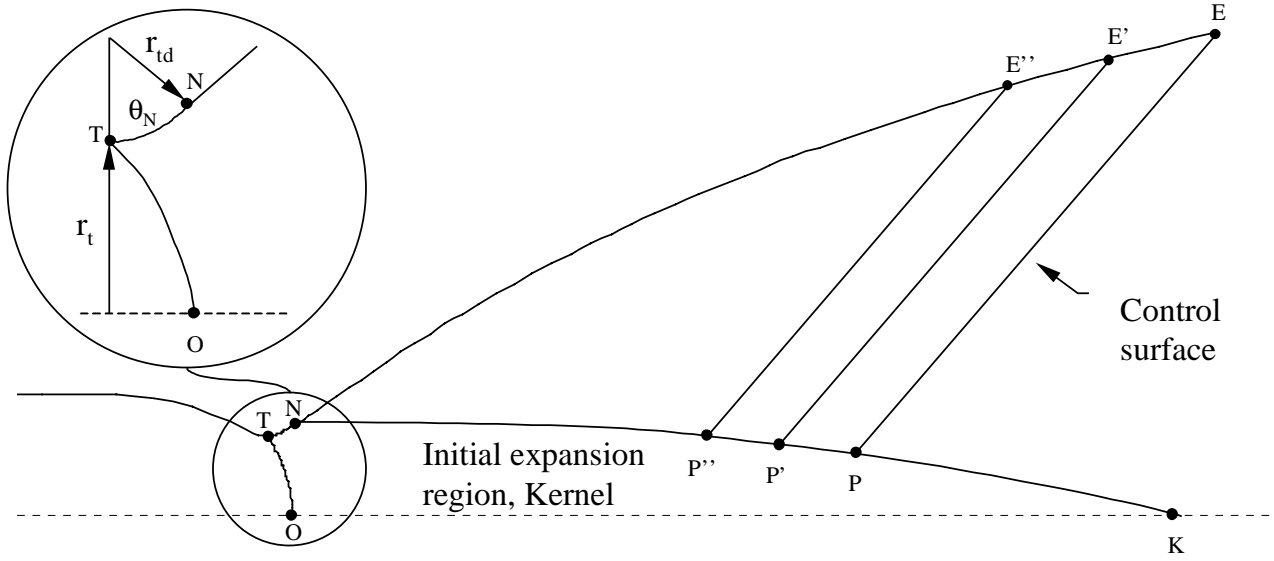
Figure 11. Thrust optimised nozzle contour.

Once N and P are known, the kernel line TNKO is fixed, and the contour line NE is constructed in the following manner: By selecting points P', P'', etc. along line NK, a series of control surfaces P'E', P''E'', etc. can be generated to define E', E'', etc. along the contour NE.

In Figure 12 and Figure 13 the left and right running characteristics are shown for a Rao-Shmyglevsky nozzle. In Figure 3 the appertaining Mach number distribution can be seen. The design expansion ratio and length is ε=43.4 and L=17.7r_t respectively and this nozzle has the same performance as the TIC nozzle presented in Figure 3 and Figure 10. The same initial conditions and gas properties as for the ideal nozzle design have been used.

It should be emphasised that the method produces a shock free flow in the region NPE governing the wall pressure. This is seen in Figure 13, where the characteristics do not cross each other. If point P is equal to point K, an ideal nozzle is produced by definitions. However, when P≠K a more drastic turning of the flow is obtained compared with an ideal nozzle, and compression waves formed in region NPE will coalesce into a right running shock downstream of the control surface PE, see Figure 3.

The thrust optimised contour has a significant increase in geometric efficiency compared with a 15° half-angle conical nozzle conical nozzle having the same expansion ratio see e.g. Huzel and Huang[R 21]. The corresponding length is in general between 80%-100% of the conical one. In Figure 14 a synthesis of the nozzle end points for 159 different Rao-Shmyglevsky contours with initial expansion angles between θ_N=25-34° are shown. Superimposed on the plot of these end points are lines of constant surface area, constant vacuum thrust coefficient and exit wall pressure. The thrust coefficient includes both drag and geometrical losses and has been calculated using the program by Frey and Nickerson[R 12]. With the use of Figure 14, the designer get the first indication of the main dimensions of a TOC nozzle for a prescribed performance value, which can be used as a first approximation.
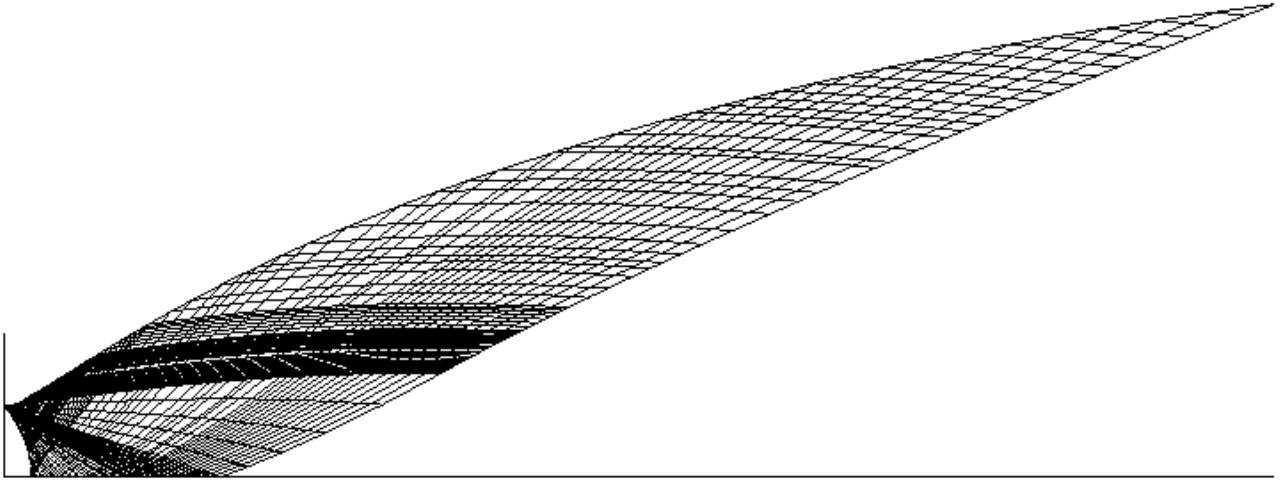
Figure 12. The left and right running characteristic lines in a Rao-Shmyglevsky (TOC) nozzle designed with a VOLVO in-house contouring program.
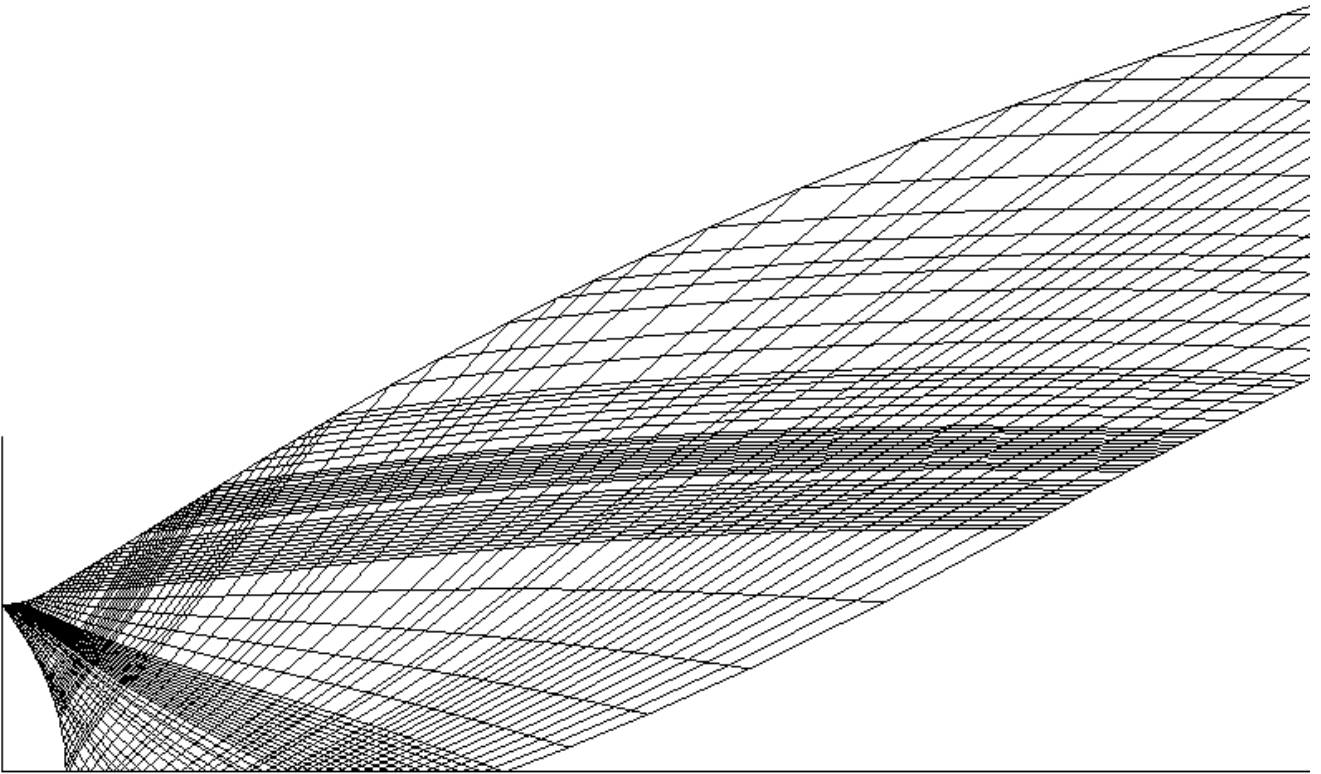
Figure 13. Close up of characteristic lines in the throat region in a Rao-Shmyglevsky nozzle.
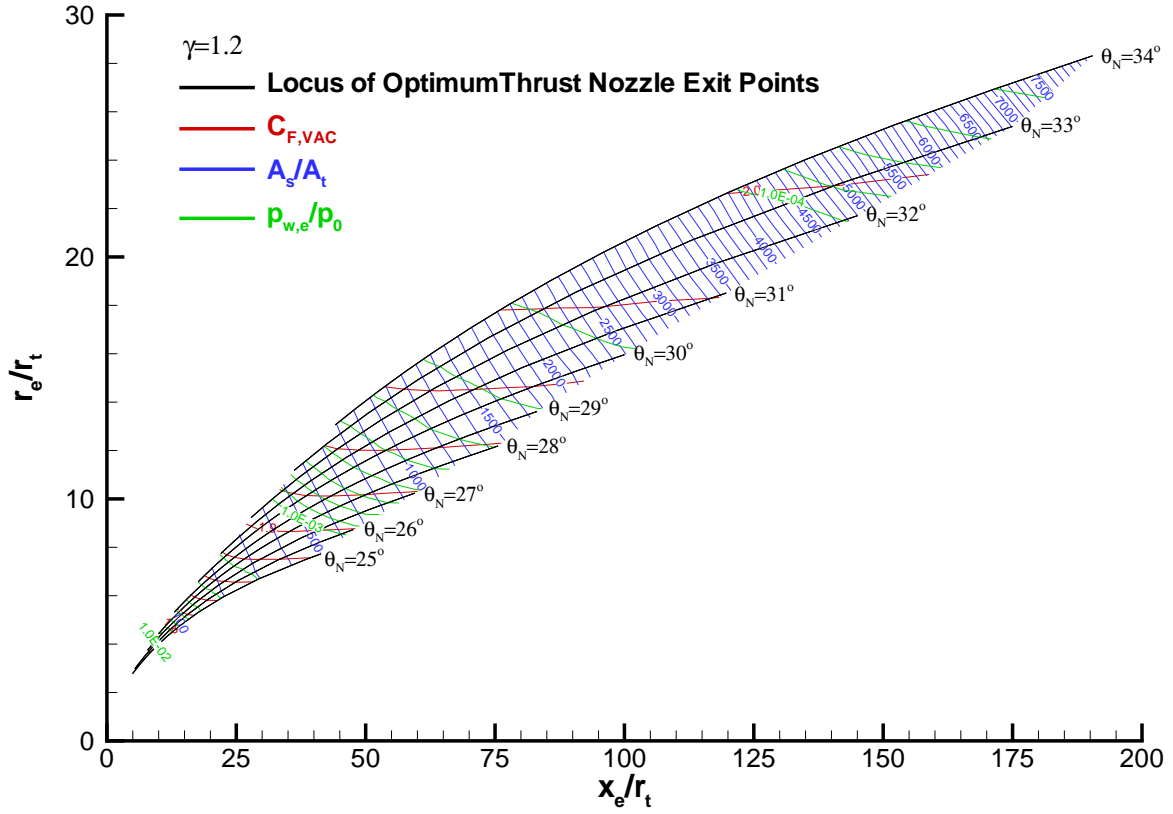
Figure 14. Locus of optimum thrust nozzle exit points for various values of θ_N together with lines of constant surface area, constant vacuum thrust coefficient and wall exit pressure.

As indicated in Figure 15, the shape of the TOC and the TIC nozzle are very similar. The main difference is that the TOC has a higher initial expansion followed by a more drastic turning of the flow compared with the TIC nozzle. This corresponds to a higher wall angle and Mach number downstream the throat and lower values of the angle and Mach number at the exit for the TOC compared with the TIC nozzle. This has no effect on the performance, however, the difference in flow structure will be seen to have large impact on the separation and side-load characteristics.
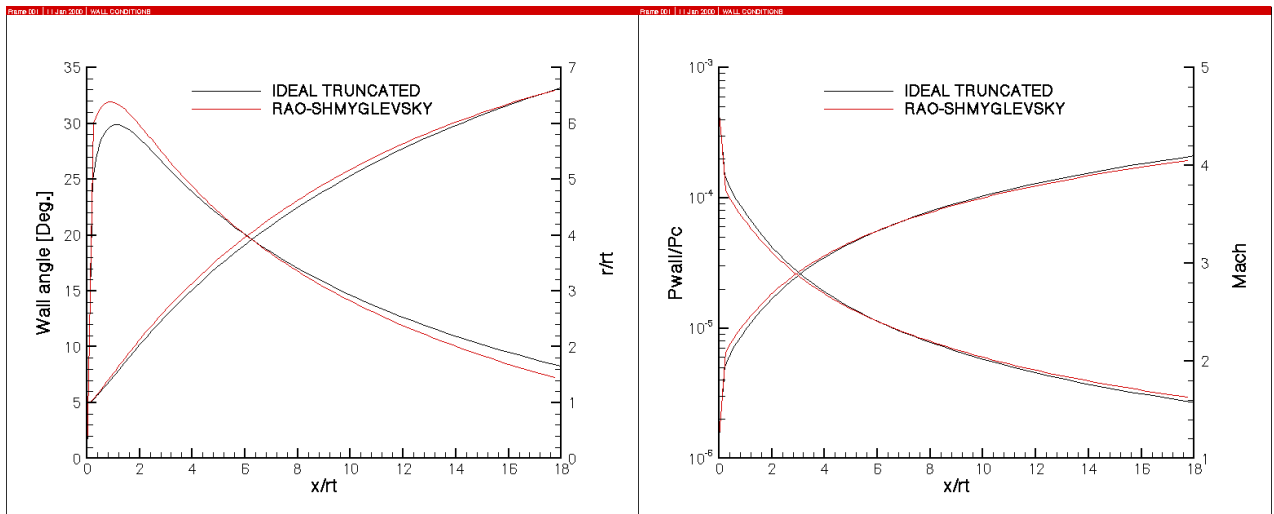
Figure 15. Comparison between an ideal truncated (TIC) nozzle and a Rao-Shmyglevsky (TOC) nozzle.

3.5   PARABOLIC BELL NOZZLES (TOP)

Since the computation leading to the Rao-Shmyglevsky nozzle is rather complicated and the resulting contour can only be described by a co-ordinate list, Rao proposed a skewed parabolic-geometry approximation to the Rao-Shmyglevsky nozzle contour from the inflection point to the nozzle exit[R 22]:

$$\left(\frac{r}{r_t}+b\frac{x}{r_t}\right)^2+c\frac{x}{r_t}+d\frac{r}{r_t}+e=0 \qquad\qquad \text{Eq. 10}$$

These types of nozzles are often referred as Thrust Optimised Parabolic (TOP) nozzles. With a skewed parabola the nozzle contour is entirely defined by the five independent variables r_{td}, θ_N, L, r_e, and θ_E, see definitions in Figure 16a. With these independent variables a infinite number of contours can be generated. Selecting the proper inputs can approximate the Rao-Shmyglevsky (TOC) nozzle accurately without introducing any significant performance loss. Parabolic approximations to a number of Rao-Shmyglevsky contours are shown in Figure 16 b-c.

These charts are used in the following manner:
1. Choose the length fraction L_f that gives the desired nozzle efficiency, Figure 16b
2. Knowing L_f and the desired expansion ratio the initial and final parabolic angles can be extracted from Figure 16c
3. Determine the nozzle configuration by using equation 10.

A common misunderstanding is that any parabolic bell nozzle of 80% length can always replace a 15° conical nozzle to yield increased performance. However, this is not a general truth. Rao[R 23] examined nozzles with an expansion ratio of 100 and found that an arbitrarily chosen parabolic nozzle of 80% length only yielded 0.07% higher inviscid specific impulse than the conical one. He also showed that this parabolic contour could be replaced with a much smaller TOC nozzle, with the same length and performance but only 80% of the expansion ratio.

In Figure 3, Figure 17 and Figure 18 a parabolic-geometry approximation to the TOC nozzle in Figure 12 and Figure 13 is shown. The flow conditions along the wall are almost equal and, as expected, the performance is slightly less then the thrust optimised nozzle. There is however one main difference between the two nozzle flows. At the point N where the circular arc is continued with the parabolic curve there is a discontinuity in the contour curvature. This discontinuity generates compression waves that coalesce into an internal shock upstream the last left running characteristic line, i.e. the crossing of the right running characteristic lines in Figure 18. In a TOC nozzle this shock is formed downstream of the last left running characteristic line and hence has no influence of the wall pressure. In contrast in a TOP nozzle the internal shock appears upstream of this characteristic line, see the comparison between TOP and TOC nozzle in Figure 3, and hence affects the flow properties at the wall, given a slightly higher wall pressure at the nozzle exit. This feature of TOP nozzles has been proved to be useful for sea-level nozzles where a margin against flow separation is important. For this reason the Vulcain and SSME nozzles where designed with parabolic contour. Actually, the initial contour design of the SSME was a TOC. However, with this design the wall pressure at the exit would be about 31 % of the ambient pressure at sea level, i.e. in a range where past experience showed that nozzle flow separation is likely to occur. In order to avoid problems with flow separation, an additional margin in exit pressure was sought. This was done by performing a parametric study of different TOP contours, which resulted in a contour where the additional flow turning (and the accompanying internal shock) resulted in a pressure increase of 24% at the nozzle exit at a cost of only 0.1% in nozzle efficiency compared with the initial TOC design.
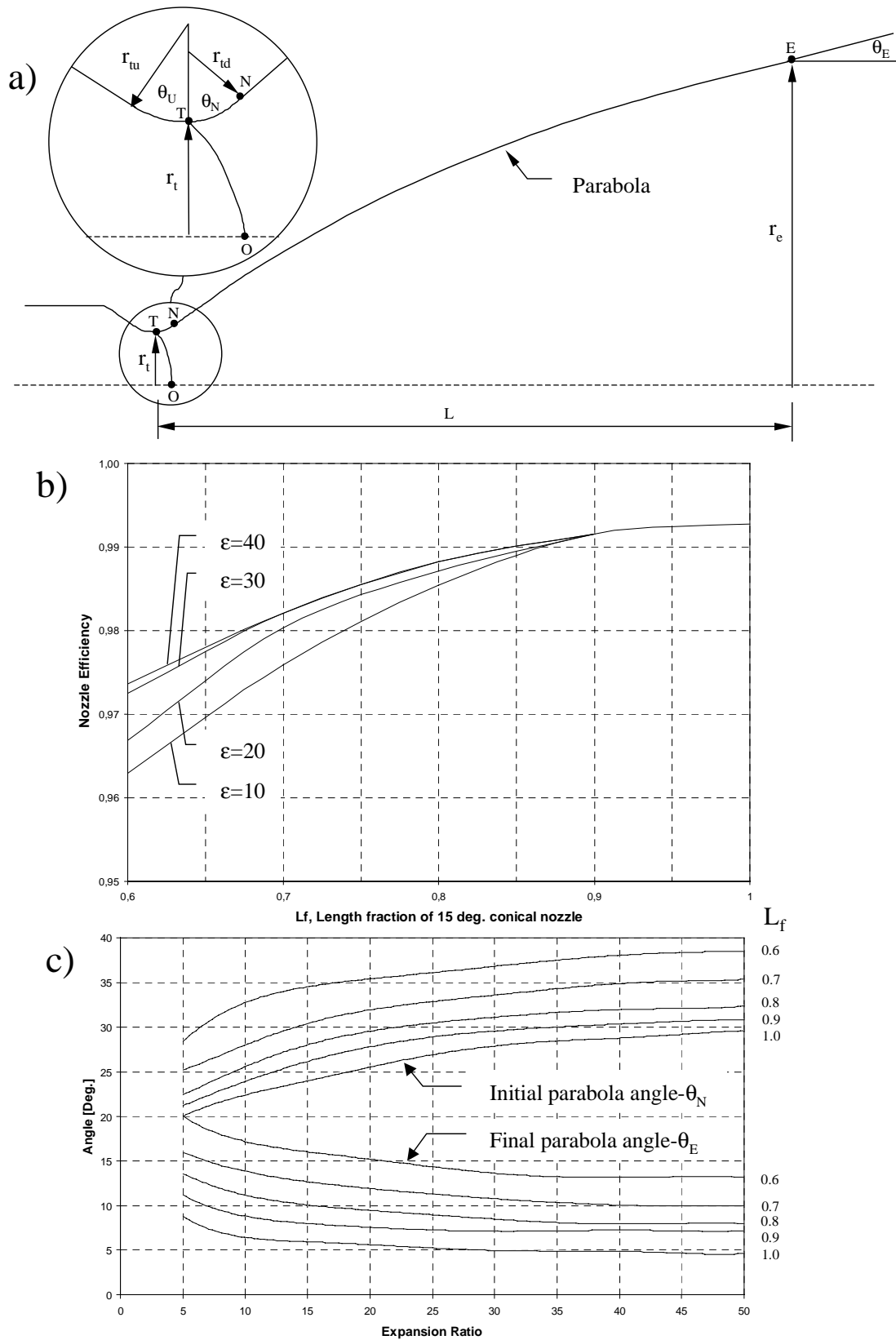
Figure 16. Performance and design data for a parabolic bell nozzle. a) the basic nozzle geometry; b) the geometric nozzle efficiency as function of percent length of an equivalent 15° conical nozzle; c) the initial and final parabolic angles versus desired nozzle expansion ratio (adapted from Rao[R 22]).

19
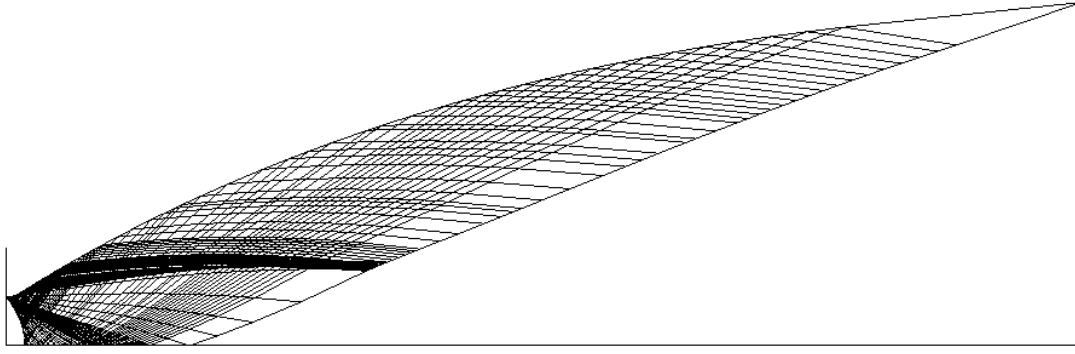
Figure 17. Left and right running characteristic lines in parabolic approximated bell nozzle.
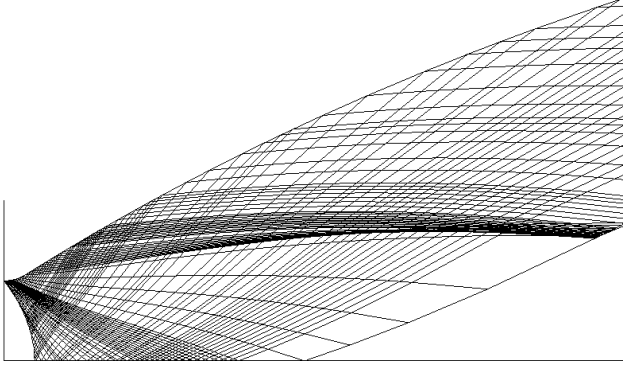
Figure 18. Close up of characteristic lines in the throat region in parabolic approximated bell nozzle.

3.5.1 Influence of skewed parabola design parameters on the flow field

As mentioned before, a skewed parabolic nozzle contour is entirely defined by the five independent variables r_{td}, θ_N, L, r_e, and θ_E, see definitions in Figure 16a. Each of this design parameter has its own influence on e.g. the Mach number distribution in the nozzle. This is illustrated by a series of calculation of TOP nozzle, see Figure 20.

The initial expansion angle, θ_N, specifies the maximum Mach number that can be reached in the nozzle. Increasing this angle will increase the final kernel Mach number M_K, and the wall Mach number M_N at the end of the expansion contour, see illustration in Figure 19 and Figure 20 c) and e). When increasing the value of the downstream wall throat radius of curvature, r_{td}, the extension of the expansion contour and the length of the kernel will increase, Figure 20 c) and d) (The approximate location of the kernel is found by connecting the "knee"-points of the iso-M lines).
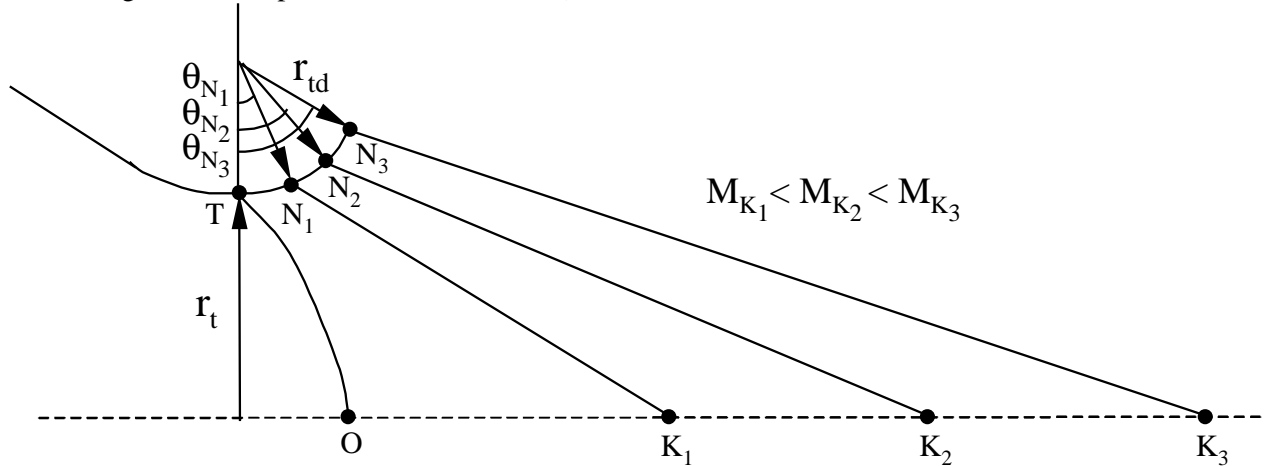
Figure 19. Illustration of kernel region OTNK. Flow inside the kernel is only determined of contour TN.
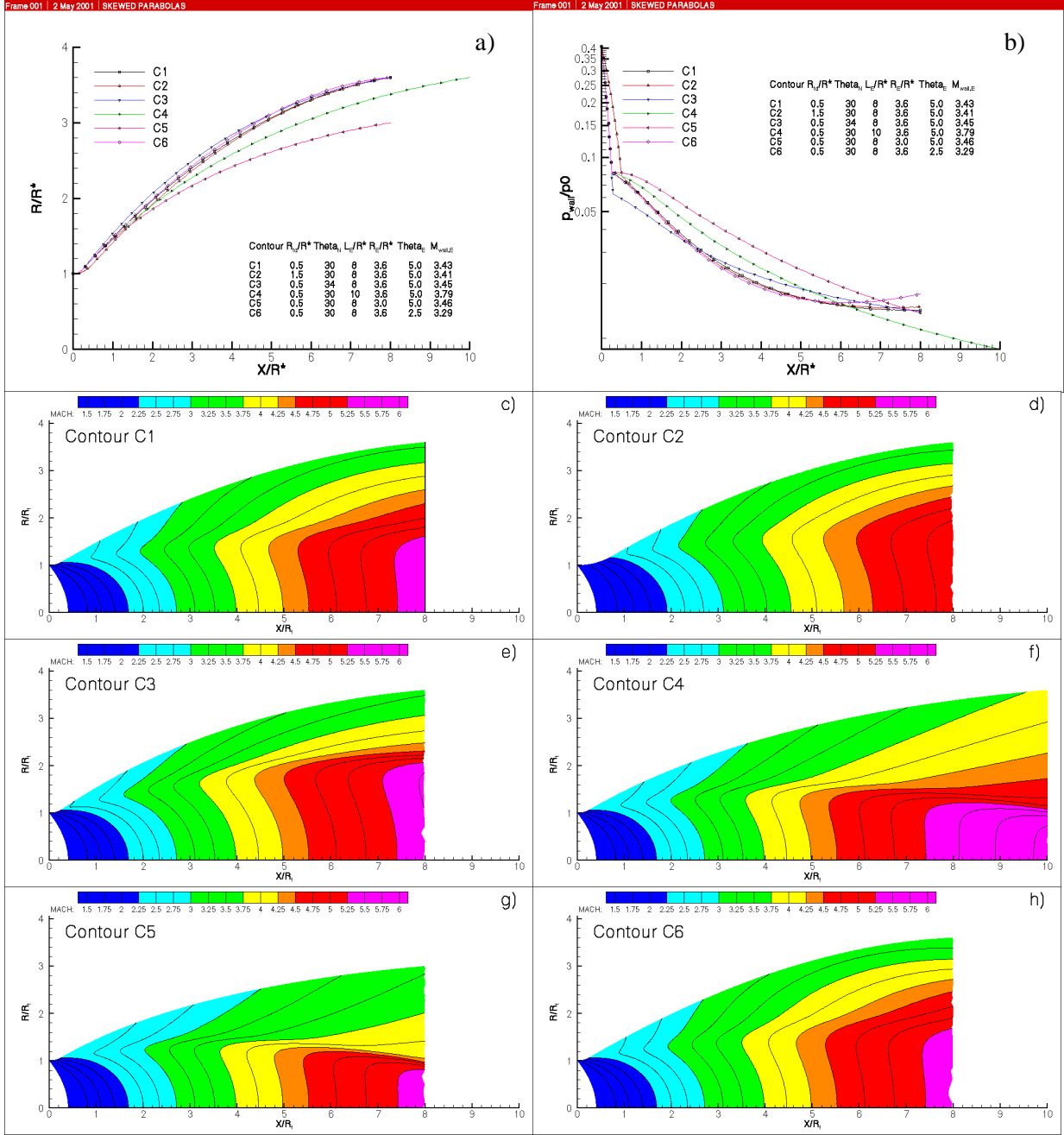
Figure 20. Skewed parabolas. a) Contour definition, b) Wall pressure profiles, c)-h) Iso Mach lines.

The nozzle length, L gives the value of the Mach number on the centre line at the exit for given values of r_{td} and θ_N. When the nozzle length corresponds to the length of the kernel the exit centre line Mach number will be identical to the final kernel Mach number M_K. With a shorter nozzle this value will be reduced. The nozzle length together with the exit radius, r_e, are the main parameters that define the average exit Mach number. The average Mach number and the wall Mach number at the exit will increase when increasing the length of the nozzle, see Figure 20 c) and f). Reducing the exit radius will of course reduce the average exit Mach number. However, no general truth can be said about the influence of the exit radius on the exit wall Mach number. For some cases a reduction of the exit radius will reduce the exit wall Mach number and in other cases increase it. The reason for this is that the contour is not only affected locally at the exit when changing the exit radius, but the entire contour will change. As can be seen in Figure 20 c) and g) a reduction of the exit radius for this special case will give a more severe compression close to the throat followed by a second expansion. This cause the nozzle C5, with a smaller area ratio compared to nozzle C1, to have a higher exit wall Mach number.

The wall pressure gradient and the wall Mach number distribution from the end of the expansion contour to the exit is governed by the nozzle length, exit radius and the nozzle exit lip angle, θ_E. Reducing the exit lip angle will increase the strength of the shock emanating from the inflection point at the end of the expansion contour. Increased shock strength will in turn result in an increase of the wall exit pressure and a reduction of the absolute value of the pressure gradient and the wall Mach number at the exit is achieved. The pressure gradient can even change sign if the exit lip angle is sufficiently reduced, as can be seen in the wall pressure profile for contour C6 in Figure 20 b).

3.6 DIRECTLY OPTIMISED NOZZLES

The classical design methods described above rely on an inviscid design. After an inviscid design has been completed, a boundary layer correction is added to compensate for the viscous effects. The main reason for calculating the inviscid and viscous flows separately was that the computational capability in the past was such that the Navier-Stokes (N-S) equations could not be used in the design of contours. Advances in the computational technology since the 1950's allow scientists nowadays to use N-S solvers in parallell with direct optimisation techniques in the design loop. A typical design or an optimisation may include the following steps:
1. The design requirements are specified.
2. An objective function is constructed. The minimum or maximum of which yields the design requirements, e.g. max. performance and min. nozzle weight etc..
3. The set of design parameters or variables is specified.
4. An initial value for each of the design parameters is estimated.
5. An initial solution is computed by using the estimated design parameters.
6. The objective function is computed from the difference between the design requirements and the computed solution.
7. The sensitivity of the objective function to the design parameters is calculated.
8. An optimisation problem is solved to generate a new set of design variables.
9. A new solution is computed and compared with the design requirements.
10. If the design requirements are met or a minimum or maximum is reached, then the procedure stops, otherwise the process is repeated from step 6 onward.

Since the resulting contour with this method deviates from an ideal contour, compression waves will be generated in the nozzle. These waves can in some cases converge and an internal shock is formed inside the nozzle in the same way as in parabolic or compressed truncated ideal nozzles.

Direct optimisation of nozzle contours takes into account the whole range of specific impulse losses unlike the other design methods described, and thus produces slightly better results. However, comparison has shown that the improvement in performance does not exceed 0.1% [R 25-R 26]. Hence, the choice of contouring method has thus little influence on the performance of conventional nozzles. This is however not the case for all rocket nozzles. For engines operating on metal-containing fuels (liquid or solid), high expansion ratio nozzles can at present only be contoured by direct optimisation methods, since the Rao-Smyglevsky or the Ahlberg method do not rule out the precipitation of metal oxide particles on nozzle walls, and the consequent loss of specific impulse, eroding and destroying the contour[R 27-R 28]. Another example where direct optimisation must be used is for low Reynolds number nozzles, since the classical approach with a boundary layer correction of an inviscid designed contour breaks down when the viscous effects are large.[R 29]

3.7 DESIGN CONSIDERATIONS OF CONVENTIONAL ROCKET NOZZLE

When designing a rocket nozzle the appropriate configuration is highly dependent on manufacturing methods, given limitations on the main dimensions, cooling requirements, the influence of the nozzle weight on overall rocket performance, etc. Detailed examination of all these aspects requires knowledge in several engineering field's, not considered in this work. However, it should be pointed out that one of the most basic demands in the design loop of a real rocket nozzle is to keep the nozzle weight down. With increasing nozzle weight a number of problems arise. The nozzle will be more difficult to handle and fabricate. The loads and power required for gimbaling (vector control) and moving the engine increase, and thereby the weight and

complexity of the thrust vectoring system etc. As a result it seems reasonable to keep the nozzle length or surface area at a minimum. The main gas dynamic problem lies in optimally contouring the nozzles in order to minimise losses of efficiency and the main design methods have been outlined above. For the sake of simplicity the exhaust gases have here been assumed to expand adiabatically and behave like an ideal gas with a constant ratio of specific heats. Analysis of rocket nozzle flows in any real case should of course include radiative heat loss, chemical reactions due to incomplete combustion, and chemical properties of the exhaust gases, however these features do not alter the general methodology or results shown above.

It should also be mentioned that the choice of contour type is will depend upon the application, i.e. if the nozzle is to be used as an upper-stage, first-stage or booster nozzle etc. The TIC nozzle is the only rocket nozzle that produces a shock free flow, whereas in a conical, CTIC, TOC, TOP and the direct optimised nozzles an internal shock is formed inside the nozzle. In Figure 3 the difference of the internal flow field between the conical, TIC, TOC and TOP nozzle is illustrated. For first-stage nozzles, which operate from sea-level to high altitudes, this differences is essential since the internal shock has a strong influence on the global shock pattern of the exhaust plume and determine the flow separation shock pattern and the side load behaviour of the nozzle, see paragraph 6.2 and 8.1. If upper-stage engines are not used for stage separation there is no considerable flow separation at start up, hence the choice of contour has a much smaller importance.

4 EXHAUST PLUME PATTERN

Nozzles of high performance rocket engines in use for first- or main stage propulsion, e.g. the American SSME, the European Vulcain, or the Japanese LE-7, operate from sea-level with one bar ambient pressure up to near vacuum. At ground, these types of engines operate in an overexpanded flow condition with an ambient pressure higher than the nozzle exit pressure. As the ambient pressure decreases during ascent, the initially overexpanded exhaust flow, passes through a stage where it is adapted i.e. the ambient pressure is equal to the nozzle exit pressure, and then finally becomes underexpanded. Figure 21 and Figure 22 shows photographs of nozzle exhaust flows during these two types of off-design operation. At high altitudes, the underexpansion of the flow results in a further expansion of the exhaust gases behind the rocket as impressively illustrated in Figure 21 d), taken during a Saturn 1-B launch.

In the case of overexpanded flow, the exhaust flow adapts to the ambient through a system of oblique shocks and expansion waves, which leads to the characteristic barrel-like form of the exhaust plume. Different shock patterns in the plume of overexpanded rocket nozzles have been observed, the classical Mach disk, Figure 21 a), the cap-shock pattern, Figure 21 b) and the apparent regular shock reflection at the centreline, Figure 21 c).[*] In ideal and TIC nozzles, a transition between Mach disc and the apparent regular shock reflection can be observed as the degree of overexpansion is decreased[R 110]. This is because a nozzle flow with a small overexpansion can adapt to the ambient without forming a strong shock system, i.e. the Mach disc. In nozzles featuring an internal shock, e.g. TOC, TOP and CTIC nozzles, the cap-shock pattern can be observed. The difference between the Mach disc and cap-shock pattern is illustrated in Figure 22. Figure 21 b) proves the existence of the cap shock pattern in the exhaust plume of the Vulcain nozzle, which has a parabolic contour.[R 2-R 4] This is the pattern first observed at the nozzle exit during start up. By increasing the combustion chamber pressure, the flow becomes less overexpanded. At some point the internal shock intersects the centreline and a transition to a Mach disc pattern takes place, see Figure 21 a) and Figure 23.
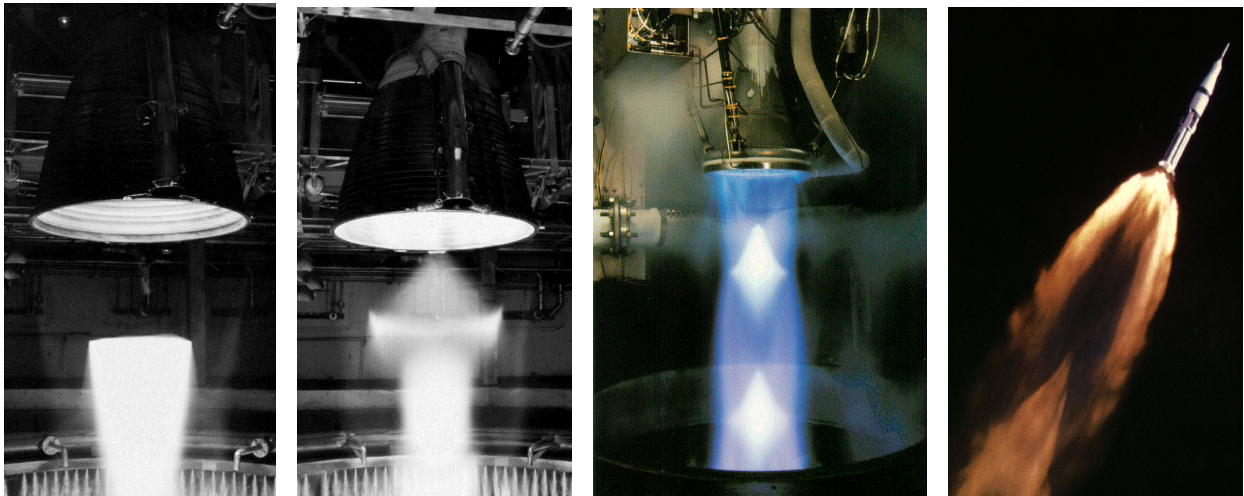
Figure 21. Exhaust plume pattern: a) Vulcain, overexpanded flow with classical Mach disk, b) Vulcain, overexpanded flow with cap-shock pattern, c) RL10-A5, overexpanded flow with apparent regular reflection, and d) underexpanded flow, photographed during launch of Saturn 1-B, also published in R 105. (Courtesy photos: SNECMA, CNES, NASA).

Recent sub-scale experiments performed within the European FSCD group also confirmed the stable existence of the cap shock pattern in the plume of parabolic sub-scale rocket nozzles.[R 5-R 8]

---

[*] In case of axisymmetrical flow, a pure regular reflection at the centreline is not possible. Instead, a very small normal shock exists at the centreline.[R 1]

a)

b)

c) **d)**

Cap shock pattern   Mach disc Pattern

internal shock   shear layer

nozzle contour

shear layer

nozzle contour
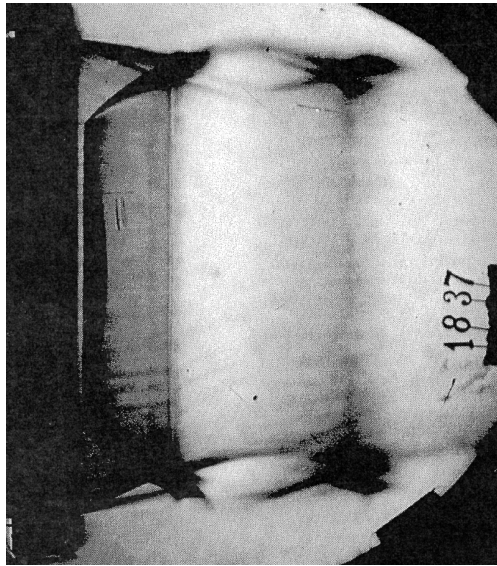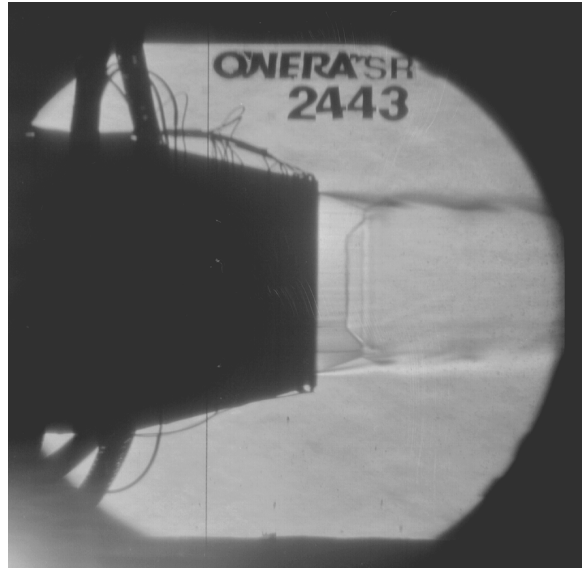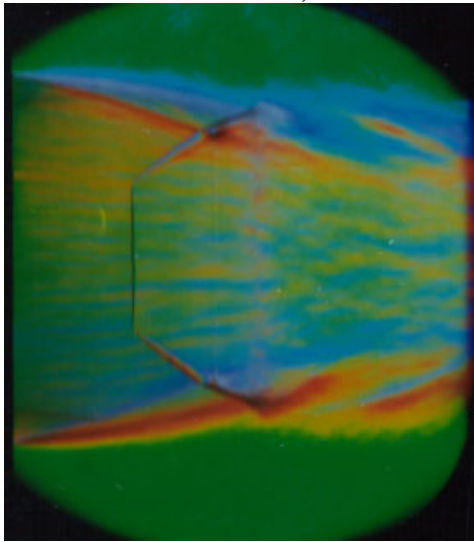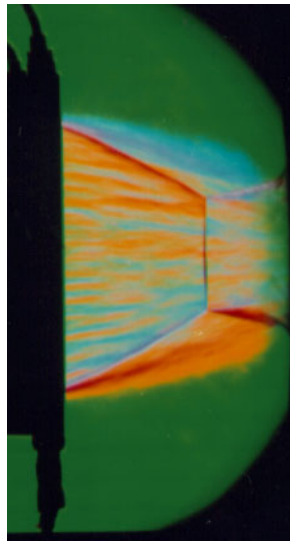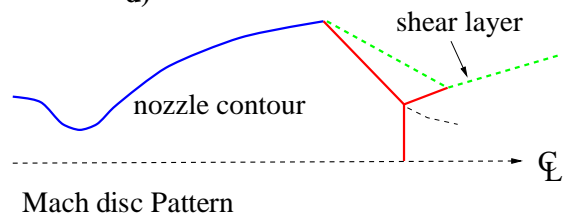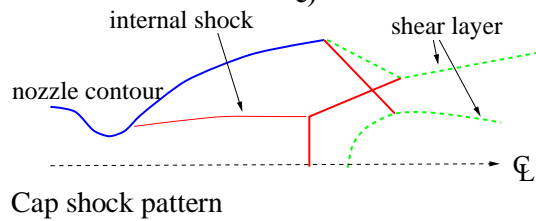
Figure 22. Exhaust plume patterns for parabolic subscale nozzles, with cap-shock pattern, a) S1 VAC FFA, b) TOP ONERA, c) P6 TOP DLR, and d) for a truncated ideal nozzle, with Mach disk, P6 TIC DLR, also published in R 105.

Figure 22 a-c) show Schlieren images of the exhaust plume of parabolic sub-scale nozzles tested at DLR, ONERA, and FFA. For comparison, the exhaust plume of a truncated ideal nozzle is also shown where the classical Mach disk is clearly visible.[R 8]

25
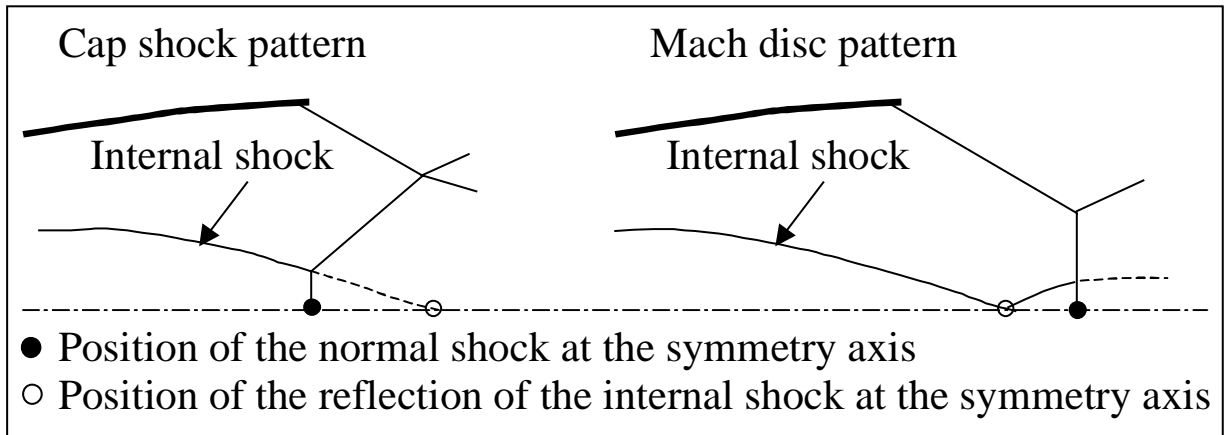
Figure 23. Illustration of transition between cap shock and Mach disc pattern: The transition occurs when the normal shock hits the reflection point of the internal shock at the symmetry axis.

The above described shock patterns are not only an exhaust plume phenomenon. They also exist inside the nozzle at highly overexpanded flow conditions, when the jet is separated from the nozzle wall. As will be shown later in section 6 and 8, the different shock patterns determine the characteristics of the nozzle separation and side-loads.

5 FUNDAMENTALS OF FLOW SEPARATION

5.1 FLOW SEPARATION AS A BOUNDARY LAYER PHENOMENON

In 1904, Prandtl[R 30] showed that flows with low friction in the vicinity of bodies can be subdivided into two regions: a thin layer close to the body, the so-called boundary layer (originally called *friction layer* due to the predominance of friction), and the remaining flow, the potential flow where friction effects can be neglected. In the boundary layer itself, the flow at the wall must follow a no-slip condition. Hence, the boundary layer is decelerated by the wall, but accelerated by the outer flow. The static pressure, constant across the boundary layer, is governed by the main flow.

In flows with favourable or zero wall pressure gradient, the boundary layer is attached to the wall. This can be different in the case of an adverse wall pressure gradient. If the wall pressure increases in the main flow direction, kinetic energy of the fluid particles is transformed into potential energy. However, fluid particles close to the wall only have a small kinetic energy because of their lower velocity. Therefore they are stopped by the pressure rise, and may be even forced to flow in the reverse direction. In this case the boundary layer is separated from the wall, and the recirculation region is developed in the vicinity of the wall.

Flow separation requires the existence of both friction and an adverse wall pressure gradient in a flow along a body. If one of these two conditions is suppressed, flow separation can be prevented. Prandtl proved this with different experiments, e. g. with a flow around rotating cylinders or with a diffuser with boundary layer suction.[R 31] Also, flow separation might not occur if the adverse pressure gradient is weak. In this case, the normal exchange of momentum inside the boundary layer can be sufficient to transport momentum from the mean flow to the wall; consequently, the kinetic energy of the particles close to the wall can be high enough to withstand the pressure rise without separation. Turbulent boundary layers with their characteristic high lateral exchange of momentum therefore separate much later than laminar boundary layers, where the momentum transport only consists of molecular movements.

At the separation point of two-dimensional boundary layers, planar or axisymmetric, the wall shear stress becomes zero,

$$\tau_w = \mu \cdot (\partial u / \partial y)_w = 0 \qquad \text{Eq. 11}$$

From this equation, and the velocity profile, the behaviour of the derivatives of u in wall-normal direction can be estimated.

In order to get a closer understanding of the separation processes, the momentum equation in wall-parallel direction is considered. The chosen non-conservative formulation is valid for a Newtonian fluid in a Cartesian co-ordinate system, neglecting volumetric forces:

$$\rho\left(\frac{\partial u}{\partial t} + u\frac{\partial u}{\partial x} + v\frac{\partial u}{\partial y} + w\frac{\partial u}{\partial z}\right) =$$
$$-\frac{\partial p}{\partial x} + \frac{\partial}{\partial x}\left[2\mu\cdot\left(\frac{\partial u}{\partial x} - \frac{div\ \vec{v}}{3}\right)\right] + \frac{\partial}{\partial y}\left[\mu\left(\frac{\partial u}{\partial y} + \frac{\partial v}{\partial x}\right)\right] + \frac{\partial}{\partial z}\left[\mu\left(\frac{\partial u}{\partial z} + \frac{\partial w}{\partial x}\right)\right] \qquad \text{Eq. 12}$$

If an arbitrary point at the wall is considered, the non-slip condition yields $u = v = w = 0$ for all velocity components as well as for their derivatives with respect to time and to the wall-parallel directions x and z. Substituting $div\ \vec{v} = \partial u/\partial x + \partial v/\partial y + \partial w/\partial z$, and by assuming a constant viscosity across the boundary layer, the expression is simplified as follows:

$$0 = -\frac{\partial p}{\partial x} - \frac{2}{3}\mu\cdot\frac{\partial}{\partial x}\left(\frac{\partial v}{\partial y}\right) + \mu\frac{\partial^2 u}{\partial y^2} \qquad \text{Eq. 13}$$

Because of $\partial/\partial x \; (\partial v/\partial y) = \partial/\partial y \; (\partial v/\partial x)$, the second term on the right side of Eq.13 becomes zero. Consequently, the following formula is valid for an arbitrary location at the wall:

$$\mu\left(\frac{\partial^2 u}{\partial y^2}\right)_w = \frac{\partial p_w}{\partial x} \text{ or } \frac{\partial \tau_w}{\partial y} = \frac{\partial p_w}{\partial x} \qquad \text{Eq. 14}$$

In this context, Eq. 14, was derived directly from the momentum equation, Eq. 12, only assuming a constant viscosity in the boundary layer, and is therefore valid for any point at the wall, including separation and recirculation zones. Schlichting[R 32] derived Eq. 14 from the classic boundary layer equations, which only represent an approximation of the flow. The aforementioned derivation from the momentum equation shows that Eq. 14 is not only an approximation, but also an exact solution for the flow at the wall.

Eq. 11 can be used to show that $(\partial^2 u/\partial y^2) > 0$ at the separation point. Since the dynamic viscosity is always positive, Eq. 14 yields that in order to have separation the wall pressure gradient must be adverse:

$$\left(\frac{\partial p_w}{\partial x}\right)_{x,\, separation} > 0 \qquad \text{Eq. 15}$$

5.2   SHOCK-WAVE BOUNDARY LAYER INTERACTIONS

The above expressions are valid for subsonic as well supersonic flows. In the following we will however only discuss the case with turbulent supersonic flows, having an adverse pressure gradient of sufficient strength to cause the boundary layer to separate. When a supersonic flow is exposed to an adverse pressure gradient it adapts to the higher-pressure level by means of a shock wave system. Basically, separation occurs when the turbulent boundary layer cannot negotiate the adverse gradient imposed upon it by the inviscid outer flow. Thus, flow separation in any supersonic flow is a process involving complex shock wave boundary layer interactions.

5.2.1   The basic interactions

The shock wave boundary layer interaction has been extensively studied in the last fifty years with the help of basic experiments, see e.g. references R 33-R 73. The three basic configurations involving interaction between a shock wave and a boundary layer in supersonic flows are schematically represented in Figure 24. In all of these cases, the incoming outer flow is uniform flow streaming along a flat plate.

The first and conceptually most simple configuration is the wedge (or ramp) flow. Here, a discontinuity in the wall direction is the origin of a shock wave through which the supersonic flow undergoes a deflection equal to the ramp angle α, Figure 24 a).

The second type of flow is associated with the impingement on the wall of an incident oblique shock, which cause a deflection of the incoming flow, see Figure 24 b). The necessity for the downstream flow to be parallel again to the wall causes the formation of a reflecting shock issuing from the impingement point.

The third flow is induced by a step of height h facing the incoming flow, see Figure 24 c). Such an obstacle provokes separation of the flow at point S. The rapid pressure rise accompanying separation gives rise to a shock wave emanating from a place very close to the separation point S, and a separated zone develops between the separation point S and the step.
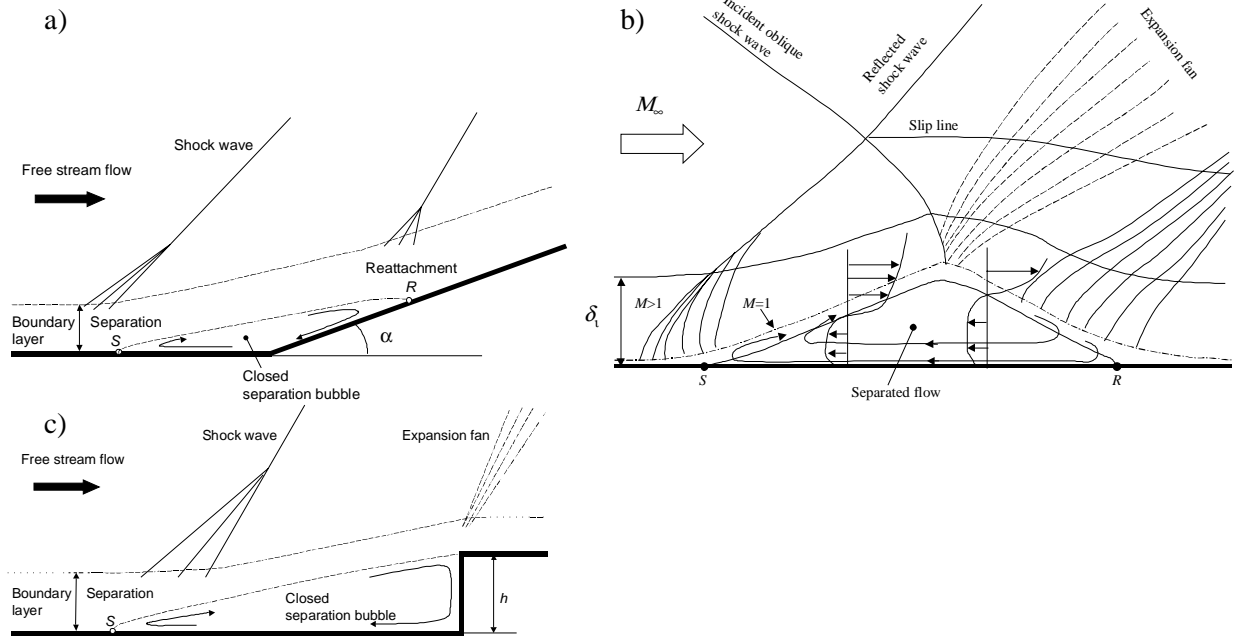
Figure 24. Basic shock/boundary layer interactions in supersonic flow. a) Ramp flow. b) Shock reflection. c) Step induced separation, adopted from R 77.

It has been shown in many experiments, that the major part of the shock / boundary layer interaction properties are nearly independent of the cause having induced the separation, whether being either a solid obstacle or an incident shock wave [R 7, R 35, R 77]. In fact the features of the static wall pressure for the above different experimental configurations are the same, see Figure 25. The wall pressure has a steep rise shortly after the beginning of the interaction at I. The flow separates from the wall at S, located a distance L_s from I. The wall pressure then gradually approaches a plateau with almost constant pressure, labelled the plateau pressure p_p. The extent of this plateau reflects the size of the closed recirculation bubble and p_p thus corresponds to the wall pressure in the bubble. A second pressure rise can be observed as the reattachment point at R is approached. These characteristics are independent on the downstream geometry, as already mentioned, everything happens as if the flow were entirely determined by its properties at the onset of the interaction. This observation led Chapman et al.[R 35] to formulate the free interaction concept.
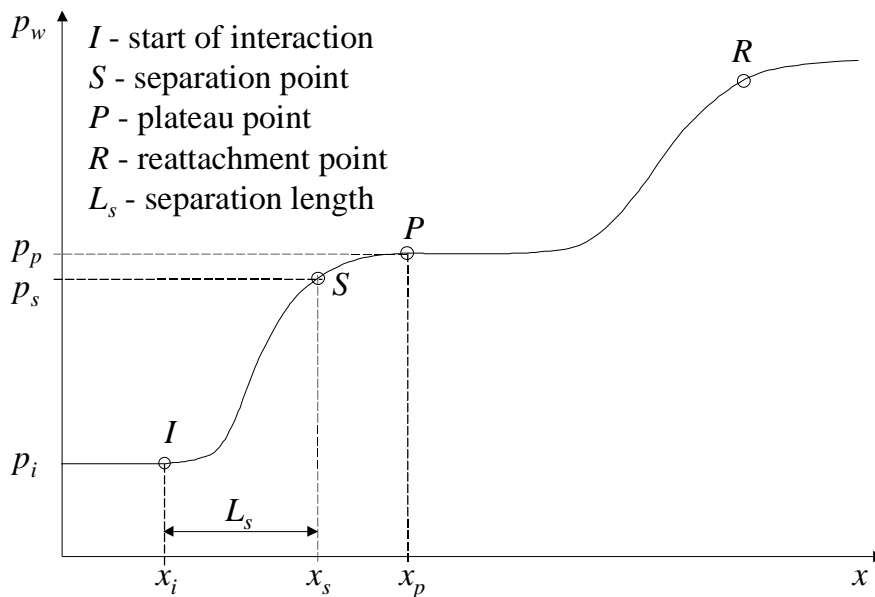
Figure 25. Typical static wall pressure distribution observed in ramp, shock reflection and step flow; adopted from R 32 and R 48.

5.2.2 The free interaction concept

Chapman considered flow separation caused by the interaction between the boundary layer formed in a plane, adiabatic, supersonic uniform flow and a shock wave. The Mach number M_i and the pressure p_i define the inviscid uniform flow. The skin friction coefficient (C_f), the displacement thickness (δ*) etc. define the local characteristics of the boundary layer. The deflection angle of the mean flow in the streamwise direction is given by θ, see Figure 26.
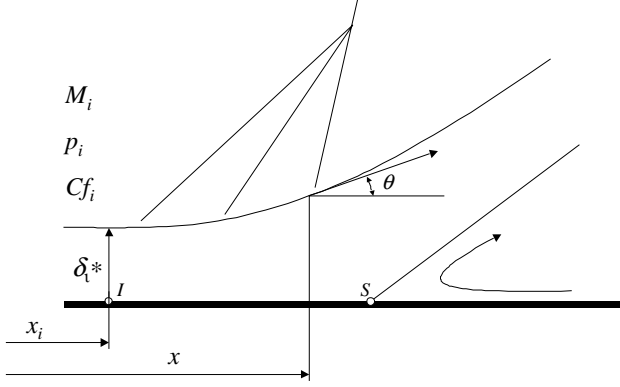
Figure 26. Flow separation in uniform flow, notations.

Chapman then made two assumptions about the flow in the interaction domain:
1. The flow structure follows a law of similarity
2. The deviation of the external non-viscid flow correspond precisely to the displacement effect of the boundary layer, i.e.,

$$\frac{d\delta*}{dx} = \theta - \theta_i \qquad \text{Eq. 16}$$

By normalising the abscissa with an appropriate length scale l characterising the extent of the domain, and the displacement thickness δ* with the value at the origin of the interaction, δ_i*, one obtains:

$$\theta - \theta_i = \frac{\delta_i*}{l} \frac{d\left(\dfrac{\delta*}{\delta_i*}\right)}{ds} = \frac{\delta_i*}{l} f_1(s) \qquad \text{Eq. 17}$$

Where $s = \dfrac{x - x_i}{l}$ and $f_1(s)$ is a non-dimensional function characterising the outer streamline deflection.

Integrating the simplified boundary layer momentum equation at the wall, Eq. 14, from $x=x_i$, after making it non-dimensional by introducing the wall friction $\tau_{wi} = \tfrac{1}{2}\rho_i u_i^2 C_{fi}$ at $x=x_i$, results in:

$$\frac{p - p_i}{q_i} = \frac{l}{\delta_i*} C_{fi} \int_o^s \frac{\partial(\tau_w/\tau_{wi})}{\partial(y/\delta_i*)} \ ds = \frac{l}{\delta_i*} C_{fi} f_2(s) \ ,$$
$$\text{where} \quad q_i = \tfrac{1}{2}\rho_i u_i^2 = \tfrac{1}{2} p_i \gamma \ M_i^2 \qquad \text{Eq. 18}$$

$f_2(s)$ is a new dimensionless function characterising the pressure rise.

By multiplying Eq. 17 by Eq. 18, $\dfrac{l}{\delta_i*}$, is eliminated and one obtains:

$$F(s) = \sqrt{f_1 \cdot f_2} = \sqrt{\frac{p - p_i}{q_i} \frac{\nu(M_i) - \nu(M)}{C_{fi}}} \qquad \text{Eq. 19}$$

Where $\theta - \theta_i = v(M_i) - v(M)$ according to the Prandtl-Mayer law. Chapman then expressed the variation of $v(M_i) - v(M)$ as function of $\dfrac{p - p_i}{q_i}$, linearised for small pressure changes $p-p_i$ (see e.g. Shapiro[R 11] p. 436) and finally obtained:

$$F(s) = \frac{p - p_i}{q_i} \sqrt{\frac{\sqrt{M_i^2 - 1}}{2C_{fi}}}$$ Eq. 20

The function $F(s)$ is assumed to be a universal function, independent of Mach number and Reynolds numbers, to be determined from experiments. Figure 27 shows the generalised wall pressure correlation function $F(s)$ obtained by Erdos and Pallone[R 78]. The axial distance from the onset of the interaction has been normalised with the separation length i.e., $l=L_s=x_s-x_i$. In the original work by Erdos and Pallone the distance to the pressure plateau of the extended separated flow was used as the characteristic length scale i.e., $l=L_p=x_p-x_i$. From the figure following particular values of F can be found, $F_s=F(1)=4.22$ at the separation point and $F_p=F(4)=6.00$ at the plateau point.
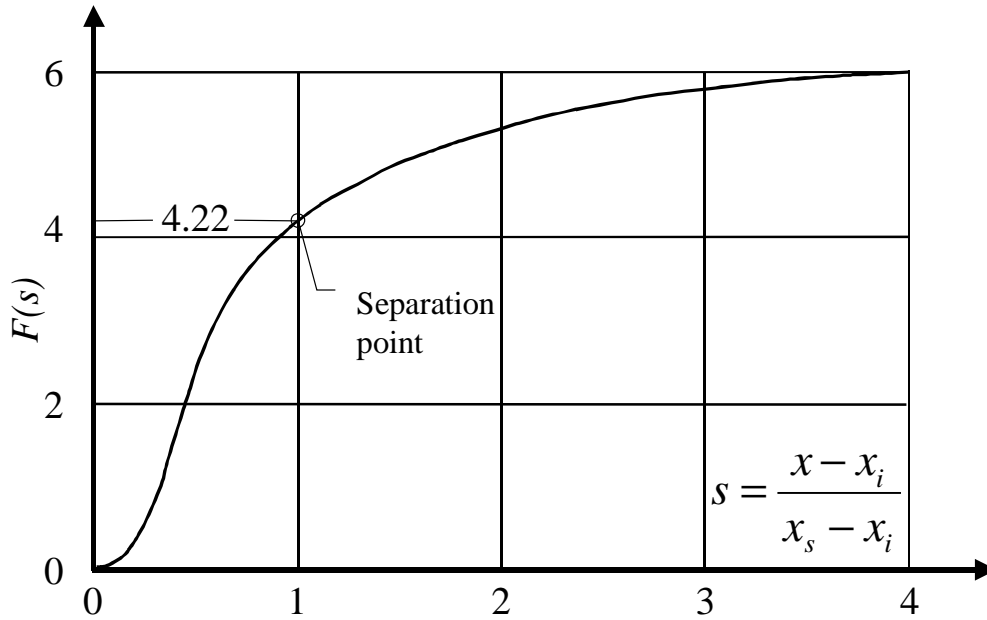
Figure 27. The generalised wall pressure correlation function $F(s)$ for uniform turbulent flow, by Erdos and Pallone[R 78].

The characteristic length l may be obtained by dividing Eq. 18 by Eq. 17, which gives: $\dfrac{l}{\delta_i *} = \dfrac{F(s)}{v(s=0) - v(s)} \cdot \sqrt{\dfrac{f_1(s)}{f_2(s)}}$. At the separation point ($s=1$), this relation can be evaluated as:

$$\frac{L_s}{\delta_i *} = k \frac{F_s}{v_i - v_s} = \{linearised\} = k \sqrt{\frac{2}{C_{fi} \sqrt{M_i^2 - 1}}}$$ Eq. 21

From different experiments an average value of $k=0.37$ has been obtained[R 77]. However, the experimental data have a significant scatter around this value, $k = 0.37^{+0.2}_{-0.1}$, presumably due to the difficulty of accurately determining the separation length, which in turbulent flows is very short.

The free interaction theory can be used to establish separation criteria for supersonic flow. The best known is the type of criteria first proposed by Erdos and Pallone[R 78] 1962. They determined the critical pressure rise

between the pressure p_r at location $s=r$ and p_i ($s=0$) by assuming that the separation occurs when the pressure jump p_r/p_i is:

$$\frac{p_r}{p_i} = 1 + F_r \gamma M_i^2 \sqrt{\frac{C_{fi}}{2\sqrt{M_i^2 - 1}}}$$

Eq. 22

This equation is obtained by rewriting equation 20 and using the expression for the dynamic pressure given in equation 18.

The pressure rise, corresponding to a "true" incipient separation case is obtained with $F_r=F_s=4.22$ and with $F_r=F_p=6.0$ (the value used by Erdos and Pallone) the "effective" incipient separation condition is obtained. The latter is observed when the separation bubble has reached a size large enough to produce a significant change in the flow field, while the former corresponds to the first appearance of a tiny separation bubble. The "effective" incipient separation condition, i.e. $F_r=6.0$, is the case, which is the most important for practical applications. Figure 28 shows the separation pressure rise for these two cases.
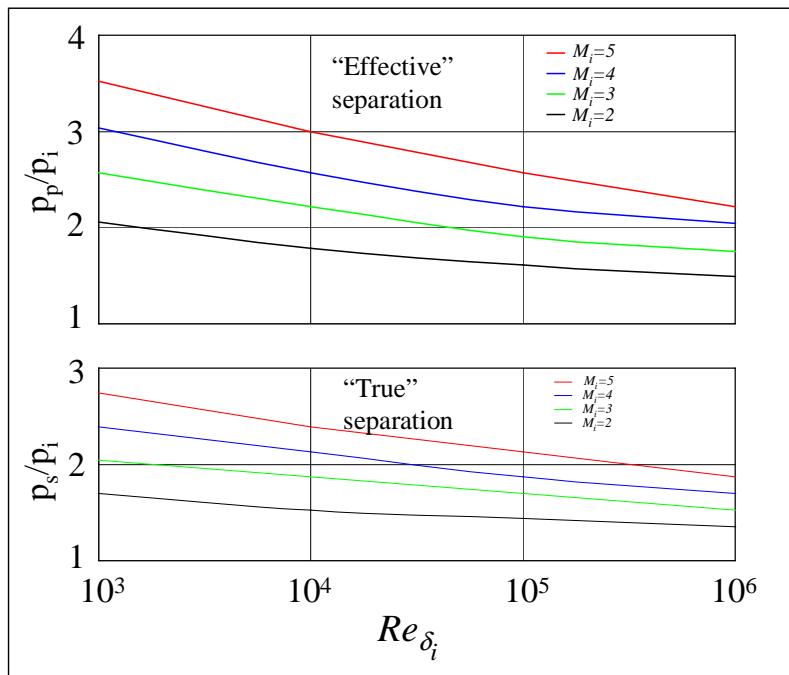
Figure 28. Separation criterion deduced from the free interaction theory for uniform flow.

From Figure 28, we can see some typical results of the pressure rise at the separation (p_p/p_i or p_s/p_i) obtained with the free interaction theory:
- The pressure rise increases when the Mach number is increased.
- The pressure rise decreases when the skin friction coefficient decreases (corresponding to an increase of the Reynolds number).

Both of these tendencies have been confirmed by experiments performed at low to moderate Reynolds numbers and the criterion in equation 22 correlate experimental data well. However, in several experiments performed at high Reynolds numbers ($Re_{\delta i} > 10^5$) it has been observed that the pressure rise (p_p/p_i or p_s/p_i) tends to become independent of the Reynolds numbers and even to slightly increase with it. As an example, Zukoski[R 45] made a series of experiments on step flows at $Re_{\delta i} > 10^5$ with M_i varying between 1.4-6.0, and found that the pressure rise at high Reynolds numbers depended only of the upstream Mach number M_i as:

$$\frac{p_s}{p_i} = 1 + 0.73 \frac{M_i}{2}$$

Eq. 23

$$\frac{p_p}{p_i} = 1 + \frac{M_i}{2}$$

<div align="right">Eq. 24</div>

This change of the influence of the Reynolds number as it becomes sufficiently high restricts criteria based on the free interaction theory to the range $Re_{\delta i} < 10^5$ and Mach numbers $M_i < 5$

5.2.3   The separation length

The Reynolds number (Re_δ), the displacement thickness (δ^*) or the boundary layer thickness (δ) are important viscous parameters that define the separation length L_s, i.e. the distance between the point where the wall pressure starts to rise to the point where the flow actually separates. Experiments on ramp flows have shown that in turbulent flow the separation length is very short, L_s/δ_i is of order 1, compared to the laminar case where the separation length is far larger than the incoming boundary layer thickness[R 77]. For turbulent flow the influence of the Reynolds number on the separation length can be divided in two regions. For low or moderate Reynolds number ($Re_{\delta i} < 10^5$) L_s increases with increasing Reynolds number (see Figure 29 a), in agreement with the free interaction theory. Whereas at high Reynolds number ($Re_{\delta i} > 10^5$), several investigators have found that the separation length tends to become independent of the Reynolds number and even to slightly decrease with it, as indicated in Figure 29b . An explanation for this behaviour may be that at low Reynolds number the viscous sublayer represents a larger part of the total boundary layer and the viscous phenomena tend to dominate the interaction. At high Reynolds number, on the other hand, the viscous sublayer becomes exponentially thin. Therefore, interaction tends to be controlled by inertia and pressure forces (the influence of viscosity being minimised). Furthermore, at high Reynolds number, the subsonic layer is far thicker than the laminar sublayer. As a consequence of these two facts, pressure propagation in a high Reynolds boundary layer is essentially an inviscid mechanism.
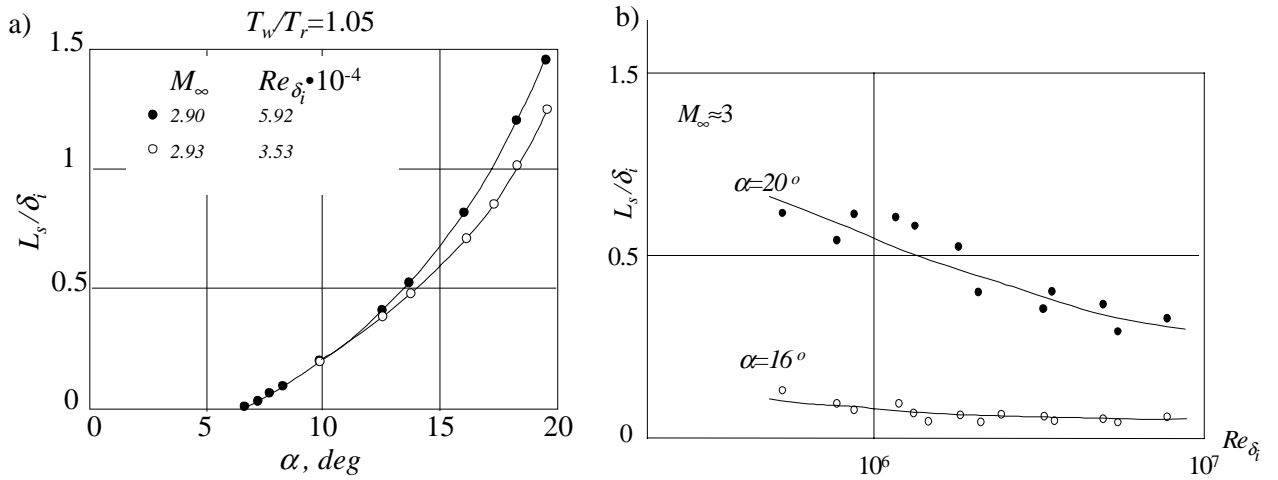
Figure 29. Influence of Reynolds number and ramp angle on separation length a) at low to moderate $Re_{\delta i}$ L_s/δ_t increases with Re, data from Spaid and Frishett[R 54] b) at high $Re_{\delta i}$ L_s/δ_t decreases with Re, data from Settles[R 40].

Besides the Reynolds number, heat transfer influences the separation length. The cooling effect can be found in Figure 30, where $\tilde{L}_s$ is plotted versus T_w/T_r based on experimental data from Spaid and Frishett[R 54]. $\tilde{L}_s$ is the ratio between L_s/δ_t when heat transfer is present and L_s/δ_t with adiabatic flow evaluated at the same $Re_{\delta i}$. As indicated in the figure wall cooling decreases the separation distance. This reduction of $\tilde{L}_s$ with decrising wall temperature can be explained with the help of the free interaction theory. When reducing T_w/T_r (T_r is the wall recovery temperature), the skin friction coefficient will increase and according to. Eq 21 this provokes a decrease of L_s. Another interpretation of the reduction of $\tilde{L}_s$ is that an overall contraction of the interaction

domain is obtained due to a thinning of the subsonic layer, as the temperature level and thus the speed of sound near the wall becomes lower.

$$\tilde{L}_s = \frac{(L_s/\delta_i) Cooled\ wall}{(L_s/\delta_i) Adiabatic\ wall\ at\ same\ Re_{\delta_i}}$$

$\tilde{L}_s$

α , deg

○ 19.67
△ 17.25
□ 13.70
● 9.81
▲ 8.07
■ 7.52
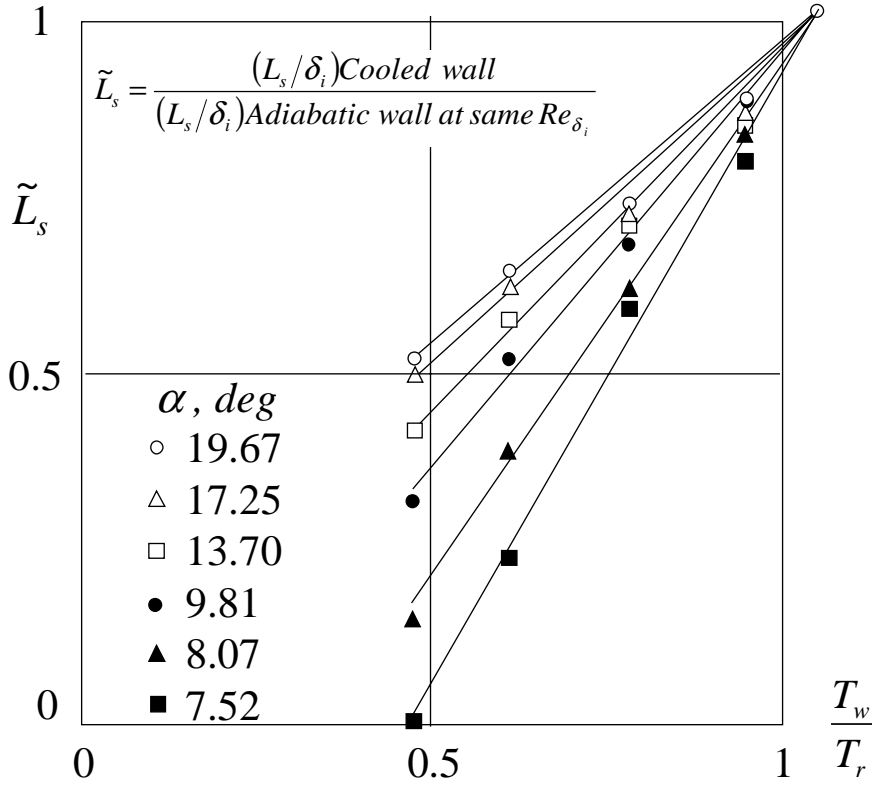
$\frac{T_w}{T_r}$

Figure 30. Influence of wall cooling on the separation length in a ramp flow. M_i=2.9, ramp angles 7.52°≤ α ≤ 19.7°, 2.18∘10^4 ≤ $Re_{\delta i}$ ≤ 5.92∘10^4 and 0.474≤ T_w/T_r ≤1.05 (data from Spaid and Frishett[R 54])

5.2.4   Unsteadiness and 3-dimensional effects

In the previous section we only looked at the mean properties of shock induced separation. However, the shock-wave boundary layer interaction is an intrinsically unsteady phenomenon. This unsteadiness may generate large fluctuating forces that can be of severe magnitude e.g. in flight vehicles and overexpanded rocket nozzles, and has therefore been the topic for several studies[R 55-R 76]. A typical distribution of the fluctuating pressure *p'* in the interaction region is shown in Figure 31. The fluctuations increase rapidly after the onset of the interaction at *I* from the level experienced in the incoming unperturbed boundary layer, p'_i, up to a peak value. It then decreases asymptotically towards the fluctuation level, p'_p, in the plateau region.

The explanation of the obtained feature, first given by Kistler[R 63], is that the flow is intermittent. In the interaction region the pressure jumps back and forth between the mean pressure levels p_i and p_p due to a fluctuation of the separation point, and at each pressure level the pressure oscillates with an amplitude characteristic of that level, i.e. p'_i and p'_p respectively, see Figure 32.

According to Kistler, the wall pressure signal near the separation can be modelled as a step function, with the jump location (i.e. the shock wave) moving over some restricted range. By defining ε as the fraction of time that the plateau pressure region is acting over the point of interest, i.e. an "intermittence" factor, the mean pressure at a given axial position *x* can be expressed as:

The mean static pressure is:

$$p(x) = \varepsilon(x)p_p + [1 - \varepsilon(x)]p_i \qquad \text{Eq. 25}$$

Thus, ε can be determined from mean pressure measurement at *x* as:

$$\varepsilon(x) = \frac{p(x)/p_i - 1}{p_p/p_i - 1}$$

Eq. 26

The mean-square fluctuation around the mean pressure then becomes:

$$p'^2(x) = \underbrace{\overbrace{\varepsilon[1-\varepsilon](p_p - p_i)^2}^{\text{Shock motion}}}_{\text{Low freq. part}} + \underbrace{\overbrace{\varepsilon p_p'^2}^{\text{Shear layer}} + \overbrace{[1-\varepsilon]p_i'^2}^{\text{Boundary layer}}}_{\text{High freq. part}}$$

Eq. 27

In Figure 33 the results from such a calculation are compared to test data from Kistler, showing a good quantitative agreement between the measured and computed results.
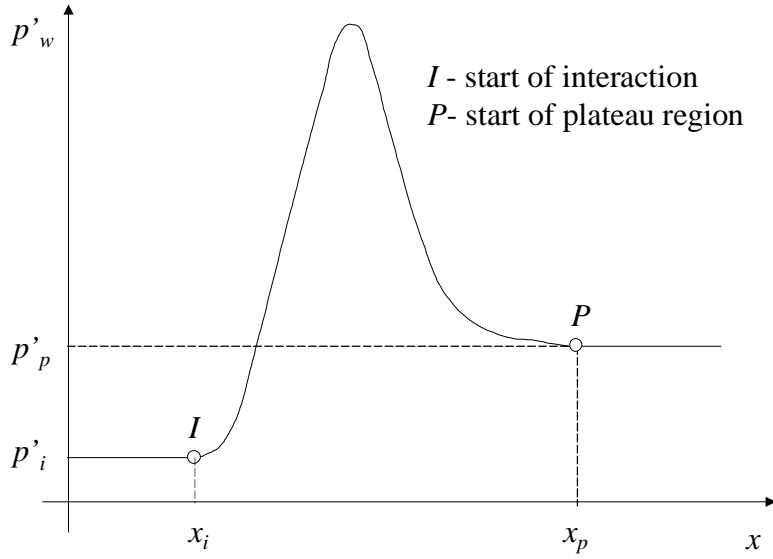
Figure 31. Typical distribution of the fluctuating pressure in the interaction region[R 58, R 59, R 63].
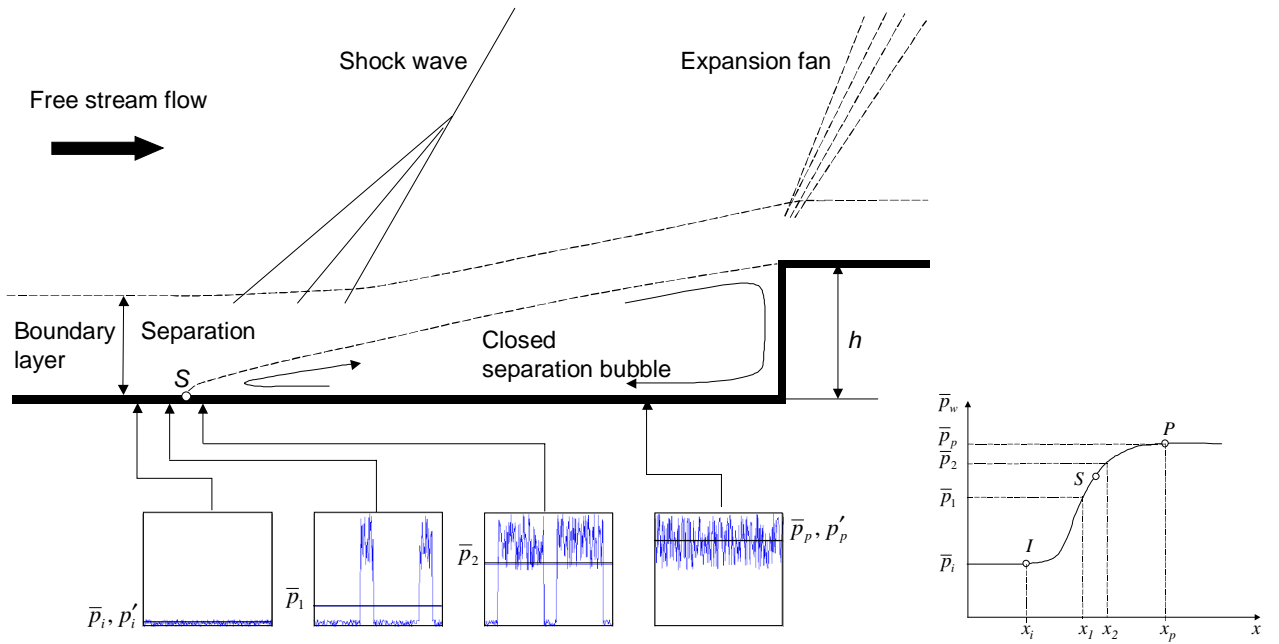
Figure 32. Sketch of the time variation of the pressure within the interaction domain.[R 59, R 63]
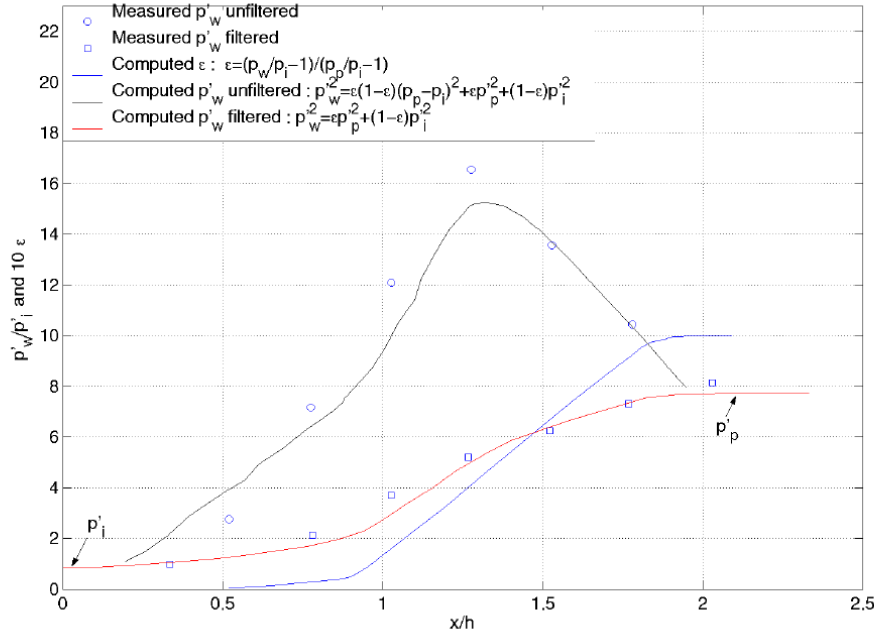
Figure 33. The fluctuating pressure in the interaction domain, test data from Kistler[R 63].
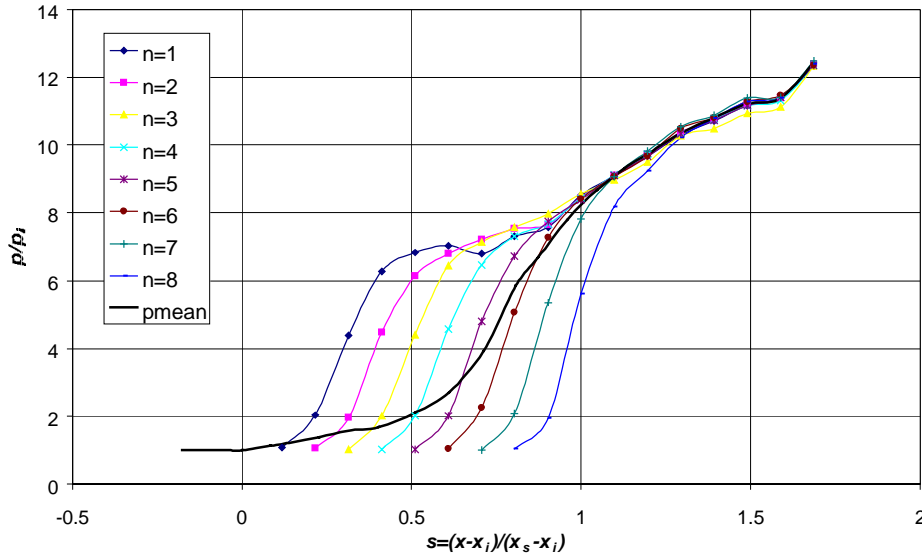
Figure 34. Ensemble-avaraged wall pressures upstream of the corner in a 28°, Mach 5 compression ramp interaction (from Erengil and Dolling[R 61])

A better understanding of the instantaneous pressure profiles was obtained by Erengil and Dolling[R 61]. Their experiment showed how the time averaged wall pressure profile is composed of instantaneous profiles with sharper gradients see Figure 34. The figure shows the ensemble-averaged pressure $\overline{p}_{E/A}$ in a Mach 5 compression ramp interaction. The profiles were obtained by picking out instants when the shock was located at various specific positions (n=1..8) in the intermittent region and ensemble-average them at each position. The solid black line in the figure represents the averaged mean pressure. The mean separation begins at s=1 and the flow reattaches somewhere downstream of the corner, which is located at $s{\approx}1.7$. As reported by Erengil and Dolling, three features of the ensemble averaged pressure distributions are evident:

1. For shock locations with $s>1.2$, i.e. in the separated flow region, the shock position in the intermittent region has no significant influence on $\overline{p}_{E/A}$.

2. For the "shock-upstream" case, i.e. $n=1$, a well-defined plateau region can be seen in $\overline{p}_{E/A}$, consistent with a large-scale separated flow.

3. As the shock moves downstream from the $n=1$ position i.e. $s>0.12$, a progressive change in $\overline{p}_{E/A}$ can be seen, to finally resemble that typical of a flow with a small separated region.

On the basis of fluctuating pressure measurements[R 59], laser field imaging methods[R 71-R 73] and numerical simulations[R 74] different researchers have suggested that the obtained shock motion is due to turbulent velocity fluctuations in the upstream boundary layer. A simple explanation given in reference R 71 is that changes of the shape of the instantaneous turbulent velocity profile yields changes in the shock position and hence produce the unsteady shock behaviour. With positive velocity fluctuations a fuller velocity profile is obtained which has a increased resistance to separation and the shock location will hence move further downstream. With negative velocity fluctuations the case will be the opposite. Since the velocity fluctuations are random they cause a random distortion of the separation line in the spanwise direction. This indicates that shock wave boundary layer interactions in nominally 2D flows are in fact a 3D phenomenon. This 3D effect is clearly seen in the surface streak pattern Settles[R 42] obtained by applying a mixture of graphite powder and silicon oil to the ramp model surface, see Figure 35. A well-defined accumulated separation line can be seen in the figure upstream the corner. Close examination of the line shows that many variable length streaks project forward of it and these are records of instants when the reversed flow extended further upstream. Thus the instantaneous spanwise separation line is ragged, i.e. the flow is 3-dimensional, and the accumulated separation line represents the downstream boundary of a band of separation. This also explains why the flow picture close to the separation is blurred in instantaneous schlieren photos taken normal to the flow, as it gives an averaged picture of the flow in the spanwise direction.

Normalised power spectra for a variety of flow types are all broadband, with a large fraction of the energy at relatively low frequencies. In this context, *low frequency* means low relative to the characteristic frequency, U_∞/δ_i^*, of the incoming turbulent boundary layer. An example from Erengil and Dolling[R 61] in Figure 36 shows power spectra in the interaction region in a 28°, Mach 5 compression ramp interaction. The ratio of U_∞/δ_i^* for this flow is about 50 kHz, which can be seen in Figure 36 d). At $\varepsilon=0.06$ and $\varepsilon=0.80$, Figure 36 b)-c), the intermittence is low and the spectra is bimodal, reflecting the contributions from both the shock-induced fluctuations (about 0.2-2 kHz) and the undisturbed and separated boundary layer. Within the intermittent region, the power spectra retains the same shape with a large fraction (~80-90%) of the energy below $f_{max} \approx 2$ kHz, see definition in Figure 36 f). In the separated flow region the pressure fluctuations are caused by the turbulent activity in the free shear layer near the dividing streamline and a increased contribution from high frequencies is again evident, see Figure 36 a). This general trend is typical for all spectral results given in the literature. The power spectra at maximum rms, i.e. at $\varepsilon=0.5$, of different type of flows indicate frequencies of the broadband fluctuation below $f_{max} \approx 1$-10 kHz[R 58, R 61, R 63, R 64]. Analysis shows that the data are well correlated, when normalising the maximum frequency value with L_s/U_i, corresponding to Strouhal numbers $Sr = f_{max}L_s/U_i = 0.07$ for these configurations, see Table 2. This indicate, that with increasing separation length an increasing fraction of the energy will be located at low frequencies, i.e. closer to the eigenfrequencies of the structure. Why an increased forced response load can be expected.
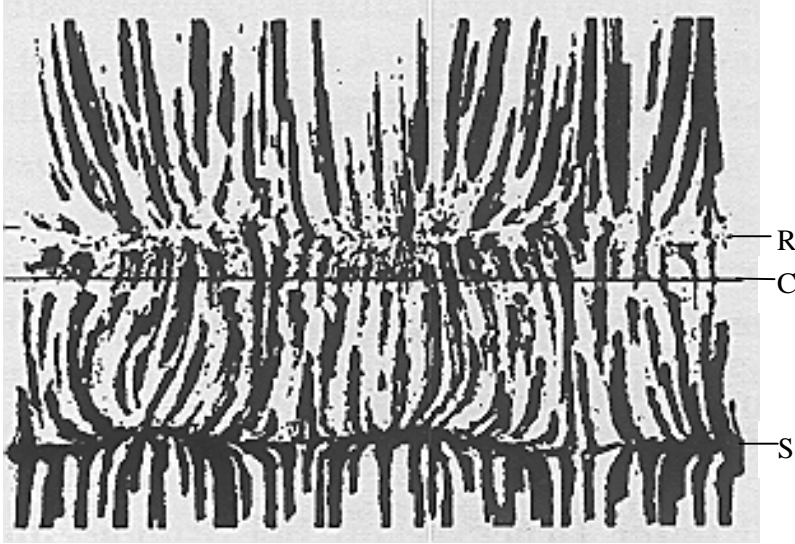
Figure 35. Surface streak patterns in a 24°-ramp flow at M_∞=2.85, from Settles[R 42], C-Corner, S-Separation, R-Reattachment. (Courtesy of Settles[R 42])
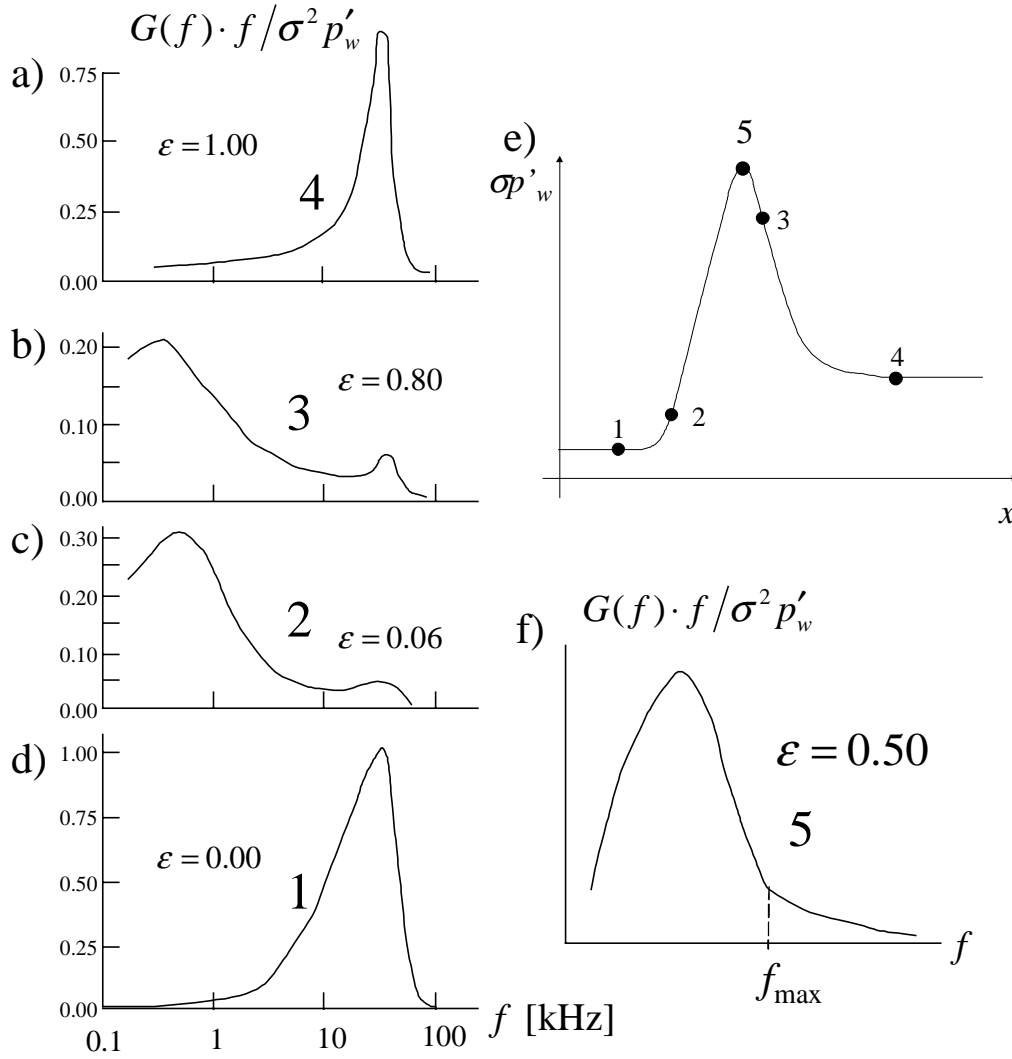
Figure 36. Typical power spectra in the intermittent region (adopted from Erengil and Dolling[R 61]). a)-d) spectra at different streamwise locations, d) sketch of the streamwise evolution of the rms wall pressure and locations where the spectra have been evaluated, f) definition of f_{max}.

$Sr = \dfrac{L_s f_{max}}{U_i}$	Test setup	Ref.	f_{max} [kHz]	U_i [m/s]	L_s [m]	L_s/δ_i
0.072	45° ramp in M=2 flow	R 58	1.0	1020	0.0737	0.72
0.072	Step in M=3 flow	R 63	1.0	635	0.0457	1.20
0.068	28° ramp in M=5 flow	R 61	2.0	$U_i/\delta_i \approx$50 [kHz]		1.70
0.07	Cylinder with D=3/4" in M=5 flow	R 64	3.5	800	0.0160	X
0.07	Cylinder with D=1/2" in M=5 flow	R 64	6.0	800	0.0094	X
0.07	Cylinder with D=3/8" in M=5 flow	R 64	8.3	800	0.0067	X
0.07	Cylinder with D=1/4" in M=5 flow	R 64	11.4	800	0.0049	X

Table 2. Obtained Strouhal numbers for different flow configurations, when normalising the maximum frequency value with L_s/U_i.

In summary the shock wave boundary layer interaction is an intermittent and 3 dimensional phenomenon. Mechanical structures exposed to this type of supersonic flow separation are affected by large, time-dependent forces, which can be resolved into two components, a low frequency buffeting caused by changes in the geometry of the separation region, and high frequency fluctuations originating from the shear layer of the separated region.

6   FLOW SEPARATION IN ROCKET NOZZLES

A flow exposed to an adverse pressure gradient of sufficient strength can cause the boundary layer to separate from the wall. In the previous section we examined the influence of such adverse pressure gradients generated by obstacles. A similar condition occurs when a nozzle is operating in an overexpanded condition. A nozzle flow is said to be overexpanded when the theoretical wall exit pressure $p_{e,vac}$ (the wall pressure obtained when the flow is ejected in to vacuum ambient conditions) is below the ambient pressure p_a. Thus at overexpanded flow condition the ratio $n=p_{e,vac}/p_a<1$. n is a parameter commonly used to define the flow condition (adapted condition $n=1$ and underexpanded condition $n>1$). As soon as n is slightly reduced below one, an oblique shock system is formed from the trailing edge of the nozzle wall due to the induced adverse pressure gradient. When the ratio n is further reduced, to about 0.4-0.8, the viscous layer cannot sustain the adverse gradient imposed upon it by the inviscid flow and the boundary layer separates from the wall. This is the case e.g. when a rocket engine designed for altitude operation is tested at sea level. It also occurs during start transients, shut off transients, or engine throttling modes. In order to provide scientists and engineers with information on the turbulent shock wave boundary layer interaction in overexpanded nozzles, many experiments have been carried out both in the past and recently for full scale and subscale nozzles, see e.g. reference R 5-R 8, R 81-R 89. Further support to the analysis of the flow separation behaviour has been provided by means of numerical simulations[R 2, R 4, R 5, R 90-R 93, R 104].

Recent research has made it clear that two different separation patterns have been observed, the classical free shock separation, and the restricted shock separation, in the following denoted by their acronyms FSS and RSS respectively. Figure 37 shows a schematic figure for both separations patterns with the definition of the characteristic points. In addition, Figure 38 compares measured and numerically calculated wall pressures for both separated flow patterns, and also includes the numerically calculated Mach number distribution for FSS and RSS, respectively.

6.1   FREE SHOCK SEPARATION

In the free shock separation case, the overexpanded nozzle flow fully separates from the wall at a certain ratio of wall- to ambient pressure. The resulting streamwise wall pressure evolution is mainly governed by the physics of shock wave boundary layer interactions occurring in any supersonic flow separation, see section 5.2. The first deviation of the wall pressure from the vacuum profile[†] is commonly named *incipient separation pressure*, p_i in Figure 37 (p_i is some times also labelled p_{sep}). The wall pressure then quickly rises from p_i to a *plateau pressure p_p*, which is in general slightly lower than the ambient pressure p_a. Analyses of subscale tests in nozzles[R 79-R 80,R 108] and flow with obstacles[R 55-R 73] have shown that the steep pressure rise is caused by fluctuations of the shock front. The shock motion between the incipient separation point x_i and the point where the plateau pressure is reached, x_p , is a low frequency wideband fluctuation with about 80-90% of the energy below the maximum frequency at $Sr = f_{max}L_s/U_i \approx 0.07$, see section 5.2.4. This observation, although not completely new, is in contrast to the classical view of a stable and well defined separation point, where the pressure rise from p_i to p_p has the origin in compression waves focussing to the oblique separation shock[R 83,R 94]

From many cold gas tests in the past decades it has been noticed, that the boundary layer effectively separates from the nozzle wall shortly before reaching the plateau pressure p_p. In the recirculation zone downstream of the separation point, the wall pressure increases slowly from p_p to p_e, see Figure 37 (top). This gradual pressure rise is due to the inflow and upstream acceleration of gas from the ambience into the recirculation region.

To predict the axial separation location inside a nozzle, the ratio of separation to ambient pressure p_i/p_a must first be known. Using the vacuum wall pressure profile in the nozzle, the separation location can then easily be determined. Of course, the separation pressure ratio p_i/p_a includes the influence of both the pressure rise at the separation location itself and the gradual pressure rise in the recirculation region. To simplify the

---

[†] The wall pressure profile obtained in the nozzle when the gas is expanded into vacuum ambient condition is called the vacuum pressure profile.

physical interpretation of the separation pressure ratio p_i/p_a, it should be subdivided into two factors $(p_i/p_p)\cdot(p_p/p_a)$, where each part refers to a single physical phenomenon, the former to the separation itself, the latter to the subsequent open recirculation with inflow of ambient gas.
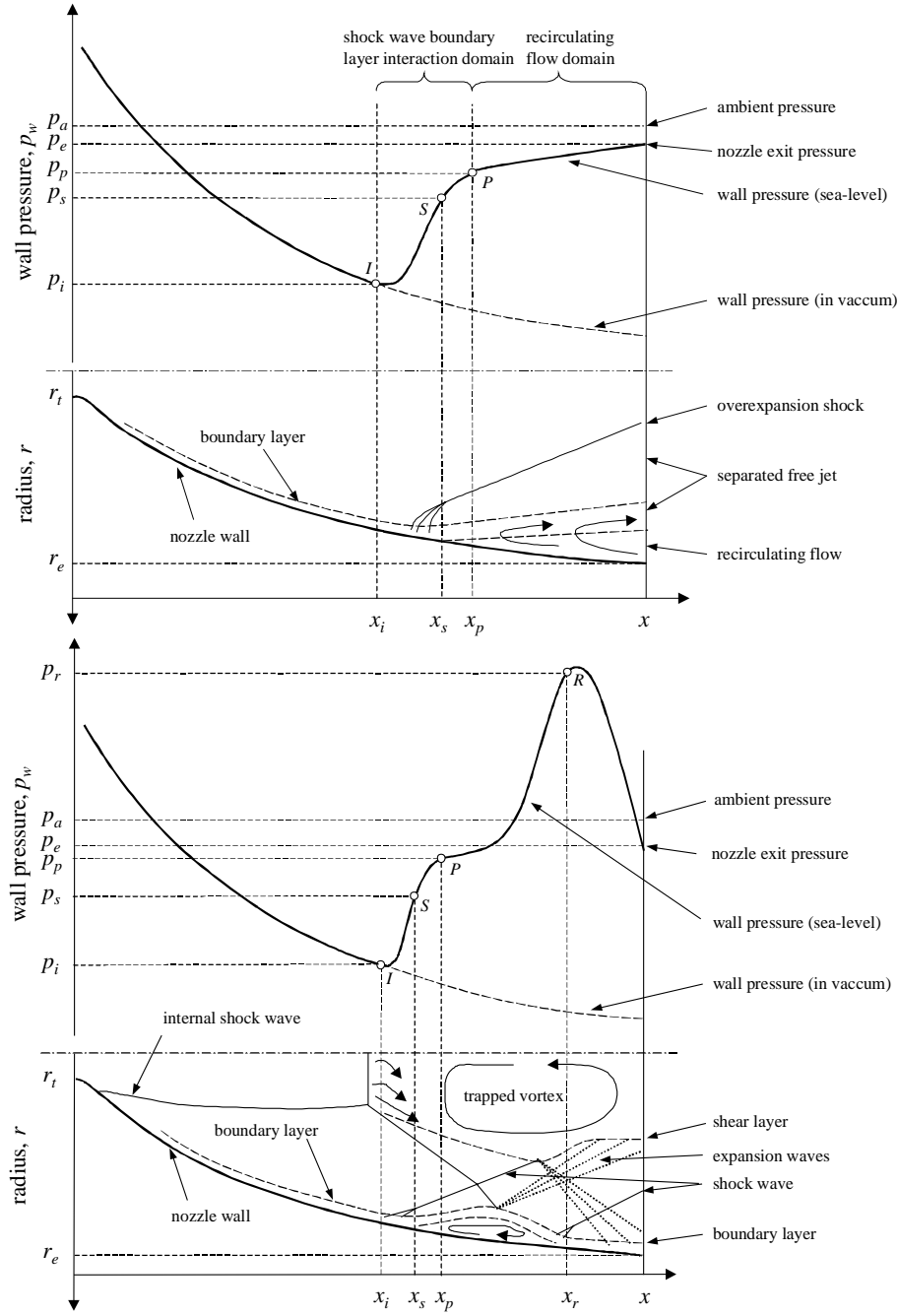
Figure 37. Phenomenological sketch of free shock separation (FSS, top), and restricted shock separation (RSS, bottom).

It was noticed already in the early 1950's, that the separation pressure ratio decreases during the start-up of nozzle flows, as the separation point moves downstream with increasing pressure ratio p_c/p_a.[R 81-R 87] This was soon attributed to the Mach number influence, as experiments in wind tunnels had shown the separation pressure ratio to decrease with increasing Mach number. However, there is a deviation from this regular behaviour as the separation point reaches the vicinity of the exit.[R 87-R 88] At a location where the local area

41

ratio of the nozzle has reached about 80% of its final value, the separation pressure ratio, p_i/p_a, reverses its previous trend and increases as the pressure ratio p_c/p_a is increased. An explanation given for this behaviour in reference R 88 is that close to the nozzle exit the plateau pressure increases to ambient pressure. For a constant pressure ratio, p_i/p_p, this would cause an effective increase in separation pressure, p_i, in this last part of the nozzle, and thus an increase in p_i/p_a. As the pressure plateau p reaches the nozzle exit, the flow is actually attached all the way to the exit even though the sensors detect a clear pressure rise. This is usually referred to as incipient separation at the nozzle exit.
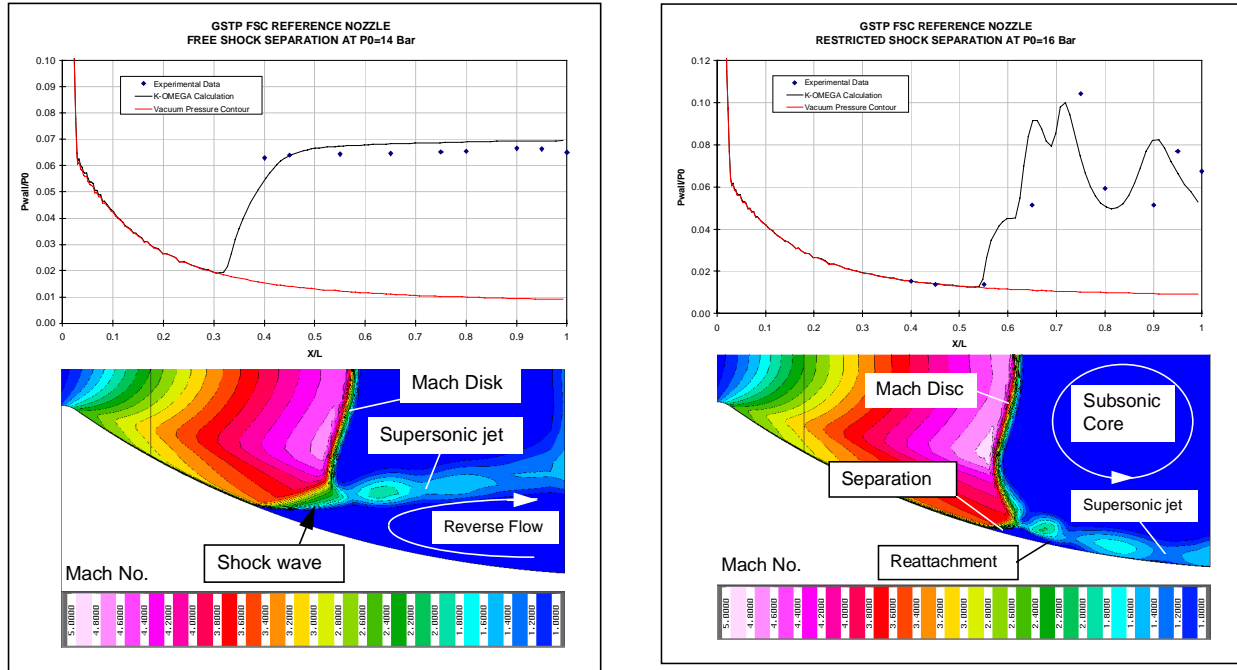
Figure 38. Free (left) and restricted shock separation (right) in the parabolic subscale nozzle VOLVO S1, comparison of measured and calculated wall pressures, and calculated Mach number distribution. Experimental data by FOI calculations performed by VOLVO (from Östlund[R 5]).

6.2   RESTRICTED SHOCK SEPARATION

During cold-flow subscale tests for the J-2S engine development in the early 70s, a different kind of separated nozzle flow was observed at strongly overexpanded conditions, which had not been known before.[R 95] In this flow regime, which only occurred at certain pressure ratios, the pressure downstream of the separation point showed an irregular behaviour and partly reached values above the ambient pressure. This is attributed to a reattachment of the separated flow to the nozzle wall, inducing a pattern of alternating shocks and expansion waves along the wall. Due to the short separated region, this flow regime was called *restricted shock separation*. The separation characteristic of *restricted shock separation*, as observed in the literature[R 95], and recently confirmed for subscale[R 5,R 7,R 8] and full-scale rocket nozzles[R 2-R 4] is described in the following.

During the start-up of the nozzle flow, featuring initially pure free shock separation, the transition from FSS to RSS occurs at a well-defined pressure ratio.[R 4,R 5] A closed recirculation zone is formed, with static pressures significantly below the ambient pressure level. Thus, the transition from FSS to RSS is connected with a sudden downstream movement of the separation point. Beyond the reattachment point in RSS, supersonic flow propagates along the nozzle, thereby inducing shocks that result in the aforementioned wall pressure peaks above ambient pressure. By further increasing the thrust chamber pressure ratio, the closed recirculation zone is pushed towards the nozzle exit. Finally, the reattachment point reaches the nozzle exit, and the recirculation zone opens to the ambient flow. This is connected with a pressure increase in the recirculation zone behind the separation shock, which pushes the separation point again further upstream. Thereby it occurs, that the recirculation zone closes again, connected with a drop in static pressure, which

results again in a downstream movement of the separation point. A pulsating process is observed, connected with the opening and closing of the separation zone. This re-transition from RSS back to FSS is in the literature also referred to as the end effect.[R 4,R 5]

The same phenomena can be also observed during shut-down. While the end-effect, and thus the transition, now from FSS to RSS, occurs at the same pressure ratio as the RSS to FSS transition during start-up, the re-transition from RSS to FSS occurs in general at a different lower pressure ratio than the corresponding transition FSS-RSS during start-up.[R 2-R 5]

The theory of reattached flow in the J-2S sub-scale nozzle was first confirmed by numerical simulations of Chen et al. in 1994[R 90]. In addition, their calculations revealed a trapped vortex behind the central normal shock, but they did not provide any explanation for the generation of such flow structure.
Later, Nasuti and Onofri[R 91-R 93] stressed the role played by the centreline vortex on the separation pattern and side-load generation. The centreline vortex acts as an obstruction for the exhausting jet, which is therby pushed towards the wall. As a consequence a radial flow component is generated that tends to reattach the separated region, thus switching the flow from FSS to RSS.

Frey and Hagemann have given another explanation of the reattached flow based upon experimental observations and numerical simulation.[R 2,R 3] According to their results, the key driver for the transition from FSS to RSS and vice versa is the specific cap-shock pattern. Thus, a transition from FSS to RSS can only occur in nozzles featuring an internal shock. According to their findings, the cap-shock pattern results from the interference of the separation shock with the inverse Mach reflection of the weak internal shock at the centreline.[R 3] A key feature of this inverse Mach reflection is the trapped vortex downstream of it, driven by the curved shock structure upstream of it which generates a certain vorticity in the flow.[R 3,R 96,R 97] Thus, the vortex would be a result of the curved shock structure, which is partially in contrast the explanation given by Nasuti and Onofri, that includes also an effect of flow gradients upstream. Further experimental and numerical verification is planned to finally conclude on the interesting vortex phenomenon.

However, it is interesting to note that both hypotheses of Nasuti and Onofri, and Frey and Hagemann identify the curved cap-shock profile as driver for the transition from FSS to RSS, which is meanwhile proven by experiments.[R 4-R 8]

6.3   CRITERA FOR FLOW SEPARATION PREDICTION IN ROCKET NOZZLES

6.3.1   Free shock separation criteria

The theoretical prediction of free shock separation is the case, which has been most extensively studied in the past since, historically, almost all experiments have been performed in conical and truncated ideal nozzle contours only featuring this separation pattern. Experimental data have been used to develop a number of empirical and semi-empirical criteria in order to give the nozzle designer a prediction tool for the separation point, although knowing that in reality there is no exact point of separation because it fluctuates between two extreme locations. But even today, an exact prediction cannot be guaranteed because of the wide spectrum of parameters involved in the boundary layer – shock interaction such as nozzle contour, gas properties, wall temperature, wall configuration and roughness.

Probably the most classical and simple criteria for FSS purely derived from nozzle testing is the one given by Summerfield et al[R 83] which is based on extensive studies on the separation phenomenon in conical nozzles in the late 1940's:

$$p_i/p_a \approx 0.4 \qquad\qquad\qquad \text{Eq. 28}$$

A first approach to include the Mach number influence was published by Arens and Spiegler in the early 1960's.[R 87] However, the major formula derived turned out to be too complex for engineering application.
Based on experiments with conical and truncated ideal nozzles, Schilling derived in 1962 a simple expression accounting for the increase of separation pressure ratio p_i/p_a with increasing Mach number,

$$p_i/p_a = k_1 (p_c/p_a)^{k2}$$ <div style="text-align: right">Eq. 29</div>

with $k_1 = 0.582$, and $k_2 = -0.195$ for contoured nozzles, and $k_1 = 0.541$, and $k_2 = -0.136$ for conical nozzles.[R 85] In 1965, based on Schilling's expression Kalt and Badal chose $k_1 = 2/3$ and $k_2 = -0.2$ for a better agreement with their experimental results.[R 86] NASA adopted a correlation similar to the one of Schilling for truncated contoured nozzles as a state of the art indication at the mid 1970's.[R 98]

Later investigations performed by Schmucker[R 94] lead NASA to recommend the semi-empirical criterion by Crocco and Probstein[R 99], which is based on a simplified boundary layer integral approach. The criterion accounts for the properties of the boundary layer, the gas and the inviscid Mach number at the onset of separation. The NASA recommendation from 1976 was to use this criterion with an additional margin of 20% from the predicted separation occurrence. Another inheritance from this time is the purely empirical criterion proposed by Schmucker: [R 94]

$$p_i/p_a = (1.88 \cdot M_i - 1)^{-0.64}$$ <div style="text-align: right">Eq. 30</div>

which has similar characteristics as the Crocco and Probstein criterion and is still widely used.
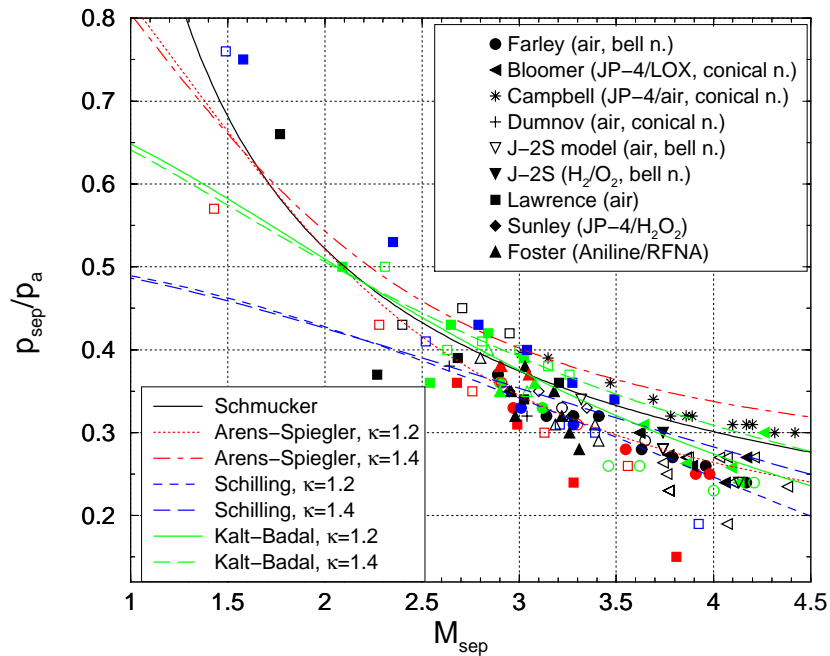
Figure 39. Comparison of simple separation prediction models for p_i/p_a with experimental results. The symbol shape in the legend indicates from which investigation the data is taken and the symbol colours correspond to different nozzle configurations tested, see Frey[R 110]. Also published in R 105. (remark $p_{sep}=p_i$ and $M_{sep}=M_i$)

In Figure 39 a comparison between these criteria with test data are shown. As indicated in the figure a significant scatter of the data points can be observed. This explains the NASA advice of a 20% margin and also points out the necessity of new and more reliable criteria. One of the major reasons for the rather poor agreement is that all above criteria include two separate mechanisms involved in the pressure rise of the flow in one single expression. This fact was realised already in the 1960's by Arens and Spiegler[R 87], Carriere[R 100] and by Lawrence[R 89]. The latter suggested that the pressure recovery p_i/p_a should be subdivided into two parts, one part for the critical pressure rise, p_i/p_p, over the separation shock and a second for the pressure rise in the recirculation zone, p_p/p_a.

The pressure rise p_i to p_p is caused by shock-wave boundary layer interaction, as described in paragraph 5.2. This is a general mechanism, not restricted to nozzle flow separation, which has been extensively studied. As

an example, Zukoski[R 45] found the following simple relation (cf. Eq. 24) to be in good agreement with experimental results for high Reynolds numbers:

$$p_i/p_p = (1 + 0.5\,M_i)^{-1}$$

<div align="right">Eq. 31</div>

for the Mach number range of $M_i = 1.4\text{-}6.0$ and $Re_\delta > 10^5$. According to the author, this correlation also agrees with the plateau pressure values measured in overexpanded conical nozzles in the Mach number range $M_i = 2.0\text{-}5.5$.

The drawback of the Zukoski criterion is that it does not include the dependency of the specific heat ratio observed in experimental data and should thus only be used for gas flow with $\gamma = 1.4$, since the experiments were performed with air. A first attempt to account for the specific heat ratio dependency by using oblique shock relations was proposed by Summerfield et al. 1954.[R 83] From experimental data they found that the flow deflection angle θ of the separated flow was nearly constant $\theta \approx 15^\circ$ for the nozzles tested. With this value and the use of oblique shock theory the pressure rise for different gas mixtures can thus be calculated. This observation has also been confirmed in later synthesis of nozzle flow separation data, from a number of experiments performed with both hot and cold gas flows[R 2]. However, the data also indicate that the Summerfield criterion with a constant θ value is too simple. In fact the data rather indicate a linear dependence of the Mach number on both the deflection angle θ and the shock angle β itself. Based on this and data from the VOLVO subscale tests[R 6] Östlund[R 109] proposed an empirical criterion based on oblique shock relations:

$$\frac{p_i}{p_p} = \left\{ 1 + \gamma M_i^2 \sin^2(\beta) \cdot \left[1 - \frac{\tan(\beta - \theta)}{\tan(\beta)} \right] \right\}^{-1}$$

<div align="right">Eq. 32</div>

with $\beta = -3.764 M_i + 42.878$ [°] and $\theta = 1.678 M_i + 9.347$ [°] for the Mach number range $2.5 \le M_i \le 4.5$. Östlund used linear expressions for both θ and β in the correlation since he found that a criterion only based on the shock angle β (and θ calculated with the θ-β-M relation) experiences a minimum already for a modest extrapolation above $M_i = 4.5$. Frey[R 110] has proposed a similar criterion based only on the shock angle β as:

$$\frac{p_i}{p_p} = \left[1 + \frac{2\gamma}{\gamma + 1} \left(M_i^2 \sin^2(\beta) - 1 \right) \right]^{-1}$$

<div align="right">Eq. 33</div>

with $\beta = -4.7 M_i + 44.5$ [°] for the Mach number range $2.5 \le M_i \le 4.5$, which produces a similar result as the criterion by Östlund (Eq. 32 reduces to Eq. 33 with the use of the θ-β-M relation). However, it does not give the correct trend of p_i/p_p for higher Mach numbers. At $M \approx 4.8$ the function has a minimum and p_i/p_p suddenly increases with the Mach number.

Although these criteria give a significant improvement, they are still pure empirical and it is always better to base a criterion on a physical model in order to correctly include the influence of governing parameters. A promising theory to build such a criterion on seems to be the generalised free interaction theory by Carrière et al[R 111], which has received new attention within the FSCD group[R 159, R 160]. These authors generalised the free interaction theory by Chapman, see 5.2.2, by taking into account both non-uniformity in the incoming outer flow and the wall curvature in the interaction region. They found that in the most generalised case, the universal correlation function takes the form (cf. Eq. 19-20):

$$F\left(\frac{x - x_i}{x_s - x_i}, p' \right) = \sqrt{ \frac{p(x) - p_i}{q_i} \frac{\overline{V}(x) - V(x)}{C_{fi}} } \quad , \quad p' = \frac{\delta_i^*}{q_i} \frac{dp}{dx}$$

<div align="right">Eq. 34</div>

Where V is the Prandtl-Meyer function for the actual pressure at x and $\overline{V}$ the value V would take at the same location in absence of flow separation. p' is the normalised pressure gradient characterising the non-uniformity of the flow. For a specific p', the function F is assumed to be a universal correlation function

independent of Mach and Reynolds numbers, to be determined from experiments. In Figure 40 the generalised wall pressure correlation function for non-uniform flow, F, and the separation length, l_s, obtained by Carrière et al. is shown. The correlation function for uniform flow is also included in the figure so the influence of p' on F can be seen. Carrière et al. based their correlation on axi-symmetrical experimental data from one ideal nozzle with design Mach number $M_D=3$ and three conical nozzles with half-angles of 5º, 10º and 17.5º respectively. With these nozzles the Mach number range $2.06 \leq M_i \leq 2.78$ and $4.12 \leq M_i \leq 5.04$ was covered for values of the pressure gradient in the range $-1.2 \leq p' \cdot 10^3 \leq -0.8$.
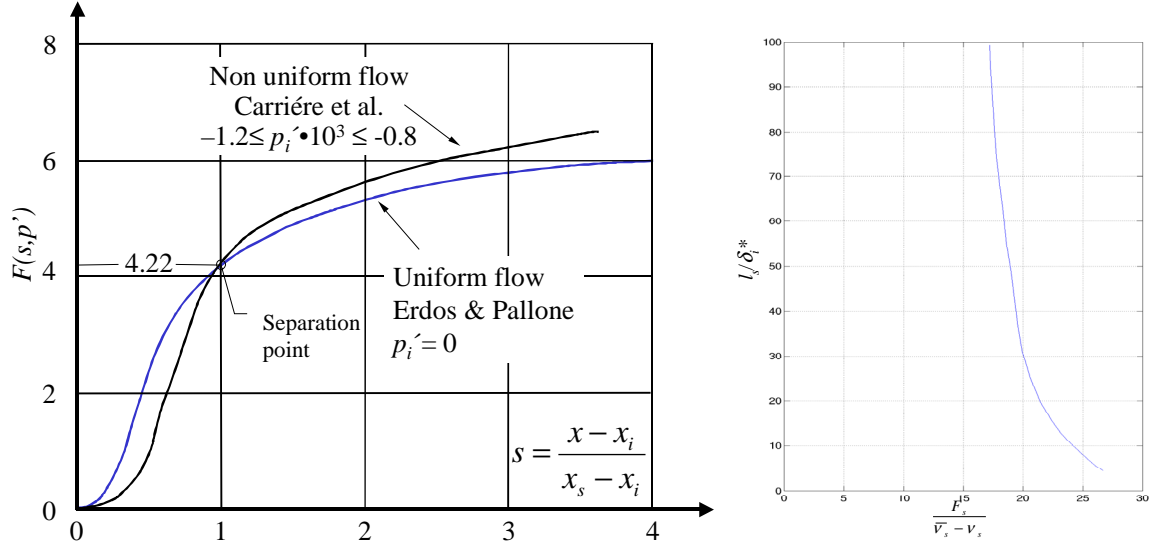
Figure 40. Free interaction theory. Pressure correlation and separation length for non-uniform flow, $F_s=4.22$, Carrière et al[R 111].

However, in order to obtain a criterion for the pressure rise p_i/p_p, a correlation for the interaction length l_p, i.e. from the start of the shock boundary layer interaction to the plateau point, is needed rather than the separation length l_s it self as given by Carrière et al. Since no rational definition of the plateau point exists for non-uniform flow, we define the plateau point to be the position where the function F has the value $F_p=6.0$ characterising the plateau point in uniform flow. A first attempt to calculate the pressure correlation function $F(s,p')$ and the interaction length by only exploiting data form the VOLVO subscale test campaigns[R 6] showed to be unsuccessful due to insufficient axial resolution of the pressure measurements in the interaction region. Instead the pressure correlation function by Carrière et al. was fitted to the experimental data by varying the values of x_i and l_s for each nozzle flow condition. Results from such a procedure, applied to experimental data obtained with the VOLVO S6 nozzle, are shown in Figure 41. The flow properties were determined using TDK together with the built in boundary layer module for each operational condition. As can be seen in the figure, the pressure correlation curve by Carrière et al. fits the experimental data well. The corresponding calculated values of the separation length and the plateau length are shown in Figure 42. The obtained values of the separation length and the ones given by Carrière et al. are very similar. The small difference is probably due to differences in the computational method used for determining of the boundary layer properties. A correlation function for the plateau length i.e. $l_p/\delta_i^* = f\left(F_p/\left(\overline{v}_p - v_p\right)\right)$ was then determined with the use of a least square curve fitting technique. The obtained correlation curve is indicated in Figure 42. In contrast to the free interaction theory for uniform flow, see 5.2.2, the interaction length for the non-uniform flow condition obtained in overexpanded nozzles also depends on the downstream conditions. The influence of e.g. the plateau pressure value on interaction length can be found by rewriting equation 34 at the plateau point as:

$$\frac{F_p}{\overline{v}_p - v_p} = \frac{p_p/p_i - 1}{\frac{1}{2}\gamma M_i^2 C_{fi} F_p}$$

Eq. 35

Inspection of equation 35 together with Figure 42 shows that l_p/δ_i^* increases as the plateau pressure is reduced, which has also been verified in experiments[R 111]. However, other empirical relations used for the interaction length in separated nozzle flows show no influence of the downstream conditions, e.g. Dumnov et al.[R 112] found that $l_r/\theta_i=f(M_i,T_{wi})$, where θ_i is the momentum thickness at the start of the interaction.

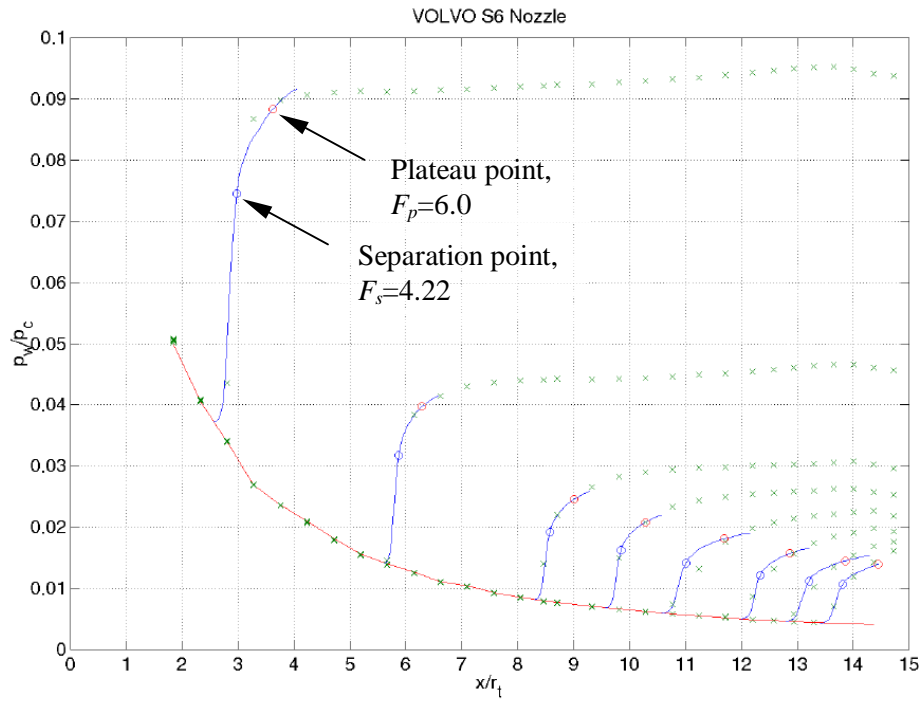Figure 41. Fit of generalised pressure correlation curve by Carrière et al. to VOLVO S6 data, x_i and l_s varied, $2.82 \leq M_i \leq 3.25$, $-0.9 \leq p' \bullet 10^3 \leq -0.5$, $n=0.04-0.24$. (Data also published in Östlund et al[R 108])
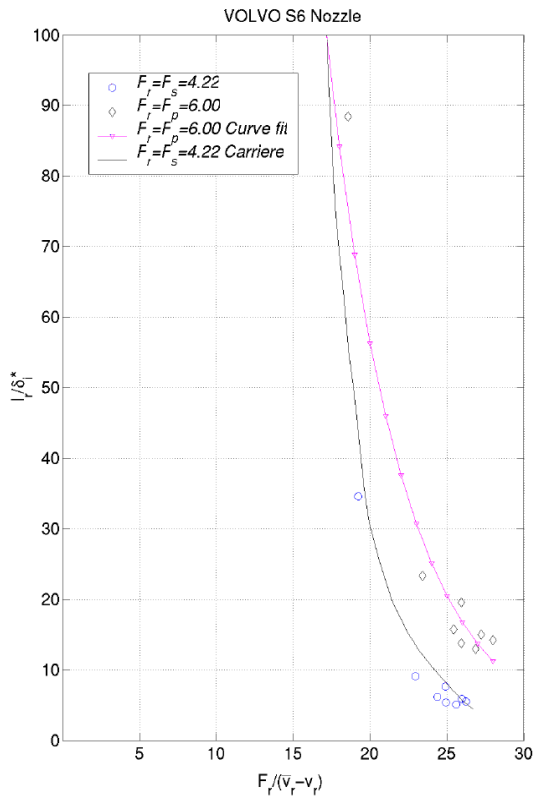

Figure 42. Interaction length correlation, to separation point (l_s) and plateau point (l_p) respectively. Symbols indicate calculated values based on VOLVO S6 nozzle test data.

With the use of equation 35 and the correlation function for the plateau length, the location of the start of the interaction process (x_i) can be determined in a nozzle at a given operation condition when the plateau pressure value is known. This is done by iteratively solving the implicit equation 36.

$$\frac{F_p}{\overline{V}(x_i + \frac{l_p}{\delta_i^*}(f_i) \cdot \delta_i^*(x_i)) - v_p(p_p)} = f_i,$$

$$\text{with} \quad f_i(x_i, p_p) = \frac{p_p/p_i - 1}{\frac{1}{2}\gamma M_i^2 C_{fi} F_p}$$

Eq. 36

In order to check the validity of this criterion it was applied to the Volvo S7 short nozzle. The flow properties at different operational condition were determined using TDK together with the built-in boundary layer module BLM. For each flow condition a plateau pressure value was specified based on experimental data. As can be seen in Figure 43, the predicted pressure profiles in the interaction zone show a good agreement with the test data for all cases.
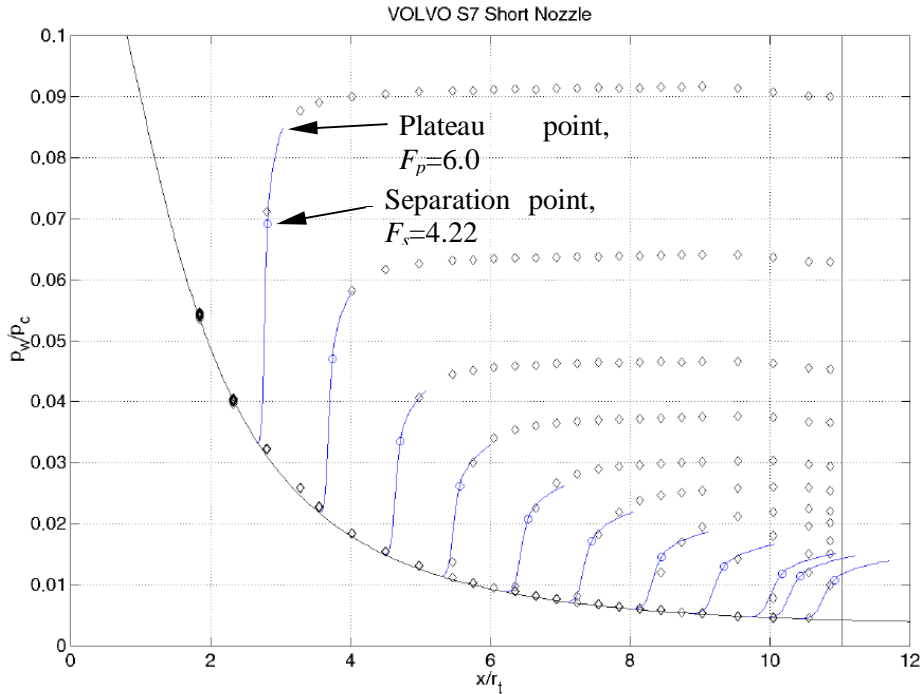
Figure 43. Predicted and measured wall pressure profile in the Volvo S7 Short Nozzle.

Although the first results look promising, a lot of effort needs to be put down before a reliable and accurate criterion can be established. More test data need to be evaluated in order to increase the accuracy of the correlation functions and the applicability to chemical reacting flow cases, where the value of the specific heat ratio is different compared with air, must also be validated. The influence of wall cooling has to be examined, a specially the wall temperature effect on the interaction length. One simple method to take this influence in to account can be to formulate a correction function i.e. $l_{r,cooled}/l_{r,adiabatic} = f(M_i, T_w/T_r)$ similar to the approach used by Lewis et al. for laminar flow[R 113], see also the results obtained by Spaid and Frishett[R 54] for turbulent ramp flow in Figure 30. The scaling of the interaction length with the displacement thickness, δ_i^*, must also be revised since δ_i^* can become negative in strongly cooled nozzle flows. The boundary layer thickness, δ_i, or the momentum thickness, θ_i, may be a better choice for scaling in such cases. In order to shad light on these opened ends, test are presently being prepared at Volvo, ASTRIUM and DLR with some test objectives specially focused on the wall temperature effects on nozzle flow separation. An example taken from the preparations of this campaign is shown in Figure 44.
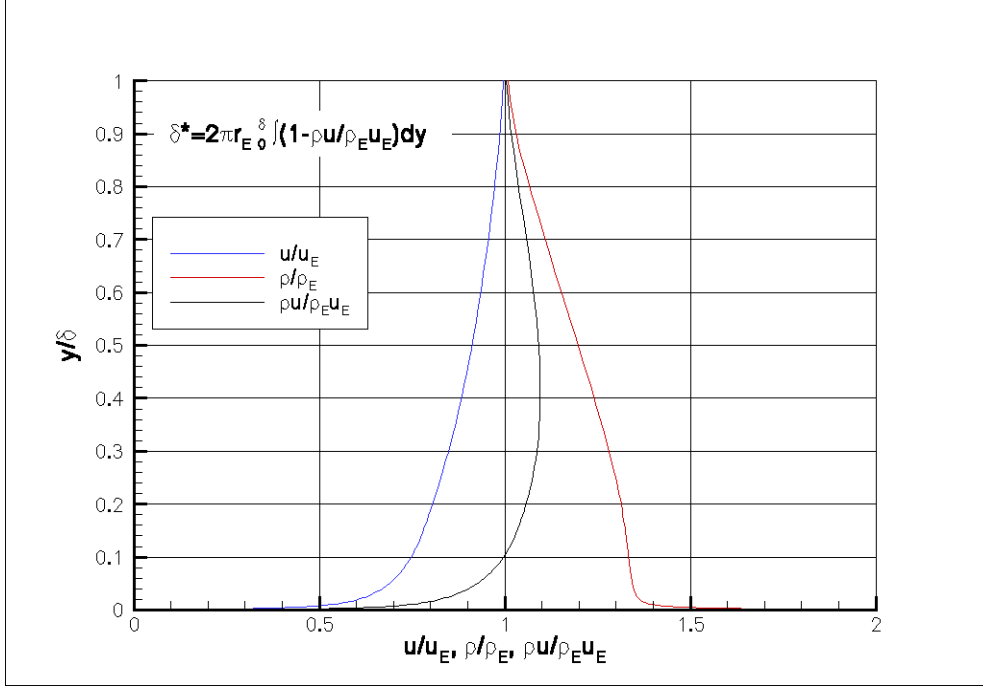
Figure 44. Illustration of negative displacement thickness in a strongly cooled nozzle flow.

As shown above, the streamwise length of the interaction zone can not be predicted with the generalised free interaction theory alone since it depends on the flow in the separated region. It needs to be coupled with a model describing the flow downstream of the shock-wave boundary layer interaction, where the pressure recovery, p_p/p_a, takes place. Such a model is currently not available for contoured nozzles. The only reported models for the recirculating flow in the literature are the ones by Kudryavtsev[R 114] and the one by Malik and Tagirov[R 115], both for conical nozzles operated with air. The model by Kudryavtsev is purely empirical. He found that in conical nozzles with a half angle $\alpha<15°$ the pressure rise in the recirculating zone could be approximated as:

$$\frac{p_p}{p_a} = \left[1+\left(\frac{0.192}{\sin\alpha}-0.7\right)\left(1-\frac{M_i}{M_a}\right)\right]^{-1}$$

Eq. 37

Where M_a is the average exit Mach number defined by the nozzle expansion area ratio ε. Whereas, in conical nozzles with a half angle $\alpha>15°$ he found that the pressure rise $p_p/p_a\approx1$, i.e. independent of the Mach number. The pressure rise calculated with equation 37 is shown in Figure 45 for conical nozzles with half angles $5°\leq\alpha\leq15°$.

The model by Malik and Tagirov on the other hand is semi-empirical and is based on Abramovich's theory for the mixing of counterflowing turbulent jets.[R 116] This model shows good agreement with test data and if it is generalised it could be a promising model for contoured nozzles operated with hot propellants. A model for recirculating flow in contoured nozzles, whether empirical or semi-empirical, must take into account a number of parameters. Experimental data indicate e.g. that the wall contour downstream the separation point has a significant influence on the pressure increase in the recirculation zone.[R 89] As reported in reference R 2, the length of the separated region, the curvature of the wall downstream of the separation and the radial size of the recirculating zone between the wall and the jet are further parameters influencing the pressure rise p_p/p_a. A clear indication of this can be found in Figure 46, where p_p/p_a is plotted versus $\varepsilon-\varepsilon_i$ which is a measure of the radial size of the recirculation zone. For large values of $\varepsilon-\varepsilon_i$, the downstream contour has a negligible influence on the pressure rise, whereas for the case when the separated jet is close to the wall (small $\varepsilon-\varepsilon_i$) there is a large variation in p_p/p_a. Besides that, the sudden increase of p_p/p_a as the incipient separation point enters the nozzle exit region must also be included. This increase of p_p/p_a is a general feature

49

for all nozzle flows and it is illustrated in Figure 47 by experimental values obtained with the short VOLVO S7 nozzle.
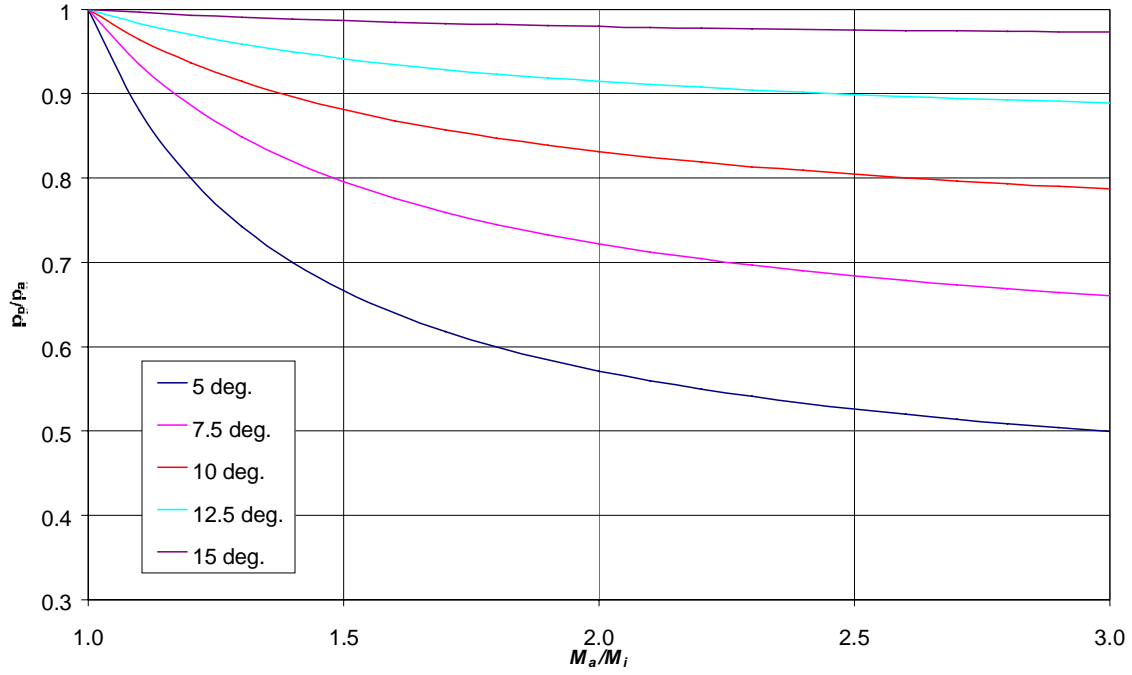
Figure 45. Pressure rise in the recirculating zone in conical nozzles with half angles $\alpha<15°$ according to the model by Kudryavtsev[R 114]
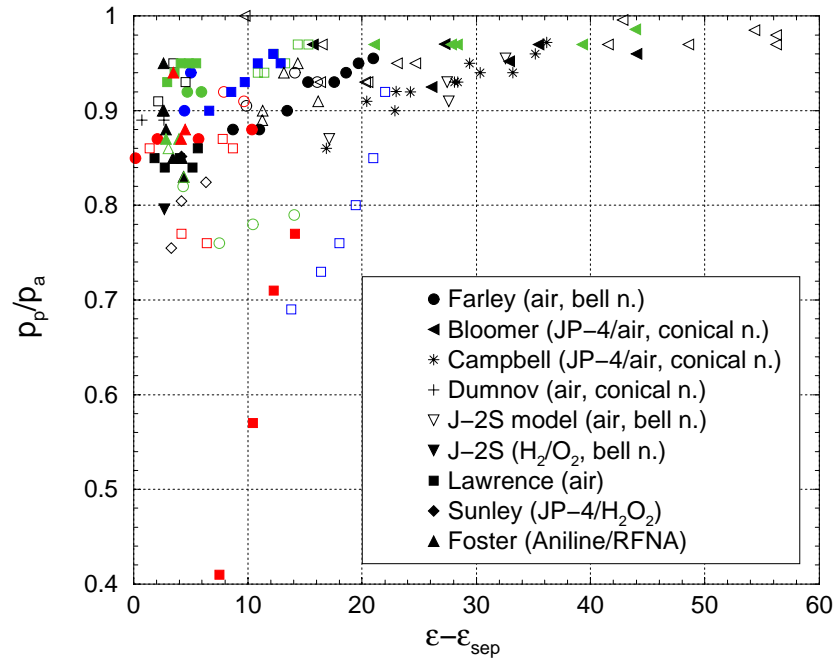
Figure 46. Experimental results for the pressure rise p_p/p_a as function of separation location. The symbol shape in the legend indicates from which investigation the data is taken and the symbol colours correspond to different nozzle configurations tested, see Frey[R 110]. Also published in R 105.
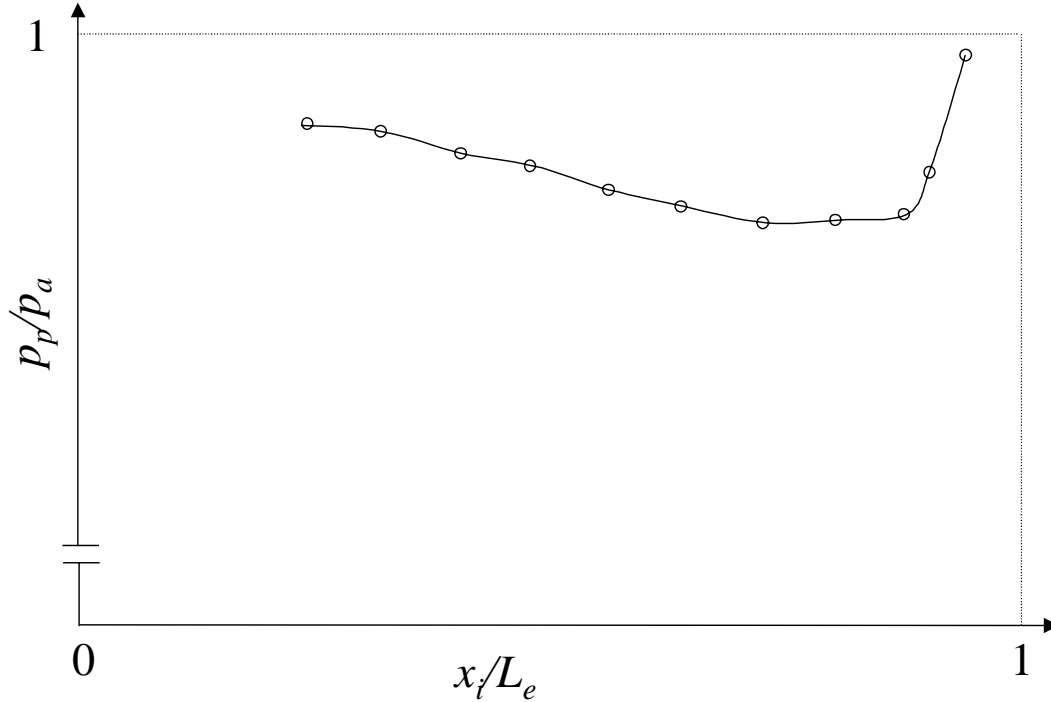
Figure 47. Illustration of p_p/p_a vs. x_i/L_e with the use of test data from the short Volvos S7 nozzle.

Thus, it is obvious that in order to predict the location of separation successfully, a separation criterion must consist of two parts, first of all a model where the shock-boundary layer interaction is properly described and secondly a model where the pressure rise in the recirculating zone is included which accounts for downstream conditions and nozzle geometry. The development and validation work of such models is currently ongoing at the different partners of the FSCD group, see e.g. the recent work by Reijasse and Birkemeyer[R 160].

6.3.2 Restricted shock separation criteria

The prediction of restricted shock separation has only been addressed in the last years, see reference R 3 and R 6. The key point for the prediction of RSS is to predict the location where the transition from FSS to RSS takes place. The driving force for reattachment of the flow is when the radial momentum of the separated jet is directed towards the wall, which can occur with a cap-shock pattern. Whereas no reattachment is possible if the momentum is directed towards the centre-line, which is always the case with a Mach disc. Thus, by quantifying the momentum balance of the jet, the transition point can be determined. On this basis Östlund and Bigert[R 6] proposed a simple empirical criterion for the prediction of transition from FSS to RSS, which relates the FSS-RSS transition to the axial position where the small normal shock at the centre-line coincide with the RSS separation front, see Figure 48. As indicated in Figure 48 and Table 3 this model shows very good results considering its simplicity.

Case	p_c for transition: predicted / actual
Vulcain NE	1.05
VolvoS1	0.94
VolvoS3	1.00

Table 3. VOLVO-model for predicting at which chamber pressure, p_c, there is an FSS to RSS transition, also published in Östlund et al[R 108].

51

VOLVO S3 NOZZLE

▲ Position where normal shock and RSS line coincides, criterion for FSS=>RSS transition
— Calculated RSS line, used to identify transition
— Predicted position of normal shock
— Predicted separation line
□ Measured separation position
○ Measured normal shock position
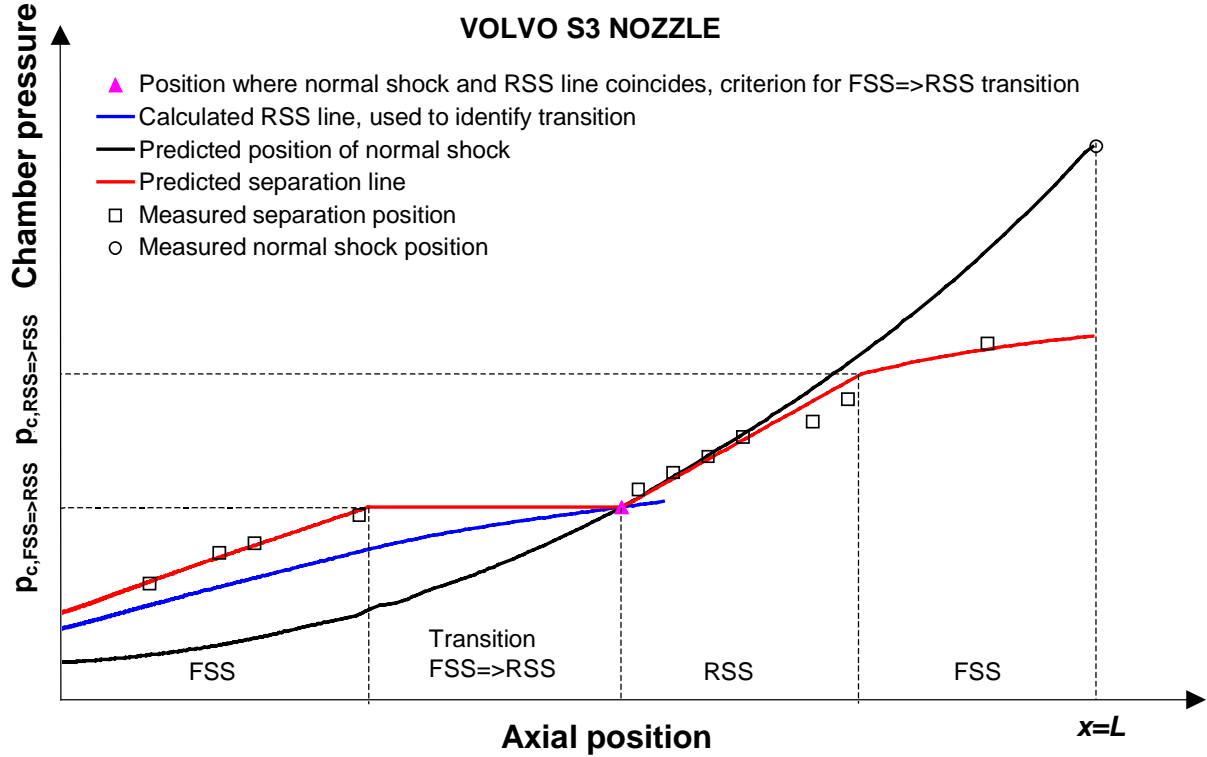
Figure 48. FSS-RSS transition model, principle of model together with comparison of predicted and measured values for the VOLVO S3 nozzle.

Frey and Hagemann have developed a more sophisticated and physical model.[R 3] In this model the FSS shock system is always prevailing before a possible reattachment is defined. Based on numerical flow field data, the cap shock pattern is re-calculated by a shock-fitting technique. By calculating the momentum balance across the cap shock pattern and the corresponding direction of the jet downstream of the cap shock pattern, the driving force for reattachment is evaluated and the location where the transition takes place is determined.

Both models account for the sudden pressure drop of the plateau pressure and the subsequent jump of the separation point when the flow reattaches and the separated region becomes enclosed by supersonic flow. Due to the complexity of the flow downstream of the reattachment point, which is characterised by subsequent compression and expansion waves, no models for this pressure recovery process exist so far. Instead a constant value of the plateau pressure based on test data experience is often used. This value is kept until the RSS is transformed back into FSS and FSS criteria are applicable again. This transformation occurs either when the cap-shock is converted into the Mach disc or when the enclosed separation zone is opened up at the nozzle exit, as shown in Figure 48.

Based on numerical simulations of the cap shock pattern with the trapped vortex, Reijasse[R 7] has proposed a further transition prediction model based on an effective area ratio for the RSS condition, estimated with the effective nozzle exit area occupied by the re-attached annular jet, and the throat area. Thus, the remaining exit area filled with the re-circulating flow of the trapped vortex is ignored in this approach.

7   MEASURMENT OF FLOW SEPARATION AND SIDE LOADS

7.1   STATIC WALL PRESSURE MEASUREMENTS

Static pressure taps are standard instrumentation in most flow applications and can give valuable information of the flow process if the instrumentation is carefully done and correct interpretations of the measurements are made. Figure 49 shows a typical wall pressure profile for a highly overexpanded nozzle flow. The location where the static wall pressure starts to rise, x_i, is the origin of the shock wave boundary layer interaction, and a correct determination of this position is essential for constructing flow separation models. In order to experimentally locate this position, an extremely narrow spacing of the pressure transducers is required. The separation length, $l_s = x_s - x_i$ (cf. Figure 25 and Figure 37), where most part of the pressure rise takes places ranges from 1 to $100\delta^*$, depending on operational condition, degree of overexpansion, nozzle contour etc., see Figure 42. A rough estimate, which should only be considered as a rule of thumb to get the order of magnitude, is $l_s < 0.5r_t$, based on "cold" sub-scale test data see e.g. Figure 41 and Figure 43. As indicated in the schematic in Figure 49, a modest increase in the wall pressure takes place before a steep and almost linear pressure rise. To resolve this initial gradual increase and locate the first deviation from the vacuum pressure profile would require a transducer spacing of about $\Delta x = l_s/10 \approx 0.05r_t$. In the VOLVO sub scale nozzles, which are considered to be of large scale in the context of cold flow model nozzles, the throat radius is $r_t = 33.54$ mm. Thus the order of magnitude of the separation length in these nozzles are about $l_s < 0.5*33.54 \approx 17$ mm, and to resolve the first deviation from the vacuum pressure profile would require a transducer spacing of $\Delta x \approx 0.05r_t = 1.7$ mm in this case. Such resolution can be realised, i.e. transducer spacings of 0.5 mm have been used at FOI[R 137], however the instrumentation cost will become high and the transducers may influence the flow. The use of modern measuring techniques such as Pressure Sensitive Paint (PSP) would overcome this problem of spatial resolution. PSP is commonly used for external high-speed flow situations[R 125], whereas there are only a few studies in the literature, where PSP has been applied to internal supersonic flow, see e.g. reference R 126-R 128. The main problem with PSP is that the paint has a strong temperature dependency. It must therefore be used together with IR-techniques or Temperature Sensitive Paint (TSP). In the case of internal flow, the visual access further complicates the situation. PSP is not as accurate as static pressure taps, the accuracy being only about 5%, why a combination of PSP and regular pressure taps is often used[R 137].

Despite obvious practical problems to obtain the necessary resolution with static pressure taps, some investigators have adopted this approach to determine the origin of the interaction e.g. Carrière et al[R 111]. However, most investigators have chosen a conventional origin obtained by extrapolating to the wall the quasi-linear pressure rise at separation, as shown in Figure 49. The origin obtained with this method is always downstream of the physical origin. Another point of interest is the location of the end of the shock boundary layer interaction, i.e. the plateau point. In the case of obstacle-induced separation in uniform flow, a well defined plateau point can be observed in the wall pressure data, see Figure 25, however this is not the case in overexpanded nozzle flows as sketched in Figure 49. A common approach is to define the plateau pressure as the pressure value at the intersection between two straight lines, one line being tangent to the steep pressure rise obtained in the interaction region, and the other one tangent to the pressure rise in the recirculating flow region. Since the determination of the plateau point is rather arbitrary with this method, Östlund proposes inhere, to determine x_i and l_s from a best fit of the generalised pressure correlation function, $F(x_i, l_s)$ by Carrière et al.[R 111] to the experimental data. Since no rational definition of the plateau point exists for non-uniform flow, the plateau point is defined as the position where the function F has the value $F_p = 6.0$ which is analogous to Erdos and Pallone[R 78] definition of the plateau point in uniform flow, cf. Figure 27. The result from such a procedure, applied to experimental data obtained with the VOLVO S6 nozzle, is shown in Figure 41.
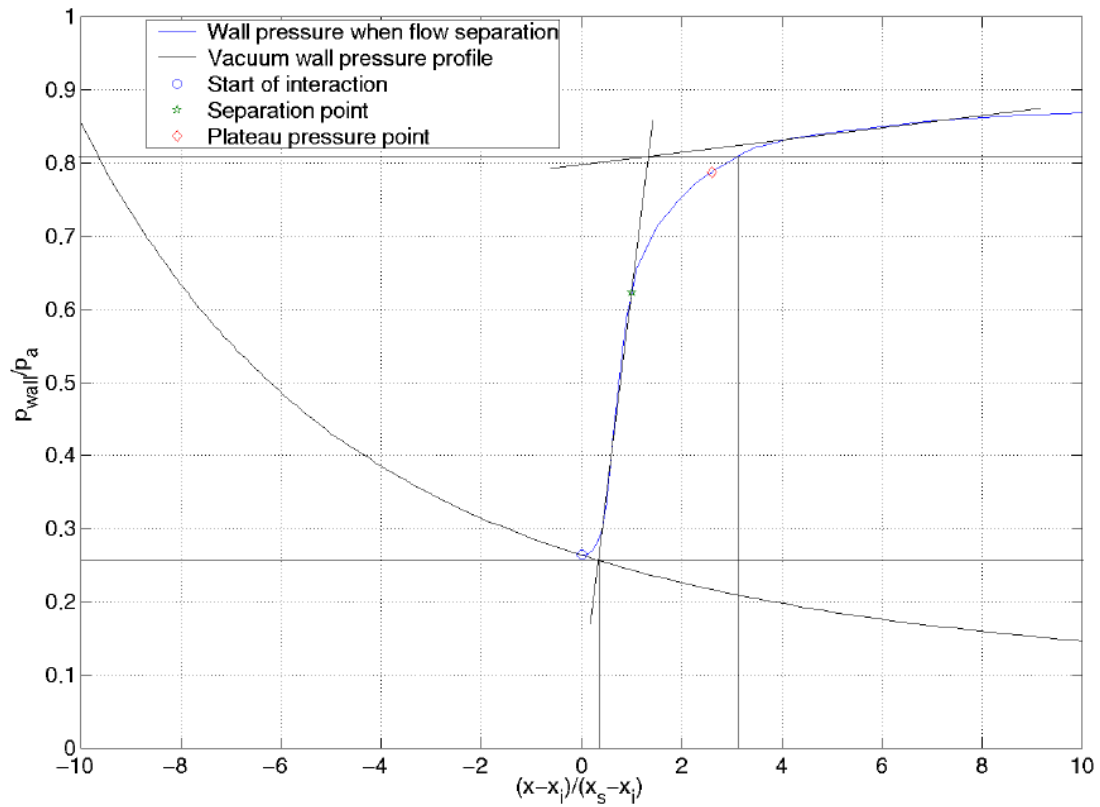
Figure 49. Typical wall pressure profile obtained in a highly overexpanded nozzle.

7.2   FLUCTUATING WALL PRESSURE MEASUREMENTS

As reported previous (see section 5.2.4 and 8.3), the shock boundary layer interaction found in highly overexpanded nozzle flows is an intermittent and three-dimensional phenomenon. Mechanical structures exposed to this type of supersonic flow separation are effected by large, time-dependent forces, which can be resolved into two components, a low frequency buffeting caused by changes in the geometry of the separation region, and fluctuations originating from the shear-layer of the separated region. Accurate models for the prediction of these loads are needed in order to mechanically define the thrust chamber structure to ensure mechanical integrity under "worst case" condition. Development and validation of such models still relies on generalisation of experimentally determined wall pressure fluctuations and their inter-correlation. Hence, the spatial resolution and accuracy of the fluctuating pressure measurements will determine the accuracy of the developed model. In practice however, the spatial resolution is limited and the sensors are placed where they can capture the most important events. Major part of the wall pressure load in a overexpanded nozzle featuring free shock separation originates from the pressure fluctuations in the shock boundary layer interaction region. In order to resolve the streamwise distribution of the rms pressure fluctuations in this region an extremely narrow spacing of the pressure transducers is required, as indicated in Figure 73-Figure 74. Based on Figure 73 we can see that an array of at least 5-10 pressure sensors along the interaction region would be needed in order to resolve the pressure rms distribution. The most important points to capture in this region are the point of maximum pressure rms and the locations of the origin and the end of the shock wave boundary layer interaction. The simplest way to capture the peak value is to find the operation condition when the peak is locked on a pressure transducer. This operation condition can be found by changing the pressure ratio p_c/p_a with small stepwise increments or with a slow continuous ramp, as in Figure 74.

Since the gradients in the separated region are small, a fine streamwise resolution is not as important in this region as in the interaction region. Thus, 5-10 evenly spaced pressure sensors would be sufficient to capture the most significant features of the recirculating flow zone.

In order to quantify the instantaneous asymmetry of the pressure load, pressure sensors must also be installed in the transversal direction in the separation and the separated zone respectively. It is difficult to specify a minimum number of pressure sensors required in the transversal direction. In general reliable quantitative data on the structures and pressure fluctuations in the transverse direction are lacking and is fruitful area of future work. However, as an indication Dumnov[R 101] used 8 fast pressure transducers in the transversal direction in order to obtain the pressure correlation function, on which he based his side-load model. For a more general survey of fluctuating wall pressure measurements for this type of flow, the work by Dolling and Dussauge[R 121] is recommended, where method of measurement, common sources of error and calibration methods are discussed.

The development of fast pressure sensitive paint (FPSP) has evolved rapidly in recent years, see e.g. reference R 129. FPSP have response times in the range 3-12 kHz. It may hence be possible in the near future to resolve the global unsteady pressure field in separated nozzle flows with this method.

7.3   SIDE LOAD MEASURMENTS

Direct measurement of the global asymmetric fluctuating pressure load obtained during nozzle operation with flow separation would require a fast and global surface field measuring method, i.e. either the use of an enormous number of fast pressure transducers or the use of fast pressure sensitive paint. The commonly used measuring technique is to measure the mechanical side-load response caused by the aerodynamic side-load as it acts on the structure. If the structural dynamic transfer function is known the aerodynamic side-load can then be calculated. In a rocket engine the aerodynamic side-load can excite two different modes of the rocket engine structure. These modes are 1) the pendulum mode where the nozzle oscillates around the cardan and 2) the bending mode where the nozzle oscillates around the throat. An experimental set-up must simulate the most significant of these modes. In Figure 50-Figure 53 the experimental test set-ups used by VOLVO[R 5-R 6], ONERA[R 132] and DLR[R 110] are shown respectively (the test set-ups used at Keldysh[R 101] and NAL[R 122] are similar to the one used at DLR). The VOLVO test set-up simulates the bending mode whereas the experimental set-up at ONERA and DLR simulates the pendulum mode.

The device for measuring dynamic unsteady side-loads at ONERA[R 132] consists of a support-tube equipped with semi-conductor strain-gauges in order to measure the bending moment in two planes, i.e. the two perpendicular components of the general side load moment. The reference point for these torque measurements is labelled CRB Tube in Figure 52.

The side-load measuring system in the DLR test facility P6.2 consists of one thin walled Aluminium pipe which connects the rigid test nozzle to the rigid gas feeding system [R 110], see Figure 53. As side-loads are produced in the nozzle, the thin walled pipe will bend and with the use of strain gauges the two perpendicular components of the resulting side-load response is measured. By changing the length of the strain-measuring pipe different system eigenfrequencies can be obtained.

In the test set-up used by VOLVO[R 5-R 6], the nozzle consist mainly of two parts, one fixed part mounted to the downstream flange of the wind tunnel and one flexible hinged part, see Figure 50. The flexible part is suspended with a universal joint/cardan, Figure 51, permitting motion in all directions around the throat and the motion simulates the throat-bending mode of a real rocket nozzle. The bending resistance is simulated with torsion springs, which are exchangeable, that the influence of the structure stiffness on the side load response and aeroelastic coupling can be studied. The side-load response components are measured with strain gauges mounted on the torsion springs.
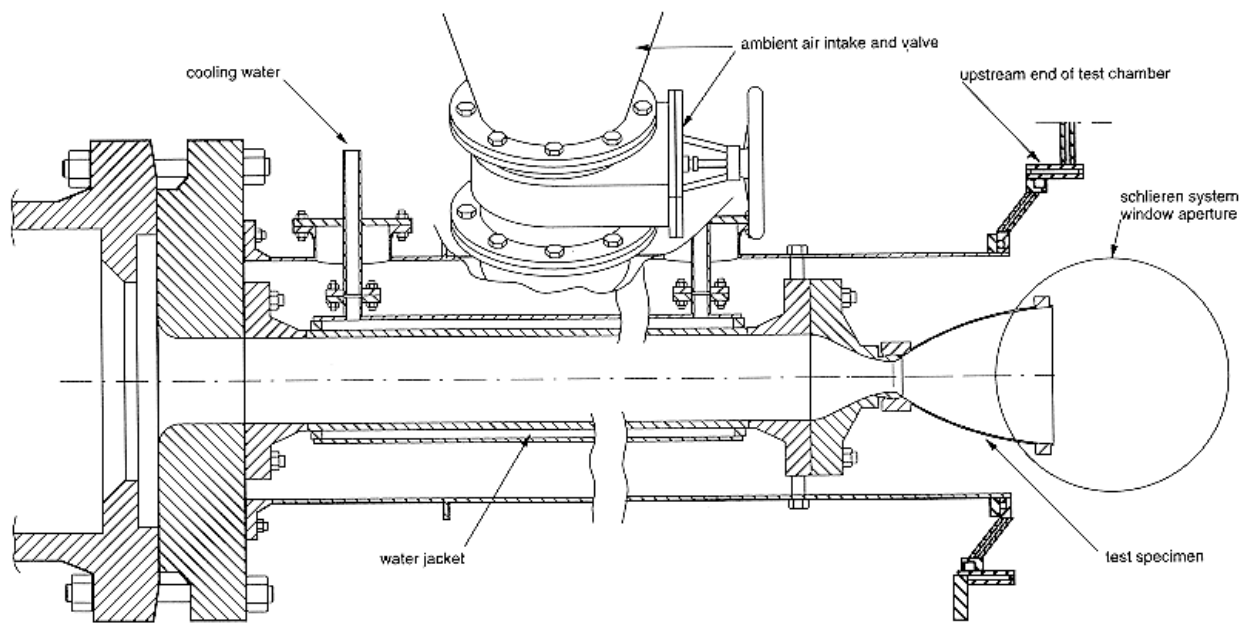
Figure 50. Schematic side view of the experimental test set-up in FFA wind tunnel HYP 500, from Östlund et al[R 5-R 6].
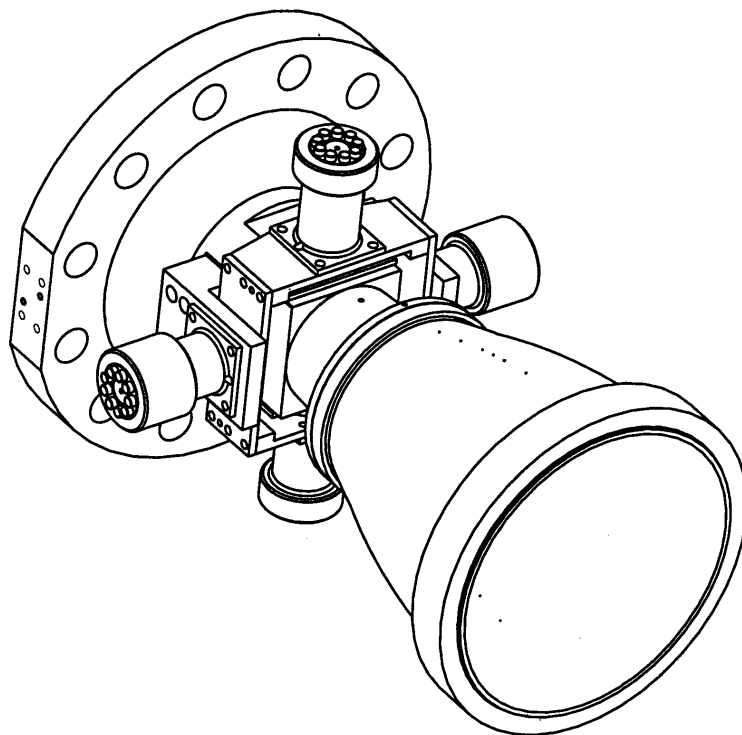

Figure 51. Schematic side view of the cardan hinged test nozzle in FFA wind tunnel HYP 500, from Östlund et al[R 5-R 6].

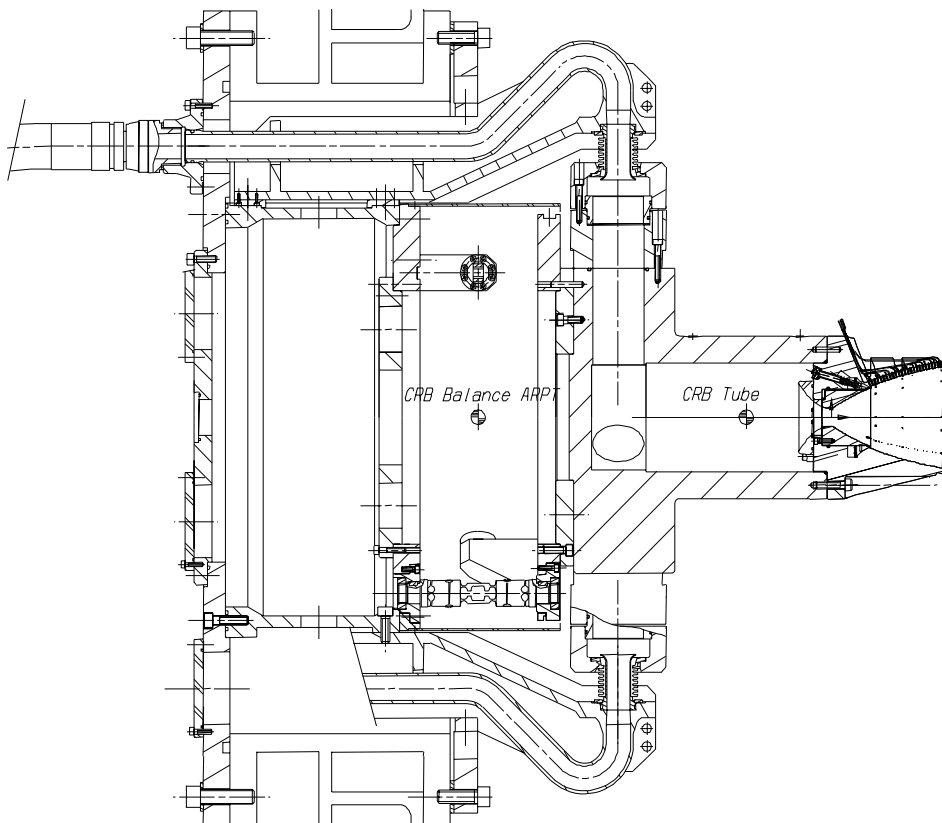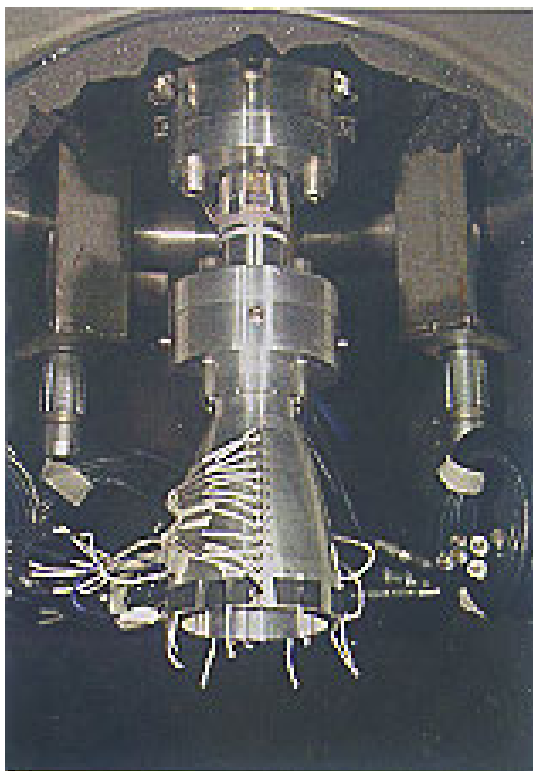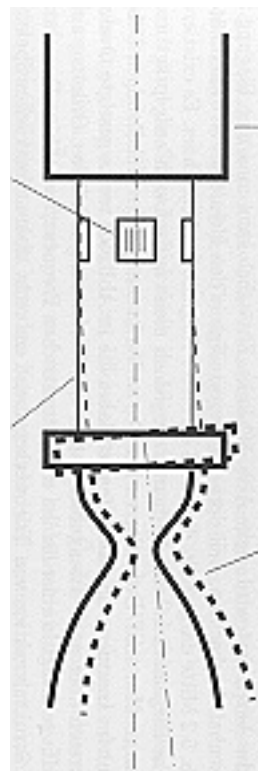Figure 52. Sketch of the experimental set-up in the ONERA R2Ch blowdown wind tunnel, from Reijasse et al[R 132].

Figure 53. Experimental test set-up and principles of the side-load measuring system in the DLR test facility P6.2, from Frey[R 110]

Since only the side-load response is measured in the test set-ups described above, a method for calculating the aerodynamic side-load is needed. During a run, the strain-gauges measure the strains, $\vec{S}(t)$, resulting from the dynamical response of the system to the aerodynamic side-load torque $\vec{M}_a(t)$. Where $\vec{S}(t)$ and $\vec{M}_a(t)$ each have two components representing motion in two directions around the main axis i.e.:

$$\vec{S}(t) = \begin{cases} S_1(t) \\ S_2(t) \end{cases} \quad and \quad \vec{M}_a(t) = \begin{cases} M_{a1}(t) \\ M_{a2}(t) \end{cases}$$

These are usually different due to the asymmetry introduced by the instrumentation and the test set-up. After Fourier transform of $\vec{S}(t)$ and $\vec{M}_a(t)$ and introducing the transfer function $H(f)$ we get:

$$\hat{\vec{S}}(f) = H(f)\hat{\vec{M}}_a(f)$$

Where $H(f)$ is a complex 2x2 matrix defined by:

$$H(f) = \begin{vmatrix} H_{11}(f) & H_{12}(f) \\ H_{21}(f) & H_{22}(f) \end{vmatrix} \quad with \quad H_{jk}(f) = \left| H_{jk} \right| e^{i\varphi_{jk}}$$

Once $H(f)$ is known, the aerodynamic load components $M_{a1}(t)$ and $M_{a2}(t)$ can be reconstructed from the strain-gauge signals $S_1(t)$ and $S_2(t)$ as:

$$\begin{vmatrix} \hat{M}_{a1}(f) \\ \hat{M}_{a2}(f) \end{vmatrix} = \begin{vmatrix} H_{11}(f) & H_{12}(f) \\ H_{21}(f) & H_{22}(f) \end{vmatrix}^{-1} \begin{vmatrix} \hat{S}_1(f) \\ \hat{S}_2(f) \end{vmatrix}$$

7.3.1 Determination of the system frequency response function

As indicated above, the system frequency response function must be known in order to be able to reconstruct the aerodynamic load components. The most accurate method to determine the transfer function $H(f)$ is by structural testing[R 133-R 134]. The best experimental estimate of $H(f)$ is obtained by imposing a sinusoidal load $M_0(t)$ at frequencies f_e to the system with a vibration exciter. For one excitation frequency two experiments are carried out: one where the excitation acts in the S_1-plane and another in the S_2-plane. The transfer function at frequency f_e, $H(f_e)$, is then obtained by solving the system of four equations:

$$\begin{cases} \begin{vmatrix} \hat{M}_0(f_e) \\ 0 \end{vmatrix} = \begin{vmatrix} H_{11}(f_e) & H_{12}(f_e) \\ H_{21}(f_e) & H_{22}(f_e) \end{vmatrix}^{-1} \begin{vmatrix} \hat{S}_1(f_e) \\ \hat{S}_2(f_e) \end{vmatrix} \\ \begin{vmatrix} 0 \\ \hat{M}_0'(f_e) \end{vmatrix} = \begin{vmatrix} H_{11}(f_e) & H_{12}(f_e) \\ H_{21}(f_e) & H_{22}(f_e) \end{vmatrix}^{-1} \begin{vmatrix} \hat{S}_1'(f_e) \\ \hat{S}_2'(f_e) \end{vmatrix} \end{cases}$$

Where "^" denotes Fourier transform and "'" indicates that the measured signals are different when applying the excitation load in the different planes.

This process is then repeated for different frequencies f_e within the frequency band of interest and the frequency resolution is adapted during the process so the response at normal modes are resolved. Finally a curve-fitting technique can be used to improve the modal parameter estimation.

If the experimental set-up is carefully designed it can be approximated fairly well as a dynamic system with one degree of freedom (1-DOF), which facilitate the determination and description of the transfer function $H(f)$. This approximation is only valid if the system is isotropic, i.e. $H_{11}=H_{22}=H$ and $H_{12}=H_{21}=0$, and the eigenfrequencies of any higher order modes are far from the fundamental eigenfrequency f_0. If this is the case one can reconstruct the aerodynamic load components from the strain-gauge signals as:

$$\hat{M}_{a1,2}(f) = H^{-1}(f) \cdot \hat{S}_{1,2}(f)$$

An expression for the transfer function can be obtained from the characteristic differential equation for a system with 1-DOF, which is:

$$\ddot{S}(t) + 2\zeta\omega_0\dot{S}(t) + \omega_0^2 S(t) = \frac{1}{m}M_0(t)$$

Where

$\omega_0 = 2\pi f_0 = \sqrt{\dfrac{k}{m}}$ is the fundamental eigenfrequency

ζ is the damping coefficient
k   is the system stiffness
m   is the system mass

Taking the Fourier transform of this equation yields the transfer function as:

$$H(f) \cdot k = \frac{\hat{S} \cdot k}{\hat{M}_0} = \left[1 - \left(\frac{f}{f_0}\right)^2 + i2\zeta\frac{f}{f_0} \right]^{-1}$$

Thus the parameters to be experimental determined have been reduced to f_0, k and ζ.
The stiffness k is determined from static calibration, i.e. by applying different static loads and measure the corresponding strain, as illustrated in Figure 54.
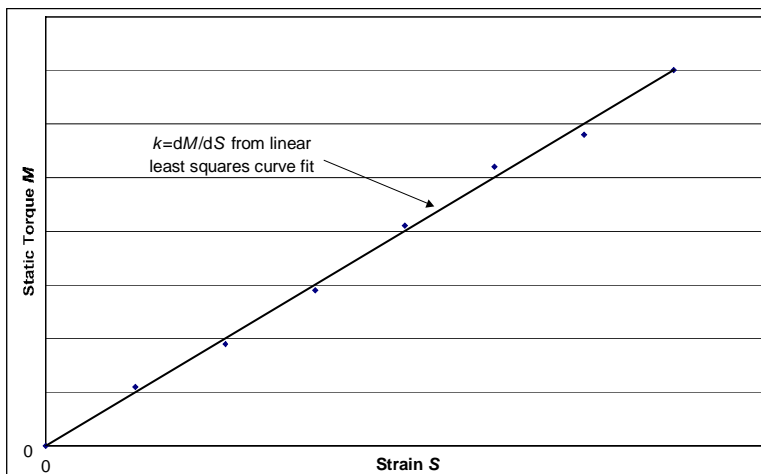
Figure 54. Illustration of static calibration of the spring stiffness (from VOLVO S1 testing).

The damping and the fundamental frequency are found from a dynamic calibration, i.e. a hammer test or applying a step function to the system or anything similar. In Figure 55 the measured response is shown when applying a step function to the VOLVO S7 nozzle.

The theoretical response to a step function to a 1-DOF system is:

$$S(t) = S_0 e^{(-a \cdot t)} \sin(2\pi f_d t + \varphi) \quad where \quad \begin{cases} f_d = f_0 \sqrt{1 - \zeta^2} \\ a = 2\pi f_0 \zeta \end{cases}$$

Thus, after analysis of the rate of decay, a, and the oscillating frequency, f_d, of the response signal, see Figure 56-Figure 57, the damping coefficient and fundamental frequency can be determined as:

$$\zeta = \left[1 + \left(\frac{2\pi f_d}{a} \right)^2 \right]^{-1/2} \quad and \quad f_0 = \frac{f_d}{\sqrt{1 - \zeta^2}} \quad .$$
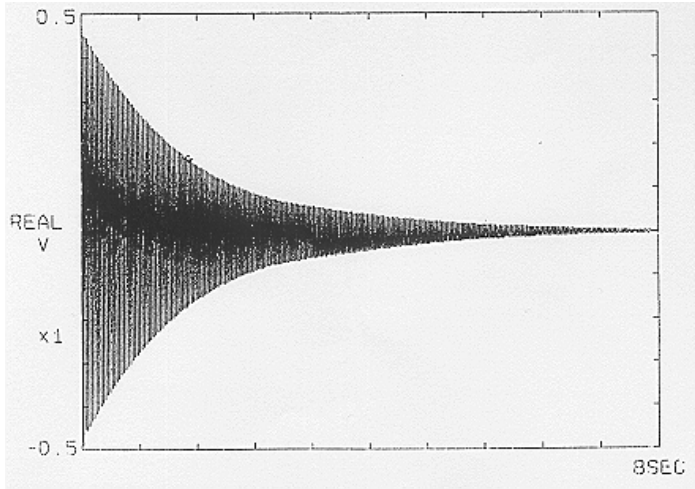
Figure 55. Oscillating decay test with the VOLVO S7 nozzle.
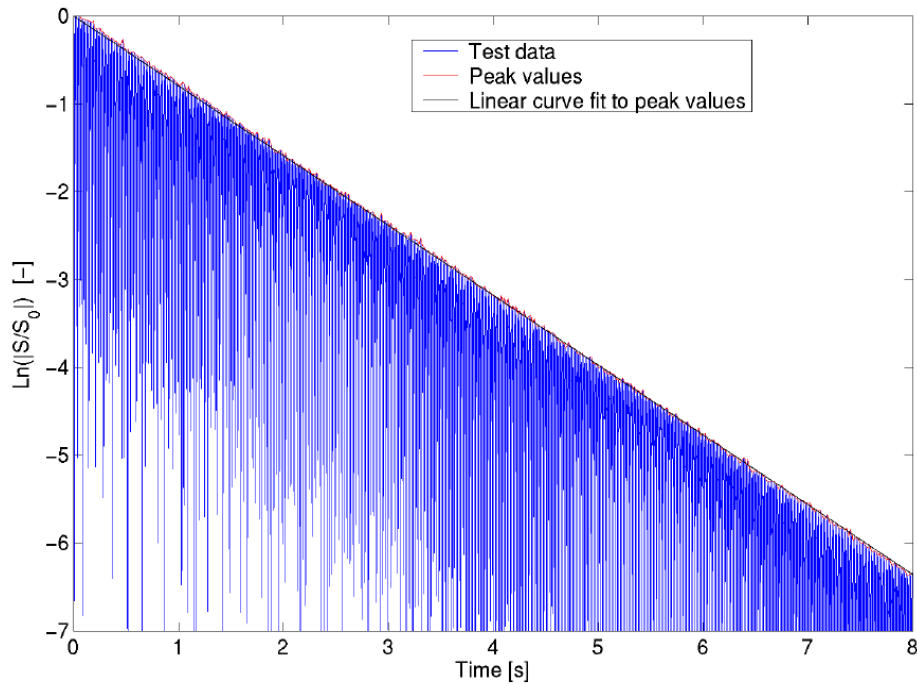
Figure 56. Analysis of the decay rate of a response signal, example taken from the S7 test campaign.

60
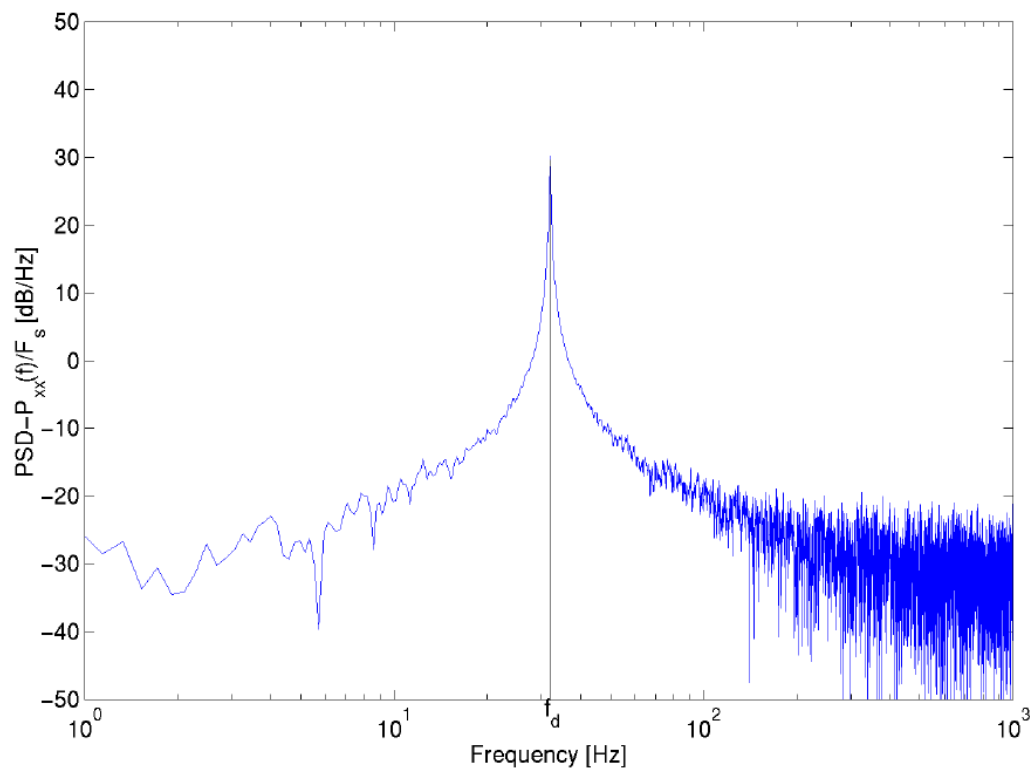
Figure 57. Analysis of the oscillating frequency of a response signal using FFT example taken from the S7 test campaign..

8   SIDE-LOADS – PHYSICAL ORIGINS AND MODELS FOR PREDICTION

Side-loads have been observed both in sub-scale and full-scale rocket nozzles during transient operations like start-up or shut-down, as well as during stationary operation with separated flow inside the nozzle. Such forces, acting lateral to the main thrust direction are an undesired phenomenon, and may become a severe design constraint for new rocket engine concepts. The first important report dealing with side forces was published in the 1970's within the frame of the J-2S testing[R 95].

Potential origins for side-loads generated by an asymmetric wall pressure evolution inside the nozzle are:
- transition in separation pattern, FSS to RSS and vice versa.
- tilted separation line,
- pressure pulsations in the separation region and in the re-circulation flow region,
- aeroelastic coupling.

Furthermore, pressure pulsations acting from the outside on the nozzle shell, asymmetry arising from the manufacturing process, or asymmetric injection of propellant or/and film cooling gases may generate lateral forces, which however are not further considered in this discussion.

In the following we will discuss different models, developed on the basis of different origins.

8.1   SIDE-LOADS DUE TO TRANSITION IN SEPARATION PATTERN

It has been shown in sub-scale cold-gas experiments, that a transition in separation pattern from the free-shock separation (FSS) to the restricted shock separation (RSS) and vice-versa may occur [R 90,R 95]. That these transitions also are the origin of two distinct side-load peaks was first shown by Östlund[R 5] based on his analysis of the VOLVO S1 test.

8.1.1   Origin of side load: observations of the VOLVO S1 nozzle flow

Figure 58 shows some typical measured steady-state wall pressure profiles in the VOLVO S1 nozzle during start up, i.e. the pressure ratio between the feeding and ambient pressure p_0/p_a is increased from 1 and upwards. As can be seen, the wall pressure profiles indicate FSS for $p_0/p_a<15$ and RSS for $p_0/p_a>15$ (cf. Figure 37). Hence, there is a transition of the flow separation pattern at $p_0/p_a\approx15$. This transition from FSS to RSS can also be seen in the schlieren photos in Figure 83. To support the understanding of these schlieren photos, the corresponding calculated Mach number contours are shown in Figure 61. At $p_0/p_a<15$, the exhaust jet is seen to occupy only a fraction of the nozzle exit whereas at $p_0/p_a>15$ the exhaust is attached to the nozzle wall.

The measured wall pressure distributions during shut down are shown in Figure 59, where it can be seen that the transition between RSS and FSS occurs at a pressure ratio of about $p_0/p_a=12$, it is hence clear that there is a hysteresis effect. Figure 60 compares the wall pressure profiles at FSS and RSS condition at a pressure ratio of $p_0/p_a=13$. As can be seen the wall pressure distribution is quite different for the two cases. One of the most remarkable differences is that the RSS separation line is located much further downstream of the FSS separation line (the reason for this difference is explained in section 6.2). Thus, at the FSS to RSS and RSS to FSS transition inside the nozzle there is a considerable jump of the separation line, in connection with the RSS-FSS or RSS-FSS transition.
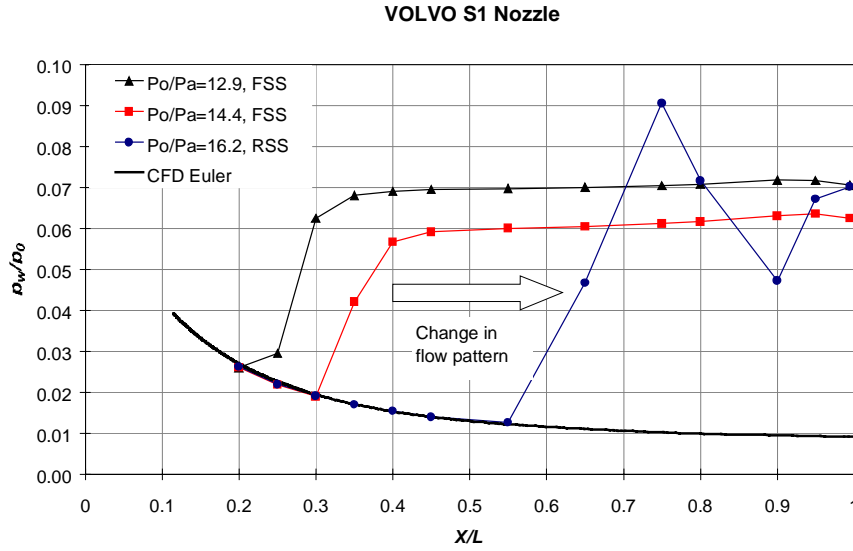
VOLVO S1 Nozzle

Figure 58. Wall pressure profiles in the VOLVO S1 nozzle during start up, see also Östlund et al[R 5].
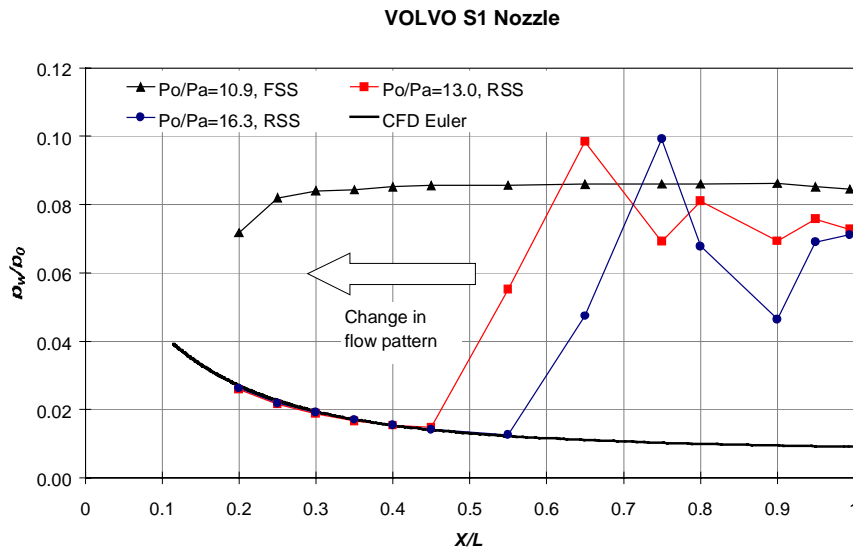
VOLVO S1 Nozzle

Figure 59. Wall pressure profiles in the VOLVO S1 nozzle during shut down.
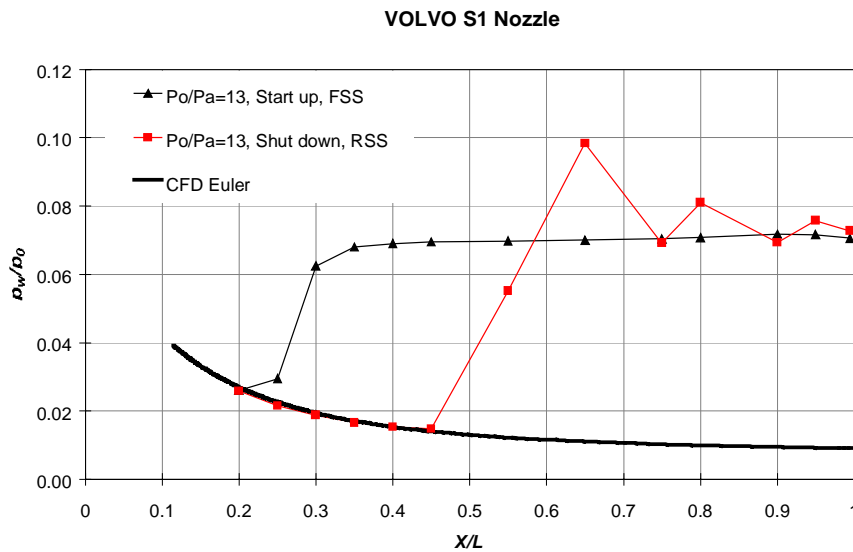
VOLVO S1 Nozzle

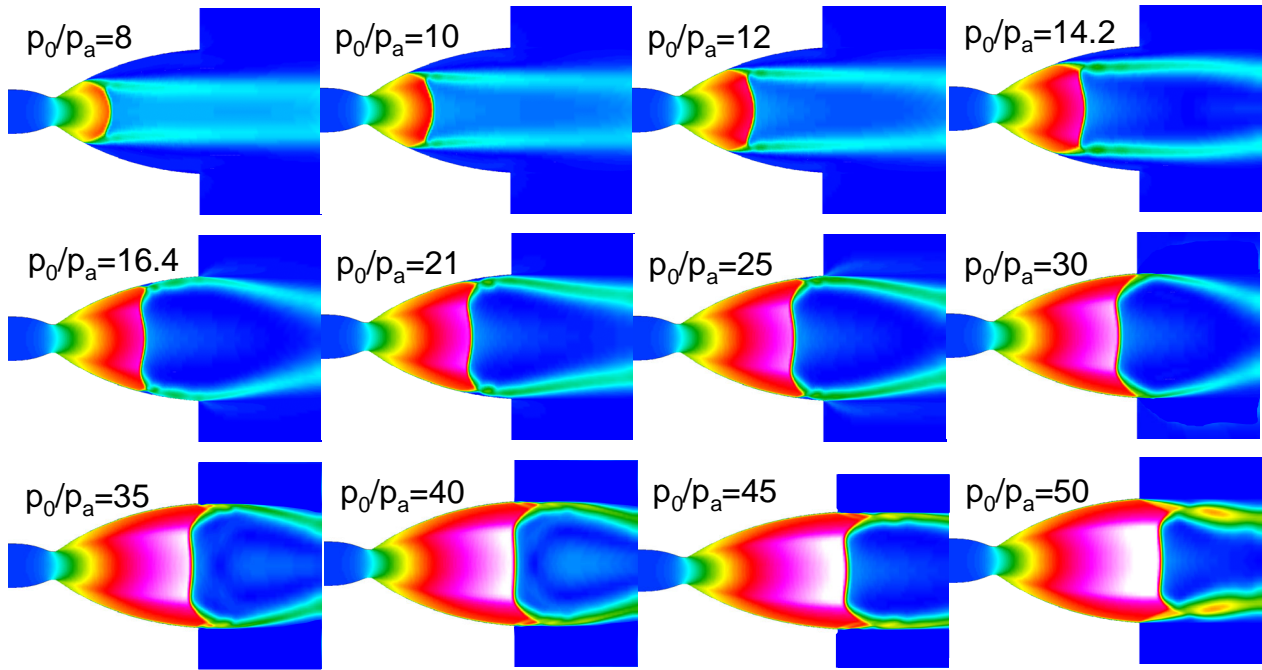Figure 60. Comparison between wall pressure profile at FSS and RSS condition at p_0/p_a=13.

Figure 61. Calculated Mach number contours[‡] in the VOLVO S1 nozzle at different pressure ratios[R 138, R 139].

Analysis of high-speed video recording of the schlieren pattern, see Östlund[R 5, R 138], indicates that while the FSS flow field is moving towards the flow field transition point at $p_0/p_a \approx 15$, the free jet experiences a few cycles with a tilted separation plane. Next an unsteady asymmetrical reattachment of the flow occurs as the feeding pressure is increased further, successively occupying more and more of the nozzle wall, until the entire flow is reattached, i.e. the RSS state prevails. In this state, the degree of asymmetric separation is small and the flow is quite stable and only small fluctuations of the flow can be observed as a compression wave (or possible a secondary separation bubble) is ejected from the nozzle exit lip at $p_0/p_a=23$. However, when the reattachment point reaches a position close the nozzle exit, the flow begins to pulsate with a frequency of about 100 Hz. This happens at a pressure ratio of 25. This is caused by a sudden increase of the plateau pressure behind the separation shock, which occurs when the enclosed recirculating zone is opened up and ambient air is sucked in to the nozzle. The increase in pressure, forces the separation point to move upstream again, once more closing the recirculating zone. The cycle repeats itself until the feeding pressure is sufficiently large to move the reattachment zone completely out of the nozzle, which in this case occurs at a pressure ratio of 30. When decreasing the feeding pressure, this procedure is repeated, however, now in the reversed order. Large fluctuations of the flow field can be observed as the pressure ratio is reduced below 28. At this pressure ratio, the separation line has moved into the nozzle and a repeated closing and opening of the recirculating zone takes place, until a stable reattachment is achieved at $p_0/p_a \approx 26$. Between $p_0/p_a \approx 26$-13, the flow field is again stable showing only small fluctuations at $p_0/p_a \approx 23$, 21 and 20, which corresponds to instants when compression waves is moving into the nozzle. At $p_0/p_a \approx 12$ the flow becomes unsteady and the stripy pattern, see Figure 83, characterising RSS suddenly disappears.

Figure 62 shows a time record of the measured side load torque during a start up and shut down process. Two distinct load peaks can be identified both during start up and shut down. The main characteristic of these side forces is their high value and the impulsive occurrence. In Figure 63 and Figure 64 these data are given in terms of percent of peak measured loads versus the feeding to ambient pressure ratio for the start up and shut down transient respectively.

[‡] For the computations the standard Wilcox k-ω model with an ad hoc realizability correction, $\mu_t=\min(\mu_t, 0.1)$, was used together with the same computational model and type of grid as presented in section 11.3. More details of the computations can be found in R 138- R 139.

As indicated in the figures it is one significant load peak at a pressure ratio $p_0/p_a \approx 15$ and second at a pressure ratio of 28 during the start transient. Corresponding side load peaks during the throttle down occurs at pressure ratio of 12 and 28. It is thus obvious that these side load peaks is coupled to the transitions from FSS to RSS or vice versa as described above.
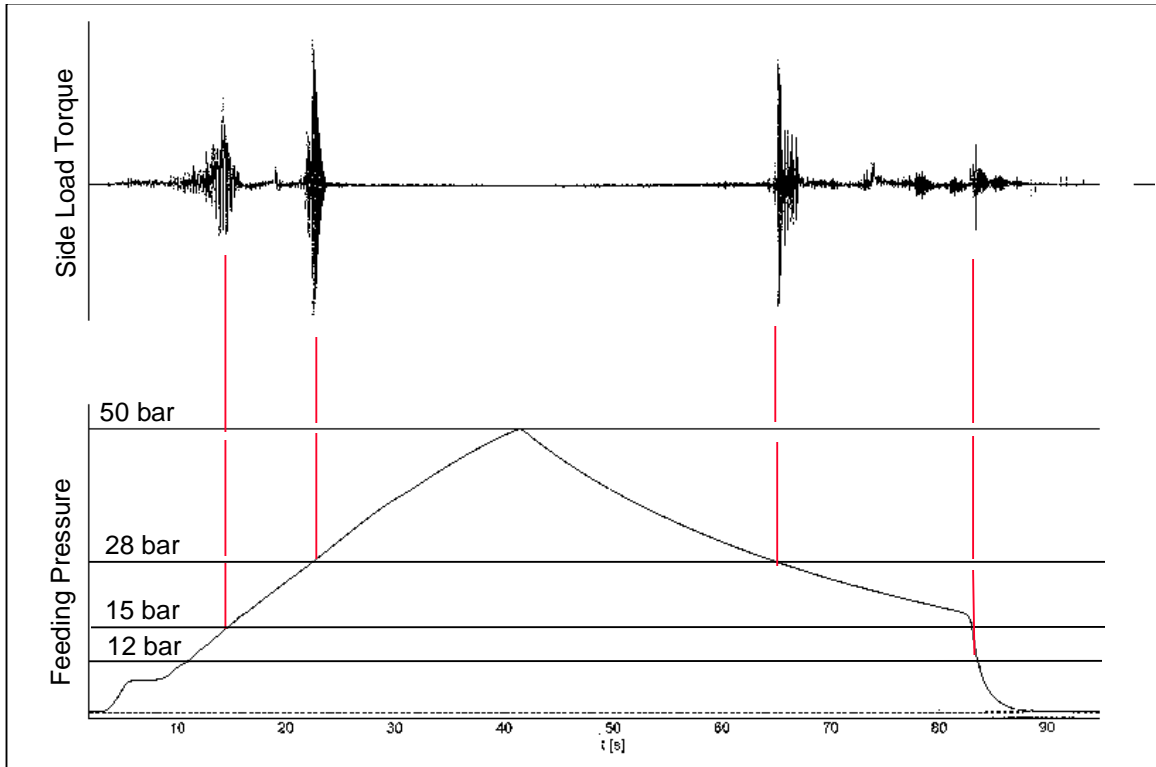

Figure 62. Side-loads due to transition in separation pattern, also published in R 5
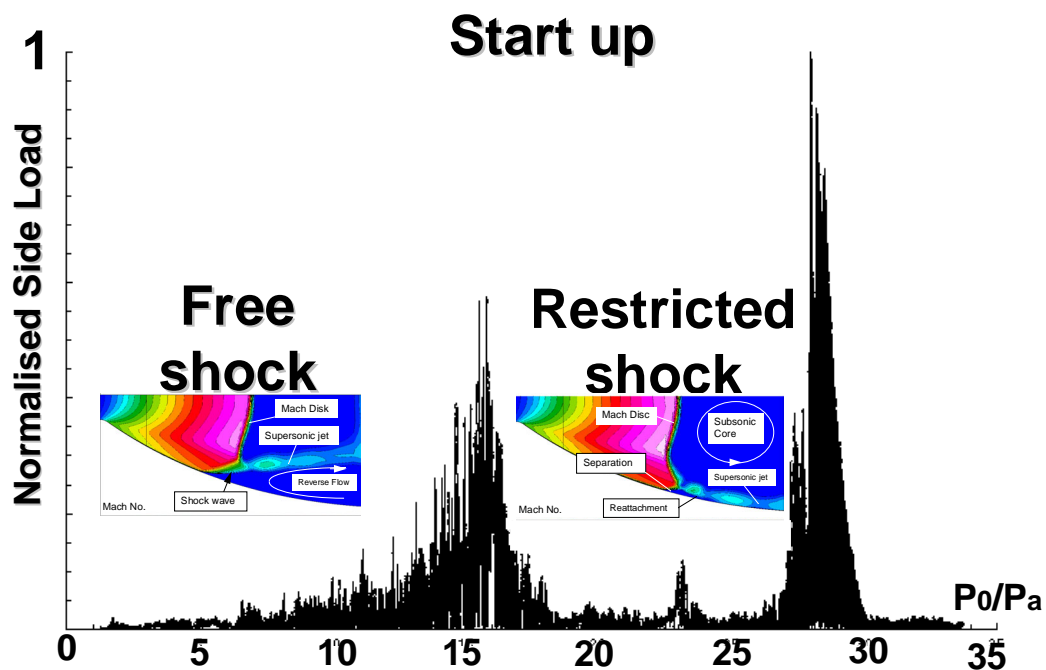
Figure 63. Normalised side load torque vs. feeding to ambient pressure ratio during start up, also published in R 5.
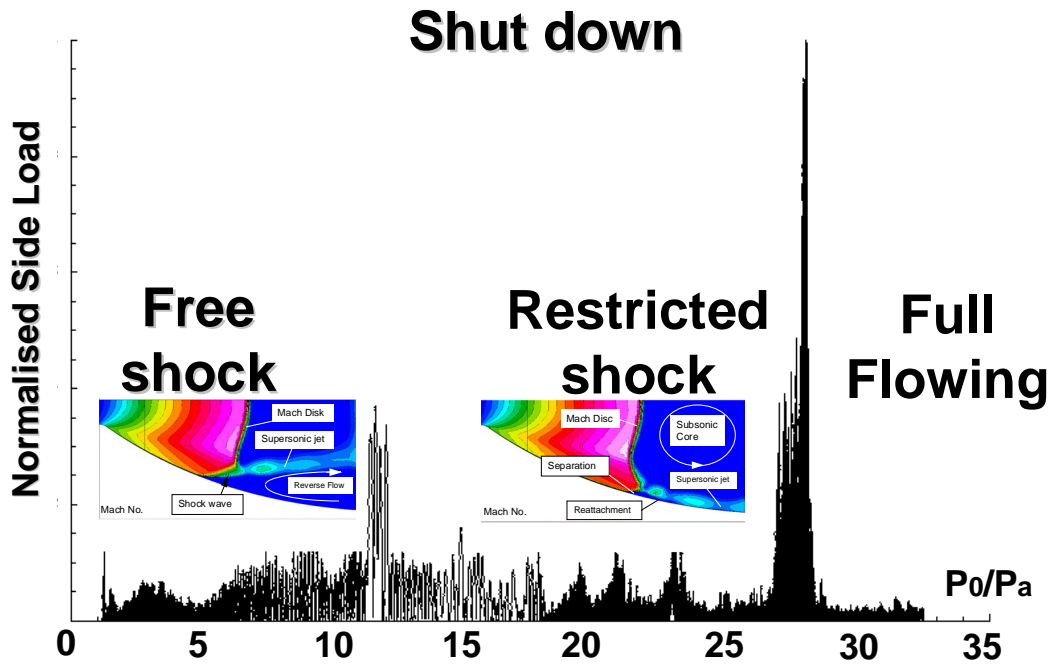
Figure 64. Normalised side load torque vs. feeding to ambient pressure ratio during shut down, also published in R 5.

The above observations and conclusion, which has been partly published in reference R 5, was the ignition for intensive research both within and outside Europe. Further sub scale experiments performed within different FSCD test campaigns[R 6-R 8] and recent Japanese experiments[R 122] confirmed this mechanism for TOP and CTIC nozzles both featuring an internal shock. In addition, test results of the Vulcain 1 engine confirmed this mechanism as key driver during both start-up and shut-down.[R 4].

8.1.2 Side-load model

By assuming that the initial transition from FSS to RSS requires a certain time, a phase might exist during which one side of the nozzle experiences a free shock separation while at the other side the flow reattaches. Since the separation point is located further downstream in the restricted shock case and the wall pressure behaviours are totally different between the two cases, severe lateral forces are acting on the nozzle. The main characteristic of these side forces is their high value and the impulsive occurrence as shown above.

Based on the briefly described restricted shock separation models of reference R 3 and R 6, see chapter 6.2, Dasa/DLR[R 4] and Volvo[R 6] have developed side-load models by assuming that the initial transition from free- to restricted shock separation is the key side-load driver in TOP and CTIC rocket nozzles. The basic idea behind is, that at the instant of transition a maximum side-load is expected if one half of the nozzle features FSS-, while the other half shows already RSS flow condition. For this case, the side-load calculation is squarely based on physical reasoning namely from a momentum balance across the complete nozzle surface, as illustrated in Figure 65.

With this model the aerodynamic side-load can be calculated. Due to the short duration of the aerodynamic side-load, pulse excitation theory can be used when evaluating the mechanical load.

For a single pulse excitation, the dynamic response factor (i.e. the amplification of the applied load due to the dynamic system) is always less than 2. The most critical pulse is the single square wave, since it contains the highest energy that any single pulse can have. Figure 66 shows the Shock Response Spectrum (SRS) for a single square wave. A further example of waves is the half-sine wave with its SRS depicted in Figure 67. The half-sine and the triangular pulse, see Figure 68, are often good approximations to actual pulse shapes, e.g. the pulse creating the side-load when the separation pattern is changed from FSS to RSS. With the

66

knowledge of the transition time, t_1, and the mechanical eigenfrequency, $\omega=2\pi/\tau$, the dynamic response factor can be obtained from Figure 66-Figure 68.

In Table 4, values with this side-load model are compared with the maximum measured values in different subscale and full-scale experiments showing that the accuracy is within 6%.

Nozzle	$p_{0,m}/p_{o,c}$	M_m/M_c
VolvoS1	0.94	1.01
VolvoS3	1.0	1.02
Vulcain	1.05	1.05

Table 4. Comparison between VAC calculated (subscript c) and measured (subscript m) transition feeding pressure (p_0) and aerodynamic torque (M) , also published in Östlund et al[R 108].
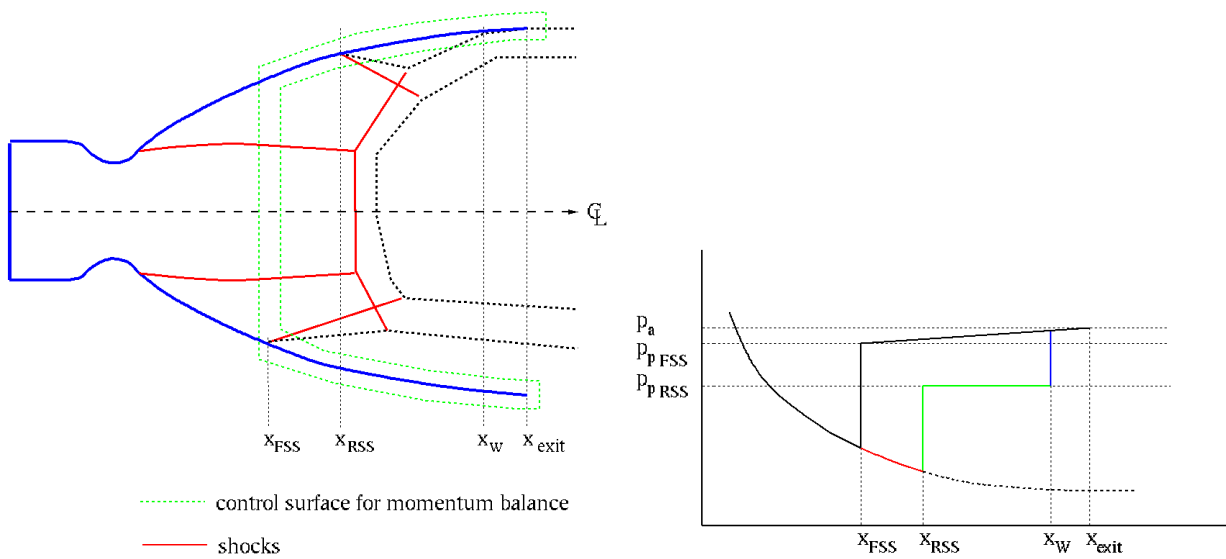
Figure 65. Asymmetric flowfield inside nozzle at instant of FSS-RSS transition for worst case side-load prediction. Control surface for momentum balance included. Momentum of impinging jet on wall taken into account at x_w, also published in R 105.
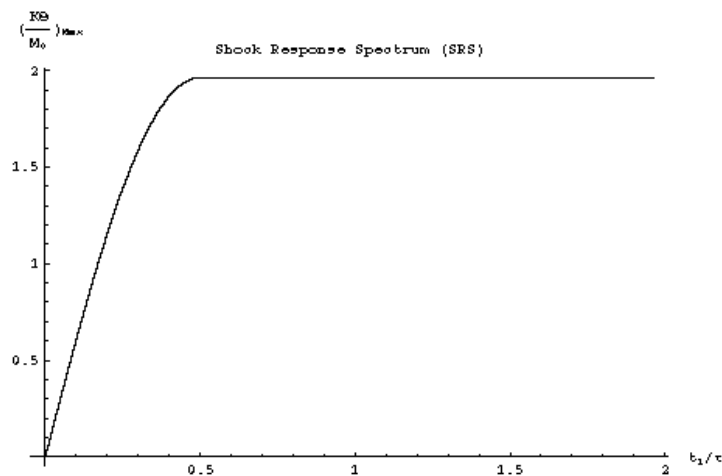
Figure 66. Shock response spectrum (SRS) for a single square wave, t_1=pulse duration time, τ=period time, also published in Östlund et al[R 108].
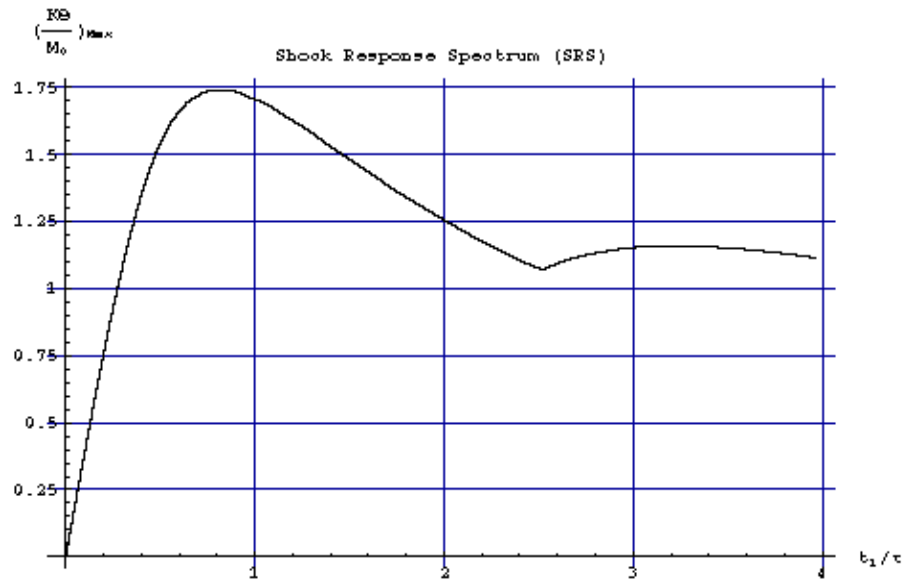
Figure 67. SRS for half sine wave, also published in Östlund et al[R 108].
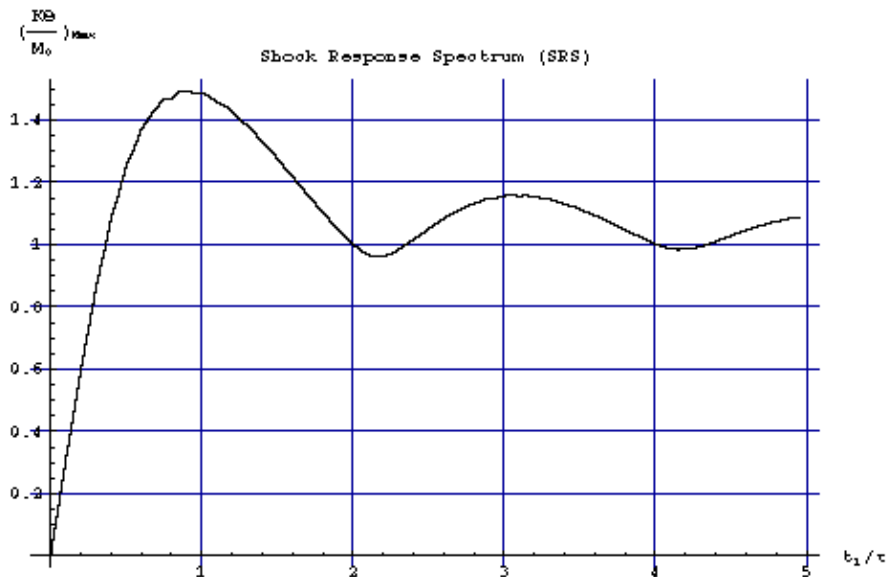
Figure 68. SRS for a triangular wave, also published in Östlund et al[R 108].

8.2 SIDE-LOADS DUE TO TILTED SEPARATION LINE

The assumption of a tilted separation line under pure free shock conditions is the basis of several side-load models, e.g. of Pratt and Whitney, Rocketdyne, Aerojet and Schmucker[R 94]. The principle of this basic idea is illustrated in Figure 69.
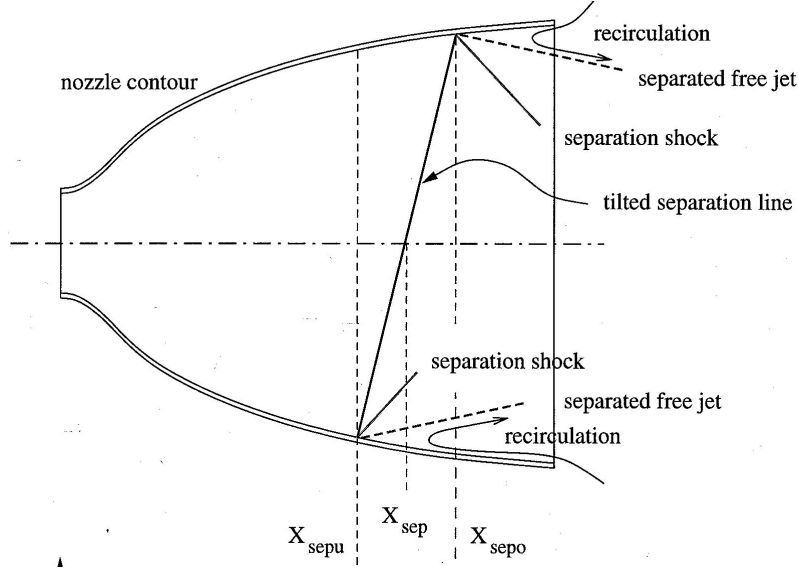
Figure 69. Principle idea of a tilted separation line.

The side load force acting on a nozzle wall is determined by:

$$F_{sl} = \int_0^{L_e} \int_0^{2\pi} (p_a - p_w) \cos \ \tau \ d\vec{A} \qquad \text{Eq. 38}$$

Where $d\vec{A}$ is a nozzle surface element and τ is the local contour angle.

If the wall pressure distribution is axisymmetric, no side loads are present, however, if an asymmetry appears, as in Figure 69, a side force arises given by integration over the separation region, i.e.:

$$F_{sl} = \int_{x_{sepu}}^{x_{sepo}} \int_0^{2\pi} (p_a - p_w) \cos \ \tau \ d\vec{A} \qquad \text{Eq. 39}$$

where x_{sepu} and x_{sepo} are the distances at which the asymmetric flow separation occurs. This equation can be written in a simplified form as:

$$F_{sl} \approx (p_a - p_{sep}) A_{sl} \qquad \text{Eq. 40}$$

Where A_{sl} is the projection of the region with asymmetric flow separation on a plane perpendicular to the side force direction.

Knowing the distance between the point where the side force is applied, l_{sl}, and the nozzle gimballing point, the force acting on the engine actuator denoted by subscript ac can be determined as:

$$F_{ac} = F_{sl} \frac{l_{sl}}{l_{ac}} \qquad \text{Eq. 41}$$

In order to predict the magnitude of the side loads, the wall pressure difference and the area of the region with an asymmetric flow separation needs to be known. The wall pressure difference can be predicted with a flow separation criterion, whereas in order to determine a zone of asymmetric flow separation, it is necessary to have a model of this phenomenon.

Schumcker made the following conclusions concerning the character of the side loads based on the experimental work performed by Nave and Coffey[R 95] with the J2-S engine and its sub-scale models.

- The value and direction of the side loads are unsteady.
- The value of the side loads depends on the area of the asymmetric flow separation zone.
- The side loads are amplified due to dynamic effects.
- The stability of the separated flow increases with increasing nozzle contour angle.
- The value of the side loads decreases with increasing wall pressure gradient.
- Zero or negative wall pressure gradient leads to very high side loads.
- The maximum side loads are obtained at chamber pressures 10-20% below the minimum chamber pressure providing attached flow.

He further assumed that:

- The main part of the side load is generated due to a bias of the separation line from the its averaged symmetric position; therefore the separation point is the location where the side force is applied.
- Fluctuations of the separation zone are caused by pressure fluctuations arising due to:
  - pressure oscillations in the combustion chamber
  - recirculation of the atmospheric air
  - chemical reactions in the boundary layer

Schmucker then proceeded to construct a method, where the aerodynamic side-load, F_{sl}, due to the unsymmetrical separated area, A_{sl}, is calculated as:

$$F_{sl} = \left(p_a - p_i \right) A_{sl} = \left(p_a - p_i \right) \ b \left(x_{sepo} - x_{sepu} \right) = \left(p_a - p_i \right) \ b \Delta l_{fl} \qquad \text{Eq. 42}$$

where Δl_{fl} is the length of the unsymmetrical separated area and b is a measure of the effective asymmetry of the separation zone in the circumferential direction. In order to calculate Δl_{fl} Schmucker made the assumption that the fluctuations, and hence the unsymmetrical pressure release at the wall are proportional to the nominal wall pressure p_w, i.e.:

$$\frac{\Delta p_w}{p_c} = K_{fl} \frac{p_w}{p_c} \qquad \text{Eq. 43}$$

By applying a separation criterion, Δl_{fl} can then be obtained from the angle of intersection between the curves enclosing the wall pressure fluctuation and the separation criterion, as shown in Figure 70.
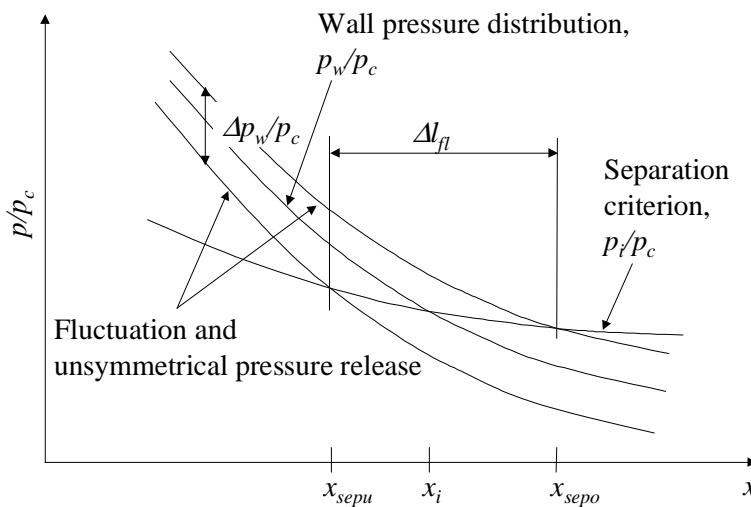
Figure 70. Computation of the length of the unsymmetrical separated area.

$$\Delta l_{fl} = \frac{\Delta p_w}{\dfrac{dp_w}{dx} - \dfrac{dp_i}{dx}} = K_{fl} r_t \frac{p_w}{p_c} \frac{1}{\dfrac{d\left(p_w/p_c\right)}{d\left(x/r_t\right)} - \dfrac{p_a}{p_c}\dfrac{d\left(p_i/p_a\right)}{d\left(x/r_t\right)}} \qquad \text{Eq. 44}$$

After some manipulation and the use of the Schmucker separation criterion, Eq. 30, one can write:

$$\frac{d\left(p_i/p_a\right)}{d\left(x/r_t\right)} = \frac{d\left(p_w/p_c\right)}{d\left(x/r_t\right)} \frac{1+\left(\gamma-1\right)/2M_i^2}{\left(1.88M_i-1\right)M_i} \frac{1.2032}{\gamma} \frac{p_a}{p_c} \qquad \text{Eq. 45}$$

Thus, one obtains:

$$\Delta l_{fl} = K_{fl} r_t \frac{p_w}{p_c} \frac{1}{\dfrac{d\left(p_w/p_c\right)}{d\left(x/r_t\right)}} \frac{1}{1 - \dfrac{1+\left(\gamma-1\right)/2M_i^2}{\left(1.88M_i-1\right)M_i}\dfrac{1.2032}{\gamma}} \qquad \text{Eq. 46}$$

The value of the fluctuation coefficient needs to be determined from test data, e.g. Schmucker found an average value of K_{fl}=0.05 for the J2-D engine.

The shape of the unsymmetrical separation line is described by the coefficient K_g as:
$b = 2r_i K_g$
For this shape coefficient, which cannot exceed 1, the following values apply:

$K_g = 1$: unsymmetry at 180° of nozzle circumference (maximum side-load).
     $= \pi/4$: inclined separation line.
     $= 0.3\text{-}0.4$: effective value, used as default values in the Schumcker model.
     $= 0$: symmetrical separation line.

With the above equations, the aerodynamic side-load can finally be expressed as:

$$F_{sl} = 2 \ K_g \ K_{fl} \frac{r_i}{r_t} r_t^2 \frac{p_i}{p_a} \frac{p_a}{p_c} p_a \left(1 - \frac{p_i}{p_a}\right) \frac{1}{\dfrac{d\left(p_w/p_c\right)}{d\left(x/r_t\right)}} \frac{1}{1 - \dfrac{1+\left(\gamma-1\right)/2M_i^2}{\left(1.88M_i-1\right)M_i}\dfrac{1.2032}{\gamma}} \qquad \text{Eq. 47}$$

As the value Δl_{fl} is proportional to $\left(dp/dx\right)^{-1}$, the wall pressure gradient is the most important factor that influences the value of the side load. When the pressure gradient increases the side load decreases. When the separation location moves towards the nozzle exit the pressure gradient decreases. This will thus result in an increase of the side load as Δl_{fl} increases. When the forward boundary of the separation fluctuation zone has reach the nozzle exit, the side load has its maximum value. In the further motion of the separation zone the fluctuation zone decreases too finally disappear. By that Schmucker explains the qualitative dependence of the side force as function of the chamber pressure.

A comparison of the model results with the side forces measured in the J-2S engine is shown in Figure 71.
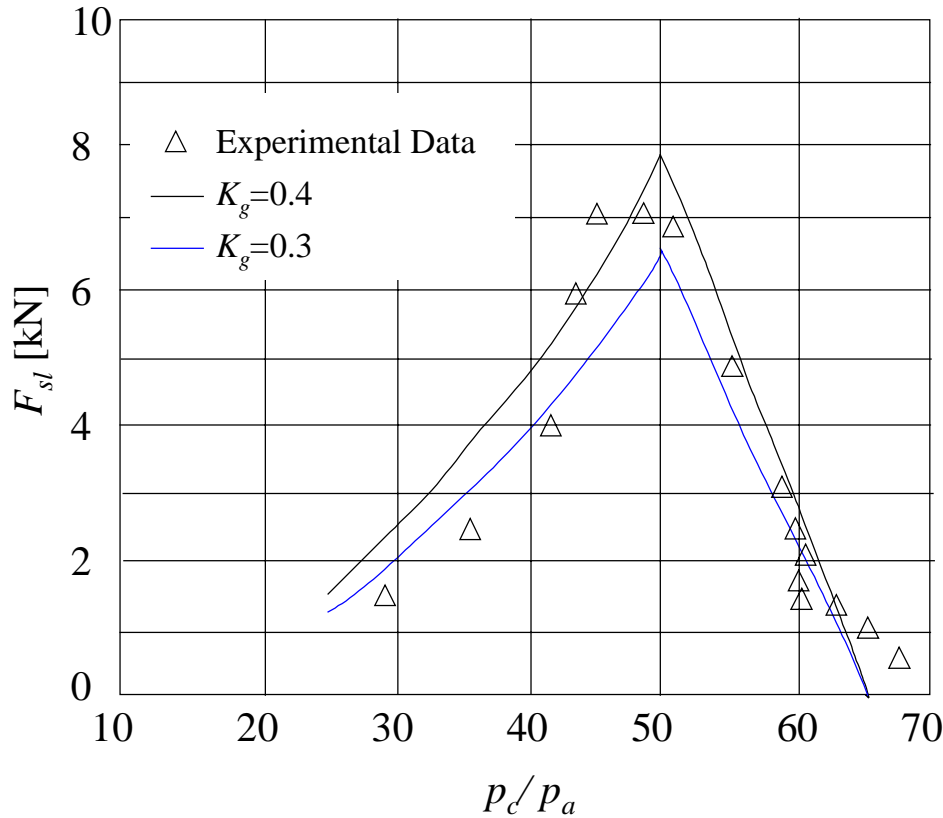
Figure 71. Comparison between experimental and computed side-loads in the J2-S engine. Test data from Schmucker[R 94].

Schmucker's model is based on an analysis of experimental data obtained from tests with J-2S engine and J-2S sub-scale model tests. The logic of this model construction is faultless. Nevertheless, a disagreement between "hot" and "cold" experimental data indicates that the physical treatments of some elements of the model are incorrect. A model intended for the determination of the fluctuation of the separation zone is the main element of the Schmucker model. The value of Δl_{fl} predicted with the model is significantly greater than the boundary layer thickness and does not connect with it in any way. Besides, the zero pressure gradient is a singular point with Schmucker's method.

Experiments, see section 5.2.3 and 6.3.1, have shown that when the flow separates intense pressure pulsations are observed in the separation zone. The length of this zone is connected with the boundary layer properties just before the separation point and is e.g. equal to several (2-3) boundary layers thickness' in obstacle induced separation. Experiments of nozzle flow separation conducted by VOLVO validate these conclusions of the length of the separation zone and the wall pressure pulsations, see Figure 42 and R 108.

However, there is a possibility for another physical phenomenon, which can not manifest itself in "cold" experiments. That is a possibility for the existence of chemical reactions in the separation zone between the hydrogen incompletely burned in the near-wall region and the atmospheric air entering from the reciculating zone. This phenomenon has a chaotic nature and causes additional pressure disturbances which increases the length of the fluctuating separation zone.

The side load models of Pratt and Whitney, Rocketdyne, Aerojet[R 94] is similar in the form to the Schmucker model. However, these models essentially differ from the Schmucker model in both physical and logical bases. According to the current author's opinion, these methods have no physical logic. Besides, they are based on dispersion of incorrectly generalised experimental data of flow separation.

8.3   SIDE-LOADS DUE TO RANDOM PRESSURE PULSATION

Random oscillation of the separation line and random pressure pulsation in the separated flow region are the basic idea of the Dumnov side-load model[R 101]. The method is based on a statistical generalisation of empirical data for the pulsating pressure field at the wall. The empirical data are mainly based on sub-scale cold-gas experiments with separated nozzle flows. For these experiments, only conical and truncated ideal nozzles were used.

The Dumnov model can be outlined as follows.

The momentary side force acting on the nozzle wall from the gas is:

$$F_{sl}' = \int p_w' r(x) \cos\varphi \, dx \, d\varphi$$

Eq. 48

with the corresponding autocorrelation as:

$$K_F(\tau) = 2\pi \int_0^\pi \iint_{(x,\xi)} K_p(\tau, x, \xi, \Delta\varphi) r(x) r(\xi) \cos\Delta\varphi \, d\xi \, dx \, d\Delta\varphi$$

Eq. 49

where
$$K_F(\tau) = <F_{sl}'(t) \cdot F_{sl}'(t+\tau)>$$
$$K_p(\tau) = <p_w'(x,\varphi,t) \cdot p_w'(\xi, \varphi-\Delta\varphi, t+\tau)>$$
and $<....>$ denotes the statistical averaging.

K_p gives the intercorrelation function of the pressure pulsation at the nozzle wall.
The correlation function can be transformed in to the spectral density of the side force using Fourier transform, i.e.:

$$W_F(f) = 2\pi \int_0^\pi \iint_{(x,\xi)} W_p(f, x, \xi, \Delta\varphi) r(x) r(\xi) \cos\Delta\varphi \, d\xi \, dx \, d\Delta\varphi$$

Eq. 50

From the above equations we can see that the key to determine the side-load is the interspectral density of the pressure fluctuations, W_p, acting on the nozzle wall. The determination of W_p is a fairly difficult problem and Dumnov solved this by generalising test data in the following form:

$$\overline{W}_p = W_p \cdot \frac{U}{\sigma_p^2 \theta_i}$$

Eq. 51

Where U is the velocity of the separated jet, σ_p is the rms level of the pressure pulsations, θ_i is the momentum thickness just before the start of the interaction.

Dumnov neglected the pressure fluctuations in the boundary layer of the attached flow, since they are substantially smaller than the ones in the separation point region, $x_i \leq x \leq x_p$, and the recirculating flow region, $x_p < x < L$, cf. Figure 31. Thus, the side force in the Dumnov model is only governed by the pressure fluctuations in the latter two regions.

According to Dumnov, the rms value of the pressure fluctuation in the separation point region can be evaluated by assuming a sinusoidal fluctuation between the two pressure levels p_i and p_p i.e.:

$$\sigma_{sh} \approx \frac{p_p - p_i}{2\sqrt{2}}$$

Eq. 52

By introducing the Mach number at $x=x_i$ and assuming an isentropic expansion

$$\pi\left(M_i\right) = \frac{p_i}{p_0} = \left(1 + \frac{\gamma-1}{2}M_i^2\right)^{\frac{\gamma}{1-\gamma}} \qquad \text{Eq. 53}$$

the rms value can be calculated as:

$$\sigma_{sh} = \frac{p_0}{\left(1 + \frac{\gamma-1}{2}M_i^2\right)^{\frac{\gamma}{\gamma-1}}} \frac{p_p/p_i - 1}{2\sqrt{2}} \qquad \text{Eq. 54}$$

For calculation of the rms pressure level in the recirculating zone, Dumnov proposes the following expression:

$$\sigma_{rec} = \frac{p_p}{2\sqrt{2}}\left(\frac{1}{\pi\left(M_i\right)}\frac{d\pi\left(M_i\right)}{dM_i} + \frac{1}{p_p/p_i}\frac{d\left(p_p/p_i\right)}{dM_i}\right)\frac{dM_i}{dx}L_{sh} \qquad \text{Eq. 55}$$

Which is derived by differentiating the relation $p_{crit}=p_p/p_i$. Here L_{sh} is the length of the interaction region i.e., $L_{sh}=x_p-x_i$.

The local and mutual spectral densities were then obtained at various operating modes of a selected TIC nozzle and normalised according to eq. 51. From there, the side force in different nozzles induced by the gas can then be determined.

The obtained aerodynamic side force is translated into a mechanical load on the test stand or rocket by use of a transfer function, $H(f)$, which characterise the mechanical system.

The spectral density of the mechanical system oscillations, W_M, can then be expressed as:

$$W_M\left(f\right) = \left|H\left(f\right)\right|^2 W_F\left(f\right) \qquad \text{Eq. 56}$$

The total rms level of the mechanical side force then becomes:

$$\sigma_Q = \,<F_{sl}> \,= \sqrt{\int_0^\infty W_M\left(f\right)df} \qquad \text{Eq. 57}$$

The application of the Dumnov-model to the Russian rocket nozzle RD-0120 gives reasonable agreement between measured and predicted side-load[R 101], as can bee seen in Figure 72. In reference R 101, the mechanical system representing the test stand with the RD-0120 nozzle is basically a 1-degree of freedom harmonic oscillator.
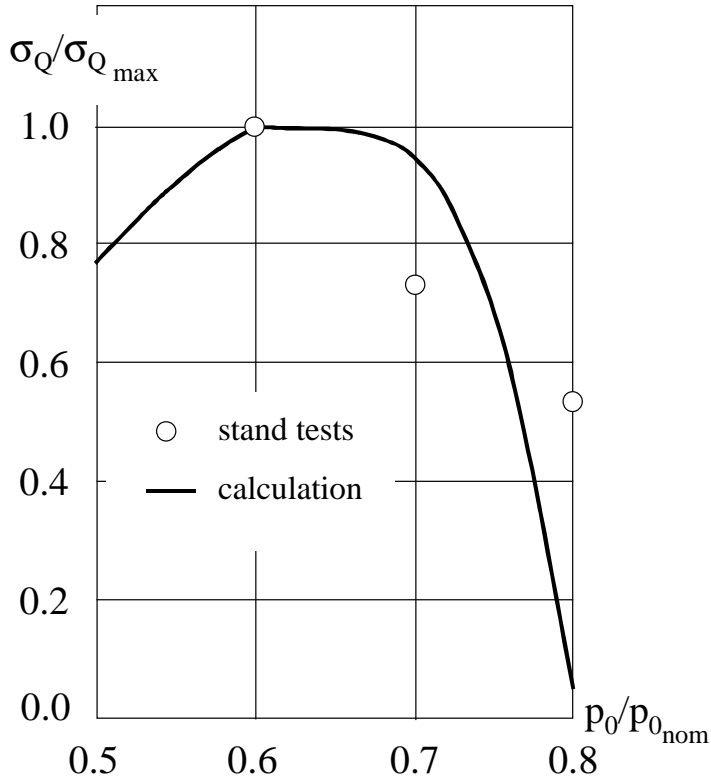
Figure 72. Rms level of the mechanical side force in the RD-0120 engine versus operational condition, $p_{0_{nom}}$ is the chamber pressure when the nozzle is full flowing (from Dumnov[R 101]).

The basic idea of the Dumnov side-load model, i.e. a random oscillation of the separation line and random pressure pulsation in the separated flow region are correct and in agreement with experimental observations found in experiments of obstacle induced separation, see section 5.2.4. The interaction length is one of the main elements in this type of side load model and a correct value of L_{sh} is thus essential. Dumnov[R 101] gives no information of the interaction length in his paper. However, he probably used experimentally determined values of the interaction length when calibrating the model. When applying it to other nozzles, Dumnov uses a semi-empirical correlation function for the interaction length similar to that derived from the free interaction theory, see Figure 42, where the interaction length is coupled to the incoming boundary layer properties. Since no detailed information has been given of this interaction length correlation, except that $l/\theta_i=f(M_i,T_{wi})$ according to Dumnov et al.[R 112], the validity and the influence of this correlation can not be assessed. Nevertheless, the approach is superior to the Schmucker model, where the interaction length has no coupling to the boundary layer properties at all.

The dumnov approach was tested by applying the model on data obtained in tests with the LEA TIC nozzle by Girard and Alziary[R 117]. This yields a constant rms level of the pressure fluctuation in the separation point region of $\sigma_{sh}/\sigma p_i'\approx83$, in fair agreement with max values of the test data[§], see Figure 73. The Dumnov approach predicts further one constant fluctuation level $\sigma_{rec}/\sigma p_i'\approx17$ in the recirculating region, whereas the measurements indicates a decreasing rms level, from $\sigma_{rec}/\sigma p_i'\approx20$ to $\sigma_{rec}/\sigma p_i'\approx12$, with increasing distance from the interaction region. A more accurate method to determine the pressure fluctuations in the interaction domain on physical basis would be to use the Kistler[R 63] approach, see section 5.2.4. In contrast to the Dumnov model, which only gives one constant value of $\sigma p'$ throughout the interaction region, the Kistler approach renders the streamwise evolution of $\sigma p'$. According to Kistler the mean-square pressure fluctuation around the mean pressure in the interaction zone can be expressed as (cf. Eq.27):

[§] The difference in the measured values in the interaction region between the two tests is an effect due to the operational conditions, which were not exactly identical in the two tests. This influences the start and the extension of the interaction region, see Figure 73.

$$\sigma p'^2(s) = \varepsilon[1-\varepsilon](p_p - p_i)^2 + \varepsilon \sigma p_p'^2 + [1-\varepsilon]\sigma p_i'^2 \qquad \text{Eq. 58}$$

Where $\sigma p_i'^2$ and $\sigma p_p'^2$ is the mean-square pressure fluctuation in the unperturbed boundary layer upstream the interaction and in the plateau pressure region respectively. ε is the fraction of time that the plateau pressure region is acting over the point of interest, i.e. an "intermittence" factor. According to Erengil and Dolling[R 61] the error function shows a good fit to the intermittence factor ε, which means that the location of the separation shock has a Gaussian distribution within the intermittent region.

The rms distribution and the corresponding level of $\sigma p'$ spatial average over the interaction domain, obtained with the Kistler method is included in Figure 73. As can be seen the calculated rms curve fits the measured values surprisingly well. Figure 74 shows the change of the rms level in the short VOLVO S7 nozzle as the interaction zone moves upstream during down ramping of the chamber pressure. The figure shows this behaviour for two different pressure transducers located at axial positions corresponding to M_i=3.8 and M_i=4.1 respectively. As can be seen the curves are very similar for the two positions. The interaction zone moves over the transducers during the time t_p-t_i, where subscript i and p refers to the start of the interaction and the plateau point respectively. Since the global movement of the separation front is slow and almost constant and the changes in p_i and p_p are modest during the down ramping, the obtained curves can be interpreted as the streamwise evolution of $\sigma p'$, i.e. $(t\text{-}t_i)/(t_i\text{-}t_p)\text{=}s$. When comparing Figure 73 with Figure 74 it can seen that the streamwise distribution of the rms levels obtained with the Kistler approach also corresponds well with test data obtained during this transient operation of the VOLVO S7 nozzle.

Based on the experimental evidence we can see that $\sigma p_i'$ and $\sigma p_p'$ are small compared to (p_p- p_i), thus a reasonable approximation of the Kistler expression is:

$$\sigma p'^2 \approx \varepsilon[1-\varepsilon](p_p - p_i)^2 \qquad \text{Eq. 59}$$

According to this expression, the maximum rms, $\sigma p'_{max}$, occurs at ε=0.5 (i.e., the mid-point of the intermittent region) and has a value of $\sigma p'_{max} = 0.5(p_p - p_i)$. Equation 59 then gives the corresponding average rms value in the intermittent region $\sigma \overline{p}' = 0.2420(p_p - p_i)$. This is close to the averaged value $\sigma \overline{p}' = 0.2514(p_p - p_i)$ obtained by inserting $\sigma p_i'$ and $\sigma p_p'$ from the LEA TIC test. The averaged rms level obtained with the Dumnov approach is significantly higher compared with the one obtained with the Kistler approach. The difference of the averaged rms level between the two approaches is $\sigma \overline{p}'_{Dumnov}/\sigma \overline{p}'_{Kistler} \approx \sqrt{2}$. This implies that the assumption of a sinusoidal fluctuation between the two-pressure levels p_i and p_p done by Dumnov is too simple and over predicts the averaged fluctuation level in the intermittent region.
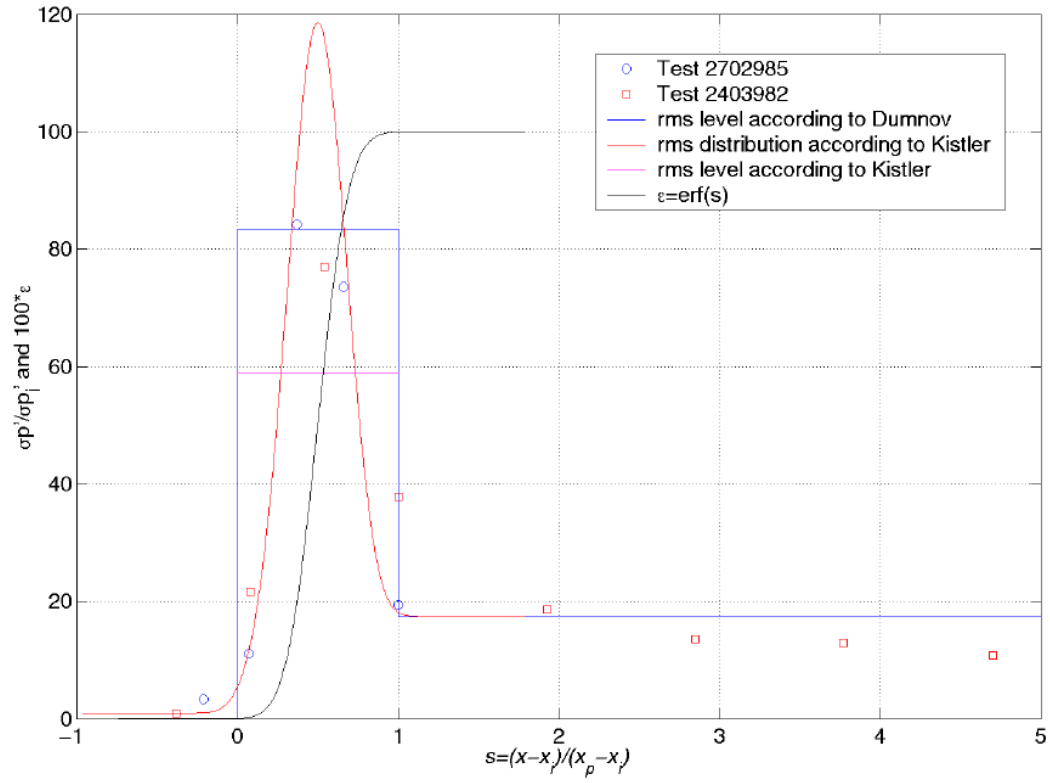
Figure 73. Rms pressure fluctuations in the LEA TIC nozzle, comparison between measured and calculated values, (Test data taken from Girard and Alziary[R 117])
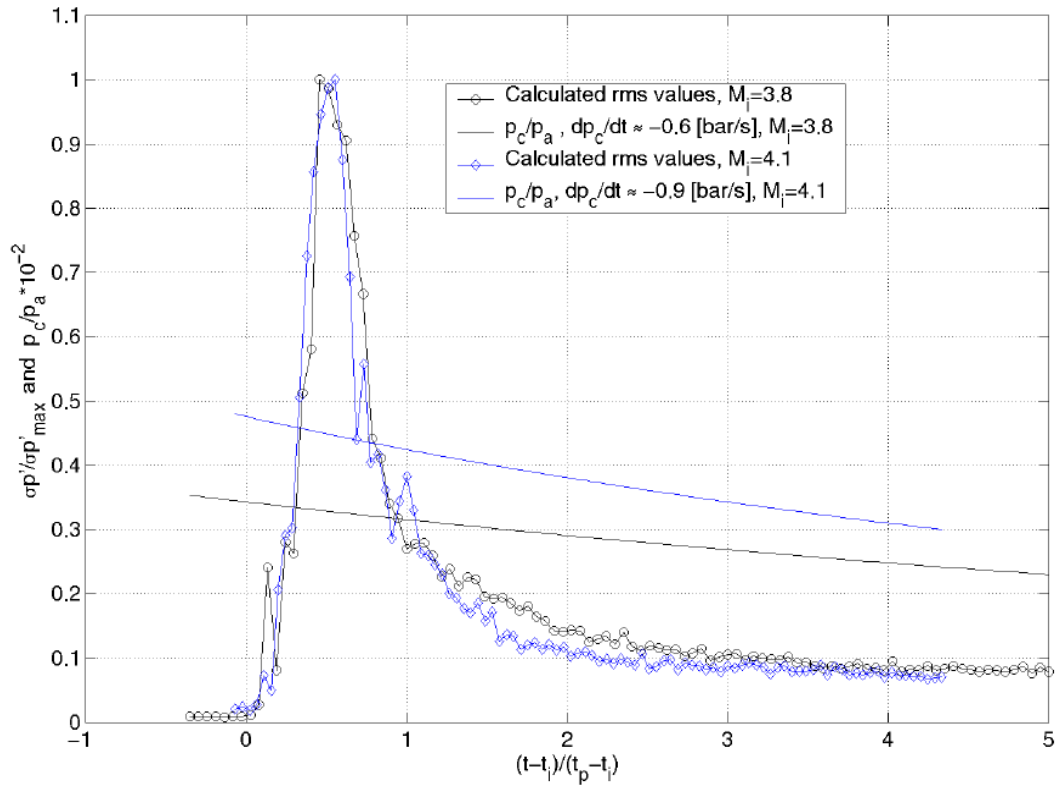

Figure 74. Integrated rms values of pressure signal at two different axial locations in the VOLVO S7 short nozzle during down ramping of p_c. Each value based on 800 samples = 0.2 [s].

Analysis of the expression of the rms pressure level in the recirculating zone proposed by Dumnov, equation 55, leads to:

$$\sigma_{rec} = \frac{p_p'}{\sqrt{2}} = \frac{dp_p}{dx} \frac{L_{sh}}{2\sqrt{2}}$$

Eq. 60

Which means a sinusoidal fluctuation with amplitude p_p'. Hence it is assumed that purely the pressure behind and the motion of the separation shock causes the pressure fluctuation level in the recirculating zone. As the mean pressure in the interaction region is a result of the intermittence of the flow, i.e. the separation shock moving back and forth see Figure 32, the gradient of the mean pressure is a kind of measure of this motion. Thus the proposed expression as a first order of approximation of the fluctuation at the plateau point seems to be a good assumption especially when comparing it with test data. The decrease of the rms level in the recirculating region as indicated in the measurements might be interpreted as a damping of the fluctuation level originating from the shock motion as the distance from the interaction region is increased. The calculated value with the Dumnov approach is thus conservative when used as a mean rms value over the entire recirculation region.

In general it can be said that appropriate parameters for normalising intermittent region power spectra are an area requiring substantially more work. However, Gonsalez and Dolling[R 118] showed that the spectra in the intermittent region, generated by different diameter cylinders, collapsed when plotting the magnitude $W_p(f) \cdot f / \sigma_p^2$ versus a reduced frequency given as $f L_{sh}/U_\infty$. This scaling using the length of the of the intermittent region, L_{sh}, appears to have a firm foundation, but the use of the free stream velocity just before the onset of the interaction, U_∞, should be viewed as tentative, since all of the experiments were carried out at the same U_∞. Dumnov uses $U/\sigma_p^2\theta_i$ for normalising the magnitude of the experimental determined spectral and interspectral characteristics of the pressure pulsations whereas no information is given of how and if the frequency axis is normalised. This together with the lack of experimental data in the paper by Dumnov makes it impossible to estimate how generalised the spectrum obtained actually is.

One of the main advantages with the Dumnov approach is that the structure dynamic characteristic of the rocket engine or the model facility is taken into account in a more psychical manner compared to the common approach with a constant dynamic response factor used in older models. Even if the amplification in the Dumnov model is only accounted for through a transfer function characterising a 1DOF system, it was a significant improvement in the methods of side-load modelling at the time it was published. It gave the engineer a valuable tool to estimate expected side-loads, needed to mechanically define the thrust chamber structure to ensure mechanical integrity under worst case condition and to design gimbaling system dampers etc such that the amplified load is kept within reasonable limits.

Finally, it must be stressed again that the overall logic of the Dumnov approach is correct. However, as indicated in the above analyses corrections and improvements could be done. The development and validation work of such improved models is currently ongoing at the different partners of the FSCD group. E.g. at Volvo Aero[R 108], a model is under development to calculate this type side-loads due to random pressure fluctuations. Figure 75 shows a comparison between a first prediction with this model and experimental side-load data for the S7 nozzle. As can be seen, the general trend of the side-load is captured well, whereas there are some deviations in the prediction of its magnitude.
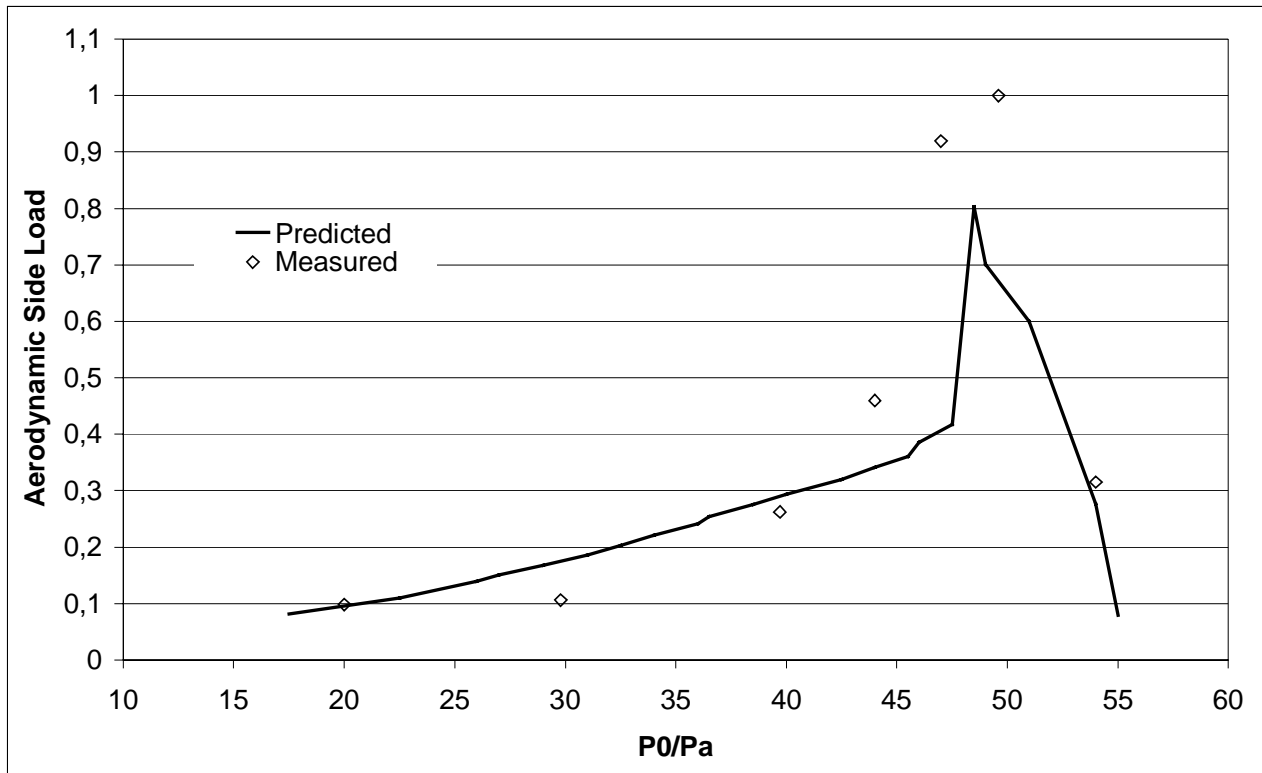
Figure 75. Side-loads in the S7 nozzle, comparison between prediction and experiment, also published in Östlund et al[R 108].

8.4 SIDE-LOADS DUE TO AEROELASTIC COUPLING

A possible reason for side-loads is the aeroelastic interaction between flow induced wall-pressure fluctuations and the mechanical eigenmodes of the nozzle and thrust chamber. Slight variations in wall pressure may a cause significant distortion of the contour, which in turn results in a further variation in wall pressure and the system forms a closed loop, which may result in a significant amplification of the initial load. The study of these closed-loop effects in separated nozzle flows is rather complex, requiring dynamic models of the mechanical nozzle-engine support system, the flow separation, as well as the coupling between these two. However, a simple technique for handling these difficult coupling problems has been proposed by Pekkari.[R 102,R 103] The model consists of two main parts, the first dealing with the equation of motions of the thrust chamber as aerodynamic loads are applied, and a second part modelling the change of the aerodynamic loads due to the distortion of the wall contour. The wall pressure in the attached region is the nominal vacuum pressure profile with a pressure shift due to the displacement of the wall. In the original work by Pekkari, this pressure shift is determined with the use of linearised supersonic flow theory. However, experience has shown that this theory tends to overpredict the pressure shift and Östlund[R 108] therefore proposed a modified approach where the pressure shift is extracted from 3D Euler simulations. The separation line in the nozzle is assessed with a simple separation criterion of Summerfield type (cf. Eq.28). The wall pressure in the separated region is assumed to be equal to the ambient pressure. This model predicts the aeroelastic stability, the modification of eigenfrequencies due to aeroelastic effects, as well as the transient behaviour during start up and shutdown of the nozzle. Different mechanical eigenmodes can be treated, however, from side-load point of view, the aeroelastic behaviour of the bending mode is the most relevant one. In the following paragraphs, the model is outlined for the first bending mode, simplified as a pure bending around a flexible joint or cardan located at the throat. The model is also compared with VOLVO S1 and S6 sub scale test data.

8.4.1 Aeroelastic analysis

In the following section we will describe the aeroelastic theory applied to VOLVO S1 and S6 test cases. We consider the geometry for the flow and the nozzle wall motion as indicated in Figure 76.
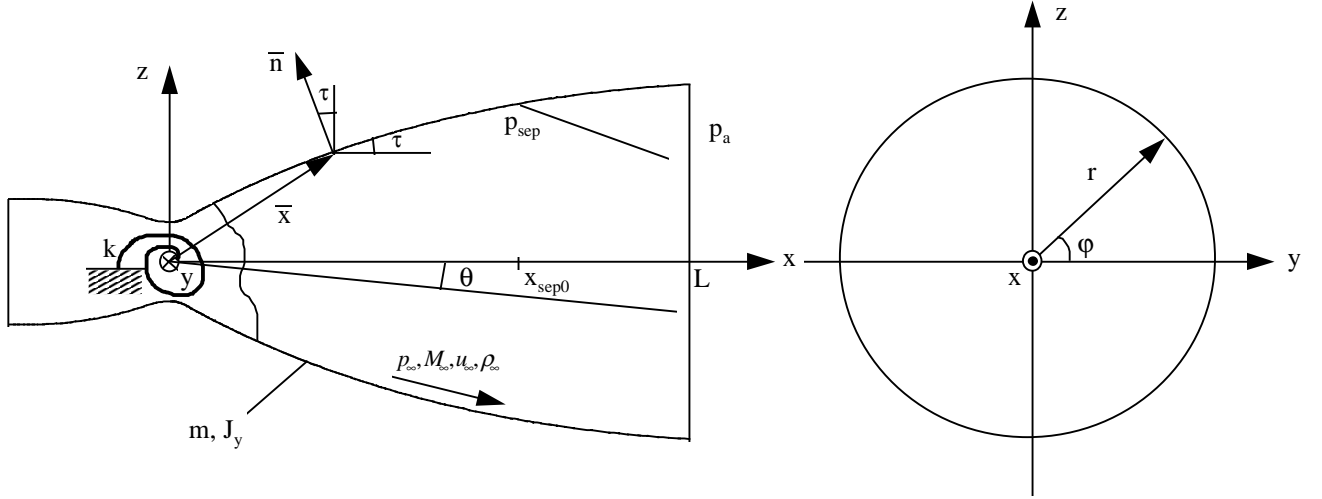
Figure 76. Nozzle and flow separation geometry.

In order to simulate the first bending mode the nozzle is mounted on a flexible joint or cardan with stiffness k located at the throat. θ is the tilt angle between the nozzle centre line and the combustion chamber centre line. L is the length (from the throat to the exit), m is the mass, J_y is the mass of inertia around the y-axis, τ is the local contour angle, and r is the local radius of the nozzle. $\vec{w}$ is the displacement of the nozzle wall. The azimuthal location is denoted by φ.

Following the analysis of Pekkari.[R 102,R 103], the system is considered as quasi static with respect to the flow, i.e. the characteristic time scales of the flow are considered to much larger than the characteristic time scales of the mechanical system. The equation of motion in the y-direction for the bending of the nozzle by an angle θ is:

$$J_y \ddot{\theta} = M_m(\theta) + M_a(\theta, P_{cc})$$

Eq. 61

At equilibrium,

$$M_m(\theta) + M_a(\theta, P_{cc}) = 0$$

Eq. 62

Here M_m is the mechanical torque, i.e the restoring torque of the spring in the nozzle suspension, which for small displacements is:

$$M_m(\theta) = -k\theta$$

Eq. 63

and M_a is the aerodynamical torque induced by the pressure load onto the nozzle wall, i.e.:

$$\vec{M}_a(\theta, P_{cc}) = \oiint \vec{x} \times \left[p_\infty(\vec{w}(\theta), x, P_{cc}) - p_a \right] \cdot \vec{n} \quad dS$$

Eq. 64

where $\vec{n}$ is the wall surface normal vector facing the flow and $\vec{x}$ is the corresponding vector of location:

$$\vec{n} = \left\{ -\sin\tau, \cos\tau \, \cos\varphi, \cos\tau \, \sin\varphi \right\}$$

Eq. 65

$$\vec{x} = \left\{ x, r(x)\cos\varphi, r(x)\sin\varphi \right\}$$

Eq. 66

Upstream of the separation point, x_{sep} (the point of minimum static wall pressure is usually indexed "*sep*" or "*i*" although the physical separation occurs later), the pressure is the free stream pressure, p_∞. Downstream

of the separation point a pressure recovery occurs and the pressure gradually approaches the ambient pressure. For simplicity, the pressure downstream of the separation is here set equal to the ambient pressure, p_a, i.e.

$$p_\infty(\vec{w}, \vec{x}, P_{cc}) = \begin{cases} P_{cc}\left(\dfrac{p_{\infty,o}(x)}{P_{cc}} + \Psi(\vec{w}, \vec{x}) \right) & ; \quad x \leq x_{sep} \\[4mm] p_a & ; \quad x > x_{sep} \end{cases}$$

Eq. 67

Here $p_{\infty,0}(x)$ denotes the vacuum pressure profile in the undeflected nozzle. The second term in the pressure upstream of separation is the disturbance of the free stream pressure due to a small wall displacement, i.e.

$$\Psi(\vec{w}, \vec{x}) = \frac{p_\infty(\vec{w}, \vec{x}, P_{cc}) - p_{\infty,0}(x)}{P_{cc}}$$

Eq. 68

The location of the separation point is given by a separation criterion of Summerfield type (cf. Eq.28):

$$p(x_{sep}) = p_{sep} = 0.3 p_a$$

Eq. 69

In the original work by Pekkari, the pressure shift, ψ, was calculated with the use of the small perturbation theory (SPT) (cf. Eq.19-20) , i.e.:

$$\Psi(\vec{w}, \vec{x}) = \frac{\rho_{\infty,0} u_{\infty,0}^2}{P_{cc}\sqrt{M_{\infty,0}^2 - 1}} \frac{\partial w}{\partial s} = B' \frac{\partial w}{\partial s}$$

Eq. 70

Here $w = \vec{w} \cdot \vec{n}$ denotes the normal displacement of the nozzle wall surface facing the flow and s is the arclength along the wall in the axial direction. B' is the normalised pressure shift coefficient, which expresses the change in pressure with the wall slope.

However, experience has shown that SPT tends to overpredict the pressure shift in cases where 3D effects are significant. A modified approach was therefore proposed by Östlund[R 108] where the pressure difference B' is directly extracted from 3D Euler simulations:

$$B'(x) = \frac{\Psi(\vec{w}, \vec{x})}{\partial w / \partial s} = \frac{p_\infty(\vec{w}, \vec{x}, P_{cc}) - p_{\infty,0}(x)}{P_{cc} \, \partial w / \partial s}$$

Eq. 71

This can be seen in Figure 77, where the measured and the calculated wall pressure profile are shown for the undeflected and deflected (1°) S1 nozzle, respectively. The improvement obtained with CFD/Euler is obvious and is more pronounced in corresponding normalised pressure shift coefficient B', shown in Figure 78. As indicated in the figure, the SPT method overpredicts the pressure shift coefficient by approximately a factor 4 for this case. The CFD predictions on the other hand show close agreement with the experimental data and thus validate the use of Euler simulations for calculating the pressure shift coefficient.
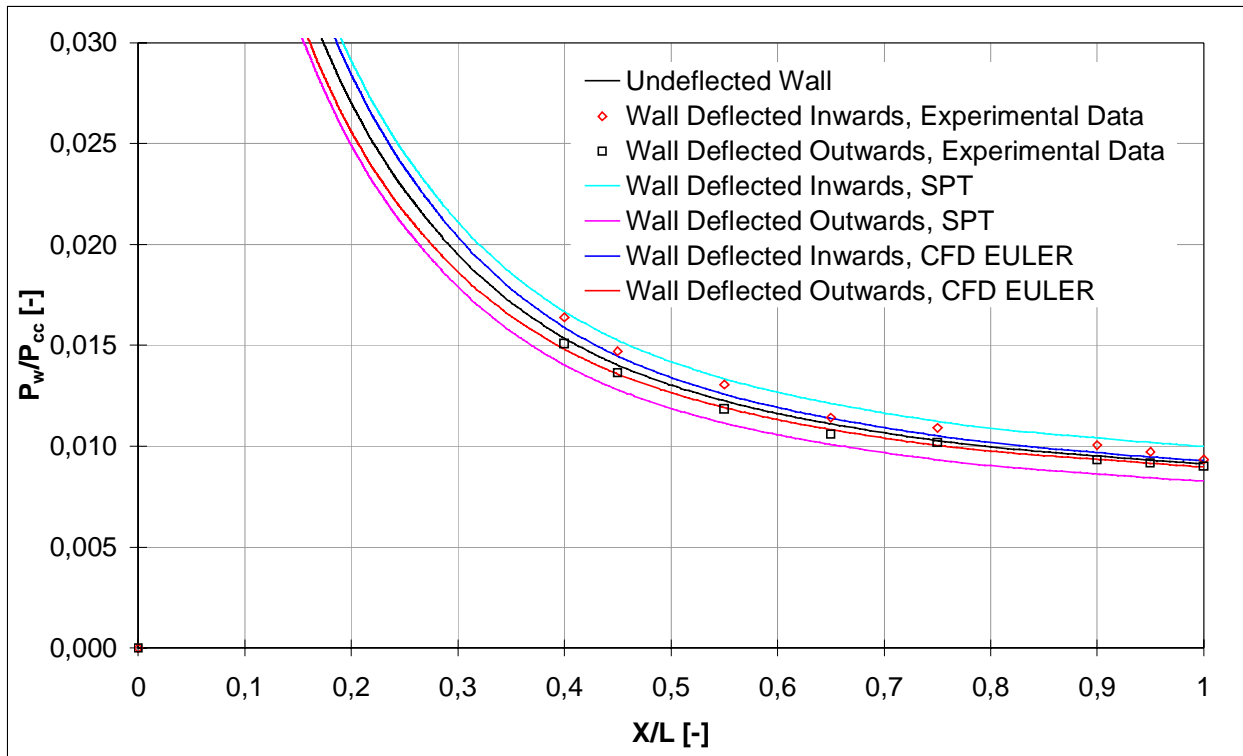
Figure 77. Measured and calculated wall pressure in the S1 nozzle static deflected 1 degree, also published in Östlund et al[R 108].
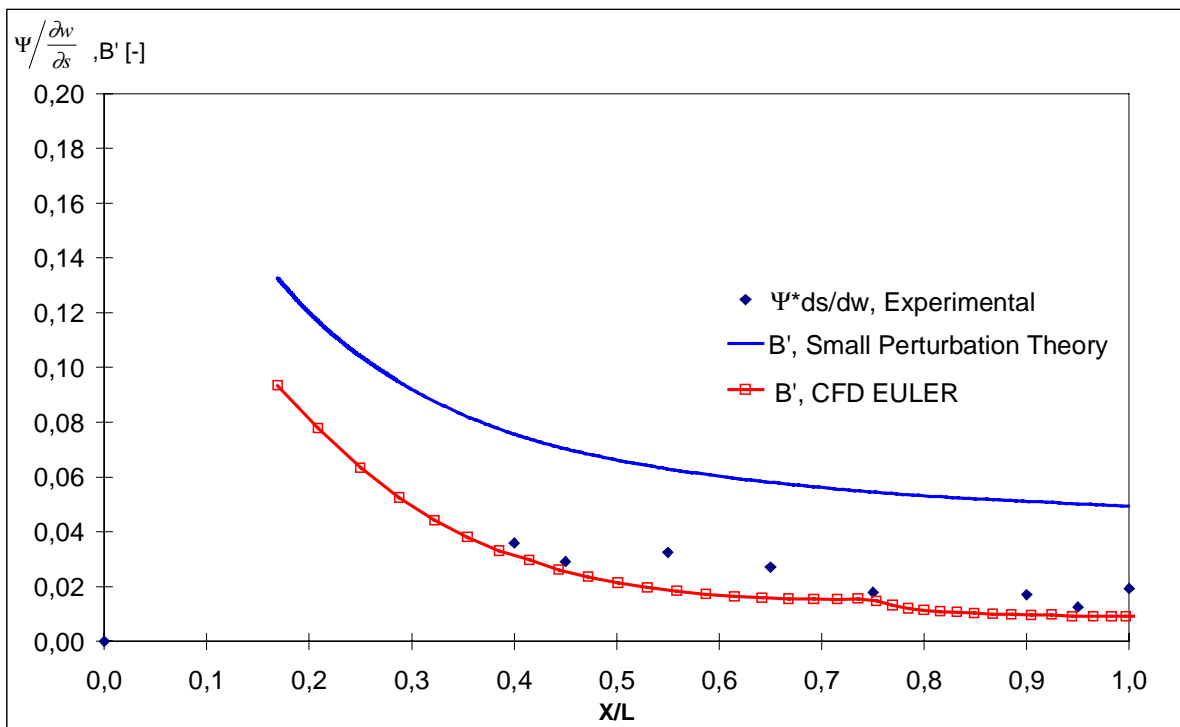
Figure 78. Comparison between calculated and measured normalised pressure shift coefficient *B'* in the S1 nozzle, also published in Östlund et al[R 108].

It must be emphasised that the deviation of the wall pressure due to bending around the throat is highly dependent on the nozzle contour itself. As shown in reference R 110 and R 119, the induced compression and expansion waves in a bent 15° conical nozzle interacts such that the pressure deviation trend is actually reversed, cf. Figure 79 and notice the negative value of *B'*. It was observed that on the side that was deflected

away from the flow, where more expansion is expected, the wall pressure was in some portions of the nozzle even higher than on the opposite side, which was deflected into the flow. This finding has been confirmed by own numerical simulations, see Figure 79, and underlines the necessity of case-sensitive methods.
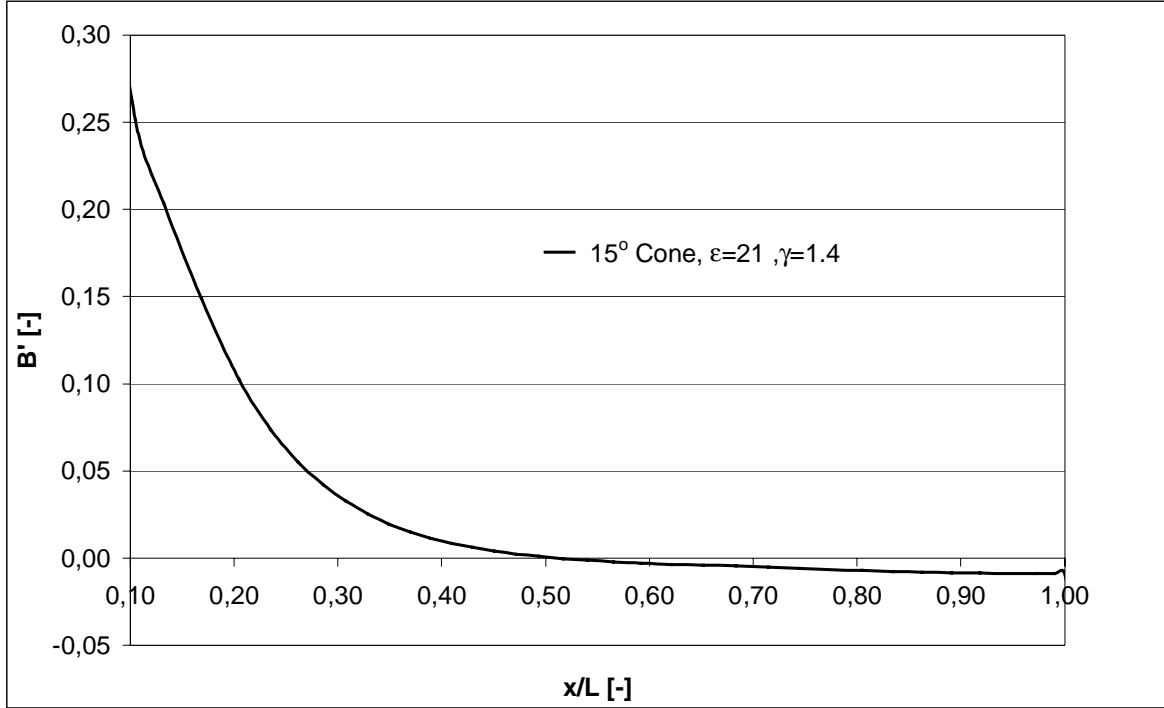
Figure 79. Normalised pressure shift coefficient in conical nozzle, also published in Östlund et al[R 108].

To procede with the aeroelastic stability analysis, we next expand the free stream pressure around the initial location of the separation line, x_{sep0},

$$p_{\infty,0}(x_{sep}) = p_{\infty,0}(x_{sep0}) + \frac{dp_{\infty,o}}{dx}(x_{sep} - x_{sep0}) + ..$$

Eq. 72

Equation 67 written at the axial station x_{sep} is:

$$p_{\infty}(\vec{w},\vec{x},P_{cc}) = p_{\infty,0}(x) + P_{cc}B'\frac{\partial w}{\partial s} \; ; x = x_{sep}$$

Eq. 73

The separation pressure p_{∞} at $x=x_{sep}$ approximated for the deformed wall contour by equation 73, will be the same as the separation pressure $p_{\infty,0}(x_{sep0})$ for the undeformed wall contour included in equation 72, which can be written as:

$$p_{\infty,0}(x_{sep0}) = p_{\infty} \, at \; x=x_{sep}$$

Eq. 74

and hence equation 73 and 72 give:

$$x_{sep0} - x_{sep} = \frac{P_{cc}B'}{-\frac{dp_{\infty,o}}{dx}}\frac{\partial w}{\partial s}\bigg|_{x=x_{sep0}} = C\frac{\partial w}{\partial s}\bigg|_{x=x_{sep0}}$$

Eq. 75

where $C = C(x_{sep0})$ gives the shift of the separation point due to the shift of the nozzle wall slope.
The aerodynamic pressure force per arc length due to a small wall displacement, may be written as:

$$\vec{F}'_a(\vec{w}) = \vec{n}(p_a - p_{sep})(x_{sep} - x_{sep0}) =$$
$$= \vec{n}(p_a - p_{sep})C(x_{sep0})\frac{\partial w}{\partial s}$$

Eq. 76

By integrating the force contribution around the separation line the aerodynamic pressure force becomes:

$$\vec{F}_a(\vec{w}) = \oint_{lsep} \vec{F}'_a \ dy = (p_a - p_{sep})\oint_{lsep} \vec{n}C\frac{\partial w}{\partial s} \ dy\Big|_{x_{sep0}}$$

Eq. 77

The corresponding aerodynamic torque is:

$$\vec{M}_a(\vec{w}) = \oint_{lsep} \vec{x}\times\vec{F}'_a \ dy = (p_a - p_{sep})\oint_{lsep} \vec{x}\times\vec{n}C\frac{\partial w}{\partial s} \ dy\Big|_{x_{sep0}}$$

Eq. 78

The change of the nozzle wall slope at different azimuthal locations, φ, due to a small tilt angle, θ, of the nozzle can be expressed as:

$$\frac{\partial w}{\partial s} = \theta \sin \varphi$$

Eq. 79

Using this and

$$\oint_{l_{sep}}...dy \approx \int_0^{2\pi}...r\left(x_{sep0}\right)d\varphi$$

Eq. 80

for small wall displacements, the aerodynamic torque can be expressed as:

$$\vec{M}_a(\theta, x_{sep0}) = (0, M_a, 0) \quad where$$
$$M_a(\theta, x_{sep0}) = (p_{sep} - p_a)Cr\pi(xCos\tau + rSin\tau)\theta \quad at \ x = x_{sep0}$$

Eq. 81

The eigenfrequency for the mechanical system alone is formed by inserting a harmonic amplitude ansatz:

$$\theta \sim e^{i\omega t}$$

Eq. 82

into equation 61 and leaving out the aerodynamical torque $M_a(\theta, P_{cc})$:

$$-J_y\omega^2\theta = -k\theta$$

Eq. 83

This gives:

$$\omega^2 = \frac{k}{J_y}$$

Eq. 84

Now, consider the nozzle displaced when subjected to mechanical and aerodynamical loads and again assume the motion to be purely harmonic, i.e.:

$$\theta \sim e^{i\Omega t}$$

Eq. 85

Introducing equation 84 and 85 in 61 and rearranging gives:

$$\left(\frac{\Omega}{\omega}\right)^2 = 1 - \frac{M_a(\theta, P_{cc})}{k\theta} \qquad \text{Eq. 86}$$

Inspection of equation 86 shows that:

1. When $M_a(\theta, P_{cc}) < 0$, the aeroelastic torque acts to restore the nozzle to its nominal position, i.e. the system becomes stiffer than the mechanical structure itself and the frequency of the eigenmode is shifted to a higher frequency, i.e. $(\Omega/\omega)^2 > 1$. This is for instance the case in a full flowing Vulcain nozzle.

2. When $M_a(\theta, P_{cc}) \in [0, k\theta]$, the aeroelastic torque acts in the same direction as the displacement of the nozzle wall, i.e. the system becomes weaker than the mechanical structure itself and the frequency of the eigenmode is shifted to a lower frequency, i.e. $(\Omega/\omega)^2 \in [0, 1]$.

3. When $M_a(\theta, P_{cc})/_y > k\theta$, the unconditionally stable eigenmode becomes aeroelastically unstable, i.e. $(\Omega/\omega)^2 < 0$, and the displacement of the nozzle will thus start to grow exponentially.

The aeroelastic stability of the system can also be investigated for small displacements by substituting the linearised aerodynamic torque, equation 81, in equation 86, which gives:

$$\left(\frac{\Omega}{\omega}\right)^2 = 1 - \frac{(p_{sep} - p_a)C\,r\pi(xCos\,\tau + rSin\,\tau)}{k}\bigg|_{x=x_{sep\,0}} \qquad \text{Eq. 87}$$

8.4.2   Experimental verification of the aeroelastic analysis

Within the GSTP FSC test programme, the influence of structural response and aeroelastic coupling were investigated for the VOLVO S1 model nozzle. This was done by varying the natural eigenfrequency of the bending mode with the use of exchangeable torsion springs. The mechanical eigenfrequencies of the bending mode are listed in Table 5 for the different spring set-ups used. The frequencies were determined by performing a ping test on the model set up, see section 7.3.1. A more detailed description of the test programme is presented in R 5.

Spring name	Super weak	Weak	Medium	Stiff	Rigid
Natural frequency [Hz]	25,2	36,3	45,0	57,5	120

Table 5. Mechanical eigfrequencies of the bending mode for the different spring set-ups with the VOLVO S1 nozzle, also published in Östlund et al[R 5, R 108].

The aeroelastic stability of the S1 nozzle can be calculated from Eq.87 for the different spring set-ups. Such a calculation is presented in Figure 80 with $p_{sep}/p_a = 0.3$ and B' from an Euler calculation according to Figure 78. From the figure we can conclude that the only areoelastic unstable system is the S1 nozzle with the super weak spring, $(\Omega/\omega)^2 < 0$ when $x/L > 0.83$, whereas the other systems are aeroelastic stable.
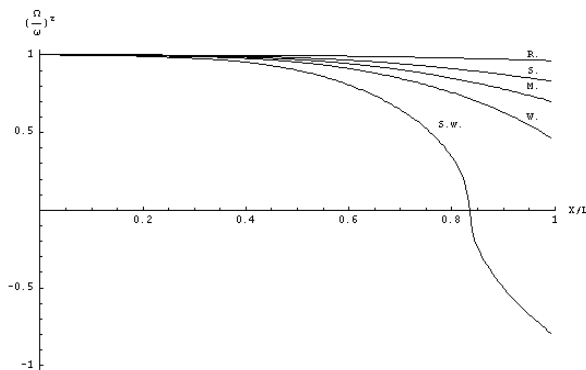

Figure 80. Aeroelastic stability of the S1 nozzle for the different spring setups, S.W. =Super Weak, W. = Weak, M.=Medium, S.=Stiff and R.=Rigid spring respectively, also in Östlund et al[R 6, R 108].

The aeroelastically stable system will almost behave like a regular forced response system, i.e. the closer the mechanical egienfreqencies are to the frequencies of the aerodynamic load the higher generated loads. The only aeroelastic effect is that a small shift of the system eigenfreqency and a corresponding small amplification of the forced response load will occur. The frequency shift and the aeroelastic side-load amplification depend on the degree of coupling. For the weak, medium, stiff and rigid spring set-ups considered here the coupling is considered to be weak and the aeroelastic effect small.

For an aeroelastically unstable system, on the other hand, we would expect a significantly higher side-load magnitude compared to the classical forced response theory. When the separation enters the section of the nozzle that is unstable, the displacement of the nozzle will start to grow exponentially. At the same time the separation line will be displaced accordingly. The non-linear growth of the nozzle displacement will eventually saturate as parts of the separation line start to move out of the nozzle when the displacement becomes sufficiently large. This can be seen in the non-linear stability relation, equation 86, displayed in Figure 81 for the S1 nozzle with tilt angles $\theta=0.1^o$ and $\theta=2.6^o$. As the nozzle displacement saturates, the amplitude will eventually drop and the process will be repeated in a cyclic way.

Figure 81 shows that the aeroelastic instability occurs at a pressure ratio of p_0/p_a=26-28. When the pressure ratio is increased further, the nozzle will eventually become full flowing at $p_0/p_a \approx 30$, and the system becomes stiffer than the mechanical structure itself, i.e. $(\Omega/\omega)^2 > 1$, since the aerodynamic torque now acts to stabilise the nozzle.
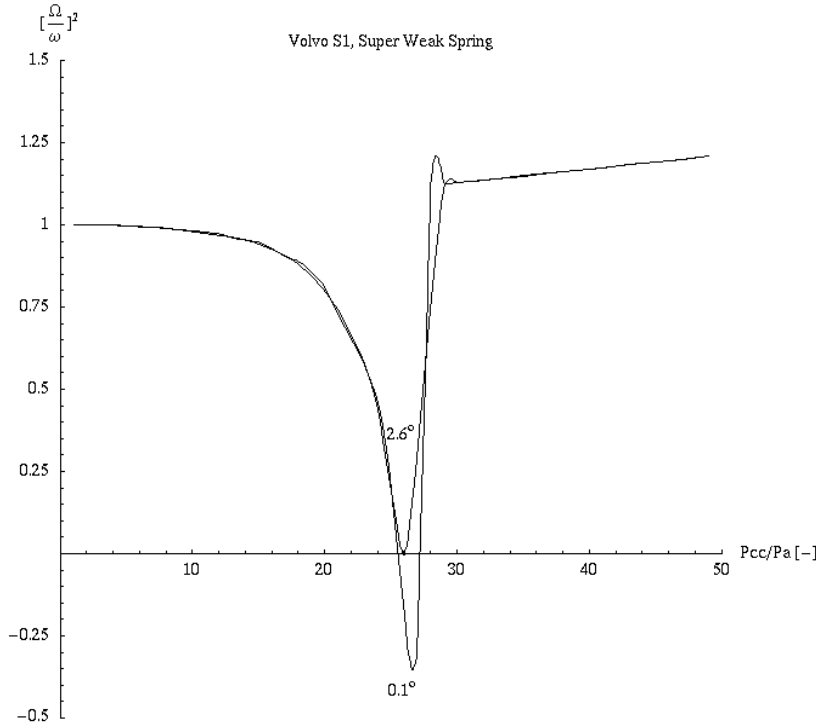
Figure 81. Non-linear stability relation for the S1 nozzle flexible hinged with the super weak spring, also published in Östlund et al[R 108].

Let us now compare the model result with experimental data. For the side-load peak at PR= 28, Table 6, we can see that the test data correlate well with the aeroelastic predictions in Figure 80 and Figure 81. The aeroelastic system, i.e. super weak spring set-up, gives the highest loads (M/M_{max}) and interrupts the trend obtained for the aeroelastically stable systems. The systematic behavior of decreasing response load with decreasing spring stiffness for the rigid to the weak spring which are aeroelastic stable can be explained with classical forced response theory. The side-load peak at PR=28 is caused by the separation shock system pulsating with a frequency of about 100 Hz at the exit. Forming the frequency ratio between the aerodynamical force and the mechanical systems, Table 4, we can see the above stated fact. The highest response load is obtained for the rigid spring, which has the frequency ratio closest to unity and the response

decreases with increased distance from the resonance value. The conclusion is thus that the aeroelastic theory is capable of predicting the obtained side-load features.

Spring	$\dfrac{\omega}{\omega_n}$ [†]	No. of tests	$\dfrac{M}{M_{max}}$
Rigid	0.8	2	0.66
Stiff	1.7	10	0.63
Medium	2.2	10	0.48
Weak	2.8	10	0.45
Super Weak	3.9	5	1

Table 6. Measured side-load magnitude versus frequency ratio between the exiting load and the mechanical system, peak at PR=28, also published in Östlund et al[R 108].

Finally, we compare the predictions of the aeroelastic stability for the S6 nozzle with experimental data, see Figure 82. The experimental frequency shift of the eigenmode has been determined from the strain signal. This was done by applying the Welch method[R 120] for power spectral analysis on the measured steady state side-load at different constant pressure ratios. The sampling time was at least 8 seconds for each case in order to achieve a sufficient frequency resolution. The linearised aeroelastic stability relation, equation 87, for the S6 nozzle has been calculated with p_{sep}/p_a=0.3 and B' extracted from an Euler calculation. In Figure 82 the linear stability relation based on small perturbation theory is also shown in order to visualise the effect of the over-prediction of the pressure shift this theory causes.
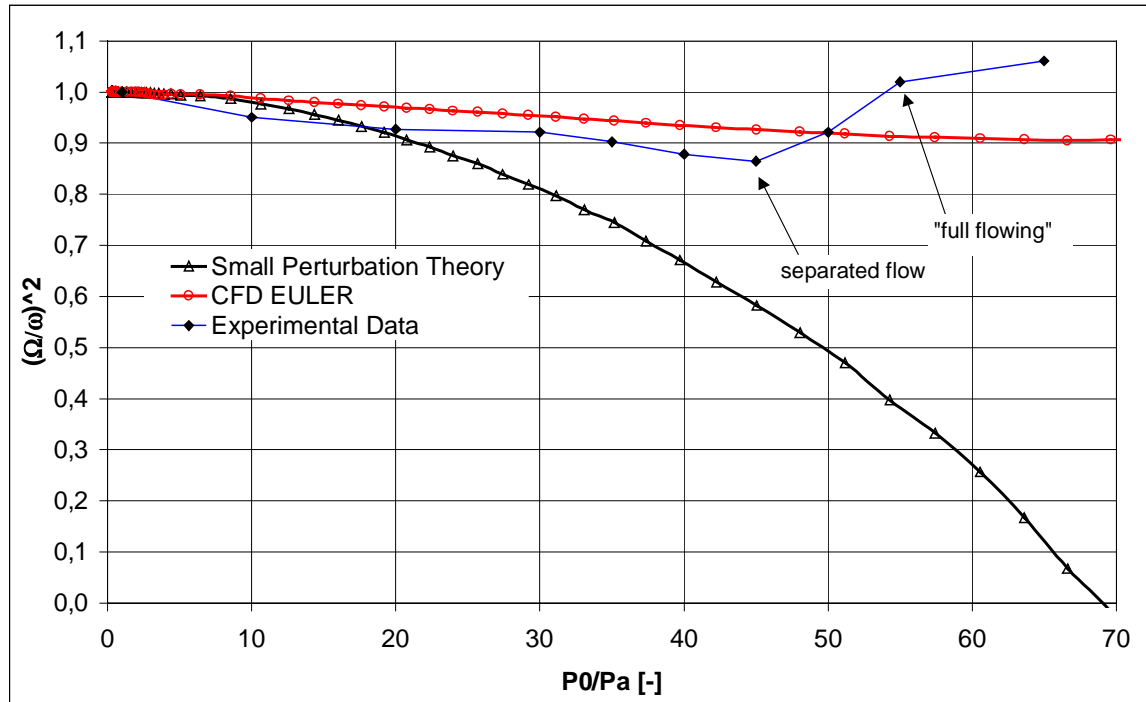
Figure 82. Comparison between measured and calculated frequency shift for the S6 nozzle, also published in Östlund et al[R 108].

In the separated flow region, the linearised stability theory predicts the same trend for the frequency shift as observed in experiments. The discrepancy is mainly due to the fact that both structure and gasdynamic damping are neglected in the model. If damping were included in the model the frequency shift would increase and the model prediction come closer to experimental data. However, the influence of the damping

---

[†] ω=100*2π [s^{-1}] is the frequency of aerodynamical load, evaluated from Schlieren video and pressure measurements. ω_n natural frequency of mechanical system.

is only significant during steady state operation whereas during short transient phases, such as a rocket engine start up, the damping plays a minor role and the model assumptions will thus come closer to reality. The increased system frequency observed in the experimental data when the nozzle is full flowing can not be captured with the linearised stability relation, i.e. Eq.87. However, as indicated in Figure 81, this effect can be captured with the non-linear relation given by Eq.86.

To summarise, we have seen that the modified aeroelastic model is capable of predicting the aeroelastic behaviour experienced in the tests. Further, the necessity of a case-sensitive method to determine the normalised pressure shift coefficient B' has been pointed out.

9   FIELD MEASUREMENT TECHNIQUES IN OVEREXPANDED NOZZLES

9.1   SHOCK VISUALISATION

Compressible gas flows lend themselves particularly well to optical methods of investigation. As a light ray travels through a compressible gas with density variations (which are related to variations in index of refraction), it undergoes three effects. First, a displacement from the path it would have taken in a uniform medium. Second, the angular displacement with respect to an undisturbed path, and third, a phase shift from the undisturbed light ray. These three effects correspond to the three main experimental visualisation techniques for compressible flow.

1. *Interferometry*. The fringe patterns in an interferogram arise due to the phase shift of light as it moves through a density field. This method is primarily suited for quantitative determination of the density field as it measures directly the changes of density.

2. *Schlieren imaging*. This experimental technique depends upon the change in the refractive index as a function of the density of the gas. In fact, schlieren imaging relies on the angular deflections of light rays. The intensity of the schlieren images corresponds to the gradient of the density, i.e. $\nabla_y \rho$ or $\nabla_x \rho$ in a 2-dimenasional case depending on the test set-up. Although it is theoretically adaptable to quantitative use, it is inferior to the interferometer in this respect, and its greatest utility is in giving an easily interpretable picture of the flow field together with a rough picture of the density variations in the flow.

3. *Shadowgraphs*. This technique relies on the displacement of a light ray due to the change in refractive index because of spatial density variations in the gas. It can be shown that the displacement experienced by a light ray depends on the second derivative of the density, i.e. $\nabla^2 \rho$. Therefore it makes visible only those parts of the flow where the density gradients change very rapidly, and it has found its greatest utility in the study of shock waves.

Of the three methods mentioned, the interferometer yields most information and the shadowgraph least. On the other hand, the interferometer is the most costly and the most difficult to operate, whereas the shadowgraph is the least costly and the easiest to operate. Each method therefore has its own useful niche in experimental work, and the choice of method depends on the nature of the investigation.

For supersonic, axially symmetric nozzle flows, these methods are only practically applicable to the exhaust flow. Typical results obtained with the schlieren method and with the shadowgraph method are shown in Figure 22, Figure 83 and Figure 84 respectively for a number of different sub-scale nozzles. To exemplify the usefulness of these methods in the case of highly overexpanded nozzle flows it can be mentioned that schlieren photos as the ones shown in Figure 22 have been an important source for the understanding of the physics behind the cap shock pattern. High-speed video recording of the schlieren pattern during transient operation was used extensively in the VOLVO S1-S8 campaigns, and has given valuable information of e.g. the transition from FSS to RSS and vice versa, see Figure 83. While schlieren photos at stationary conditions have been used to validate CFD results, see Figure 106.
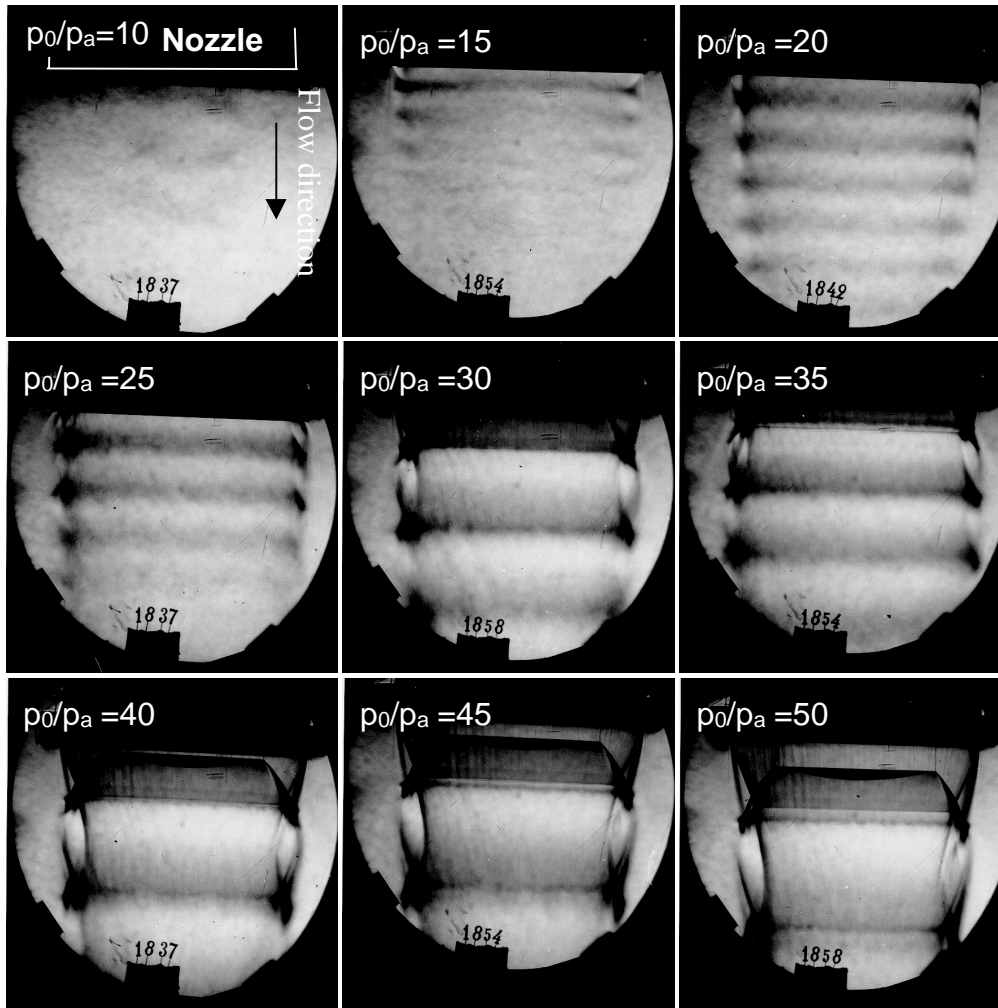
Figure 83. Schlieren photos of the exhaust plume in the VOLVO S1 nozzle at different operational conditions (from Östlund[R 138])

Figure 83 shows schlieren photographs of the flow field at 9 different steady state operational points, p_c/p_a=10-50 in steps of 5 for the VOLVO S1 nozzle. To support the understanding of the schlieren photos, cf. the corresponding calculated Mach number contours shown in Figure 61. From the schlieren photos we can see some typical flow features:

- At p_c/p_a=10 no sharp density changes in the flow field can be detected and FSS is prevailing in the nozzle.
- At p_c/p_a=15 the flow pattern has changed to RSS (the nozzle appears to be full flowing as the jet is attached to the wall) and the expansion and compression waves in the supersonic jet causing the stripy pattern can clearly be seen.
- Between p_c/p_a=25-30 the reattachment point moves out of the nozzle.
- At p_c/p_a =40 the mach disc has completely moved out of the nozzle.

Typical shadowgraph photos are shown in Figure 84 for two different CTIC nozzles at FSS condition tested at NAL[R 122]. In the left photo the flow field is shown for the CTP86L nozzle at a low-pressure ratio, i.e. at significant overexpansion of the flow, and as can be seen the change of the density gradients is small and jet occupies only about 50% of the nozzle exit diameter. The flow field in the CTP50-R5-L nozzle can be found in the right photo. Due to less overexpansion, the CTP50-R5-L jet occupies a larger fraction of the nozzle exit diameter, ~75%, and the shadowgrap image is sharper compered to the CTP86L case.
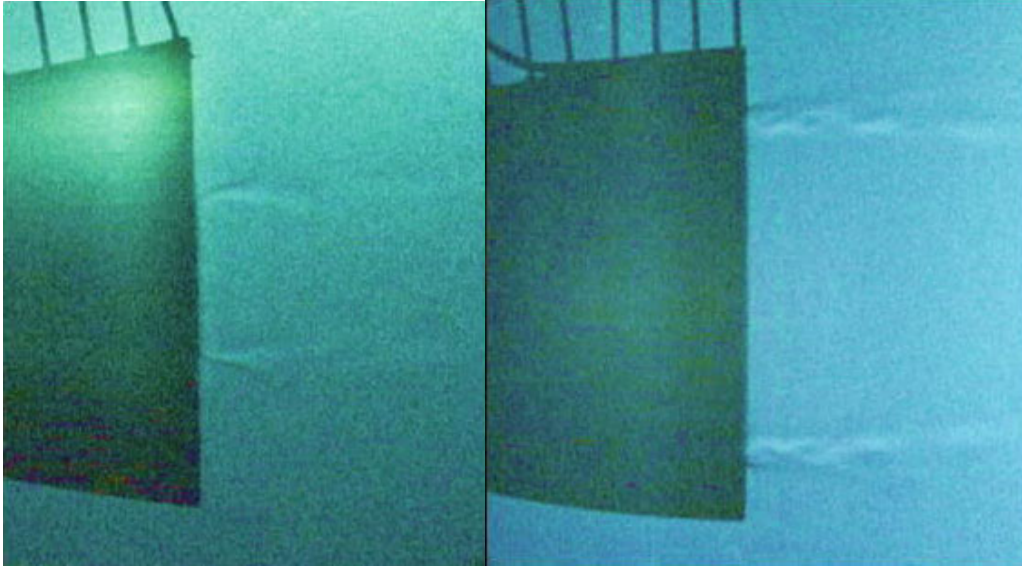
Figure 84. Shadowgraph photos of shock structure in the CTP86L (left) and CTP50-R5-L (right) nozzles by Tomita et al[R 122]. (Courtesy of NAL)

9.2 INFRARED CAMERA IMAGING

Infrared radiometry (IR) is another experimental technique by which can contribute to the insight in the separation behaviour of nozzle flows. In recent experiments performed at DLR, IR has been used to visualise the wall temperature inside a sub-scale TOP nozzle operated at separated flow conditions.[R 123] Typical results from this test campaign are shown in Figure 85-Figure 87 at FSS and RSS conditions respectively. It is clearly seen that a wall temperature increase is induced in the incipient flow region, in where the flow is still physically attached to the wall, see Figure 85 and Figure 86. In the case of reattachment of the jet to the wall, Figure 86, the wall temperature reaches a plateau value after this first temperature increase and then begins to decrease towards a constant value at the point where the flow reattaches the wall. In between the incipient separation line and the reattachment line a closed recirculating zone is established. Further downstream a second temperature peak can be observed, which is believed to be the affect of a second recirculation zone. IR-images have also made it possible to detect axial lines along the wall, which are belived to be caused by Görtler vortices. Figure 87 shows an image where such lines are clearly visible downstream of the throat. As seen in Figure 86, traces of such vortices, which originate in the upper part of the nozzle, can be found downstream of the flow separation line and it is believed that they may have an influence on the separation and wall heat transfer behaviour.
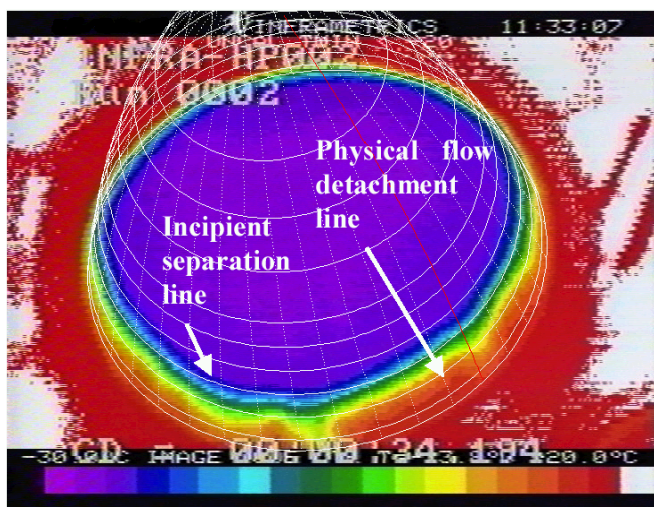
Figure 85. Infrared image: DLR TOP nozzle, pressure ratio p_c/p_a=42.4 during start-up, temperature range: 253-303 K, experiment by Stark et al[R 123]. (Courtesy of DLR and ASTRIUM)
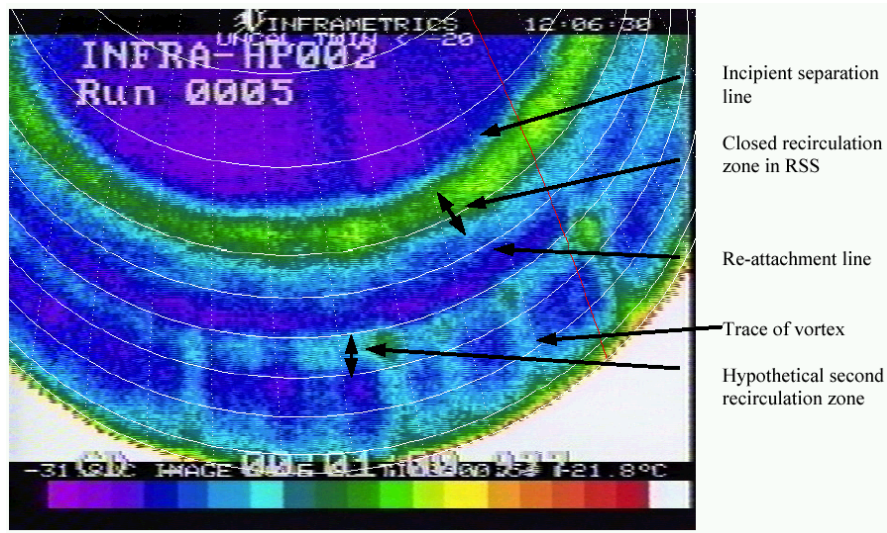
Figure 86. Infrared image: DLR TOP nozzle, pressure ratio p_c/p_a=21.8 during shut down, temperature range: 241-295 K, experiment by Stark et al[R 123]. (Courtesy of DLR and ASTRIUM)

Figure 87. Infrared image: DLR TOP nozzle, vortex origin shortly after nozzle throat, experiment by Stark et al[R 123]. (Courtesy of DLR and ASTRIUM)

In a paper by Hagemann et al[R 124] an illustrative figure is given on the transition process from FSS to RSS, see Figure 88. The figure shows pictures obtained by a regular Video recording of the nozzle wall. Here the separation and reattachment line can be identified from the onset of intensive radiation from the wall as the attached jet heats up the nozzle wall.
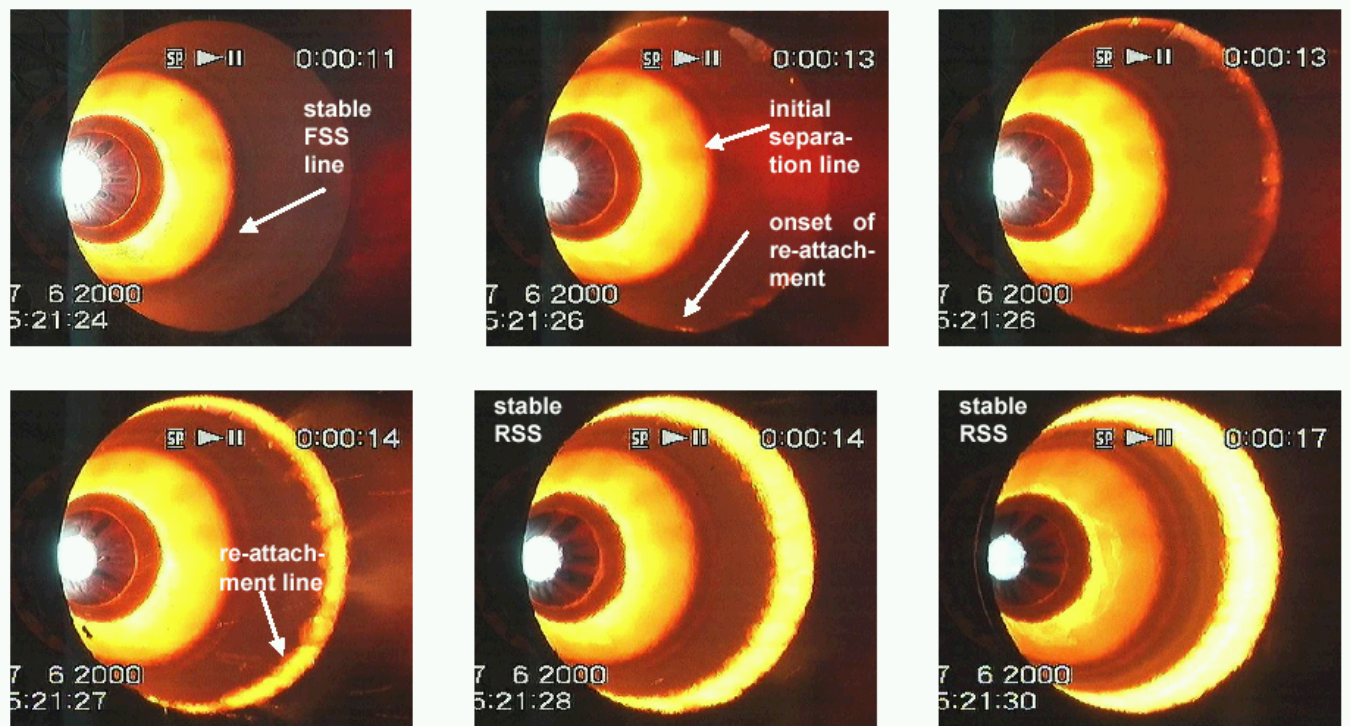
Figure 88. Details of the transition process from FSS to RSS in the long Vulcain C/SiC sub-scale nozzle at p_c/p_a=40 from Hagemann et al[R 124]. (Courtesy of ASTRIUM)

9.3 SEPARATION LINE VISUALISATION

The most basic common for detection of the separation line is by means of surface flow visualisation techniques consisting of a light coating of oil on the wall surface. In Figure 89 typical results obtained with this method are shown from the experimental study of a TOP nozzle by Girard and Alziary[R 130]. They used a mixture of oil and carbon black to visualise the separation line. In order to visualise the reattachment line a much more viscous mixture of oil and grease was used. The mixtures were painted on the wall before each run downstream of the estimated separation and in a band over the estimated reattachment line respectively. During the run the oil and carbon black mixture would move upstream towards the separation line allowing a precise determination of its location. At the same time some of the oil and grease mixture would move downstream of the stagnation point and some would move upstream in the recirculation zone. Due to the low shear stress in the vicinity of the reattachment line, an amount of the mixture will remain around the reattachment line for several seconds.

Figure 89. Oil film visualisation of separation line in a TOP nozzle, experiment by Girard and Alziary[R 130]. FSS line (left) and separation and reattachment line (right). (Courtesy of LEA Poitiers)

A novel method for separation line visualisation in internal flow is the use of Shear Sensitive Liquid Crystals (SSLC).[R 122,R 131] The method consists of applying SSLC on the inner wall surface of a transparent specimen. As the colour of the crystals is a fu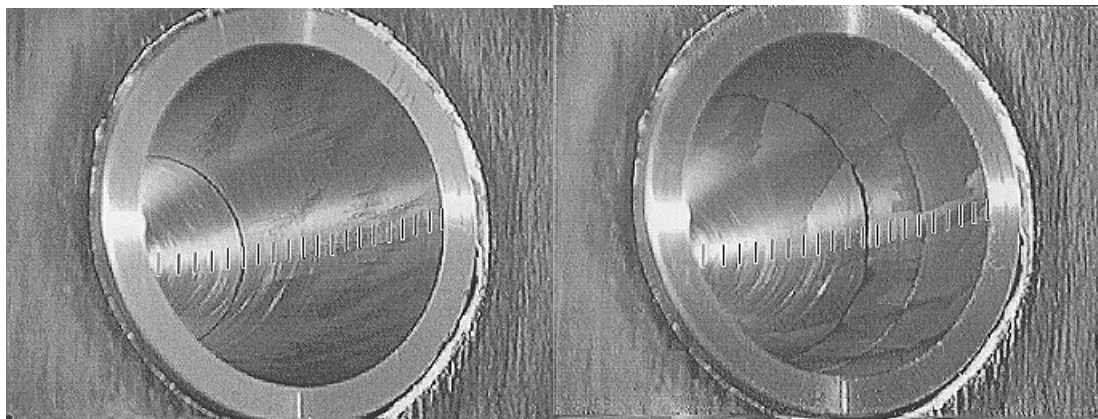nction of the shear stress, the separation line corresponding to $\tau_w=0$ is visualised. This technique has recently been applied to highly overexpanded nozzle flows by Tomita et al. [R 122], see Figure 90-Figure 91. Figure 90 shows the SSLC pattern and the corresponding shadowgraph image, also shown in Figure 84, for two different compressed truncated ideal nozzle contours at free shock separation conditions. As can bee seen in the figure a sharp and symmetric separation line is visible in both nozzles. The asymmetrical movement of the separation line and the sudden downstream shift of the separation position during transition from FSS to RSS are clearly visible in Figure 91.
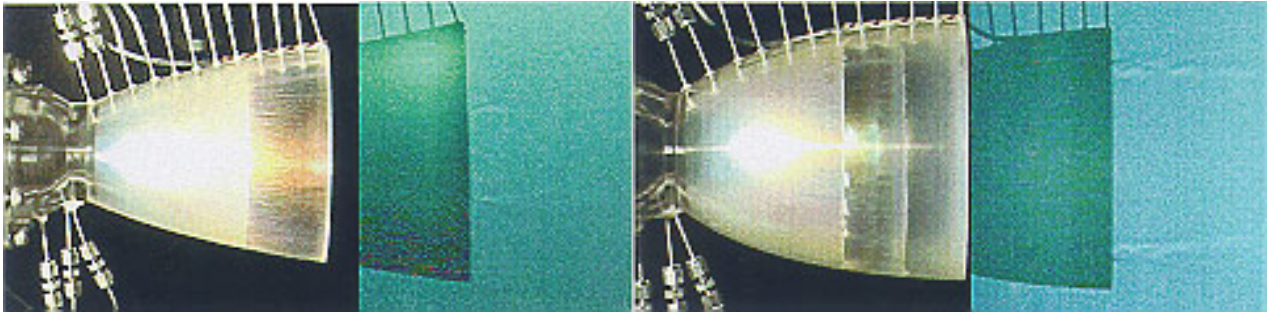
Figure 90. Visualisation of separation line with Shear Sensitive Liquid Crystals (SSLC) and shock visualisation with shadowgraph in the CTP86L (left) and CTP50R5L (right) nozzle by Tomita et al[R 122] (Courtesy of NAL)
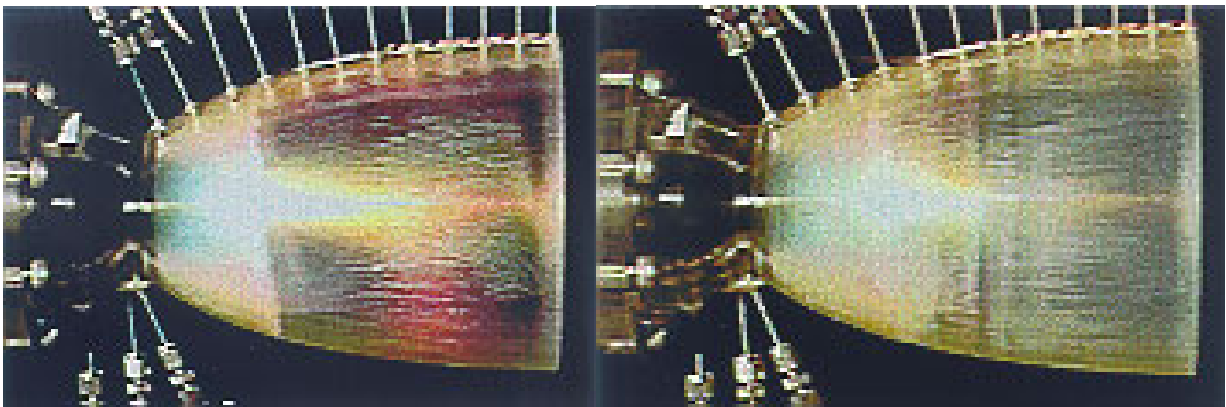
Figure 91. Two instant pictures of the wall shear stress field before (left) and after (right) transition from FSS to RSS in the CTP50R5L nozzle[R 122]. (Courtesy of NAL).

9.4 FLOW VECTOR VISUALISATION OF EXHAUST PLUME FLOW

The simplest method to visualise the flow direction in an exhaust plume is to insert a wire with threads (tufts) into the flow. Figure 92 shows typical experimental results obtained by Stark et al. [R 123] when applying this technique to a TOP nozzle together with a numerical calculation superimposed on the photo. The figure clearly shows the presence of a stable recirculating flow region in the plume by the threads, which are directed upwards. The indicator shows strong fluctuations in the recirculating zone downstream of the nozzle as well as in some outer regions. The movement of the threads is in good agreement with the calculated flow vector field, especially the location of the recirculating flow region at the centre line. The trapped vortex behind the cap shock pattern has been found in several CFD calculations, however, it has been questioned whether the trapped vortex is a numerical artefact or if it really exists in this type of flow. The experiment by Stark et al, Figure 92, is important, as it is the first to validate the existence of a

recirculation region behind the cap shock. At present more detailed analysis of this phenomenon using laser imaging techniques is carried out by various partners in the FSCD group.

Figure 92. Visualisation of flow field in the plume of the DLR TOP nozzle by using threads, experiment by Stark et al. [R 123]. (Courtesy of DLR and ASTRIUM)

10   SCALING CONSIDERATIONS

Model experiments give valuable information for the understanding of physical phenomena in nozzle flow as well as for validation of models for separation and side-load prediction. The main advantages with scaled laboratory experiments compared to full scale testing are that:

- the boundary conditions are more well defined and easier to control and vary
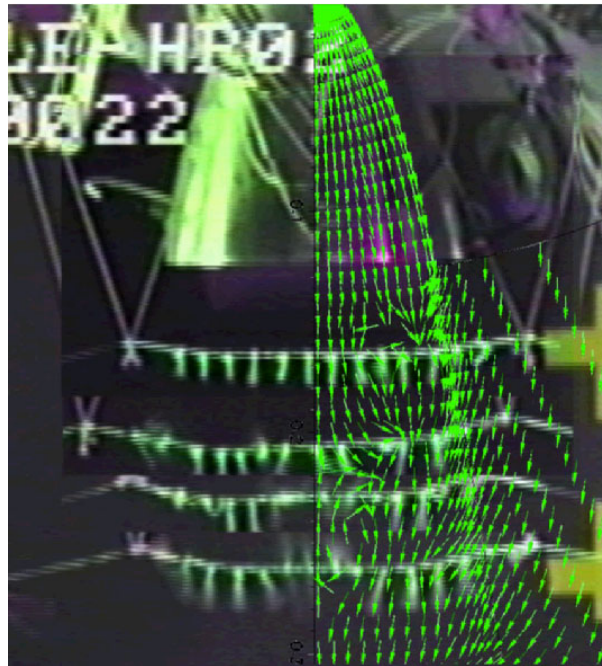
- more sophisticated and accurate measurement techniques can be used and thus more detail information of the examined phenomenon can be extracted

- the model are cheaper to manufacture and instrument

- the cost for the testing is lower

When performing experimental studies in laboratory scale, scaling laws are required to define an experiment, which simulates the actual phenomenon in focus in the full-scale configuration. A complete matching of all parameters between sub-scale and full scale is not always possible, hence a priority must be made and as a consequence the similarity becomes restricted to the most significant parameters for the process studied. In this section we will give some basic ideas of the scaling considerations for the investigation of separation and side-loads in a real rocket nozzle, and in particular the Vulcain nozzle. A more general description of scaling laws for nozzle aerodynamic design can be found in the report by Koppenwallner[R 106]. This report treats similarity and scaling of inviscid and viscid nozzle flow of ideal gases based on stream tube approximation.

10.1   AERODYNAMIC SCALING OF NOZZLE FLOWS WITH IDENTICAL GASES

When gas (mixture ratio of the propellant) and operational condition (total pressure and total temperature) are the same as in the full-scale nozzle, a pure geometrical scaling can be used. In this case, the inviscid variables, such as Mach number, pressure, temperature etc. distributions, will be identical between the scaled nozzle and the original nozzle, i.e.

- $M(x/L_{ref}, r/L_{ref})|_{scaled} = M(x/L_{ref}, r/L_{ref})|_{original}$

- $p/p_0(x/L_{ref}, r/L_{ref})|_{scaled} = p/p_0(x/L_{ref}, r/L_{ref})|_{original}$

- $T/T_0(x/L_{ref}, r/L_{ref})|_{scaled} = T/T_0(x/L_{ref}, r/L_{ref})|_{original}$

where L_{ref} is a reference length, such as e.g. the nozzle length or throat radius.

Parameters containing length, such as Reynolds number and boundary thickness etc., on the other hand, will be reduced proportional to the geometric scaling factor $s = L_{ref}|_{scaled}/L_{ref}|_{original}$. Flow separation is rather insensitive to Reynolds number as long as $Re_\delta > 10^5$ and it is hence important to make sure the subscale Re_δ is in the same range as the full-scale nozzle. In the Vulcain engine the Reynolds number, based on the displacement thickness of the boundary layer, is of order 10^5, i.e. the Reynolds number is high and the flow is turbulent, thus the viscid flow features will not become significant different in a scaled nozzle with e.g. $s=0.1$. This type of sub-scale tests was performed during the development of the Vulcain engine. The test nozzle[R 107] in this case was a complete scale-down of the Vulcain nozzle. As expected the separation characteristics in the scaled nozzle[R 107] showed close agreement with the Vulcain nozzle[R 3]. For instance, the transition of the separation pattern inside the nozzle from FSS to RSS and the transition from RSS to FSS at the exit of the nozzle occurred at the same operation conditions as in the Vulcain nozzle. However, the test and instrumentation cost for this kind of test is high. Further more, the test duration time is usually short due to test rig limitations, restricting the information level. It is therefore necessary to complement with subscale testing in wind tunnels, where testing and instrumentation are less expensive and the test duration time can be significantly increased.

10.2 AERODYNAMIC SCALING OF NOZZLE FLOWS WITH DIFFERENT GASES AND NOZZLE CONTOURS

When changing the working medium, as e.g. from the hot propellant gases in Vulcain with a specific heat ratio varying between $\gamma=1.14\text{-}1.24$ to air with $\gamma=1.4$, no simple scaling law as the one above exists. Using air in a wind tunnel model, a given pressure ratio or Mach number is reached at a smaller area ratio than for Vulcain, and an exact correspondence between the flows can thus not be achieved. Within the flow separation activities at VAC[R 5, R 6] two different attempts were made to scale the Vulcain nozzle for sub-scale testing with air, which resulted in the VOLVO S1 and S3 model nozzles. The idea behind the scaling of these two nozzles and their resulting properties will be discussed below.

10.2.1 Reynolds number similarity

In general viscous and inertial length scales differs, and hence it is impossible to have both an inviscid and viscid similarity. Since the inviscid similarity is more important for the physics of flow separation, the Reynolds numbers was simply chosen to be of the same order of magnitude in the scaled nozzle as in the original nozzle. Based on a characteristic length y, e.g. axial distance or local nozzle diameter, the local Reynolds number along the nozzle can be written as:

$$\mathrm{Re}_{y1} = \frac{\rho_1 V_1 y}{\mu(T_1)}$$

The dynamic vicosity at T_1, $\mu(T_1)$, can be related to $\mu(T_0)$ by a viscosity law, e.g. the law of Sutherland or an exponential law. The local Reynolds number is thus related to the stagnation condition Reynolds number based on throat diameter,

$$\mathrm{Re}_{0d_t} = \frac{\rho_0 a_0 d_t}{\mu(T_0)} = \frac{p_0 d_t}{\sqrt{R_0 T_0}} \frac{\sqrt{\gamma_0}}{\mu(T_0)}$$

by

$$\mathrm{Re}_{y1} = \mathrm{Re}_{0d_t} \cdot \frac{y}{d_t} f(M_1 \text{ and gas properties})$$

The function f is independent of nozzle size and gives the distribution of the local Reynolds number in the nozzle as a function of Mach number and gas properties. Although an identical Mach number distribution can be achieved, the difference in gas properties, in particular γ, makes it impossible to reproduce the Reynolds number distribution in the scaled nozzle. However, using the same stagnation Reynolds number, similar order of magnitude is achieved. A similar argument can be made concerning the similarity of Reynolds number based on boundary layer thickness.

10.2.2 Geometric and dynamic similarity

The effect of changing the working gas is easily demonstrated by the stream tube relations for calorically perfect gases. If we assume an identical Mach number distribution between the original and the scaled nozzle operated with gases with different γ, the Mach number – area ratio formula (Eq. 1) shows that the area ratio must be different in the scaled nozzle:

$$\frac{\varepsilon\left(x/L_{ref}\right)_{sc.}}{\varepsilon\left(x/L_{ref}\right)_{or.}} = \frac{\left[\dfrac{2}{\gamma_{sc.}+1}\left(1+\dfrac{\gamma_{sc.}-1}{2}M\left(x/L_{ref}\right)^2\right)\right]^{\left(\frac{\gamma_{sc.}+1}{2\gamma_{sc.}-2}\right)}}{\left[\dfrac{2}{\gamma_{or.}+1}\left(1+\dfrac{\gamma_{or.}-1}{2}M\left(x/L_{ref}\right)^2\right)\right]^{\left(\frac{\gamma_{or.}+1}{2\gamma_{or.}-2}\right)}}$$

With $\gamma_{or.}=1.2$ in the original nozzle and $\gamma_{sc.}=1.4$ in the scaled nozzle will thus result in a nozzle with a smaller area ratio, as shown in Figure 93.
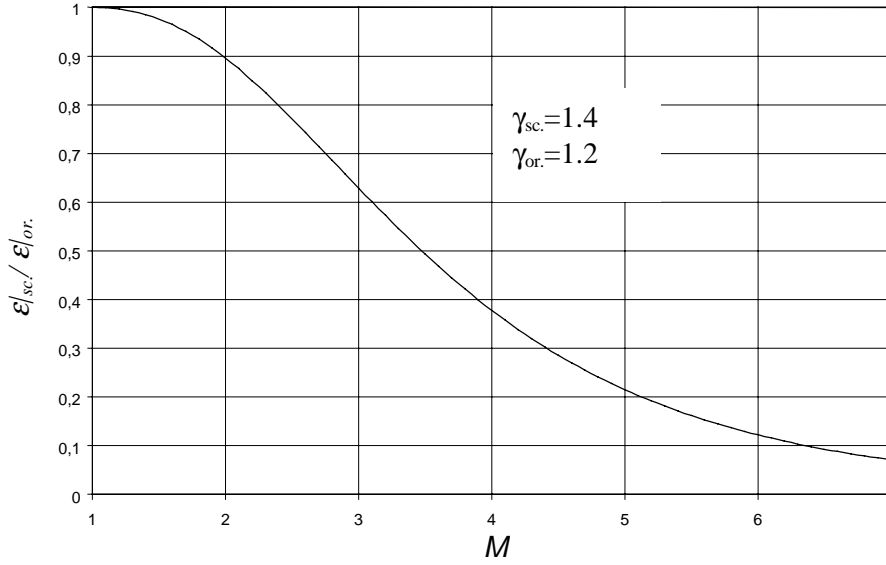

Figure 93. Ratio between scaled and original expansion ratio to keep identical Mach number distribution.

The above equation is only valid for scaling between nozzle flows with constant specific heat ratio. In Vulcain, the scaling relation is actually more complex, since the specific heat ratio varies in the range $\gamma=1.14\text{-}1.24$. Therefore a parametric study of model contours was done varying the values of the different contour variables r_{td}, θ_N, L, r_e, and θ_E (see section 3.5.1), in order to reach a final test nozzle contour that fulfilled the specified similarities.

Since the separation and side-load characteristics differ between different families of contours, the least requirement for geometric similarity is that the model nozzles must be of the same type as the original nozzle. Hence, in order to simulate the flow features in the Vulcain nozzle, the model nozzle should have the same parabolic type of contour as the Vulcain nozzle.

According to the Schmucker criteria[R 94] the separation position is a function of the wall Mach number and the wall pressure, thus we need to achieve a similarity of these distributions in order to model the separation behaviour properly i.e.:

$$M_{wall}\big|_{model} = M_{wall}\big|_{Vulcain}$$

$$\frac{p_{wall}}{p0}\bigg|_{model} = \frac{p_{wall}}{p0}\bigg|_{Vulcain}$$

According to both the Schmucker side load model, see equation 47, and the aeroelastic side load model by Pekkari, see equation 75 and 87, the side load magnitude is further influenced by the local pressure gradient along the wall. The following similarity was therefore considered:

$$\frac{dp_{wall}}{dx}\frac{L_{ref}}{p0}\Bigg|_{model} = \frac{dp_{wall}}{dx}\frac{L_{ref}}{p0}\Bigg|_{Vulcain}$$

Apart from the flow properties along the wall, the internal flow field has a strong influence on the separation and side load characteristics in the nozzle, since the shape and strength of the internal shock emanating from the inflection point of the contour affects FSS to RSS transition. Therefore the entire flow field needs to be correctly modelled, in particular the Mach number distribution i.e.:

$$M(\frac{x}{L_{ref}},\frac{r}{L_{ref}})\Bigg|_{model} = M(\frac{x}{L_{ref}},\frac{r}{L_{ref}})\Bigg|_{Vulcain}$$

The choice of a characteristic length, L_{ref}, is not obvious. The prime candidates are the nozzle exit radius, r_e, and the nozzle throat radius, r_t. Using $L_{ref}=r_e$ the model contour will become closer to the original nozzle contour at the nozzle exit, whereas $L_{ref}=r_t$ results in longer and thus a more slender contour, and the contour similarity will be restricted to the throat region.

10.3   S1 AND S3: TWO WAYS OF SCALING DOWN THE VULCAIN NOZZLE FLOW

Based on the similarity considerations above, a parametric study of different TOP nozzles simulating Vulcain was performed. The resulting dimensions of model nozzles S1 and S3 are given in Table 7 together with the Vulcain dimensions. In Vulcain (ε=45) the averaged exit Mach number is $M_e \approx 5$ and the nozzle length is $L_e=15.7r_t=2.3r_e$. For a nozzle operated with air, Mach 5 is reached with an area ratio of 25 according to stream tube relations, see equation 1. If the exit radius is used as the characteristic length, the length of the model nozzle will then be $L_e=2.3r_e=2.3*\sqrt{25} r_t=11.5 r_t$, while the corresponding length when using the throat radius is $L_e=15.7r_t$, i.e. a much longer and a more slender contour is obtained. The chosen characteristic length, L_{ref}, was the nozzle exit radius, r_e, in sub-scale nozzle S1 and the nozzle throat radius, r_t, in sub-scale nozzle S3. In both cases, similarities of properties along the wall were considered. In addition to this, similarity in the overall flow field and shape of the internal shock was considered in the S3 nozzle.

Nozzle	Vulcain	S1	S3	
Parameter	Value	Value	Value	Dimension
Area ratio (ε)	45	20	18.2	-
Nozzle length (L)	2065.5	350	528.2	mm
Throat diameter (D_t)	262.4	67.08	67.08	mm
Normalised inlet wall radius (r_{td}/r_t)	0.5	0.5	3.0	-
Throat wall angle (θ_N)	35.025	35.025	27.000	°
Nozzle exit angle (θ_E)	6.5	4.0	0.0	°
Nozzle exit diameter (D_E)	1760.2	300.0	286.5	mm
Design feeding pressure ($p0$)	11.0	5.0	5.0	MPa
Design feeding temperature ($T0$)	3500	450	450	K
Feeding gas	LOX/LH2	Air	Air	-

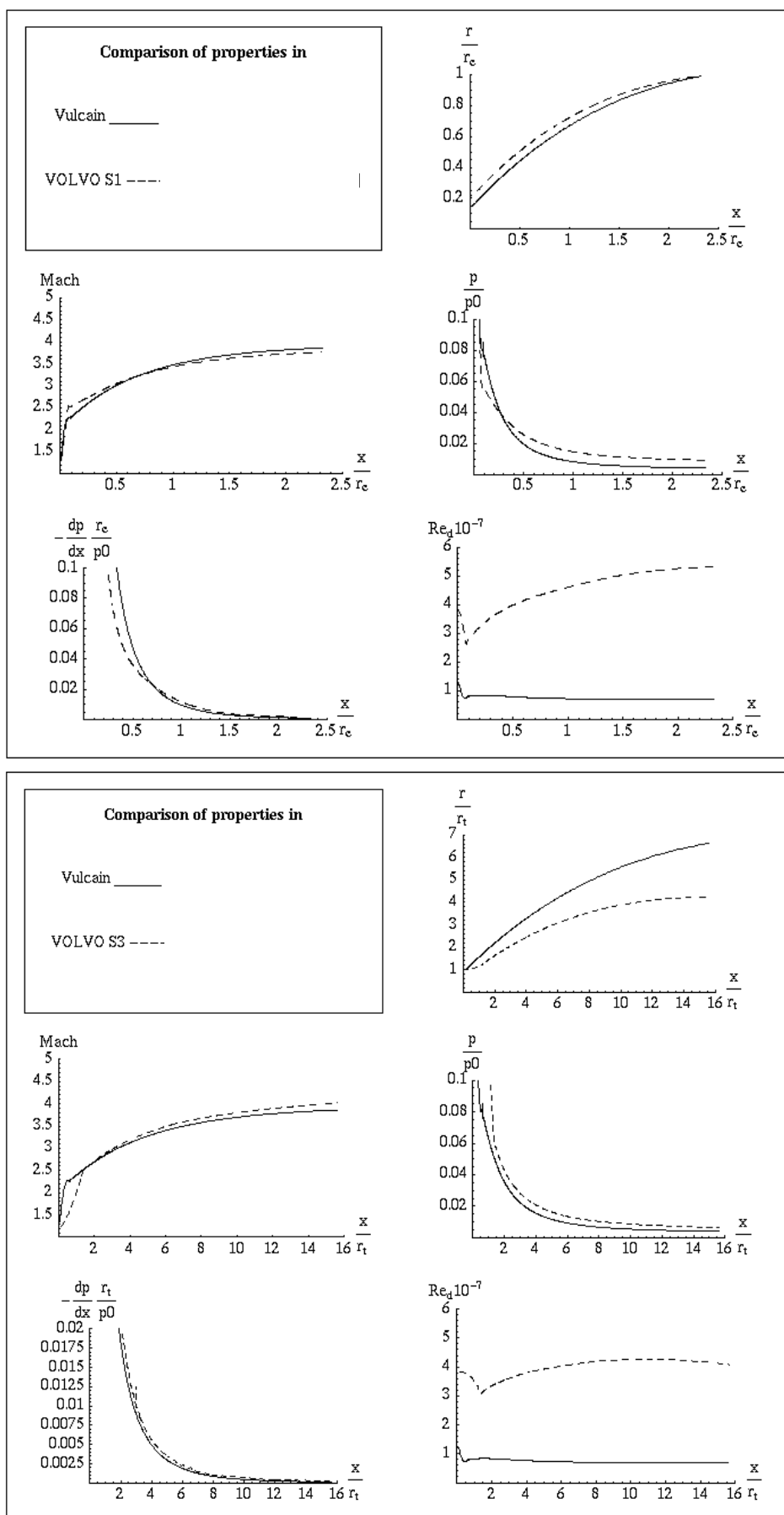Table 7. Main characteristics of the different nozzles.

Figure 94. Comparison of wall properties between Vulcain and model nozzle S1 and S3.

Figure 94-Figure 99, compares the distribution of different geometrical and dynamic quantities. As anticipated, see Figure 94, the S1 nozzle has the same bell like shape as Vulcain, whereas S3 is much more slender. The wall Mach number, wall pressure and pressure gradient of both model nozzles are similar to those in the Vulcain nozzle. We can also see the effect of different initial expansion regions. In S1, the same values of θ_N and r_{td}/r_t were used as in Vulcain. This result in a higher wall Mach number at the end of the initial expansion compared to Vulcain, which is an effect of the higher value of γ in air[**]. In S3, θ_N was reduced, and as a consequence the wall Mach number is somewhat reduced at the end of the initial expansion region compared to the S1.

Comparing the internal Mach number distribution in the different nozzles, shown in Figure 95-Figure 97, we can see that the higher initial expansion in the S1 nozzle together with the relatively short nozzle length cause the kernel to occupy about 70% of the local nozzle cross section at all streamwise positions. As a consequence, the internal shock emanating from the contour inflection point is located closer to the wall compared to Vulcain. The higher wall Mach number at the inflection point and the more drastic turning of the flow will further result in a stronger internal shock in S1 compared to the S3 and Vulcain. Comparing the S3 and Vulcain nozzle flow, it can be seen that the similarity of the kernel flow is better. The radial extension of the kernel is gradually reduced from about 70-80% of local nozzle radius near the throat region to about 30% at the nozzle exit. Note also that the curvature of the Mach number contours is more similar to Vulcain in S4 than in S1, affecting the shock and separation pattern.

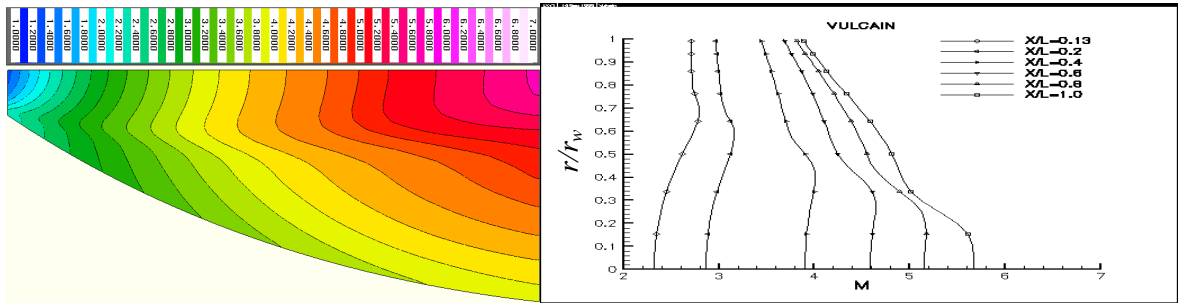Figure 95. Mach number distribution in the Vulcain nozzle, also published in Östlund et al[R 6].
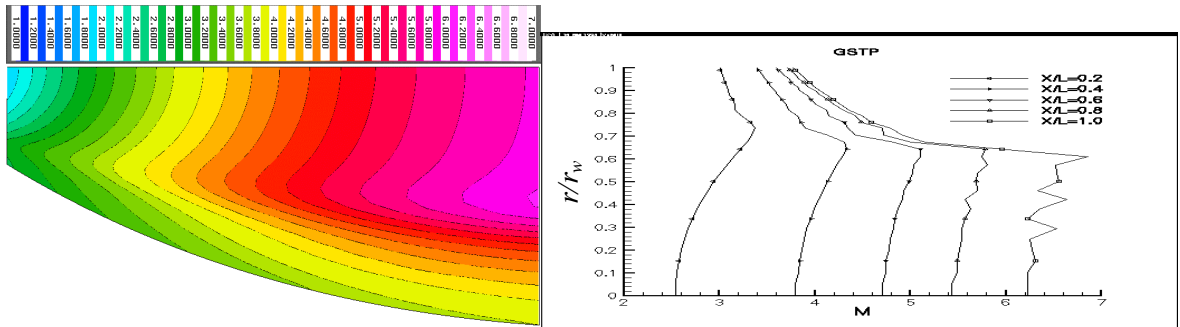

Figure 96. Mach number distribution in Volvo S1 nozzle.

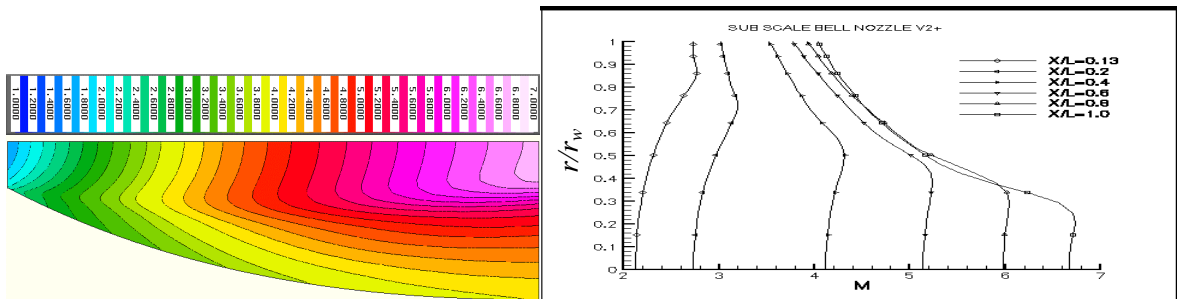Figure 97. Mach number distribution in Volvo S3 nozzle, also published in Östlund et al[R 6].

[**] With increasing γ, a smaller expansion angle is required to reach a specified Mach number as can be seen from the Prandtl-Mayer function.

Figure 94 shows the Reynolds number based on local nozzle diameter, Re_d. It can be seen that Re_d increases monotonically along the wall of both S1 and S3, while it is approximately constant in the Vulcain. As discussed above, this is a problem which is inherent in the scaling of nozzle flows with different gas properties. Moreover, despite there small size, the sub-scale nozzles have a much larger Re_d than Vulcain due to the higher stagnation density for air at reasonable values of the stagnation temperature compared with the hot propellant gases. In the test nozzles the value of the design stagnation temperature was 500 K in order to avoid condensation of the nitrogen when expanding the gas to high Mach numbers and this value was also the limit of the rig where the tests were performed. For a complete matching of the stagnation Reynolds number, the throat radius of the model nozzles would have to be about 0.01 m, however for instrumentation purposes a larger scale size, $r_t \approx 0.03$ m, was chosen. The larger Reynolds number is expected to affect the separation length, L_s/δ^*, with less than 10 percent[††]. The effect of the difference in Reynolds number between the Vulcain and the model nozzles can thus be considered to be small.

The Reynolds number based on the displacement thickness, $Re_{\delta*}$, is shown in Figure 98. The higher levels of $Re_{\delta*}$ for S3 compared with S1 is due to the thicker boundary layer obtained in the much longer S3 nozzle, see Figure 99.
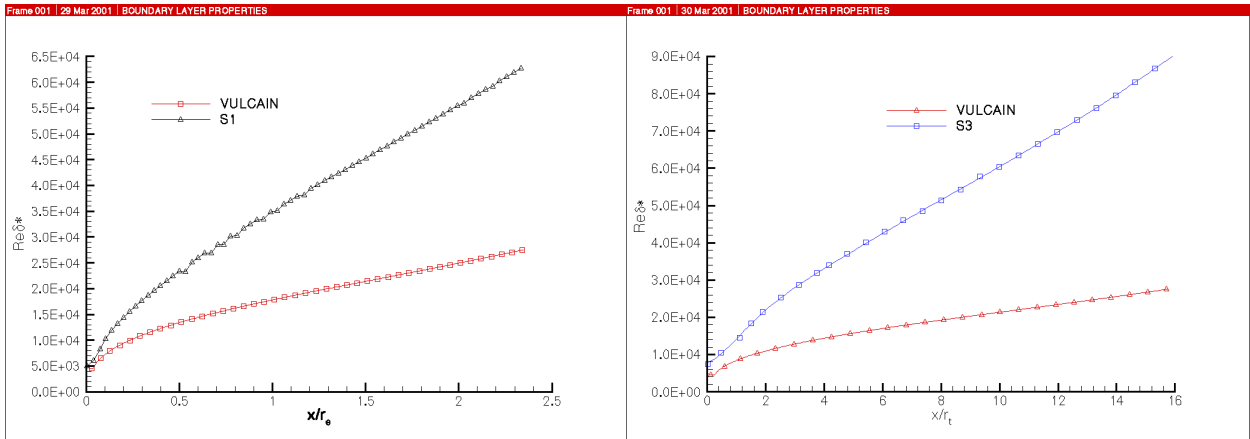
Figure 98. Reynolds number based on displacement thickness in the Vulcain, S1 and S3 nozzle.
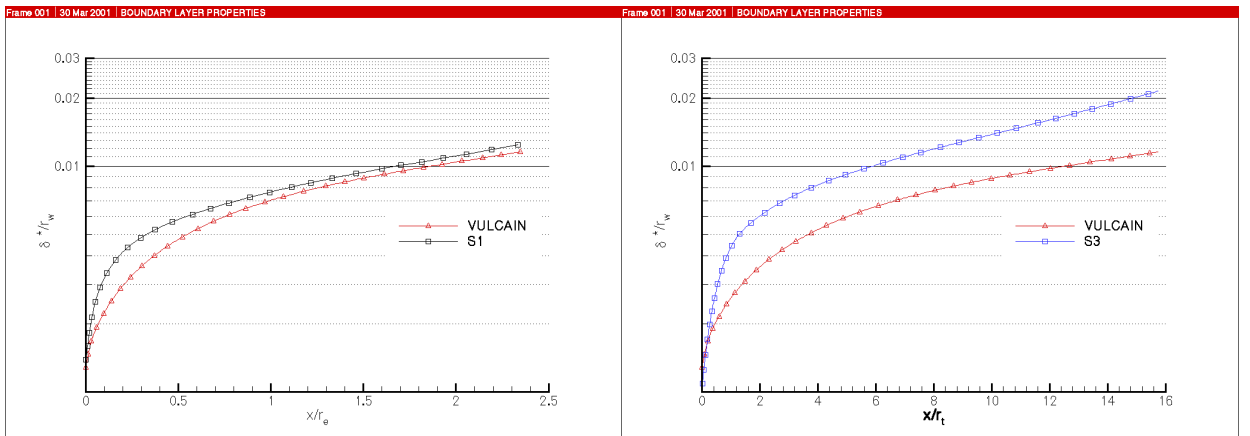
Figure 99. Displacement thickness normalised with wall radius vs. axial distance in the Vulcain, S1 and S3 nozzle.

[††] According to experiments by Spaid and Frishett[R 54], see Figure 29a, a variation of $Re_{\delta i}$ by a factor of 2 results in an increase of L_s/δ_i with less than 10% at a shock angle of 14^0 and $Re_{\delta i} \sim 10^4$. At $Re_{\delta i} > 10^5$ L_s/δ_i is almost constant according to the experiments by Settles[R 40], see Figure 29b.

10.3.1 Experimental verification of the scaling

Figure 100 shows the shock pattern obtained for the model nozzles and Vulcain. As can be seen, the similarity to Vulcain regarding the shock patterns, especially the size of the normal shock, in the over-expanded jet is closer in the S3 nozzle compared to the S1 nozzle. This reflects the good similarity in the overall flow field and shape of the internal shock between S3 and Vulcain.

a)   b)   c)
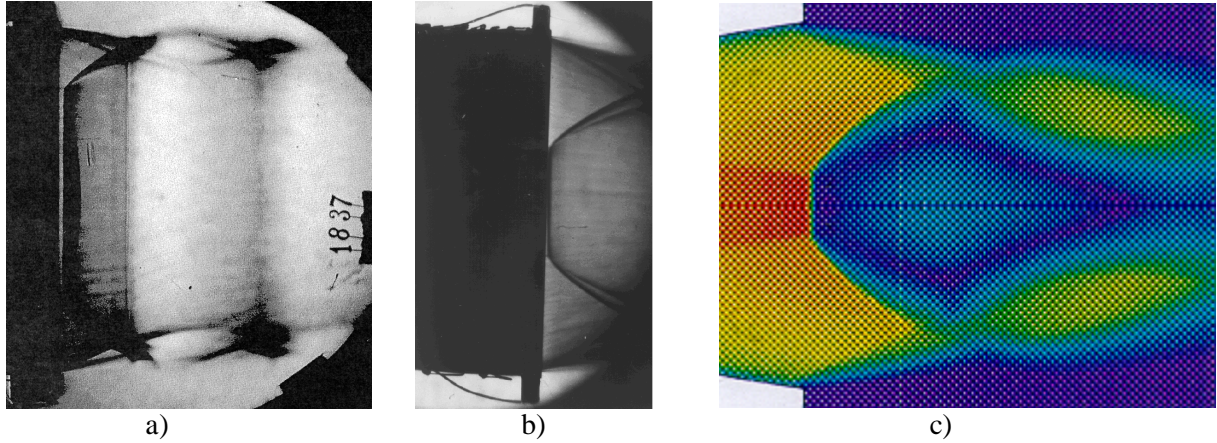
Figure 100. Exhaust plume patterns for the different nozzles, a) Schlieren photo of S1 VAC FFA, b) Schlieren photo of S3 VAC FFA, c) Calculated Mach number field (from blue to red) in the Vulcain nozzle.

Table 8 gives a comparison between the model nozzles and Vulcain regarding separation, side-loads and transition between separation patterns. We recall that S1 was designed with the exit radius as reference length while the throat radius was used for S3. The global separation and side load characteristics in the scaled nozzles, S1 and S3, show close agreement with Vulcain. Both S1 and S3 have the same type of transition phenomenon as Vulcain, one from FSS to RSS inside the nozzle and a second from RSS to FSS at the nozzle exit. These transitions occur almost at the same thrust levels in the model nozzles as in Vulcain. However, when it comes to the location of the incipient separation, x_i, which occurs at the FSS condition before the transition, a large difference between the two models and Vulcain is obtained. The table shows that in the model nozzles x_i is located about 30% upstream of corresponding location in Vulcain. One reason is that the pressure recovery in the recirculating zone at FSS is sensitive to the downstream contour geometry, see Figure 46. This is the case especially in the S3 nozzle, which has a contour shape that looks quite different from Vulcain. In the S1 nozzle the discrepancy is rather due to an earlier transition compared with Vulcain, which is in turn an effect of the difference in the internal flow field between the nozzles. The pressure recovery in RSS on the other hand may be assumed to be less geometry-dependent due to the reattachment and subsequent shock/expansion system.

	$\dfrac{x_i/L_{ref}\big|_{Model}}{x_i/L_{ref}\big|_{Vulcain}}$				$\dfrac{p_{0,transition}/p_{0,nom}\big|_{Model}}{p_{0,transition}/p_{0,nom}\big|_{Vulcain}}$		$\dfrac{M_{SL}/L_{ref}^3\big|_{Model}}{M_{SL}/L_{ref}^3\big|_{Vulcain}}$	
	FSS, before transition		RSS, after transition		FSS→RSS	RSS→FSS		
	$L_{ref}=r_t$	$L_{ref}=r_e$	$L_{ref}=r_t$	$L_{ref}=r_e$			$L_{ref}=r_t$	$L_{ref}=r_e$
S1	(0.45)	0.67	(0.66)	0.99	0.84	0.92	(0.43)	1.47
S3	0.72	(1.13)	0.88	(1.38)	0.94	1.03	0.64	(2.50)
Vulcain	1*	1*	1*	1*	1	1	1	1

Table 8. Comparison of measured quantities between model nozzles and Vulcain. (*=from CFD calculations, x_i=incipient separation point, L_{ref}=reference length, r=radius, t=throat, e=exit, $p_{0,nom}$=nominal stagnation pressure see Table 7 , M_{SL}=side-load tourqe at FSS→RSS transition, values normalised with irrelevant L_{ref} are included within brackets for information)

Table 8 shows that the side-load level (M_{SL}) is about 50% larger in S1 compared to Vulcain, while it is 35% lover than Vulcain in S3. This discrepancy is due to the large difference in contour geometry obtained when scaling Vulcain flow to a nozzle operated with a different gas (γ). This makes the relation between x_i and r_i different in the model nozzles compared to Vulcain, and thus scaling of quantities involving different length parameters can not be expected to be successful, such as the side-load. The sensitivity of M_{SL} to different length scales can be understood by considering the following expression of the FSS to RSS transition side-load (cf. Section 8.1):

$$\vec{M}_{SL} = \int_0^{L_e} \int_0^{2\pi} x \cdot (p_w - p_a)\vec{n}_\perp \, r \, d\varphi \, dx = \int_{x_{i,FSS}}^{x_{i,RSS}} \int_0^{2\pi} x \cdot (p_w - p_a)\vec{n}_\perp \, r \, d\varphi \, dx + \int_{x_{i,RSS}}^{L_e} \int_0^{2\pi} x \cdot (p_w - p_a)\vec{n}_\perp \, r \, d\varphi \, dx$$

The first term is associated with the sudden downstream shift of the separation line during the FSS to RSS transition. The second term is the side-load contribution due to the difference in the wall pressure distribution between the separation patterns downstream of $x=x_{i,RSS}$. Neglecting the second term and approximating the first integral relation by:

$$\int_{x_{i,FSS}}^{x_{i,RSS}} \int_0^{2\pi} x \cdot (p_w - p_a)\vec{n}_\perp \, r \, d\varphi \, dx \sim \left(x_{i,RSS}^2 - x_{i,FSS}^2 \right)\left(r_{i,FSS} + r_{i,RSS} \right)\Delta p$$

we finally get:

$$M_{SL} \propto \left(x_{i,RSS}^2 - x_{i,FSS}^2 \right)\left(r_{i,FSS} + r_{i,RSS} \right)$$

This gives

$$\frac{M_{SL}/L_{ref}^3\big|_{Model}}{M_{SL}/L_{ref}^3\big|_{Vulcain}} \approx \frac{\left(\dfrac{x_{i,RSS}^2 - x_{i,FSS}^2}{L_{ref}^2} \right)_{Model}}{\left(\dfrac{x_{i,RSS}^2 - x_{i,FSS}^2}{L_{ref}^2} \right)_{Vulcain}} \cdot \frac{\left(\dfrac{r_{i,FSS} + r_{i,RSS}}{L_{ref}} \right)_{Model}}{\left(\dfrac{r_{i,FSS} + r_{i,RSS}}{L_{ref}} \right)_{Vulcain}} = C_1 \cdot C_2$$

and with values inserted we obtain:

$$\frac{M_{SL}/r_e^3\big|_{S1}}{M_{SL}/r_e^3\big|_{Vulcain}} \approx 1.54 \cdot 0.95 = 1.5$$

and

$$\frac{M_{SL}/r_t^3\big|_{S3}}{M_{SL}/r_t^3\big|_{Vulcain}} \approx 1.04 \cdot 0.57 = 0.6$$

which corresponds well to the scaled values of measured side-load, M_{SL}, given in Table 8. This also demonstrates that the side-load model described in section 8.1 is basically correct. We can also see that the source of the discrepancy is different for the model nozzles. In the S1 nozzle it emerges from a bad similarity of the separation locations, whereas in the S3 nozzle it comes from lack of similarity in geometrical proportions. One may therefore conclude that it is necessary to use two different length scales instead of only one. As seen in Figure 101, the exit radius, r_e, would be a better choice for the scaling of the nozzle radius.
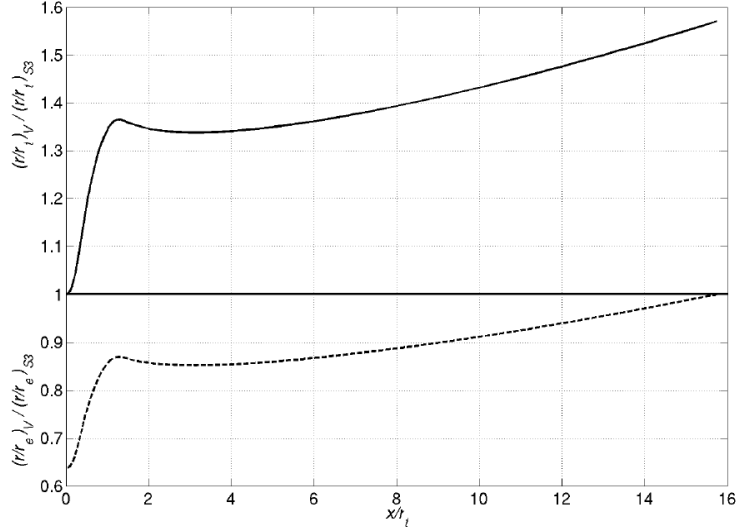
Figure 101. Influence of different reference lengths on the scaling of nozzle radius between the S3 and Vulcain nozzle (top: $L_{ref}=r_t$ and bottom: $L_{ref}=r_e$).

When scaling axial coordinates with r_t and radius with r_e in the simplified expression for the side-load, i.e.:

$$\frac{M_{SL}/\left(r_t^2 r_e\right)\Big|_{Model}}{M_{SL}/\left(r_t^2 r_e\right)\Big|_{Vulcain}} \approx \frac{\left(\dfrac{x_{i,RSS}^2 - x_{i,FSS}^2}{r_t^2}\right)_{Model}}{\left(\dfrac{x_{i,RSS}^2 - x_{i,FSS}^2}{r_t^2}\right)_{Vulcain}} \cdot \frac{\left(\dfrac{r_{i,FSS} + r_{i,RSS}}{r_e}\right)_{Model}}{\left(\dfrac{r_{i,FSS} + r_{i,RSS}}{r_e}\right)_{Vulcain}} = \begin{cases} \left(0.69 \cdot 0.95 = 0.64 \quad for \ S1\right) \\ 1.04 \cdot 0.89 = 0.92 \quad for \ S3 \end{cases}$$

we obtain a much better agreement between S3 and Vulcain. The agreement is even more striking when applying the mixed scaling is applied to the measured side-load:

$$\frac{M_{SL}/\left(r_t^2 r_e\right)\Big|_{Model}}{M_{SL}/\left(r_t^2 r_e\right)\Big|_{Vulcain}} = \begin{cases} \left(0.65 \quad for \ S1\right) \\ 1.01 \quad for \ S3 \end{cases}$$

The results and analysis shown above verify that the used methodology for scaling Vulcain to a sub-scale model operated with air has been successful. Both S1 and S3 have captured the relevant physical phenomenon found in Vulcain. The results from the model tests have been the basis for the understanding of the separation and side-load characteristics. They have, for the first time revealed the transition between the different separation patterns as a basic mechanism behind for side-load generation. It must be kept in mind that the key for a good similarity between a sub-scale and full-scale nozzle is still the design of a representative sub-scale nozzle contour. The S3 nozzle shows a good similarity to Vulcain, because the overall flow field and shape of the internal shock were considered in addition to flow properties along the wall. We have also shown that if this is done, the side-load moment is accurately reproduced by combining the two length scales as $r_t^2 r_e$. The S1 nozzle, however, were only the wall properties were taken into account, is only capable of reproducing the basic separation and side-load phenomena of Vulcain. Attempts to scale the model test results to Vulcain show that no simple generalised relation for scaling of separation location and side-load exists. The scaled results with S3 show good agreement whereas the scaled results with S1 show a large discrepancy. However, the detailed information of the different phenomenon obtained in the model tests has made it possible to develop generalised mathematical descriptions of the processes. With these analytical models the separation location, the transition between FSS and RSS and the corresponding side-load in rocket nozzles very different from the S1, S3 and Vulcain nozzle can be accurately predicted.

11 REYNOLDS-AVERAGED NAVIER-STOKES CALCULATION METHODS

The most common approach for predicting turbulent shock wave boundary layer interactions, including those involving separation, is to solve the Reynolds-averaged Navier-Stokes (RANS) equations. In the following a few problems specific to shock boundary layer interactions and flow separation will be addressed.

11.1 INTERACTIONS IN BASIC CONFIGURATIONS

A critical survey of current numerical prediction capabilities for simulation of laminar and turbulent interactions in basic configurations, such as the single fin, double fin and hollow cylinder flare, were presented by Knight and Degrez[R 140] in 1998. The objective of their study was to determine how well current codes could predict quantities needed in the design of high speed vehicles, including flowfield structure, and mean and fluctuating aerodynamic and thermal loads. They concluded that for laminar flows existing codes accurately predict both aerodynamic and thermal loads. However, the situation for turbulent flows is not as satisfactory. They concluded that mean pressure distribution in 3-D interactions can be computed quite well, with little variation between computations using different turbulence models. On the other hand, skin friction and heat transfer distributions are generally poor, except for weak interactions (no separation), with different turbulence models producing different results. The differences between measured and predicted heat transfer are substantial. Knigh and Degreze note differences up to 100% for strong interactions (separated flow). In 2-D interactions, especially strong ones, the situation is somewhat bleaker. Mean surface pressure distributions are satisfactory only for weak interactions. In strong interactions, the models generally predict too little upstream influence, i.e. the calculated separation length is shorter compared with the one observed in experimental data.

11.2 REALIZABILITY CONSTRAINTS

Much effort has been spent by different researchers on corrections that cure some of the apparent anomalies in RANS simulations of strong interactions. The most common corrections for compressible boundary layers are the realizability, the turbulent length scale limit and the compressibility correction. The first of these is described below.

The mathematical concept of realizability[R 142, R 143] is that the variance of the fluctuating velocity components must be positive and the cross-correlations bounded by the Schwartz inequality. Solutions obtained for strong interactions with common two-equation turbulence models violate this realizability constraint in the outer part of the boundary layer and outside[R 141]. The size of the unrealizable zones increases with the interaction strength and they are clearly related to the largest values of the dimensionless strain rate invariant in the flow, especially across the shocks.

A recent review of realizability correction of two-equation turbulence models[R 144] recalls that the idea is to enforce the realizability constraints by limiting the value of the constant in the definition of the eddy-viscosity $\mu_t = \alpha_v C_\mu \rho k / \omega$ (where $\omega = \varepsilon/k$) as follows:

$$\alpha_v = \min\{1, \bar{\alpha}_v\}$$

where $\bar{\alpha}_v$ is defined by:

$$\frac{1}{\bar{\alpha}_v C_\mu} = A_0 + A_s (s^2 + A_r \bar{\varpi}^2)^{1/2}$$

C_μ is the usual constant 0.09, s is the dimensionless mean strain rate S/ω with $S^2 = 2 S_{ij} S_{ji} - \frac{2}{3} S_{kk}^2$, and ϖ is the dimensionless vorticity invariant $\sqrt{2 \Omega_{ij} \Omega_{ij}} / \omega$ where:

$$S_{ij} = \frac{1}{2}(\frac{\partial U_i}{\partial x_j} + \frac{\partial U_j}{\partial x_i}) \qquad \text{and} \qquad \Omega_{ij} = \frac{1}{2}(\frac{\partial U_i}{\partial x_j} - \frac{\partial U_j}{\partial x_i}) \; .$$

Moore and Moore[R 144] propose a set of constants (i.e. A_0, A_s and A_r) derived from an Algebraic Reynolds Stress Model (A_0=2.85, A_s=1.77) and assumed, in a first approximation, that the strain rate and rotation have symmetrical effects (A_r=0). They show that, in the case of flows near leading edges, where the inviscid strain rate is very large (s=100-400), the modifications ends up with a much better prediction of the level of the turbulent kinetic energy (k_t). Other researchers have proposed other values of the constants, e.g. Durbin[R 145, R 146] proposed a similar correction with A_0=A_r=0 and $1/A_s$=0.29. This gives smaller values of α_v then those obtained by Moore and Moore, but and is virtually identical to those by Coakley[R 147, R 148] or by Menter[R 149] using the SST model, where $1/A_s$=0.3.

The effect of this type of correction is illustrated in Figure 102, showing the pressure, Mach number, turbulent kinetic energy (k_t) and dissipation (ω) distribution in a quasi one-dimensional nozzle, which adapts to the exit condition through a normal shock. The turbulence model used is the Wilcox standard k-ω model, with and without a realizability correction similar to the one proposed by Moore and Moore. Here after we label the standard model without correction as *WI* and the one with correction as *WM* respectively. The pressure and Mach number distribution obtained with the Euler equations are also included in the figure for comparison. As can be seen in the figure, the *WI* model gives an unphysical increase of k_t and ω already in the convergent part of the nozzle, where the flow is accelerated to sonic conditions. In a real case, strong acceleration can lead to relaminarisation of the flow and this trend is captured with the *WM* model. With the *WI* model the production of k_t explodes over the shock, which smears out the shock and affects its predicted position. The *WM* model cures this stagnation point anomaly at the normal shock. With this type of correction the results are generally improved, however, the results are still not satisfactory as will be illustrated in the following example of a nozzle at overexpanded flow conditions.
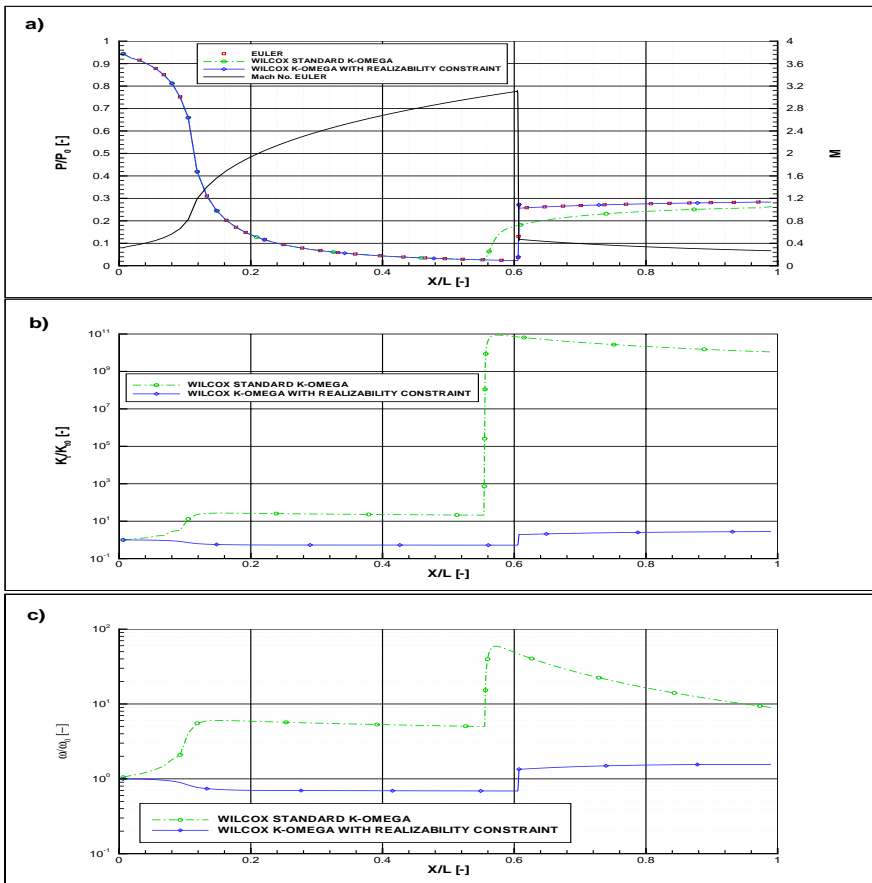

Figure 102. Influence of realizability corrections on a normal shock in a quasi one-dimensional nozzle

11.3 OVEREXPANDED NOZZLE FLOW

11.3.1 Geometry and Mesh

The nozzle studied is the VOLVO S6 nozzle tested in the HYP 500 windtunnel at FOI. The nozzle is an ideal truncated nozzle with design Mach number M_D=5.15 truncated at ε=20.6. The two dimensional axis-symmetric flowfield is discretised by 305x97 cells inside the nozzle with a y^+ value of the first wall cell lower than 1. Outside the nozzle about the same amount of cells are spent additionally. The extension of the ambient region in axial direction is around 85 throat radii and 75 in the radial direction. The grid distribution in the axial direction is increased in two zones, one over the separation shock and the other over the Mach disc. The position of these regions is adjusted to different operation conditions, as the separation shock and the Mach disc moves further downstream when the pressure ratio p_0/p_a is increased. A typical grid is shown in Figure 103 for an operational condition where the separation shock and the Mach disc are both located near the nozzle exit region. The solutions were checked for grid independence for all operational conditions examined.
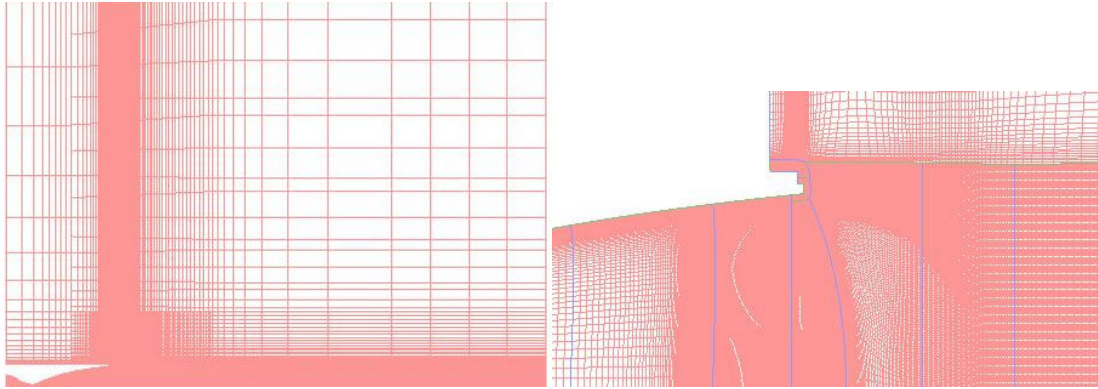

Figure 103. Grid distribution in VolvoS6, the whole mesh domain (left) and a close up of nozzle exit lip (right).

11.3.2 Computational model

The Volvo finite volume multi block structured grid RANS code VolSol is used to obtain steady state solutions. The numerical method used is an explicit third order Runga-Kutta time marching method using a local time-step. The mean flow convective flux is calculated with a third order accurate upwind-biased scheme. The same scheme with a TVD limiter is used for the turbulent convective flux. Viscous terms are discretized with a compact second order scheme. The effects of turbulence are incorporated through the eddy viscosity assumption and the turbulent Prandtl number Pr_t=0.9. The turbulence model used to determine the turbulent eddy viscosity is the Menter[R 149] SST two-equation model. The working fluid is air, modelled as a calorically perfect gas with the gas constant R=287.2 $J/(kgK)$ and an isentropic coefficient of γ=1.4 and Prandtl number Pr=0.72. The molecular viscosity is computed from Sutherlands law for air. A pressure boundary condition is used for all inflow and outflow boundaries, and a condition of T_a=288 K and p_a=1 bar is applied at the ambient boundaries. The stagnation conditions prescribed at the nozzle inlet were the ones obtained at the different operational conditions in the tests, i.e. T_0=450-500 K and p_0=10-70 bar. An adiabatic wall with a low Reynolds formulation is applied to the internal nozzle wall. At the external wall surfaces of the nozzle slip conditions (Euler walls) are applied. The computations were performed at Volvo Aero Corporation and more details of the numerical method and this specific simulation can be found in reference R 150-R 152.

11.3.3 Comparison of computations with experiment

Figure 104 shows calculated and measured wall pressure profiles are shown for three different operational conditions, p_0/p_a=10, 20 and 70 respectively. As can be seen, the predicted incipient separation point, i.e. the first deviation from the pressure profile obtained with attached flow condition, occurs upstream of the

measured one for all operation conditions. The incipient separation position predicted for the p_0/p_a=10 case is closest to the experimental data and as p_0/p_a increases the discrepancy increases, to finally become significant for the p_0/p_a=70 case. In all cases the predicted separation length is shorter than observed in the test data, which gives a steeper pressure rise in the separation region compared with experimental values.

The misprediction of the location of incipient separation point at high-pressure ratios also influences the predicted position of the Mach disc. Figure 105 shows the calculated Mach number distribution at p_0/p_a=55 and in Figure 106 the predicted shock system is compared with a schlieren image obtained for VOLVO S6 at the same operational condition. It can be seen that the Mach disc obtained in the simulation is located to far upstream compared with the test data. It is not clear if it is only the separation line that drives the location of the Mach disc or if other factors are involved.
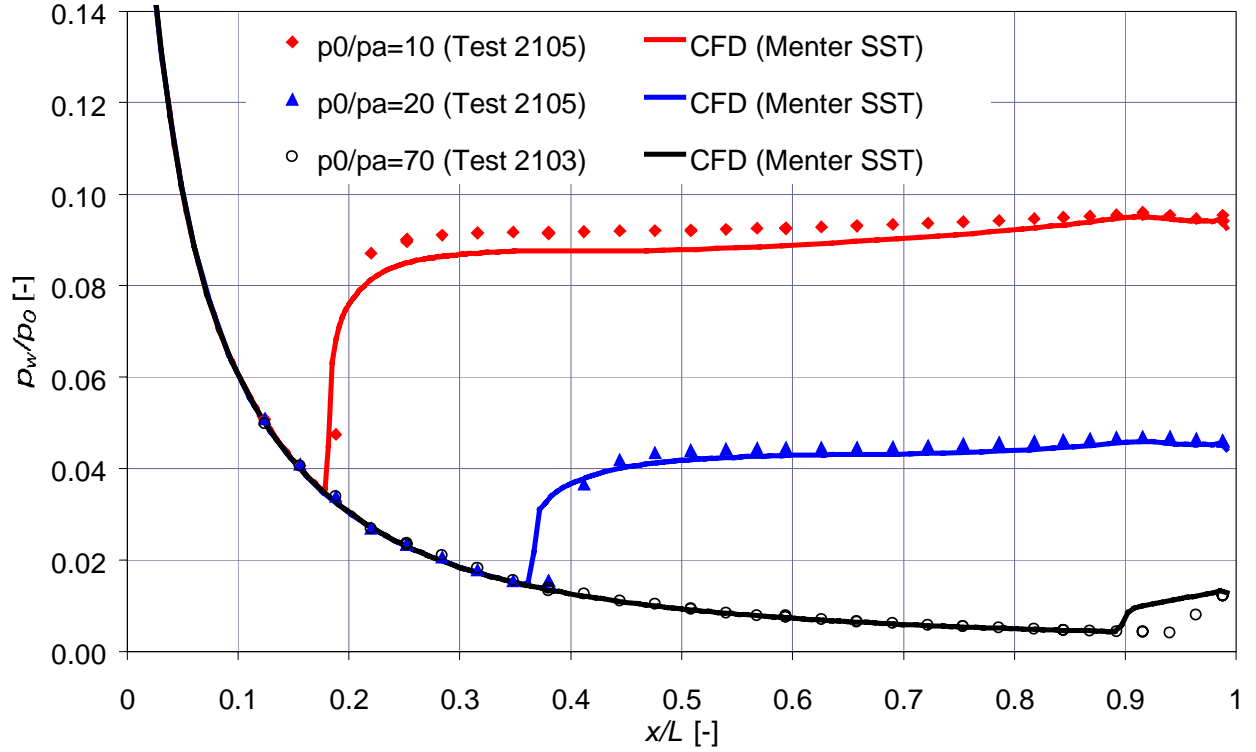

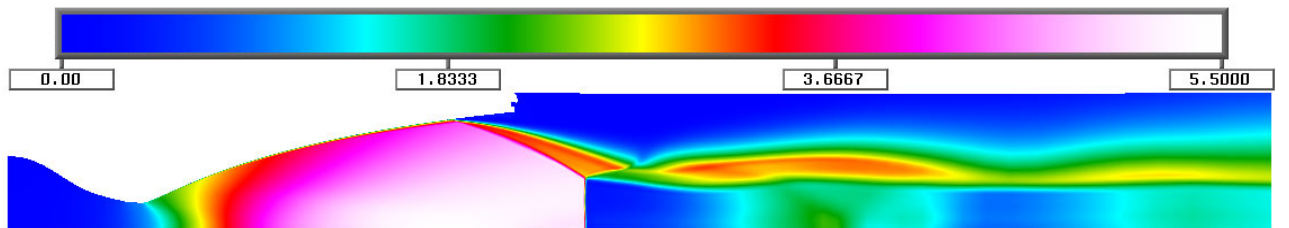Figure 104. Wall pressure in the VOLVO S6 nozzle, comparison between Menter SST and test data.

Figure 105. Mach number distribution in the VOLVO S6 nozzle at p_0/p_a=55.
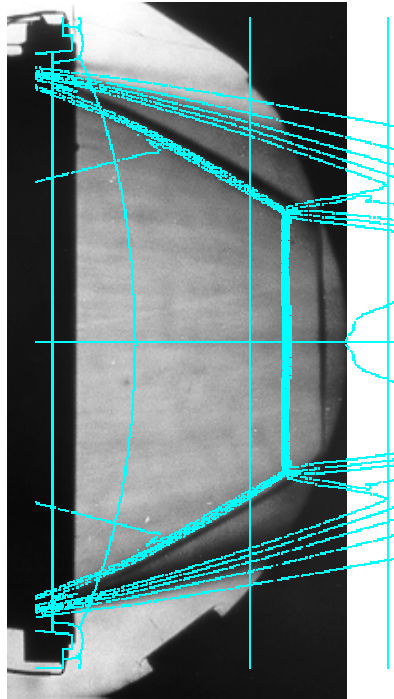
Figure 106 Comparison of shock system position at p_0/p_a=55. The simulated value is compared to a Schlieren photo from the test.

The coefficients in the realizability constraint used in the Menter SST model is $A_0=A_r=0$ and $A_s=10/3$. Since researchers have proposed different values, it was necessary to assess the influence of A_s on the computed flow field. Such a study was performed[R 152], where A_s was varied within the range 1/3-10/3, and lead to the conclusions that when A_s is reduced the incipient separation point and corresponding shock system is moved further downstream and the opposite happens if it is increased. Thus by adjusting A_s, a better prediction can be obtained at high-pressure ratios, however, this will instead cause increased discrepancies at low pressure ratios. On the whole, the procedure of adjusting turbulence model parameters "on hand" is not satisfying, since it is somewhat arbitrary and does not guarantee adequate results for new types of flow fields.

It is clear from the above that the current capability to predict critical quantities for design of applications featuring strong shock wave boundary layer interactions is not satisfactory. One of the drawbacks is that the eddy-viscosity models use a single length scale to represent the turbulence, which is insufficient in separated flow. Secondly RANS calculations do not model flowfield unsteadiness. As noted earlier (see section 5.2.4 and especially Figure 34) the global flowfield unsteadiness is such a dominant feature in this type of flow, and that without modelling it, not even mean quantities can be computed accurately.

To address these deficiencies Knight and Degrez recommend the development of Large Eddy Simulation (LES) solvers. Unlike Direct Numerical Simulation (DNS) in which all scales of motion that contains significant energy are resolved. LES attempts "to resolve the eddies that are large enough to contain information about the geometry and dynamics of the specific problem under investigation and to regard all structures on a smaller scale as universal following the viewpoint of Kolmogorov" (Ghosal, 1999)[R 153]. In that sense LES occupy the middle ground between RANS methods (which are relatively cheap computationally) and DNS, which is presently prohibitively expensive, if not impossible, for most aerospace applications. However, from an engineering perspective, it is questionable whether LES or its variants will ever become design tools. Jameson[R 154] notes that it is unlikely that designers will ever "need to know the details of the eddies in the boundary layer". But he also argues that it is possible that LES may provide "an improved insight into the physics of turbulent flow, which may in turn lead to the development of more comprehensive and reliable turbulence models", which in turn would improve RANS based modelling. From the recent literature[R 155-R 157] it is evident that some very interesting work is now being done in LES and variants of LES. Additionally there is reason to hope that innovative approaches will evolve, which will solve existing problems and address the new ones, which will undoubtedly arise as LES is applied to higher Mach number flows.

12 SUMMARY AND CONCLUSIONS

The concern of the present work is to model flow separation and separation-induced side-loads in rocket engine nozzles. The aim is to prevent flow separation at design condition, or to predict the position of flow separation and the ensuing side-loads at overexpanded flow conditions. Different types of traditional bell-shaped nozzles exist, each producing their own specific internal flow field. The TIC nozzle is the only nozzle type that produces a shock free flow, whereas with other nozzle contours, such as the conical, CTIC, TOC, TOP or directly optimised nozzles, an internal shock is formed inside the nozzle as shown in Figure 3. The contour type also determines the flow pattern that can be observed in the exhaust plume. Basic patterns that can be observed are the classical Mach disk, the apparent regular reflection, and the cap-shock pattern, which are all shown in Figure 21-Figure 22. The latter is only observed for nozzles featuring an internal shock that exits the nozzle and is then reflected at the centreline. In a nozzle operating with separated flow, there can be two different separation patterns, the free shock separation (FSS) and restricted shock separation (RSS), see Figure 37-Figure 38. The cap shock pattern is a driver for a transition of the flow from FSS to RSS, and hence the RSS pattern exists only in nozzles that produce a cap-shock. Transitions between FSS and RSS and vice versa are the origin of side-load peaks, characterised by their high level and impulsive occurrence. As a consequence, the separation and side-load characteristics are radically different for different contour families, and hence the choice of contour type an essential for the mechanical load picture. This is of particular importance for first-stage nozzles, since they are started and partly operated at high ambient pressure. For upper-stage engines, the choice of contour is of minor importance, since in that case there is no considerable flow separation at start up, unless they are used for stage separation.

12.1 NOZZLE FLOWS WITH FREE SHOCK SEPARARATION (FSS)

12.1.1 Flow separation prediction

All nozzle types display FSS as long as the pressure difference between the combustion chamber and the ambient is still low and the separation is located well inside the nozzle. In this case, the separation position is predicted on the basis of models for the pressure rise from attached flow wall pressure to ambient pressure. Various simplified models of this kind have been published in literature, and show qualitative agreement with experimental data. However, to achieve a higher accuracy in quantitative prediction, two different physical phenomena associated must be de-coupled, namely (i) the pressure increase due to the shock wave boundary layer interaction, and (ii) the pressure recovery associated with the recirculating flow in the separated region.

For the first of these, the shock wave boundary layer interaction phenomenon, the present thesis suggests a new criterion based on the generalised free interaction theory by Carrière et al[R 111]. With this criterion the start of the interaction region as well as the pressure distribution and the corresponding length of the intermittent zone can be predicted in a nozzle at a given operation condition and a prescribed plateau pressure. A correct value of the interaction length is essential, since it is one of the main elements in FSS side-load models. The results look encouraging when comparing to sub-scale test data, however more effort are needed before a reliable and accurate criterion can be established for real rocket nozzles. Especially, the applicability to chemically reacting flow cases, where the value of the specific heat ratio is different compared to air, needs to be validated. The influence of wall cooling is another topic, which needs to be investigated in detail. VOLVO, ASTRIUM and DLR are currently preparing a test campaign in order to shad light on these open ends. Further, this criterion must be coupled with an accurate model describing the pressure rise in the recirculating zone. Today, a constant value of the plateau pressure is often used, based on test data experience. This approach works quite well for flow separation far from the nozzle exit whereas the discrepancy increases with decreasing distance to the nozzle exit. Thus, for accurate prediction of the separation location, models for the pressure rise in the recirculating zone in contoured nozzles operated with hot propellants needs to be developed. A possible semi-empirical approach to construct such a model on is Abramovich's theory for the mixing of counterflowing compressible turbulent jets[R 116].

12.1.2 Side-load prediction

Experiments on basic interactions have shown that the shock wave boundary layer interaction is an intermittent and 3-dimensional phenomenon. Mechanical structures exposed to this type of supersonic flow separation will be affected by large, time-dependent forces, which can be resolved into two components, a low frequency buffeting caused by changes in the geometry of the separation region, and high frequency fluctuations originating from the shear layer of the separated region. In the Schmucker model these geometry changes of the separation region are modelled in a quasi-static manner as a tilted separation line, i.e. as asymmetric pressure distribution acting over an effective area. The logic of the Schmucker model construction is in that sense correct. However, the physical treatments of some elements in the model are incorrect, e.g. the interaction length, which has no coupling to the incoming boundary layer properties at all and is not influenced by changes of the geometry downstream of the separation region. Apart from the Schmucker model, a number of other side-load models based on the tilted separation line approach can be found in the literature, which differ from the Schmucker model regarding both physical and logical bases, however their usefulness is questionable.

The oscillation of the separation line and pressure pulsation in the separated flow region is also the basis of the Dumnov side-load model. In contrast to Schmucker, however, Dumnov uses experimentally determined wall pressure fluctuations and their inter-correlation to construct a generalised pressure fluctuation function from which the side-load level is estimated. According to Dumnov, the accuracy of the model is within 20%. Magnitude of the experimentally determined pressure fluctuation function is normalised with $U/\sigma_p^2 \theta_i$, however, no information is given concerning frequency scaling. This together with the lack of experimental data in the paper by Dumnov make it impossible reproduce the model or estimate how general the obtained spectrum actually is. However, it is encouraging to note that there appears to exist some universal features for pressure fluctuations in the separation region, for instance Gonsalez and Dolling[R 118] showed that the spectra in the intermittent region, generated by different diameter cylinders, collapsing when plotting the magnitude $W_p(f) \cdot f/\sigma_p^2$ versus a reduced frequency given as $f L_s/U_i$. A comparison of intermittent power spectra for different basic flow cases[R 58, R 61, R 63, R 64] was made in the present work, which showed that the low frequency pressure fluctuations are characterised by a Strouhal number of 0.07 based on the interaction length and the incoming free stream velocity. This indicates that the intermittent motion of the separation line is a generalised feature, common for various types of shock boundary layer interactions.

Other key elements in the Dumnov approach were investigated in the present work by applying the model on data obtained in tests with the LEA TIC nozzle by Girard and Alziary[R 117]. Dumnov describes the intermittence by assuming a sinusoidal fluctuation between the two-pressure levels p_i and p_p. The present analysis shows that this is an oversimplification, which overpredicts the average fluctuation level in the intermittent region. An accurate and physically more correct method is proposed inhere, based on the work by Kistler[R 63] on external flow protuberances. In contrast to the Dumnov model, which only gives one constant value of the pressure fluctuation, $\sigma p'$, throughout the interaction region, the Kistler approach renders the streamwise evolution of $\sigma p'$. This is done by defining an intermittence factor, which gives the fraction of time that the plateau pressure region is acting over the point of interest. According to Erengil and Dolling[R 61] the error function shows a good fit to the intermittence factor, which means that the location of the separation shock has a Gaussian distribution within the intermittent region. This method was applied to the LEA TIC nozzle flow and shows a close agreement with test data.

On the whole, the basic idea of the Dumnov model constitutes a valid approach, which is supported by the present analysis. The correction and improvements suggested will contribute to the quantitative prediction of side-loads. The development and validation work of such improved models is currently ongoing at the different partners of the FSCD group, see e.g. the work by Volvo Aero in reference R 108.

In general it can be said that appropriate parameters for normalising power spectra in the intermittent region still requires more work. In general reliable quantitative data on the structures and pressure fluctuations in the transverse direction are lacking and is fruitful area of future work.

12.2 NOZZLES WITH TRANSITION OF SEPARATION PATTERN

12.2.1 Observations in tests

It was observed already in the early 1970's by Nave and Coffey[R 95] that a transition in separation pattern from the free-shock separation (FSS) to the restricted shock separation (RSS) and vice-versa might occur. However, it was not understood that these transitions also are the origin of two distinct side-load peaks, until Östlund[R 5] et al presented the detailed analysis of the VOLVO S1 nozzle flow. Östlund observed that when the flow reattaches and the separated region becomes enclosed by supersonic flow it is a sudden pressure drop of the plateau pressure and a subsequent jump of the separation point in the downstream direction. This transition is unsteady and asymmetrical, the reattachment of the flow occurs successively by occupying more and more of the nozzle wall, until the entire flow is reattached, i.e. the RSS condition prevails with a wall pressure distribution totally different from the one obtained at the previous FSS condition. When the reattachment point is close the nozzle exit, the flow begins to pulsate. The reason for this is the sudden increase in the plateau pressure behind the separation shock, which occurs when the former enclosed recirculating zone is opened up and ambient air is sucked in to the nozzle. This increase in pressure, forces the separation point to move upstream again, once more closing the recirculating zone. The procedure repeats itself until the increase of the feeding pressure is sufficient to move the reattachment zone out of the nozzle. This is known as the "end effect". Östlund was able to correlate the occurrence of two distinct side-load peaks observed in test to the FSS-RSS transition and to the end effect respectively.

The observations and conclusions by Östlund[R 5] were the ignition for intensive research both within and outside Europe. Further sub scale experiments performed within different FSCD test campaigns[R 6-R 8] as well as recent Japanese experiments[R 122] confirm the transition mechanism for TOP and CTIC nozzles, both featuring an internal shock. In addition, full-scale engine tests for the Vulcain 1 engine have confirmed this mechanism as key driver during both start-up and shut-down[R 4].

12.2.2 Models for prediction

Stimulated by the test results, flow separation and side-load models for the transition from free- to restricted shock separation and vice versa have recently been developed within the European space community. A high accuracy have been achieved (6%) in matching model and experimental results. The key for this successful result is to predict the location where the transition takes place. The driving force for reattachment of the flow is when the radial momentum of the separated jet is directed towards the wall, which occurs only with a cap-shock pattern. By quantifying the momentum balance of the jet, the transition point can be determined.

On this basis, Östlund & Bigert[R 6] simultaneously with Frey & Hagemann[R 3] proposed criteria for the prediction of transition from FSS to RSS. Both models account for the sudden pressure drop of the plateau pressure and the subsequent jump of the separation point when the flow reattaches and the separated region becomes enclosed by supersonic flow. Due to the complexity of the flow downstream of the reattachment point, which is characterised by subsequent compression and expansion waves, no models for this pressure recovery process exist so far. Instead a constant value of the plateau pressure based on test data experience is often used. This value is assumed to be constant until the RSS is transformed back into FSS and FSS criteria are applicable again. This transformation occurs either when the cap-shock is converted into the Mach disc or when the enclosed separation zone is opened up at the nozzle exit.

Based on these separation models ASTRIUM/DLR[R 4] and VOLVO[R 6] have developed side-load models by assuming that the initial transition from free- to restricted shock separation is the key side-load driver in TOP and CTIC rocket nozzles. The basic idea is that at the instant of transition a maximum side-load is expected if one half of the nozzle features FSS-, while the other half shows already RSS flow condition. For this case, the side-load calculation is squarely based on physical reasoning namely from a momentum balance across the complete nozzle surface. With this model the maximum aerodynamic side-load can be calculated.

12.3   AEROELASTIC EFFECTS

In highly aeroelastic cases a significant amplification of the side-loads can be obtained as the flow interacts with the mechanical structure. The study of aeroelastic effects in separated nozzle flows is rather complex, requiring dynamic models of the mechanical nozzle-engine support system, the flow separation, as well as the coupling between these two. A simple technique for handling these difficult coupling problems was proposed by Pekkari[R 102,R 103] in the early 1990's. The model consists of two main parts, the first dealing with the equation of motions of the thrust chamber as aerodynamic loads are applied, and a second part modelling the change of the aerodynamic loads due to the distortion of the wall contour. The wall pressure in the attached region is the nominal vacuum pressure profile with a pressure shift due to the displacement of the wall. In the original work by Pekkari, this pressure shift is determined with the use of linearised supersonic flow theory. However, experience has shown that this theory significantly overpredicts the pressure shift, and Östlund[R 108] therefore proposed a modified approach where the pressure shift is extracted from 3D Euler simulations. The separation line in the nozzle is assessed with a simple separation criterion of Summerfield type (cf. Eq.28). The wall pressure in the separated region is assumed to be equal to the ambient pressure. This model predicts the aeroelastic stability, the modification of eigenfrequencies due to aeroelastic effects, as well as the transient behaviour during start up and shutdown of the nozzle. Different mechanical eigenmodes can be treated, however, from side-load point of view, the aeroelastic behaviour of the bending mode is the most relevant one. To verify this improved model a unique test set-up was designed by Östlund within the GSTP FSC test program.[R 5] In order to resemble the bending mode of a real rocket engine nozzle, the model nozzle was flexible hinged at the nozzle throat, where the bending resistance could be changed with the use of exchangeable torsion springs. Thanks to the simple test set-up, the mechanical system could be described analytically (in contrast to real rocket engine cases, which must relay on complex FEM analysis) and the basic model assumptions could be verified separately. With these tests the model by Östlund was successfully verified. It was found that the method was able to reproduce the aeroelastic behaviour experienced in the VOLVO S1 and S6 nozzle tests and it was also shown that aeroelastic effects can be significant in week nozzle structures.

12.4   SCALING

Model experiments are necessary for the understanding of physical phenomena in nozzle flow as well as for validation of models for separation and side-load prediction. Such model experiments can only be successful if the designed sub-scale model is able to capture the most relevant physics of the full-scale rocket nozzle. The main challenge is to reproduce the behaviour of the chemical reacting hot propellants using air with totally different gas properties. Some basic ideas of the scaling considerations for the investigation of separation and side-loads in a real rocket nozzle has been presented in this thesis. The feasibility of two different scaling approaches has been examined by designing and testing two different sub-scale models, S1 and S3, of the Vulcain nozzle. In both cases, similarities of properties along the wall were considered. In addition to this, similarity in the overall flow field and shape of the internal shock was considered in the S3 nozzle. The chosen characteristic length was the nozzle exit radius, r_e, in sub-scale nozzle S1and the nozzle throat radius, r_t, in sub-scale nozzle S3. The results and analysis of the scaling verify that the methodology used for scaling Vulcain to a sub-scale model operated with air has been successful. Both S1 and S3 have captured the relevant physical phenomenon found in Vulcain, especially the transition between FSS and RSS and vice versa and ensuing side-loads. The results from the model tests have been the basis for the understanding of the separation and side-load characteristics in TOP nozzles. They have, for the first time, revealed the transition between the different separation patterns as a basic mechanism behind for side-load generation. It must be kept in mind that the key for a good similarity between a sub-scale and full-scale nozzle is still the design of a representative sub-scale nozzle contour. The S3 nozzle shows a good similarity to Vulcain, since it reproduces the overall flow field and shape of the internal shock, in addition to flow properties along the wall. With this approach the side-load moment is accurately reproduced by combining the two length scales as $r_t^2 r_e$. The S1 nozzle, however, were only the wall properties were taken into account, is only capable of reproducing the basic separation and side-load phenomena of Vulcain.

13   REFERENCES

R 1   Moelder, A., Gluamhussein, A., Timofeev, E., and Voinovich, P.,'' Focusing of Conical Shocks at the Centreline of Symmetry'', Paper 5601, Proceedings of the 21st International Symposium on Shock Waves, Great Keppel Island, Australia, July 1997

R 2   Frey, M. and Hagemann, G., ''Status of Flow Separation Prediction in Rocket Nozzles'', AIAA 98-3619, 1998

R 3   Frey, M. and Hagemann, G., ''Flow Separation and Side-Loads in Rocket Nozzles'', AIAA 99-2815, 1999

R 4   Terhardt, M., Hagemann, G., and Frey, M., ''Flow Separation and Side-Load Behaviour of the Vulcain Engine'', AIAA 99-2762, 1999

R 5   Mattsson, J. (changed name to Östlund 1999), Högman, U., and Torngren, L., ''A Sub-Scale Test Programme on Investigation of Flow Separation and Side-Loads in Rocket Nozzles'', Proceedings of the 3rd European Symposium on Aerothermodynamics of Space Vehicles, ESA-ESTEC, Netherlands, November 24-26, 1998

R 6   Östlund J., Bigert M., ''A Subscale Investigation on Side-Loads in Sea Level Rocket Nozzles'', AIAA 99-2759, June 1999

R 7   Reijasse, P.,Servel, P., and Hallard, R., ''Synthesis of the 1998-1999 ONERA Works in the FSCD Working Group'', ONERA RTS 49/4361 DAFE/Y, December 1999

R 8   Frey, M., Stark, R., and Ciezki, H., ''Subscale Nozzle Testing at the P6.2 Test Stand'', AIAA paper, to be published at the 36th Joint Propulsion Conference, July 2000

R 9   Hagemann, G., Immich. H., Dumnov, G., and Nguyen, Th., ''Advanced Rocket Nozzles'', Journal of Power and Propulsion, Vol. 14, No. 5, September – October 1998

R 10   Oates, G. C., " Aerothermodynamics of Gas Turbine and Rocket Propulsion", New York, AIAA, 1984

R 11   Shapiro A. H., " The Dynamics and Thermodynamics of Compressible Fluid Flow, Vol I, The Ronald Press Co., New York, 1953.

R 12   Frey, H. M. , Nickerson G. R. "TDK –Two Dimensional Kinetic Reference Program", SEA Inc. NAS8-36863,1989.

R 13   Malina, F. J., "Characteristics of the Rocket Motor Based on the Theory of Perfect Gases", J. Frankling Inst., Vol. 230, 1940, pp. 433-454.

R 14   Guderley G., Hantsch E., "Beste Formen für Achsensymmetrische Überschallschubdüsen", Zeitschrift für Flugwissenschaften 3 ,pp. 305-313, 1955

R 15   Guderley G., " On Rao's Method for the Computation of Exhaust Nozzles", Zeitschrift für Flugwissenschaften 12 ,pp. 345-350, 1959

R 16   Rao G. V. R. , " Exhaust Nozzle Contour for Optimum Thrust" , Jet Propulsion , Vol. 28, No. 6, 1958

R 17   Shmyglevsky Yu. D., "Some variational problems in the gas dynamics of axially symmetric supersonic flows", (In Russian), Prikl. Mat. Mekh. 21, No. 2,1957

R 18   Shmyglevsky Yu. D., "A variational problem in the gas dynamics of axially symmetric supersonic flow", (In Russian), Dokl. Akad. Nauk SSR 113, No. 3,1957

R 19   Shmyglevsky Yu. D., "Supersonic profiles with minimum drag", (In Russian), Prikl. Mat. Mekh. 22, No. 2, pp. 269-273 ,1958

R 20   Shmyglevsky Yu. D., "Some gas dynamic variation problems", (In Russian), M.: VTs AN USSR, 1963

R 21   Huzel D. K., Huang D. H., "Modern Engineering for Design of Liquid Proppelant Rocket Engines", Revised Edition. AIAA Progress in Astronautics and Aeronautics, Vol. 147. Washington, DC: AIAA 1992.

R 22   Rao G. V. R. , " Approximation of Optimum Thrust Nozzle Contour" , ARS Journal , Vol. 30, No. 6 , p. 561, 1960.

R 23   Rao G. V. R., A. L. Dang, " Thrust Optimization of Nozzle Contour Including Finite Rate Chemical Kinetics", AIAA 92-3729, July 1992.

R 24   Ahlberg J. H., Hamilton S., Migdal D., Nilson E. N., "Truncated Perfect Nozzles in Optimum Nozzle Design" ARS Journal, Vol. 31, No. 5, pp.614-620, May 1961.

R 25   Ponomarev N. V., "Direct optimisation of rocket engine nozzle contours", (In Russia), Raketno-Kosmicheskaya Tekhnika: Raketney Dvigateli I Energeticheskie Ustanovki, Issue 2 (135), NIITP 1992.

R 26   Dumnov G. E., Nikulin G. Z., Ponomarev N. B., "A study of Promising Rocket Nozzles", (In Russian), NITTP, YDK 533.697.4

R 27   Dritov G. V., Tishin A. P. "On the contouring of nozzles operating with condensate particles", (In Russian), Izv.AN.USSR.MZhg No.1, 1971.

R 28   Davis D. K., "Investigation of optimisation techniques for solid rocket motor nozzle contour", AIAA 82-1188, 1982

R 29   Hussaini M. M., Korte J. J., "Investigation of Low-Reynolds-Number Rocket Nozzle design Using PNS-based Optimizartion Procedure", NASA Technical Memorandum 110295, 1996.

R 30   Prandtl, L., ''Ueber Fluessigkeitsbewegung bei sehr kleiner Reibung'' (On Fluid Movement at Low Friction, in German), International Mathematical Congress, Heidelberg, 1904

R 31   Prandtl, L., ''Fuehrer durch die Stroemungslehre'' (Text Book on Fluid Dynamics, in German), Friedrich Vieweg & Son, Braunschweig, 1960

R 32   Schlichting, H., and Gersten, K., ''Boundary Layer Theory'', Springer, Berlin Heidelberg, 1997

R 33   Donaldson C., Lange R., "Study of the Pressure Rise Across Shock Waves required to Separate Laminar and Turbulent Boundary Layer". NACA Technical Note 2770, Langley Aeronautical Laboratory, Langley Field, March 1952.

R 34   Elfstrom G., "Turbulent hypersonic flow at a wedge-compression corner", Journal of Fluid Mechanics, Vol. 53, part 1, 1972, pp. 113-127.

R 35   Chapman D., Huehn D., Larson H., "Investigation of Separated Flows in Supersonic and Subsonic Streams with Emphasis on the Effect of Transition", NACA Report 1536, Ames Aeronautical Laboratory, Moffet Field, 1958.

R 36   Hamed A., Kumar A., "Hypersonic Flow Separation in Shock Wave Boundary Layer Interactions", American Society of Mechanical Engineers, 92-Gt-205, 1992.

R 37   Hayashi M., Aso S., Tan A., " Fluctuation of Heat Transfer in Shock Wave/Turbulent Boundary Layer interaction", AIAA Journal, Vol. 27, No. 4, April 1989, pp. 399-404.

R 38   Holden M., "Shock Wave-Turbulent Boundary Layer Interaction in Hypersonic Flow", AIAA 72-74, San Diego, January 1972.

R 39   Horstman C., Settles G., Vas I., Bogdonoff S., Hung C., " Reynolds Number Effects on Shock-Wave Turbulent-Boundary-Layer Interactions", AIAA Journal, Vol. 15, No. 8, August 1977, pp. 1152-1158.

R 40   Settles G., "An experimental study of compressible turbulent boundary-layer separation at high Reynolds number", Ph. D. Dissertation, Aerospace and Mechanical Sciences Dep., Princeton University, September 1975.

R 41   Settles G., "Details of a Shock-Separated Turbulent Boundary Layer at a Compression Corner", AIAA Journal, Vol. 14, No. 12, December 1976, pp. 1709-1715.

R 42   Settles G., Fitzpatrick T., Bogdonoff S., "Detailed Study of Attached and Separated Compression Corner Flowfields at high Reynolds Number Supersonic Flow", AIAA Journal, Vol. 17, No. 6, June 1979, pp. 579-585.

R 43   Tyler D., Shapiro A., "Pressure Rise Required for Separation in Interaction Between Turbulent Boundary Layer and Shock Wave", Journal of the Aeronautical Sciences, Vol. 20, No. 12, December 1953, pp 858-860.

R 44   Panov, Yu A., and Shvets, A.I., ''Separation of Turbulent Boundary Layer in Supersonic Flow'', Prikladnaya meklanika 1, 1966

R 45   Zukoski, E.E., ''Turbulent Boundary Layer Separation in Front of a Forward Facing Step'', AIAA Journal, Vol. 5, No. 1, January 1967

R 46   Horstman C., "Prediction of Hypersonic Shock-Wave/Turbulent-Boundary-Layer Interaction Flow", AIAA 87-1367, Honolulu, June 1987.

R 47   Kuntz D., Amatucci V., Addy A., "Turbulent Boundary-Layer Properties Downstream of the Shock-Wave/Boundary-Layer Interaction", AIAA Journal, Vol. 25, No. 5, May 1987, pp. 668-675.

R 48   Lange R., "Present Status of Information Relative to Prediction of Shock-Induced Boundary-Layer Separation", NACA Technical Note 3065, Langley Aeronautical Laboratory, Langley Field, February 1954.

R 49   Mikulla V., Horstman C., "Turbulent Measurments in Hypersonic Shock-Wave Boundary-Layer Interaction Flows", AIAA Journal, Vol. 14, No. 5, May 1976, pp. 568-575.

R 50   Modarress D., Johnson D., "Investigation of Shock Induced Separation of a Turbulent Boundary Layer Using Laser Velocimetry", AIAA 76-374, San Diego, July 1976.

R 51   Selig M., Andrepoulos J., Muck K., Dussauge J., Smits A., "Turbulence Structure in a Shock Wave/turbulent Boundary-Layer Interaction", AIAA Journal, vol. 27, No. 7, July 1989, pp. 862-869.

R 52   Back R., Cuffel R.," Changes in Heat Transfer from Turbulent Boundary Layers Interacting with Shock Waves and Expansion Waves", Technical Note, AIAA Journal, Vol.8, No. 10, October 1970, pp. 1871-1873.

R 53   Back L., Cuffel R., " Shock Wave/Turbulent Boundary-Layer Interactions with and without Surface Cooling", AIAA Journal, Vol. 14, No. 4, April 1976, pp.526-532.

R 54   Spaid F., Frishett J., "Incipient Separation of a Supersonic, turbulent Boundary Layer, Including Effects of Heat Transfer", AIAA Journal, Vol. 10, No. 7, July 1972, pp. 915-922.

R 55   Muck K., Andrepoulos J., Dussauge J., "Unsteady Nature of Shock-Wave/Turbulent Boundary-Layer Interaction", AIAA Journal, Vol. 26, No. 2, February 1988, pp. 179-187.

R 56   Plotkin K., "Shock wave oscillation driven by turbulent boundary layer fluctuations", AIAA Journal, Vol. 13., No. 8, August 1975, pp. 1036-1040.

R 57   Andreopoulos J., Muck K., "Some new aspects of the shock-wave/boundary-layer interaction in compression ramp-flows". Journal of Fluid Mechanics, Vol. 180, 1987, pp.405-428.

R 58   Coe C., Chyu W., Dods J., " Pressure Fluctuations Underlying Attached and Separated Supersonic turbulent Boundary Layers and Shock Waves", AIAA 73-996, Seattle, October 1973.

R 59   Dolling D., Murphy M., "Unsteadiness of the Separation Shock Wave Structure in a Supersonic Compression Ramp Flowfield", AIAA Journal, Vol. 21, No. 12, December 1983, pp. 1628-1634.

R 60   Dolling D., Or C., "Unsteadiness of the shock wave structure in attached and separated compression ramp flows" Experiments in Fluids 3, Springer Verlag, 1985, pp. 24-32.

R 61   Erengil M., Dolling D., "Unsteady Wave Structure Near Separation in a Mach 5 Compression Ramp Interaction", AIAA Journal, Vol. 29, No. 5, May 1991, pp. 728-735.

R 62   Erengil M., Dolling D., "Correlation of separation shock motion with pressure fluctuations in the incoming boundary layer", AIAA Journal, Vol. 29, No. 11, November 1991, pp. 1868-1877.

R 63   Kistler, M., ''Fluctuating Wall Pressure under a Separated Supersonic Flow'', Journal of the Acoustical Society of America, Vol. 36, No. 3, March 1964

R 64   Gonsalez, J., Dolling, D. S., "Effects of Interaction Sweepback on the Dynamics of Shock-Induced Turbulent Separation", AIAA 93-0776.

R 65   Smits A., Muck K., "Experimental study of three shock wave/turbulent boundary layer interactions", Journal of Fluid Mechanics, Vol. 182, 1987, pp. 291-314.

R 66   Spina E., Smits A., Robinson S., " The physics of turbulent boundary layers", Annular Review of Fluid Mechanics, Vol. 26, 1994, pp. 287-319.

R 67   Thomas F., Putnam C., Chu H., " On the mechanism of unsteady shock oscillation in the shock wave/ turbulent boundary layer interactions", Experimental Fluids, Vol. 18, 1994, pp. 69-81.

R 68   Dolling, D.S., Bogdonoff, S. M., "An experimental investigation of the unsteady behaviour of blunt fin-induced shock wave turbulent boundary layer separation", AIAA 81-1287, June 1981.

R 69   Robertson, J. E., "Prediction of In-Flight Fluctuating Pressure Environments Including Protuberance Induced Flows", Wyle Laboratories Research Staff Rept. WR71-10, March 1971.

R 70   Schmisseur, J. D., Dolling D. S., "Fluctuating Wall Pressures near Separation in Highly Swept Turbulent Interactions", AIAA Journal, Vol. 32, No.6, June 1994, pp. 1151-1157,

R 71   Dolling, D., Clemens, N., "Investigation of Physics of Large-Scale Unsteadiness of Shock Induced Turbulent Separation Using Planar Laser Imaging Methods", Final progress report to U.S Army Research Office, Report No. ARO-32560.1-EG, May 2000.

R 72   Beresh, S. "The Effect of the Incoming Turbulent Boundary Layer on a Shock-Induced Separated Flow using Particle Image Velocimetry", Ph.D. Dissertation, The University of Texas at Austin, 1999.

R 73   Beresh, S, Clemens N., Dolling D., "The Relationship Between Upstream Turbulent Boundary layer Velocity Fluctuations and Separation Shock Unsteadiness", AIAA 99-0295, 37th Aerospace Meeting, Reno, NV, 1999.

R 74   Hunt, D., Nixon, D, "A Very Large-Eddy Simulation of an Unsteady Shock Wave/Turbulent Boundary Layer interaction", AIAA 95-2212, 1995.

R 75   Adams, N., "DNS of Shock Boundary-Layer Interaction- Preliminary Results for Compression Ramp Flow", Annual Research Briefs 1997, pp. 329-338, Center for turbulent Research, Stanford University.

R 76   Adams, N., Stolz, S., Honein A., Mahesk, K., "Analysis and Subgrid Modeling of Shock-Wave/Boundary-Layer Interaction", Proceedings of the Summer Program 1998, pp.337-349, November 1998, Center for turbulent Research, Stanford University.

R 77   Delery, J., and Marvin. J.G., ''Shock-Wave Boundary Layer Interactions'', AGARD No. 280, February 1986, ISBN 92-835-1519-6

R 78   Erdos J., Pallone A., "Shock-Boundary Layer Interaction and Flow Separation", Heat Transfer and Fluid Mechanics Institute Procs., Stanford University Press, 1962.

R 79   Salikuddin, M., "Unsteady Pressures on Exhaust Nozzle Interior Surfaces – Empirical Correlations for Prediction", DGLR/AIAA Aeroacoustics Conference, 14th, Aachen, Germany, May 1992, Proceedings. Vol. 2 (A93-19126 05-71), Bonn, Deutsche Gesellschaft fuer Luft- und Raumfahrt, pp. 873-881, 1992.

R 80   Darren, R., Hidalgo, H., "Fluctuating Pressure Analysis of a 2-D SSME Nozzle Air Flow Test", In its Thirteenth Workshop for Computational Fluid Dynamic Applications in Rocket Propulsion and Launch Vehicle Technology, Huntsville, Alabama, p 723-743 (SEE N96-29750 11- 34), April 1995

R 81   Foster, C., and Cowles, F., ''Experimental Study of Gas Flow Separation in Overexpanded Exhaust Nozzles for Rocket Motors'', JPL Progress Report 4-103, May 1949

R 82   Green, L. ''Flow Separation in Rocket Nozzles, ARS Journal, Vol. 23, No. 1, January – February 1953

R 83   Summerfield, M., Foster, C., and Swan, W., ''Flow Separation in Overexpanded Supersonic Exhaust Nozzles'', Jet Propulsion, Vol. 24, September-October 1954

R 84   Campbell, C. and Farley, J., ''Performance of Several Conical Convergent-Divergent Rocket Type Exhaust Nozzles'', NASA TN D-467, September 1960

R 85   Schilling T. W., ''Flow Separation in Rocket Nozzle'', M. S. Thesis, University of Buffalo, June 1962

R 86   Kalt S., and Badal D., ''Conical Rocket Nozzle Performance Under Flow Separated Condition'', Journal of Spacecraft and Rockets, Vol. 2, No. 3, May 1965

R 87   Arens, M., and Spiegler, E, Shock-Induced Boundary Layer Separation in Overexpanded Conical Exhaust Nozzles'', AIAA Journal, Vol. 1, No. 3, March 1963

R 88   Sunley, H., and Ferriman, D., ''Jet Separation in Conical Nozzles'', Journal of the Royal Aeronautical Society, Vol. 68, December 1964

R 89   Lawrence, R.A., ''Symmetrical and Unsymmetrical Separation in Supersonic Nozzles'', Research report 67-1, Southern Methodist University, April 1967

R 90   Chen, C., Chakravarchy, S., and Hung, C., ''Numerical Investigation of Separated Nozzle Flows'', AIAA Journal, Vol. 32, No. 9, September 1994

R 91   Nasuti, F., and Onofri, M., ''Viscous and Inviscid Vortex Generation During Nozzle Flow Transients'', AIAA 96-0076, June 1996

R 92   Nasuti, F., and Onofri, M., ''Viscous and Inviscid Vortex Generation During Start-Up of Rocket Nozzles'', AIAA Journal, Vol. 36, No. 5, May 1998

R 93   Onofri, F., and Nasuti, M., ''The Physical Origin of Side-Loads in Rocket Nozzles'', AIAA 99-2587, July 1999

R 94   Schmucker, R., ''Flow Processes in Overexpanding Nozzles of Chemical Rocket Engines'' (published in German), Report TB-7,-10,-14, Technical University Munich, 1973

R 95   Nave, L. H., and Coffey, G. A., ''Sea-Level Side-Loads in High Area Ratio Rocket Engines'', AIAA 73-1284, 1973

R 96   Gribben, B., Cantariti, F., Badcock, K., and Richards, B., ''Numerical Study of an Underexpanded Jet'', Proceedings of the 3rd European Symposium on Aerothermodynamics of Space Vehicles, ESA-ESTEC, Netherlands, November 24-26, 1998

R 97   Welsh, F., ''Electron Beam Fluorescence Measurements of Shock Reflection Hysteresis in an Underexpanded Supersonic Jet'', Proceedings of the 21st International Symposium on Shock Waves, Great Keppel Island, Australia, July 1997

R 98   NASA Space Vehicle Design Criteria (Chemical Propulsion), ''Liquid Rocket Engine Nozzles'', SP-8120, July 1976

R 99   Crocco, L., and Probstein, R., ''The Peak Pressure Rise Across an Oblique Shock Emerging from a Turbulent Boundary Layer Over a Plane Surface'', Princeton University (Princeton. NJ), March 1964

R 100   Carriere, P., '' Remarques sur les Méthodes de Calcul des Effets de la Viscosité dans les Tuyères Propulsives'' (Comments on computational methods of viscous effects in propulsion nozzles, in French), DGRR/WGLR Symposium, Bad Godesberg, also published as ONERA TP 408, October 1966

R 101   Dumnov, G.E., ''Unsteady Side-Loads acting on the Nozzle with Developed Separation Zone'', AIAA 96-3220, 1996

R 102   Pekkari, L.-O., ''Aeroelastic Stability of Supersonic Nozzles with Separated Flow'', AIAA 93-2588, June 1993

R 103   Pekkari, L.-O., ''Aeroelastic Analysis of Side-Loads in Supersonic Nozzles with Separated Flow'', AIAA 94-3377, June 1994

R 104   Östlund J., Jaran M., ''Assessment of Turbulence Models in Overexpanded Rocket Nozzle Flow Simulations'', AIAA 99-2583, June 1999

R 105   Hagemann G., Terhardt M.,.Frey M., Reijasse P, Onofri M, Nasuti F., Östlund J., "Flow Separation and Side-Loads in Rocket Nozzles",4th International Symposium on Liquid Space Propulsion, March 12-15, 2000, DLR Lampoldshausen

R 106   Koppenwallner G., "Development of Scaling Laws for Nozzle Aerodynaic Design", HTG Report 92-8, June 1992

R 107   Stanke H., "Test Report on The Results on HM60-SubScale Test Series 3", Vulcain Ne Project Report HM RT 110 0000 501, September 1986.

R 108   Östlund, J., Damgaard T., Frey M., "Side-Load Phenomena in Highly Overexpanded Rocket Nozzles", AIAA-2001-3684, July 2001.

R 109   Östlund (former Mattsson), J. "Test Synthesis – Reference and Polygon Modular nozzle", VOLVO Internal Report, Dock. No. SV RE 114 0000 E 2005 VOLV, Reg. No. 6600-98-3015, 1999-02-24.

R 110   Frey, M., "Behandlung von Strömungsproblemen in Raketendüsen bei Überexpansion", (in German), Ph.D. dissertation, Insitut für Aerodynamik und Gasdynamik Univesität Stuttgart, ISBN 3-8265-8806-1, 2001.

R 111   Carrière, P., Sirieix, M., Solignac, J.-L., "Propértiés de similitude des phénomènes de décollement laminaires ou turbulents en écoulemnt supersonique non uniforme", 12th International Congress of Applied Mechanics, Stanford University, August 1968 and ONERA TP N° 659F, 1968.

R 112   Dumnov, G. E., Nikulin, G. Z., Voinov, A. L., Zyuzin, V. I., "Nozzle Flow Separation and Unsteady Side Loads", Conference on Propulsive Flows in Space Transportation System, pp. 798-816, Bordeaux, September 1995

R 113   Lewis, J. E., Kubota, T., Lees, L., "Experimental investigation of supersonic laminar, two-dimensional boundary layer separation in a compression corner with and without wall cooling", AIAA J. 6, 7-14, 1968.

R 114   Kudryavtsev, V. M., "Fundamentals of theory and calculations of liquid rocket engines", (in Russian), Moscow, High School, 1975.

R 115   Malik, T. I. Tagirov, R. K., "A semiempirical method for calculating separated turbulent flow in a conical Laval nozzle in the reexpansion mode", (in Russian), Akademiia Nauk SSSR, Izvestiia, Mekhanika Zhidkosti i Gaza , pp. 60-66, Dec. 01, 1988

R 116   Abramovich, G. N., "The Theory of Turbulent Jets", The MIT Press, 1963

R 117   Girard, S., Alziary T., "Fluctuations Measurements in Axisymetric Sub-Scale Nozzle", European Seminar on Rocket Nozzles, Paris, October 1998.

R 118   Gonsalez, J., Dolling, D. S., "Effects of Interaction Sweepback on the Dynamics of Shock-Induced Turbulent Separation", AIAA 93-0776, AIAA 31st Aerospace Sciences Meeting, Reno, NV, January, 1993

R 119   Kwan W., ''Aeroelastic effects on a bended conical nozzle'', DLR-IB 645-2001-06, DLR Internal Report, 2001

R 120 Welch P. D., "The Use of Fast Fourier Transform for the Estimation of Power Spectra: A Method Based on Time Avaraging Over Short, Modified Periodograms", IEEE Trans. Audio Electroacoust., Vol. AU-15, June 1967, pp.70-73.

R 121 Dolling, D. S., Dussauge, J. P. "Fluctuating Wall Pressure Measurements", Ch. 8, Agardograph 315, 1990, A Survey of Measurements and Measuring Techniques in Rapidly Distorted Compressible Turbulent Boundary Layers.

R 122 Tomita, T., Takahashi, M., Ueda, S., Tamura, H., Aoki, K., "Visualization of the Formation of Separation Bubbles on a Bell-Shaped Nozzle Surface in Relation to Serious Side-Load", AIAA 2001-3559, 2001.

R 123 Stark, R., Kwan, W., Quessard, F., Hagemann, G., Terhardt, M., "Rocket Nozzle Cold-Gas Test Campaigns for Plume Investigations", 4th European Symposium on Aerothermodynamics for Space Vehicles, Capua, Italy, October 15-18, 2001.

R 124 Hagemann, G., Alting, J., Preclik, D., "Scalability Discussion for Rocket Nozzle Flows Based on Subscale and Full-Scale Testing", 4th European Symposium on Aerothermodynamics for Space Vehicles, Capua, Italy, October 15-18, 2001.

R 125 McLachlan, B. G., Bell, J. H., "Pressure Sensitive Paint in Aerodynamic Testing", Experimental Thermal and Fluid Science (0894-1777), vol. 10, No. 4, May 1995, p. 470-485.

R 126 Lepicovsky, J., Bencic, T., J., " Use of pressure sensitive paints for diagnostics in turbomachinery flows with shocks", ISABE-2001-1142, ISOABE, ISABE – 15th International Symposium on Air Breathing Engines, , Bangalore, India, Sept. 3-7, 2001

R 127 Taghavi, R., Raman, G., Bencic, T., "Pressure sensitive paint demonstrates relationship between ejector wall pressure and aerodynamic performance", Experiments in Fluids (0723-4864), vol. 26, no. 6, May 1999, p. 481-487

R 128 Lepicovsky, J., Bencic, T., J., Bruckner, R., J., " Application of Pressure Sensitive Paint to Confined Flow at Mach Number 2.5", NASA no. 19980197323,NASA/TM-1998-107527, E-10842, NAS 1.15:107527, AIAA Paper 97-3214

R 129 Sakaue, H., Gregory, J. W., Sullivan, J. P., Raghu, S., "Pressure Sensitive Paint for Unsteady Flow Fields", AIAA Paper 2001-0554, AIAA, 39th Aerospace Sciences Meeting and Exhibit, Reno, NV, January 8-11, 2001.

R 130 Girard, S., Alziary de Roquefort, T., "Measurements of side loads in an overexpanded parabolic nozzle", Laboratoire d'Etudes Aérodynamiques, CEAT, Poitiers, March 1999.

R 131 Reada, D., C., " Wilder M., C.," Shear-sensitive liquid crystal coating method applied through transparent test surfaces, AIAA Journal (0001-1452), vol. 39, no. 1, Jan. 2001, p. 195-197

R 132 Reijass, Ph, Morzenski, L., Naudin, P., Géneau, F., "Fluctuating Side-Load Measurements in Overexpanded Subscale Rocket-Nozzles", AIAA 2001-3557.

R 133 Harris, C., M., Crede, C., E., "Shock and Vibration Handbook", McGraw-Hill, Inc., 1976, ISBN 0-07-026799-5

R 134 Bendat, J., S., Piersol, A., G., "Random Data: Analysis and Measurement Procedures", 3rd Edition, John Wiley & Sons, New York, 2000, ISBN: 0-471-31733-0.

R 135 Gogish, L., V., "Investigation of Short Supersonic Nozzles", AN SSSR, Izvestiya, Mechanica Zidkosti i Gaza, 1966, No. 2, pp.175-180.

R 136 Hoffman, J., D., "Design of Compressed Truncated Perfect Nozzles", AIAA-85-1172, 1985.

R 137 Olsson, J. , personal communication, January 2002.

R 138 Mattsson (Östlund since 1999), J. ,"FSC Final Evaluation Report", Volvo Aero Corporation Internal Report, GSTP NT 114 00 E 2011 VOLV, Reg. No. 6600-98-1651, June 1998.

R 139 Mattsson (Östlund since 1999), J. , "Separation Analysis in Conventional Bell Nozzles", European Seminar on Rocket Nozzle Flows, CNES, Paris, 12-14 October 1998.

R 140 Knight, D., D., Degrez, G., "Shock Wave Boundary layer Interactions in High Mach Number Flows, A Critical Survey of Current Numerical Prediction Capabilities", AGARD Advisor Report 319, Vol II, pp. 1.1-1.35, December 1998.

R 141 Thivet, F., Knight, D., D., Zheltovodov, A., A., Maksimov, A., I., "Some Insights in Turbulence Modeling for Corssing.Shock-Wave/Boundary-Layer Interactions" AIAA Paper 2000-0131, AIAA 38th Aerospace Science Meeting & Exhibit", Reno Nevada, 10-13 January 2000.

R 142 Schumann, U., "Realisability of Reynolds Stress Turbulence Models", Phys. Fluids, Vol. 20, 1977, pp. 721-725.

R 143 Lumley, J., L., "Computational Modeling of Turbulent Flows", Advances in Applied Mechanics, Vol. 18, Academic Press, 1978, pp. 123-176.

R 144 Moore, J., G., Moore, J., "Realizability in Two-Equation Turbulence Models", AIAA Paper 99-3779, AIAA 30th Fluid Dynamics Conference, Norfolk, Virginia, 28 June-1July 1999.

R 145 Durbine, P., A., "On the k-ε Stagnation point Anomaly", Int. J. Heat & Fluid Flow, Vol. 17, No. 1, 1996, pp. 89-90.

R 146 Behnia, M., Parneix, S., Durbin, P., A., "Simulation of Jet Impingment Heat Transfer with the k-ε - v2 Model", Annual Research Briefs 1996, Center for Turbulence Research, California, December 1996, pp. 3-16, also at http://ctr.stanford.edu/ResBriefs96/behnia.ps.Z

R 147 Coakley, T., J., "Turbulence Modeling for Compressible Navier-Stokes Equations", AIAA Paper 83-1693, Danvers, Massachussetts, June 1983.

R 148 Coakley, T., J., Huang, P., G., "Turbulence Modeling for High Speed Flows", AIAA Paper 92-0436, AIAA 30th Aerospace Science Meeting & Exhibit", Reno Nevada, 6-9 January 1992.

R 149 Menter, F., R., "Two-Equation Eddy-Viscosity Turbulence Models for Engineering Applications", AIAA Journal, Vol. 32, No. 8, August 1994, pp. 1598-1605, also AIAA Paper 93-2906 and NASA-TM-103975, October 1992.

R 150 Eriksson, L.-E., "A Third-Order Accurate Upwind-Biased Finite-Volume Scheme for Unsteady Compressible Viscous Flow", VOLVO Internal Report, VAC 9370-154, 1990.

R 151 Eriksson, L.-E., "Development and Validation of Highly Modular Flow Solver Versions in G2DFLOW and G3DFLOW Series for Compressible Viscous Reacting Flow", VOLVO Internal Report, VAC 9970-1161, 1995.

R 152 VOLVO Internal Report, "Vulcan 2+ NE, TN, CFD Simulations", Prog. Nr. SV NT 114 0000 E2026, Reg. No. 6600-99-1701, Issue Date 2000-09-26.

R 153 Ghosal, S., "Mathematical and Physical Constraints on Large Eddy Simulation of Turbulence", AIAA Journal, Vol. 37, No. 4, pp. 425-433, April 1999.

R 154 Jameson, A., "the present Status, Challenges and Future Developments in Computational Fluid Dynamics", Proceedings of 12th Australasian Conference on Fluid Dynamics, Sydney, December 1995.

R 155 Speziale, G., C., "Turbulence Modelling for time-Dependent RANS and VLES A Review", AIAA Journal, Vol. 36, No. 2, pp. 173-184, February 1998.

R 156 Fureby, C., Grinstein, F., F., "Monotonically Integrated Large Eddy Simulation of Free Shear Flows", AIAA Journal, Vol. 37, No. 5, pp. 544-556, May 1999.

R 157 Urbin, G., Knight, D., Zheltovodov, A., A., "Large Eddy Simulation of a Supersonic compression Corner", AIAA Paper 2000-0298.

R 158 Terhardt, M., Hagemann G., Frey, M., "Flow Separation and Side Load Behaviour of Truncated Ideal Rocket Nozzles", AIAA-2001-3686, Salt Lake City, July 2001.

R 159 Reijass Ph., Morzenski L., Blacodon D., Birkemeyer J., " Flow Separation Experimental Analysis in Overexpanded Subscale Rocket Nozzles"AIAA-2001-3556, Salt Lake City, July 2001.

R 160 Reijass Ph., Birkemeyer J., "Semi-Empirical Flow Separation Model for Subscale Nozzles", Presented at the 4th European Symposium on Aerothermodynamics for Space Vehicles, Capua, Italy, October 15-18, 2001

R 161 Torngren, L., "Correlation Between Outer Flow and Internal Nozzle Pressure Fluctuations", Presented at the 4th European Symposium on Aerothermodynamics for Space Vehicles, Capua, Italy, October 15-18, 2001

ACKNOWLEDGEMENTS

Paper 1

A SUB SCALE TEST PROGRAMME ON INVESTIGATION OF FLOW SEPARATION AND SIDE LOADS IN ROCKET NOZZLES

J. Mattsson[1], U. Högman[2], L. Torngren[3]

[1]Volvo Aero Corporation, SE-461 81 Trollhättan, Sweden, Phone: +46 520 93735, Fax: +46 520 98578, VAC.JNMN@MEMO.volvo.se

[2]Volvo Aero Corporation, SE-461 81 Trollhättan, Sweden, Phone: +46 520 94946, Fax: +46 520 98578, VAC.UFHN@MEMO.volvo.se

[3]FFA, SE-161 11 Bromma, Sweden, Phone: +46 8 63410450, Fax: +468 6341072, tnl@ffa.se

ABSTRACT

An important factor limiting the performance optimisation of a rocket engine is the loads induced by unsymmetrical and unsteady flow separation in the nozzle extension during launch. Within the ESA/ESTEC General Supporting Technology Programme (GSTP) the flow separation phenomenon in a rocket nozzle with corresponding side load features has been investigated in sub scale wind tunnel tests. In the present paper, results from this testing are presented and discussed. First, the used test facility, hardware and logic are presented. Results from the test and associated analysis are discussed. The results from the testing demonstrate that the rig is capable of simulating flow separation and side loads in flexible nozzles. Two different steady state separation patterns are prevailing in the test nozzle. Further, numerical simulation of the flow separation with state of the art-turbulence-modelling results in good agreement with the experimental data. The separation pattern, point of separation and the wall pressure behind the separation point have been successfully predicted.

Key words: Nozzle; Over-expanded Flow; Flow Separation; Side load; Test

1. INTRODUCTION

Some rocket engines suffer severe dynamic loads during operation at chamber pressures below the design pressure. This operational condition typically occurs during the start-up and throttle down process of the rocket motor at sea level. These loads can sometimes be of such a magnitude that they present life-limiting constraints on thrust chamber components as well as on the thrust vector control system. The source of these loads is generally attributed to the instationary nature of the partially detached and partially attached flow that occurs during operation of the thrust chamber at over-expanded conditions.

The most well known of these dynamic loads that have received attention in the literature is the so called side-load[1,2]. Side loads have been observed during start-up of over-expanded sea-level liquid propellant rocket engines as well as during ignition and the staging of a multi-stage solid propellant rockets[3,4,5]. Due to the severe complications experienced due to too high levels of side-loads, it is one of the most important features in sea-level nozzle design. It has e.g. been taken into account for the contour definition for the Vulcain 2 nozzle extension[6].

The traditional design approach for bell type nozzles is to design the nozzle contour and area ratio such that attached flow and low levels of side-loads are guaranteed at nominal operation at high ambient pressure, sea level conditions. Further, the structure is designed robust enough to withstand the side-loads during the throttling up and down process. The reduced performance under vacuum ambient condition and the corresponding weight penalty with a robust design is accepted with this design approach. Increasing demands for improved launcher performance, however, push the development of new concepts. One possible solution is to adapt the nozzle contour during the flight to the changes of ambient and chamber pressure. Attempts in this direction, however, have so far not been successful due to the weight and mechanical complexities of such devices. By introducing so called Flow Separation Control Devices (FSCD), high area ratio nozzles can be operated at separated condition at sea level without severe loads, and an improved overall performance is obtained. The feasibility of such devices is under demonstration. The main reason why such devices do not yet exist in full scale is that several basic questions regarding the nature of separation phenomena and the corresponding side-loads remain to be answered.

Within the Flow Separation Control (FSC) programme at Volvo Aero Corporation (VAC) the flow separation phenomenon in sea level rocket nozzles with corresponding side load features have been investigated. In the course of the work, detailed aerodynamic and aeroelastic sub scale testing have been performed in the modified hypersonic wind tunnel HYP500 at the Aeronautical Research Institute of Sweden (FFA) under

a contract with the European Space Agency (ESA). In the present paper results from this testing are presented and discussed.

2. GSTP TEST PROGRAMME

The primary objectives of the GSTP FSC programme were to study the side load and separation behaviour in a sub scaled rocket nozzle.

More general test objectives were:

1) Study the influence of different structural response of the test nozzle on the side load magnitude and investigate the degree of aeroelastic[7,8] coupling.
2) Define the separation characteristics of the nozzle.
3) Measure nozzle vibrations.
4) Establish statistical data base on side loads
5) Provide data for calibration of design tools with respect to flow separation and side loads.

The GSTP FSC testing was performed during the period 12 August 1997 to 21 January 1998 in the modified hypersonic wind tunnel HYP500 at FFA and allowed successful completion of the test objectives.

2.1 TEST CONFIGURATIONS

The testing was performed with a bell-shaped sub-scale rocket nozzle mounted in the modified HYP500 wind tunnel, Figure 1. The test nozzle was designed to resemble the separation and structure response characteristics of the Vulcain nozzle[9]. Because the nozzle model is operated with air instead of hot propellant gases the shape and expansion ratio differs from the Vulcain nozzle. The main parameters of the model nozzle are shown in Table 1.

Table 1. Main parameters of model nozzle.

Parameter	Value	Dimension
Area ratio (ε)	20	-
Nozzle length (L)	350	mm
Throat radius (r_t)	33.54	mm
Nozzle exit radius (r_{exit})	150	mm
Design feeding pressure (P_0)	5.0	MPa
Design feeding temperature (T_0)	450	K
Feeding gas	Air	-

The nozzle consists mainly of two parts, one fixed part mounted to the downstream flange of the wind tunnel and one flexibly hinged part, see Figure 2. The flexible part is free to move in one plane perpendicular to the test section viewing direction and the motion simulates the throat bending mode of a real rocket nozzle. The bending resistance is simulated with exchangeable torsion springs. A photo of the reference hardware with the different parts can be found in Figure 3.
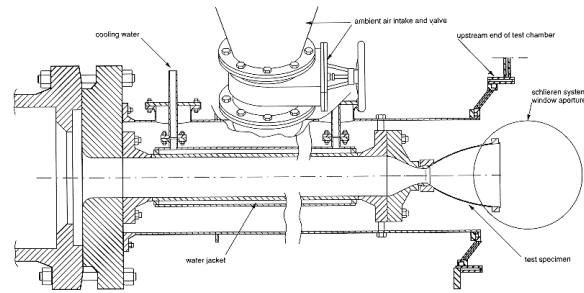
Figure 1. Schematic side view of the flexible hinged test nozzle in FFA tunnel HYP 500.
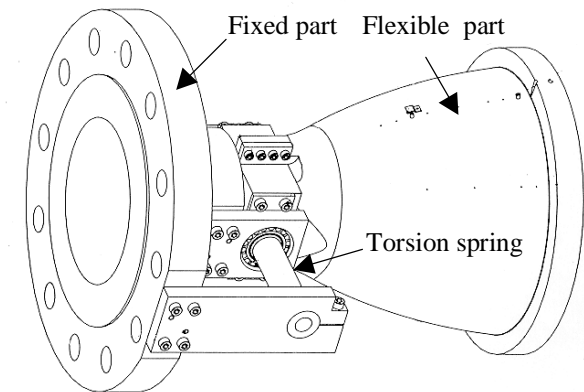
Figure 2. Side view of model nozzle assembly.
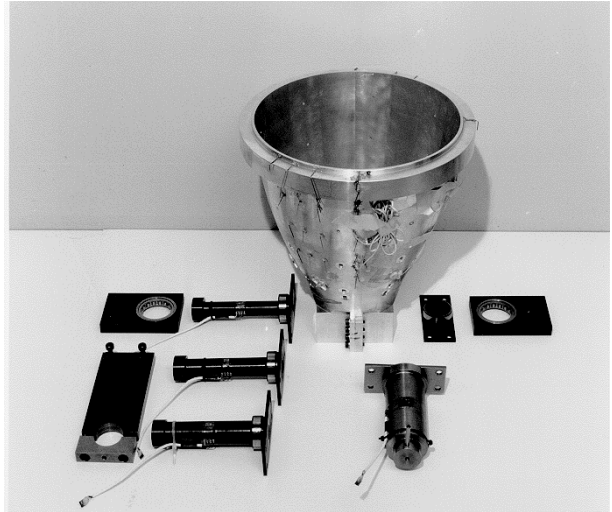
Figure 3. Photo of used hardware.

In order to investigate the influence of structural response and aeroelastic coupling[7,8] on the side load, five different torsion spring set-ups were used. The resulting natural oscillating frequencies of the bending mode are listed in Table 2 for the different set-ups.

Table 2. Resulting natural oscillating frequencies of the bending mode for the different spring set-ups.

Spring name	Super weak	Weak	Medium	Stiff	Rigid
Natural frequency [Hz]	25,2	36,3	45,0	57,5	120

2.2 INSTRUMENTATION

The quantities that were measured during the test campaign were:

- Nozzle side load
- Nozzle wall static pressure
- Nozzle wall dynamic pressure
- Nozzle wall vibrations
- Feeding pressure
- Feeding temperature
- Static pressure in test cell
- Dynamic pressure in test cell
- Schlieren visualisation of flow field

A summary of the nozzle instrumentation and the transducer locations is found in Figure 4.
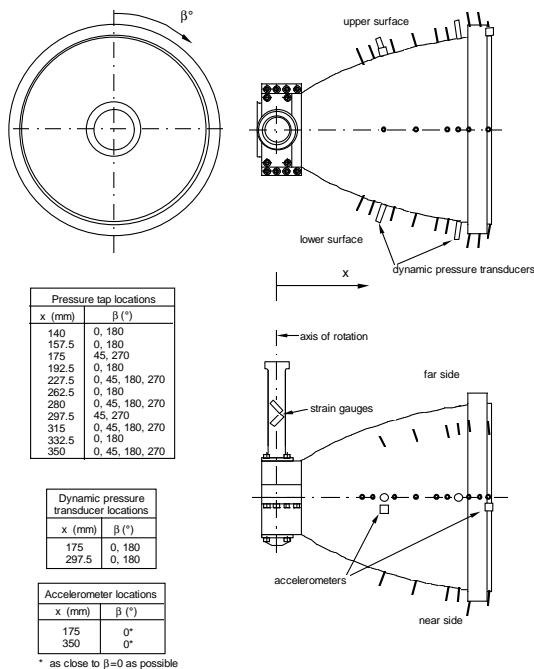

Pressure tap locations	
x (mm)	β (°)
140	0, 180
157.5	0, 180
175	45, 270
192.5	0, 180
227.5	0, 45, 180, 270
262.5	0, 180
280	0, 45, 180, 270
297.5	45, 270
315	0, 45, 180, 270
332.5	0, 180
350	0, 45, 180, 270

Dynamic pressure transducer locations	
x (mm)	β (°)
175	0, 180
297.5	0, 180

Accelerometer locations	
x (mm)	β (°)
175	0*
350	0*

* as close to β=0 as possible

Figure 4.   Instrumentation of model nozzle.

The main jet wall pressure was measured with a total number of 30 static pressure taps in the nozzle. The transducers were positioned both in axial lines in order to measure the steady state separation point and in circumferential lines in order to see possible asymmetry of the flow. Four fast response pressure transducers on the nozzle wall were used in an attempt to trace the pressure fluctuations connected with unsteady separation.

The side load was measured with strain gauge bridges mounted on the torsion springs. Corresponding nozzle dynamic behaviour was recorded with two accelerometers located at the middle of the nozzle and at the exit.

In addition to the numerical data, a Schlieren system was used to visualise the flow downstream of the nozzle exit. The Schlieren system was equipped with a beam splitter and both a camera for photographic film and a high-speed video camera with 500 frame/sec. were used simultaneously.

2.3 TEST SEQUENCES

Mainly three different types of test sequences with three different objectives were used during the testing:

1) To investigate the steady state separation of the nozzle flow, test sequences with stepwise variation of the feeding pressure were used. The runs were performed with increasing pressure and at different pressure levels, which were held constant for at least 10 sec. The test cell pressure was held constant to atmospheric pressure during the test. A typical test run is shown in Figure 5.

2) To study the stochastic variation in side loads during start and stop transients a numbers of start-up and shut down sequences were used. In these tests the feeding pressure was increased rapidly from atmospheric pressure to a maximum feeding pressure which guaranteed full flowing condition, then followed by a throttling down again to atmospheric conditions. The test cell pressure was held constant to atmospheric pressure during the test, Figure 5.

3) To assess the impact of the Reynolds number and the ambient pressure on the separation, test sequences with variation of the test cell pressure were used, Figure 5.
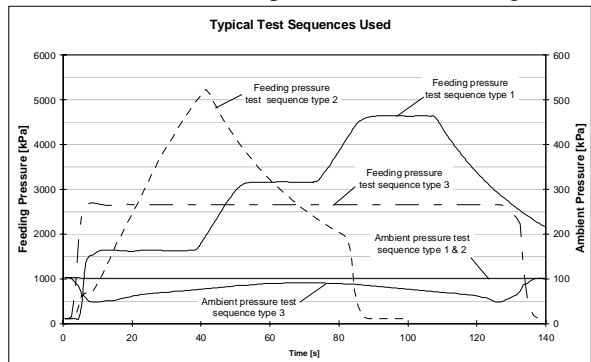

Figure 5.   Typical test sequences used.

In all test sequences performed the test model was supplied with preheated pressurised dry air through the wind tunnel circuit. The air was preheated in order avoid condensation. The operation capabilities of the wind tunnel used during the testing are listed in Table 3.

Table 3. Used operation capabilities of the wind tunnel.

Parameter	Value
Mass flow rate	Up to 36 kg/s
Feeding pressure	Up to 5.3 MPa
Feeding air temperature	450-500 K
Test cell static pressure	50–100 kPa

3. TEST RESULTS

Typical steady-state wall pressure data are shown in Figure 6 for 11 different operational conditions, feeding to ambient pressure ratio ranging from about 10 to 50. The data have been averaged over 4 seconds, the wall pressure normalised with the feeding pressure and the axial location from the throat are normalised with the
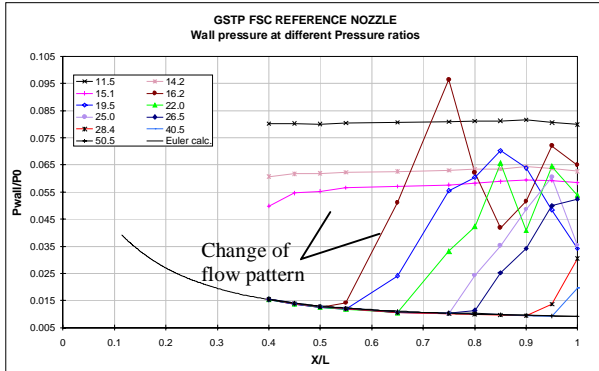
nozzle length.

Figure 6. Wall pressure profiles in the model nozzle, experimental data FFA.

As can be noted in the figure the wall pressure profile features are subjected to a drastic change when the pressure ratio between the feeding and ambient pressure is increased above 15. This is explained by a transition of the flow separation pattern.

At a pressure ratio below 15, the separation profile follows the classical concept of nozzle separation often labelled "free-shock" separation. In Figure 7 the flow field pattern predicted with CFD and the prevailing wall pressure in the nozzle at a pressure ratio of 14 is shown. From the figure we can conclude that at free shock separation the wall pressure rises nearly to ambient pressure in a very short distance. The source of this rise is due to the oblique shock originating from the separation point. Downstream the steep pressure gradient region, the wall pressure increases slowly to almost ambient pressure.

In Figure 8 we can see the corresponding picture of the flow pattern inside the nozzle at a pressure ratio of 16. As can be observed the flow first separates from the wall and that the pressure exceeds the ambient pressure downstream the separation point. The oblique shock wave emerging from the boundary layer is reflected by the Mach disc, which almost completely covers the nozzle cross section. Because of the reflection, the flow reattaches and the nozzle appears to be full flowing. The oscillatory behaviour of the wall pressure is caused by the expansion and compression waves interacting with the supersonic jet boundaries to match the ambient air. This kind of flow behaviour was first reported within the J2-S cold flow test programme and the separation and reattachment flow pattern was denoted "restricted

shock" separation after Nave and Coffey[2]. Due to the scale and the use of cold air as feeding gas a wide-spread assumption was made that this flow process could only occur in sub-scale cold flow nozzles[1]. However, recent investigations of full-scale nozzles have shown that restricted shock separation occurs both in the SSME and the Vulcain nozzle[10,11,12]. The similarity between the GSTP, J2-S, SSME and the Vulcain nozzle is that they are all parabolic nozzles of Rao type[13,14], with an internal shock induced in the throat region.
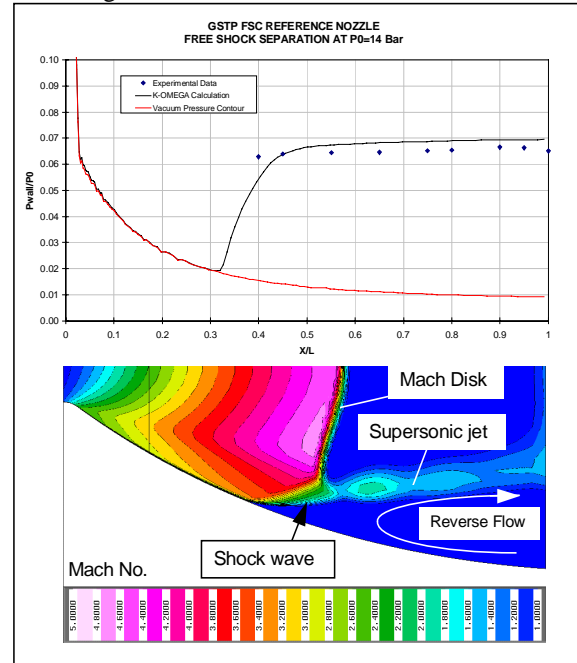
Figure 7. Free shock separation in model nozzle, experimental data FFA.
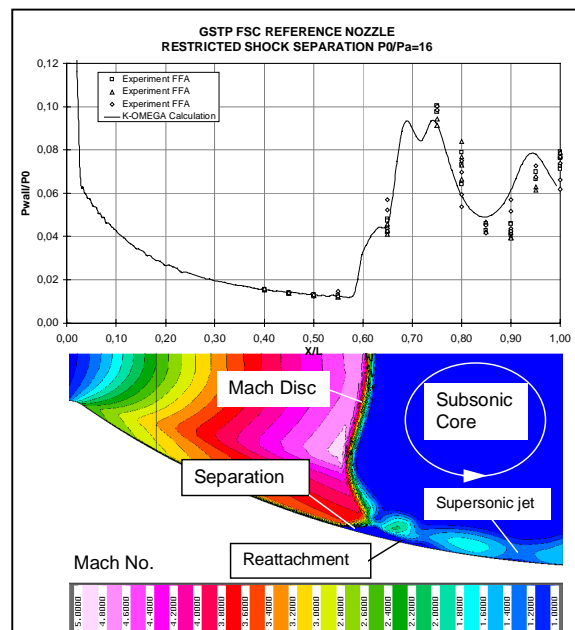
Figure 8. Restricted shock separation in model nozzle, experimental data FFA.

For the numerical flow field analysis presented in Figure 7-8 an in-house structured multi-block Navier-Stokes solver, VOLSOL[15], with a modified k-ω turbulence model was used. As can be concluded from the figures, CFD is capable of predicting the separation phenomenon. Good agreement can be seen between the calculations and the experimental data when considering the prediction of the separation point and the wall pressure down stream the separation point.

When representing the separation characteristics graphically the method of plotting the ratio between the separation pressure, p_{sep}, and the plateau pressure, p_p, behind the separation point versus the inviscid Mach number at the separation point is widely adopted [1]. The motivation of this method emerges from the physical reasoning that the pressure ratio over the oblique separation shock is only a function of the Mach number and the specific heat ratio. In Figure 9, a summary of the separation characteristics for the GSTP nozzle can be found together with the Schmucker separation criterion[1]. This is the most widely used separation criterion today in the European space industry.
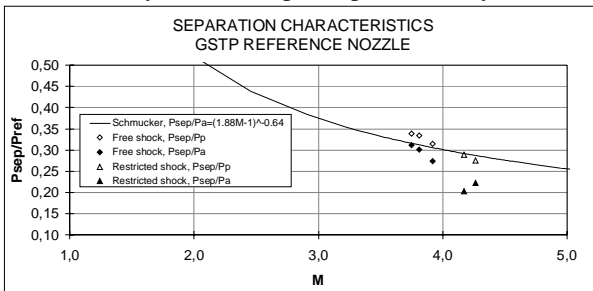
Figure 9.   Separation characteristics of the GSTP nozzle.

In the figure the measured separation pressure has been normalised with either the plateau pressure behind the shock or the ambient pressure for comparison. In the case of free shock separation the plateau pressure behind the shock is often roughly approximated as being equal the ambient pressure. This neglects the fact that the pressure recovery to ambient pressure consists of two independent mechanisms, flow separation and recirculation. When considering restricted shock separation this approximation is even coarser. The flow in the separated region is enclosed by supersonic flow and the scatter of the data when using the ambient pressure as the reference pressure indicates this. In the GSTP nozzle the ratio between the plateau pressure and the ambient pressure is of the order 0.9 in the free shock case and varies between 0.7 and 0.85 for the restricted shock case depending on the position of the separation point. This indicates that the Schumcker criterion is far too simple as it tries to account for all pressure recovery effects in one single formula, see above. There is thus a need of an improved criterion that simulates all the different recovery phenomena separately.

A time record of the measured side load torque during a start up and shut down process is shown in Figure 10. Two different distinct load peaks can be identified both during start up and shut down.
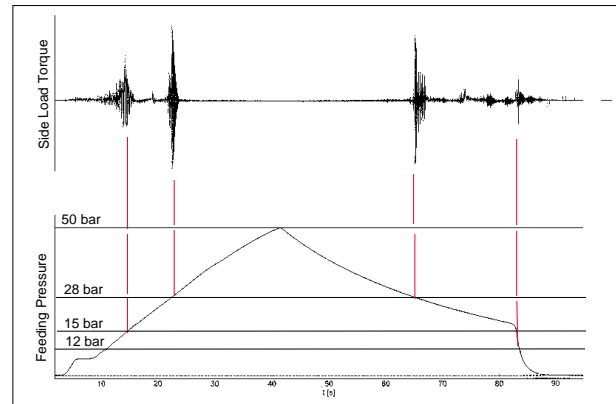
Figure 10.   Time record of the measured side load torque during start up and shut down.

In Figure 11 and Figure 12 these data are given in terms of percent of peak measured loads versus the feeding to ambient pressure ratio for the start up and shut down transient respectively.
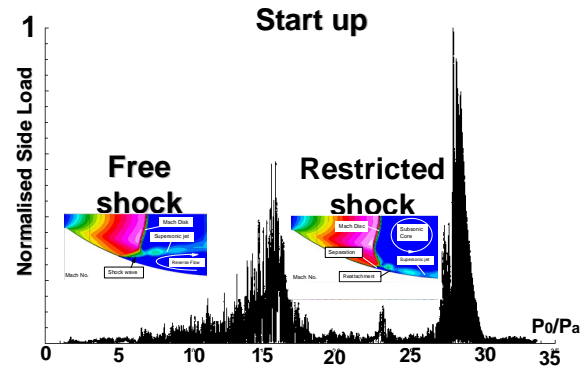

Figure 11.   Normalised side load torque vs. feeding to ambient pressure ratio, start up.
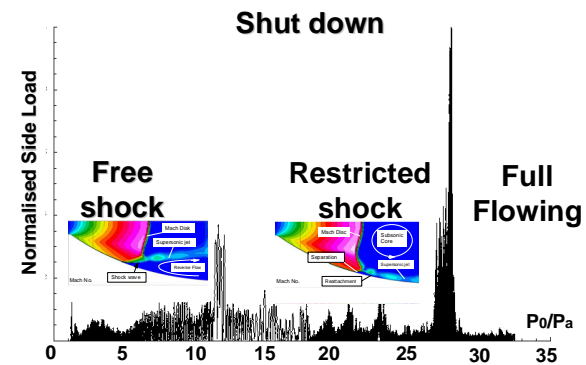

Figure 12.   Normalised side load torque vs. feeding to ambient pressure ratio, shut down.

As indicated in the figures it is one significant load peak at a pressure ratio of about 15 and second at a pressure ratio of 28 during the start transient. Corresponding side load peaks during the throttle down occurs at pressure

ratio of 12 and 28. The low pressure side load peak is obviously coupled to the transition of the separation pattern. The different values of the pressure ratio for the low pressure peak during throttling up and down indicates a hysteresis effect of the transition phenomenon. The two side load peaks and the hysteresis effect were also experienced in the J2-S sub-scale test[2].

From the high speed video recording of the flow pattern at the exit it can be seen that the flow starts to pulsate when the downstream leg of the λ shock, i.e. the reattachment point, is close / intersects the nozzle exit. This happens at a pressure ratio of 25. At this point the flow becomes highly unstable, it separates from and reattaches to the wall in a cyclic manner until the increase of the feeding pressure is enough to move the downstream leg of the λ shock totally out of the nozzle, which corresponds to a pressure ratio of 30. It is obvious that the second side load peak is connected to this end effect. This kind of unsteady flow process with a restricted shock separation converted to a free shock separation at the nozzle exit was also experienced in the SSME nozzle[10,16]. It was concluded that this effect was the reason for the failure of the SSME fuel feed line.

4. SUMMARY AND CONCLUSIONS

A sub scale test programme on the investigation of flow separation and side load experienced in rocket nozzles has been carried out. The used test facility, hardware and logic have been presented and the results from the test and associated analysis discussed. The results from the testing demonstrate that the rig and model hardware is capable of simulating the flow separation and the associated side load phenomena experienced in real rocket nozzles. The two main flow fields found in the over-expanded nozzle featured separation from the wall without reattachment at lower feeding pressure (free shock separation) and with reattachment at higher feeding pressure (restricted shock separation). The free shock separation remained to a higher feeding pressure during the start-up phase and the restricted shock separation tended to remain when the driving pressure was lowered. This accounts for a hysteresis effect. It was concluded that the phenomena with two different flow separation regimes occur in parabolic nozzles of Rao type with an internal shock emerging from the throat region. The two significant side load peaks observed are generated during transition between the separation patterns. Further, numerical simulation of the flow separation with state-of-the-art turbulence modelling results in a very good agreement with the experimental data. The separation pattern, point of separation and the wall pressure behind the separation point have been successfully predicted.

REFERENCES

1. R. H. Schmucker, "Flow processes in overexpanded chemical rocket nozzles, Part 1: Flow separation", NASA TM-77396.
2. L. H. Nave and G. A. Coffey, "Sea level side loads in high area ratio rocket engines", AIAA 73-1284
3. J. M. Bowyer, G. W. Krieter and R. E. Peterson, "An investigation of the Side Force that is Sometimes Observed in Rocket Motor Start-Up", AIAA78-1045.
4. G. D. Luke and D. E. Adams, "Use of Nozzle Trip Rings to Reduce Nozzle Separation Side Loads During Staging", AIAA-92-3617.
5. G. L. Romine, "Nozzle Flow Separation", AIAA Journal Vol.36, No. 9, September 1998.
6. M. Bigert, T. Stenholm and T. Sätmark, "Technology for the Film-Cooled Nozzle of the Vulcain Engine", IAF-98-S.3.05
7. L.-O. Pekkari, "Aeroelastic Stability of Supersonic Nozzles with Separated Flow", AIAA 93-2588.
8. L.-O. Pekkari, "Aeroelastic Analysis of Side Loads in Supersonic Nozzles with Separated Flow", AIAA 94-3377.
9. T. Stenholm et al., "The Vulcain Extension and its Evaluation", ISTS 98-a-1-08.
10. T.-S. Wang, C. Dumas, "Numerical Study of the SSME Nozzle Flow Fields During Transient Operations- A comparison of the Animated Results with Test", 11th Workshop for CFD Applications in Rocket Propulsion, Alabama April 22, 1993.
11. M. Frey and G. Hagemann, "Status of Flow Separation Prediction in Rocket Nozzles", AIAA 98-3619.
12. M. Terhardt, M. Bigert. "Vulcain Testing Analysis ANE Test Results", European Seminar on Rocket nozzle Flows, CNES, France, October 1998.
13. G.V.R Rao, "Exhaust Nozzle Contours for Optimum Thrust", Jet Propulsion, pp.377-382, June 1958.
14. G.V.R. Rao, "Approximation of Optimum Thrust Nozzle Contours", ARS Journal, p. 561, June 1960.
15. R. Ryde'n and P. Groth, "Volsol V2.6 user's Guide", VAC Report 9970-1857, Volvo Aero Corporation.
16. E. W. Larson et al.,"Structural Response of the SSME Fuel Feedline to Unsteady Shock Oscillations", 52nd Shock and Vibration Symposium , New Orleans, Lousiana 21-29 October 1981.

Paper 2

AIAA-99-2759

A Sub Scale Investigation on Side Loads in Sea Level Rocket Nozzles

J. Östlund

M. Bigert

Space Propulsion

Volvo Aero Corporation

S-461 81 Trollhättan, Sweden

**35th AIAA/ASME/SAE/ASEE
Joint Propulsion Conference & Exhibit
June 20-24, 1999 / Los Angeles, California**

A SUB SCALE INVESTIGATION ON SIDE LOADS IN SEA LEVEL ROCKET NOZZLES

Jan Östlund [##]
Mikael Bigert

Volvo Aero Corporation
Space Propulsion Division
SE-461 81 Trollhättan
Sweden
(E-mail: vac.jnos@memo.volvo.se, vac.mbig@memo.volvo.se)

Abstract

The challenge of designing first stage rocket engine nozzles is made more difficult by the unstable loads during the start-up and sea level rig testing. These side loads are a key issue for the nozzle designed. In order to understand this and to be able to optimise the future designs, Volvo is currently working with a broad program. With both tests and analysis. The program started within the GSTP framework in 1997 and is presently continuing as a National program closely co-ordinated with our European partners.

Up to June 1999, not less than 7 test campaigns have been carried out, all at the facilities of FFA in Stockholm. The paper describes the objectives of these tests together with results and conclusions.

In parallel work is ongoing to understand the side loads, their nature and the factors influencing their size. Analytical models have been developed and correlated to the test results.

The future potential of the knowledge generated in this program is very high since the side load reduction design will be a powerful instrument in increasing the performance of the next generations sea level nozzles.

Nomenclature

Abbreviations / Physics

ANE	Advanced Nozzle Extension
FSC	Flow Separation Control
FSCD	Flow Separation Control Device
FSS	Free Shock Separation.
LEA	Laboratoires d'Etudes Aérodynamiques
NE	Nozzle Extension
P	Pressure
R	Radius
RSS	Restricted Shock Separation.
TEG	Turbine Exhaust Gases
x	Axial position

Index

cc	Combustion Chamber
ns	Normal shock

: Jan Östlund changed his name from Mattson in April 1999

Introduction

Some rocket engines suffer severe dynamic loads during operation at chamber pressures below the design pressure. These operational conditions typically occur at start-up and shut-down or at off nominal operation of the engine. These loads can sometimes be of such a magnitude that they present life limiting constrains on thrust chamber components as well as on the thrust vectoring control system. The source of such loads are generally attributed to the instationary nature of the partially detached and partially attached flow that occurs during the operation of the thrust chamber at pressure below design pressure.

The most well known of these dynamic loads that have received attention in the literature is the so called side-load. Side loads have been observed during start-up of over-expanded sea-level liquid propellant rocket engines as well as during the staging of a multi-stage solid propellant rockets. Due to the severe complications experienced due to too high levels of side-loads the side-load is one of the most important features in sea-level nozzle design and has e.g. been guiding the contour definition for the Vulcain 2 nozzle extension.

The traditional design approach for bell type nozzles is to design the nozzle contour and area ratio such that attached flow and low levels of side-loads is guaranteed at nominal operation at high ambient pressure, sea level conditions. Further, the structure is designed robust enough to withstand the side-loads during the throttling up and down. The reduced performance under vacuum ambient condition and the corresponding weight penalty with a robust design is accepted with this design approach. Increasing demands for improved launcher performance, however, push the development of new concepts. To decrease the separation margin at sea level will yield clear performance benefits /4/. One possible solution is to adapt the nozzle contour during the flight to the changes of ambient and chamber pressure. Attempts in this direction, however, have not been successful due to the weight and mechanical complexities of such devices. By introducing so called Flow Separation Control Devices (FSCD), high area ratio nozzles can be operated at separated condition at sea level without severe loads, and an improved overall performance is obtained. The feasibility of such devices

are under demonstration. The main reason why such devices do not yet exist in full scale is that several basic questions regarding the nature of separation phenomena and the corresponding side-loads remain to be answered. The side load phenomena has recently received new attention in Europe /1/ and /8/.

Volvo programs for side load investigations

Within the Flow Separation Control programme at Volvo Aero Corporation (VAC) the flow separation phenomena in sea level rocket nozzles with corresponding side load features has been investigated. In the course of the work detailed aerodynamic and aero-elastic sub scale testing has been performed in the modified hypersonic wind tunnel HYP500at the Aeronautical Research Institute of Sweden (FFA) under contract with European Space Agency (ESA) and Swedish National Space Board (SNSB).

The first program was within the GSTP of ESA /1/, where a great number of tests were run in 1997.

A continuation was started in 1998 within the frame of the so-called Vulcan 2+ program at Volvo. Here, the activities have been coordinated with similar programs in France and Germany. A European FSCD Working Group has been created for technical co-operation between CNES/SEP/Dasa/DLR/ONERA/LEA/FFA and Volvo. The Vulcan 2+ program is focussed on coming sea level engine generations with drastically improved performance.

The present plans include several more test campaigns to be carried out during the year 1999.

GSTP test campaigns 1997

The tested nozzle consisted mainly of two parts, one fixed part mounted to the downstream flange of the wind tunnel and one flexible hinged part. The nozzle throat radius is about 33 mm. The flexible part was suspended with a flexible joint permitting motion in only one plane and the motion simulated the throat bending mode of a real rocket nozzle. The bending resistance was simulated with five different exchangeable torsion springs in order to investigate the influence of the structure response on the side load amplitude and possible aero-elastic coupling. The ratio in stiffness between the stiffest and the weakest spring was 25. To conclude whether the resulting side-load was measured or not with the flexible joint with one degree of freedom a test with a universal joint suspension permitting bending in all directions around the throat was also performed. With this test, both the side load level and direction of the load could be measured. A number of start-up and shutdown transients, were performed with these test configurations to achieve statistical information of the side-load behaviour.
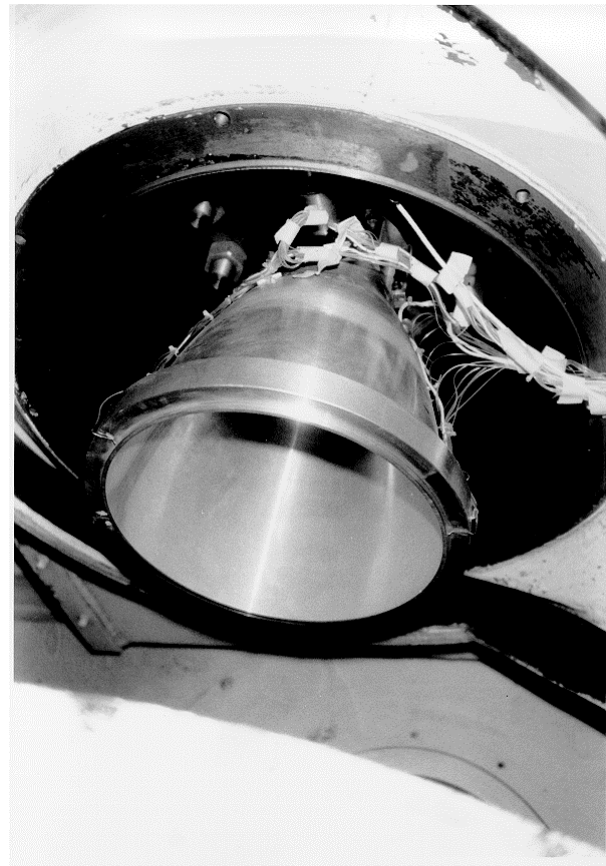
Figure 1 : GSTP nozzle installed in rig
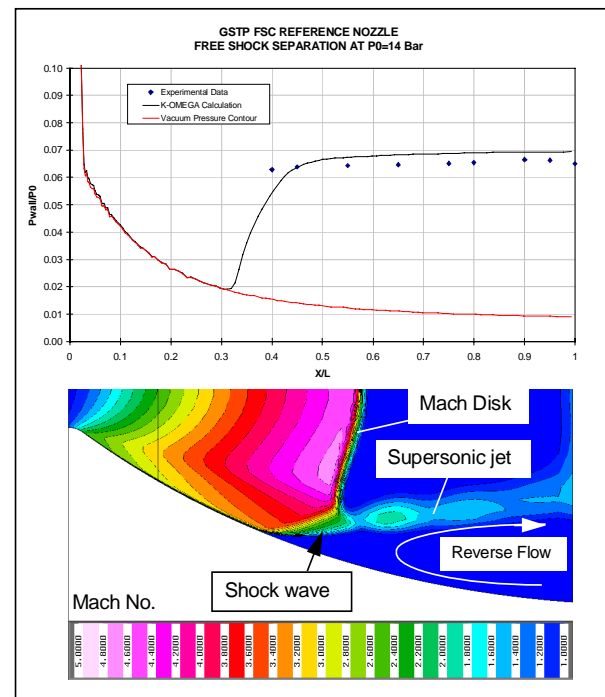
Figure 2 : Free shock separation in GSTP nozzle, CFD simulations compared with test results.

Two significant side-load peaks were identified both during the start-up and the throttle down sequence for all the different spring set-ups. The analysis shows that the low thrust level side-load peak is due to a transition between two radically different overall flow topologies, from free shock separation to restricted shock separation

2

during start-up and the reversed order during shutdown, and a related flow hysteresis effect.
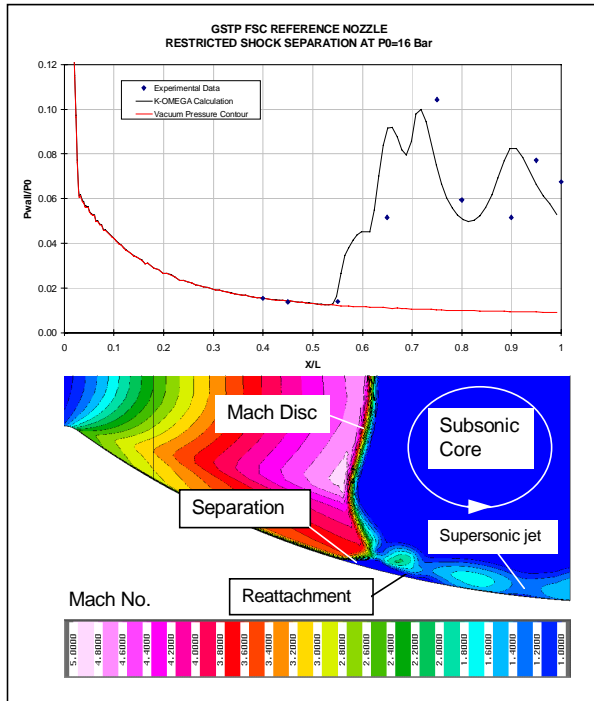

Figure 3 : Restricted shock separation in GSTP nozzle, CFD simulations compared with test results.

The high thrust level peak is connected to an end separation phenomenon. No significant influence of the spring stiffness could be seen on the side-load level for the low thrust level peak. For the high thrust level peak the side-load levels decreased with decreased spring stiffness but the trend is suddenly interrupted by the weakest spring system which experience the highest side-loads. With aeroelastic theory it is shown that the weakest spring system is aeroelastically unstable whereas the aeroelastic coupling is considered weak for the other spring systems, explaining the obtained features, see the chapter about aero-elastic analysis.

The observed side-load features in the sub-scale test show good agreement with available full-scale test experience.

After the GSTP was finished, a new phase was started with further investigations. The focus was now less on aero-elasticity and more on aerodynamic loads.

Logic for a continued program

The FSC program was now continued with more sub-scale testing. The logic was to investigate the most interesting phenomena that had been identified before:

- The influence of the degrees of freedom for the nozzle movement at the throat. The GSTP tests were done with hinging in only one axis.

- The importance of extending the nozzle contour.

- The adaptation of the nozzle contour to have similarity in internal flow field with Vulcain NE.

- The application of a three-dimensional FSC device

- The investigation of a discontinuity in the angle, a dual-bell contour.

Two-directional cardan tests

In order to demonstrate the importance of the degrees of freedom, the hardware used in the GSTP campaign was equipped with a cardan. This made it possible to have movements in both perpendicular directions at the throat. The arrangement is shown in the picture below:
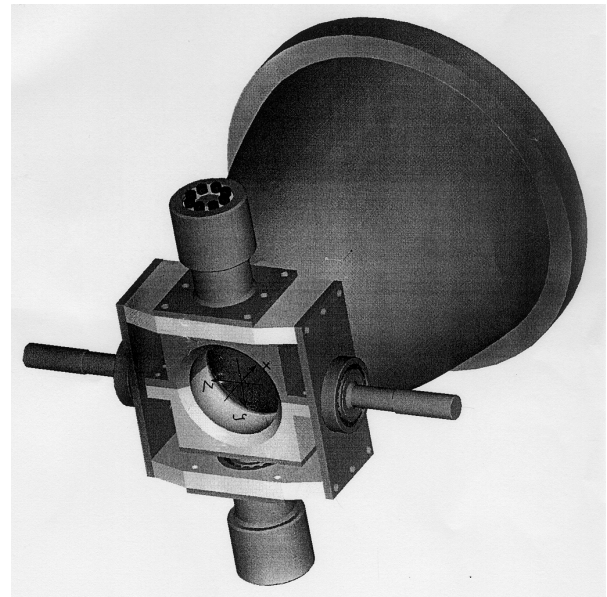
Figure 4: GSTP nozzle equipped with cardan.

The cardan made it possible to measure the side load torques in both directions. There was thus no loss of information, as it had been in the GSTP testing where only one direction was possible. In theory, the amplitude in an infinite series would be $2^{0.5}$ higher than for a one-directional side load. In the tests, the amplification varied between 1.2 and 1.9 : It was clear that the loads had random direction and that no direction was preferred. The conclusion was to use the cardan for all subsequent testing.

Extended contour tests

The next campaign was dedicated to investigating the same h/w with an applied extension. The nozzle length was increased with approximately 25 %. The extension was made in such a way that the pressure gradient was relatively high in the extension.
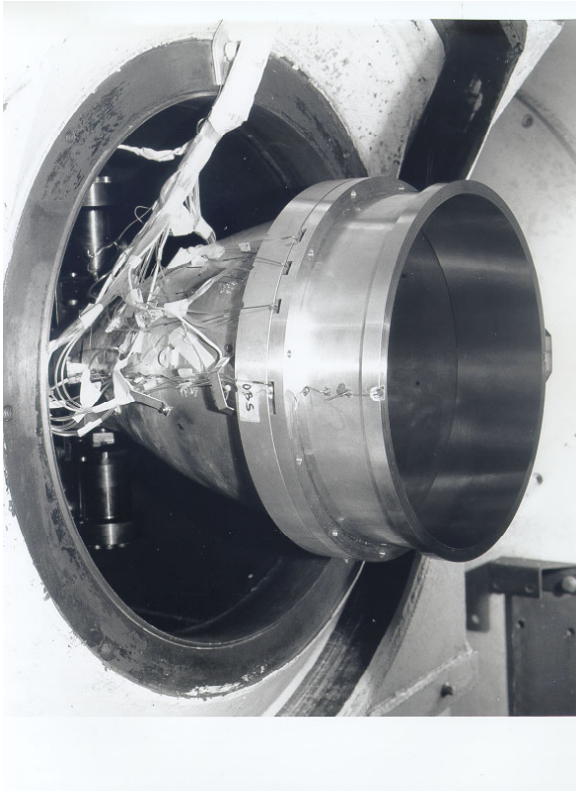
3

Figure 5: GSTP nozzle with extension in rig.

The chief objective was to study the impact on the end-effect side load peak. A small number of tests were carried out but the conclusion was very clear: The actual end-effect in the extension was almost extinguished due to the high pressure gradient.

New reference tests

The GSTP nozzle was designed with the geometrical definition of the Vulcain NE as a model. However, a more refined analysis was now employed in order to create a new reference nozzle. The idea was here not only to duplicate the nozzle wall geometry and pressure profile, but also to imitate the internal flow-field.
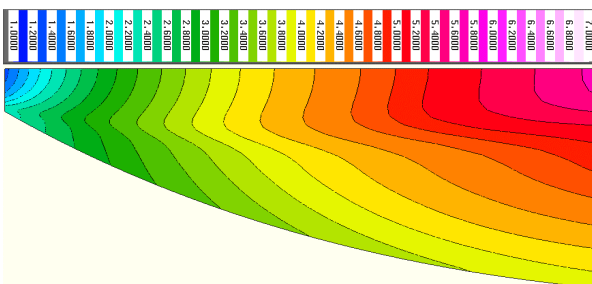
Figure 6 : Vulcain inner Mach number contours
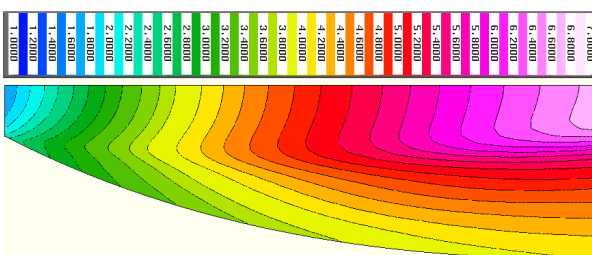
Figure 7 : V2+ sub-scale reference inner Mach number contours

As the chemistry is completely different, hydrogen / oxygen vs. air, it is impossible to get identical flow patterns. The contour was however made to have the same pressure profiles and the internal shock as close as possible to the Vulcain. The nozzle length was also increased to about 520 mm. The side load behaviour in the tests was close to the Vulcain case.
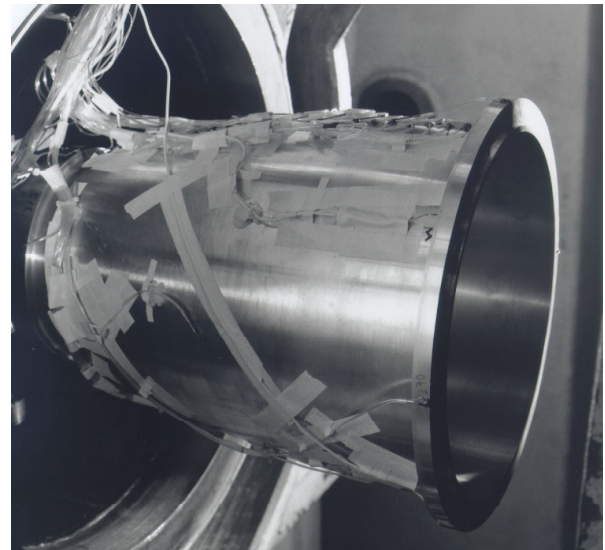
Figure 8 : Sub-scale Reference nozzle installed in rig
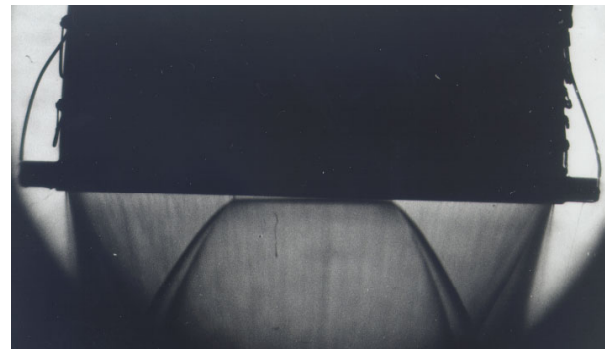
Figure 9: Schlieren picture: Reference of nozzle exit at full-flowing conditions

Polygon nozzle

The Polygon nozzle is a patented Volvo invention. The aim of the Polygon nozzle is to have a design with a side load reduction relative to a normal axi-symmetric nozzle. The shape is three-dimensional, see the figure below. The number of sides is envisaged to be 7-11. There is only a very small performance loss due to the asymmetry. The polygonisation can be done in several ways, depending on for which axial positions the effect is desired. Of high interest is also the transition from the circular to the polygon cross-section.

4
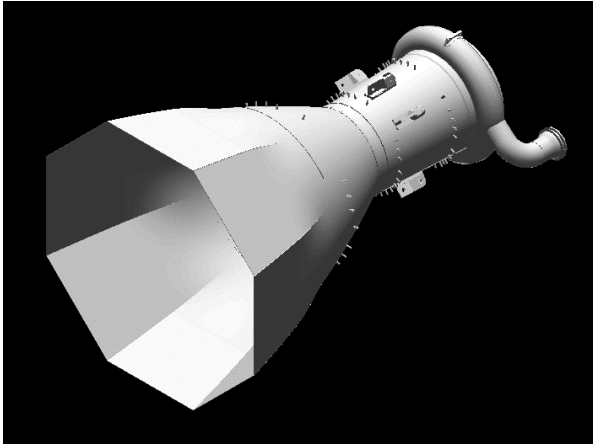
Figure 10 : Polygon nozzle, example on Viking-engine

There are three different side load reduction mechanisms that can be acting, depending on the exact design and the application.

- Stochastic circumferential flow pattern disruption. The polygon corners will act as a kind of structure-breaker leading to splitting of the separation flow pattern in circumferential direction. If the correlation in circumferential direction is indeed important for this part of the side load, it seems probable that asymmetry can give a reduction.

- Pressure difference and instability length being out of phase. When studying the resulting pressure field in the circumferential direction, it is seen that there is a phase difference between the pressure difference between attached and separated flow and the separation front instability length. This will lead to an aerodynamic side load decrease if a Schmucker-type model /5/ approach is used.

- Uneven separation leading to aero-elastic stabilisation. The aero-elastic model, such as described in /2/ was used for estimating the side load reduction of the polygon concept as a possible FSC concept. The fundamental reason for the side load reduction was the spreading-out of the separation line. When it reaches the exit, there is a smoother transition as only part of the separation line lies inside the nozzle at one time. This yields aero-elastic stability. This effect will depend very much on the design of the polygonisation in order to be efficient. The structure of the polygon can also have a stabilising effect in itself.

In the GSTP program, a second campaign was done in 1997 with polygon inserts. There were eight inserts put inside the GSTP nozzle exit to achieve asymmetric pressure distribution. These were attached at the exit, to reduce the side load stemming from the end-effect. Although the number of tests with comparable stiffness was not high, three, an average side load decrease of about 20% was recorded. The figure below shows that the pressure became highly three-dimensional in the tests.
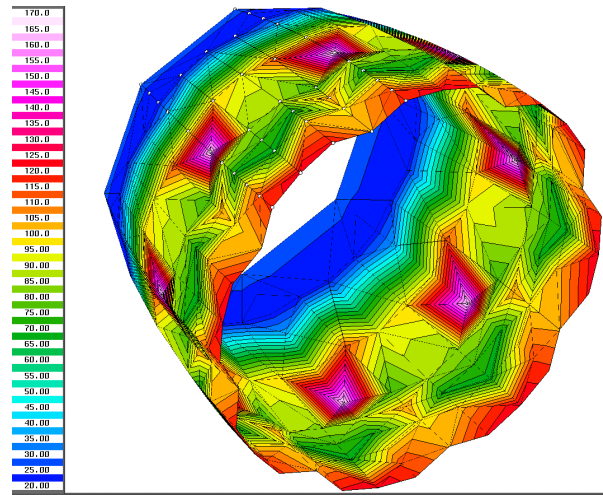
Figure 11 : Measured wall pressure distribution in GSTP nozzle with polygon inserts.

Polygon nozzle tests

Based on the experience from the GSTP activities in 1997 and 1998, a continued testing was carried out with a Polygon nozzle at FFA in late 1998. In order to have a complete comparability, the Polygon nozzle had an identical base-line contour as the Reference. The nozzle was made as an octagon with the polygonisation starting at the predicted position for the separation pattern transition.
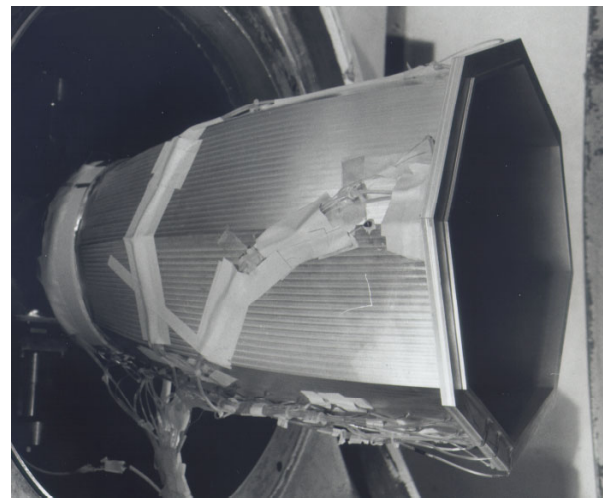

Figure 12 : Sub-scale Polygon nozzle installed in rig

The nozzle was run in 12 tests with good results. Extensive pressure measurements made a three-dimensional pressure mapping possible. The corners can be compared with the facets, defined as the point on each side with the smallest radius. In-between there is a mean point, in this case a 11.25 degrees. The mean point corresponds to the contour of the Reference axi-symmetric nozzle. Below is a plot of the pressures:
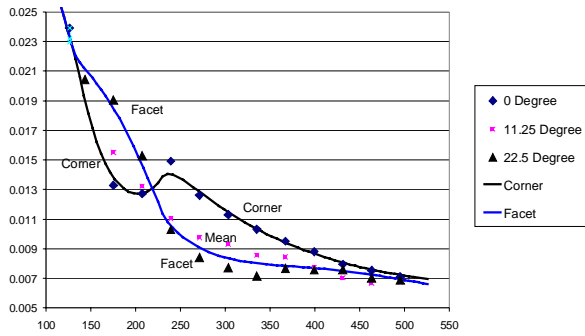
Figure 13 : Pressure measurements (bar) vs. axial coordinate (mm) compared with Navier-Stokes predictions for Polygon nozzle, full-flowing

The measured values are noted with squares, diamonds or triangles, whereas the CFD predictions are drawn as simple lines. As can be seen, the 3D-Navier Stokes predictions were very accurate. After the polygonisation has started the pressure drops rapidly in the corner, due to the larger radius. After a relatively short axial distance, the three-dimensional effect start to act however. This means that there is a flow towards the corners, and the pressure in the corner is increased. This leads to the pressure being lower on the facet than in the corner after some distance. Towards the exit, the pressures are balanced, and there is no effect from the polygon. Another illustration of the 3D-flow is shown below:
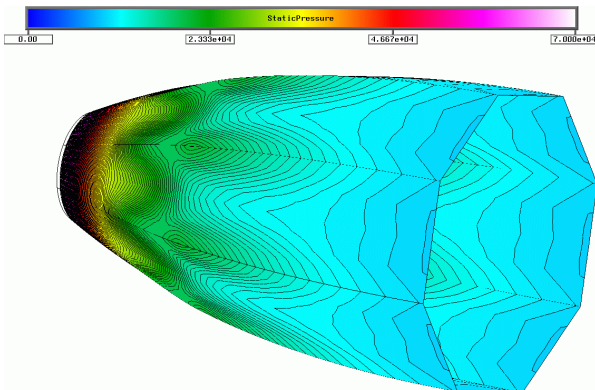
Figure 14 : CFD simulation of 3D wall pressure on Polygon nozzle

This simulation can be compared with the measured pressure distribution shown below. The flow features are very well predicted by the 3D Navier-Stokes simulation.
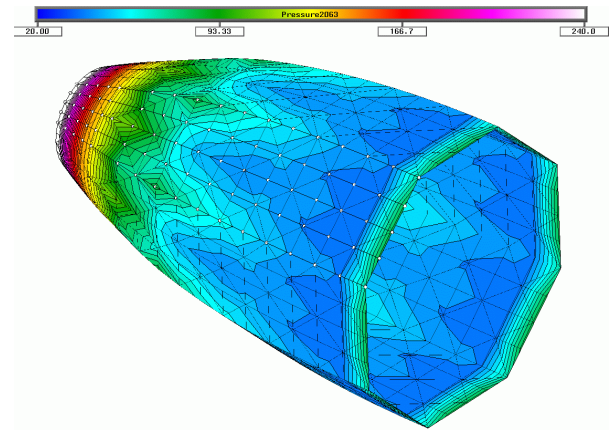
Figure 15 : Visualisation of measured wall pressures on Polygon nozzle

In order to get a feeling for the three-dimensional flow, it is also interesting to study the complex shock pattern at the exit:
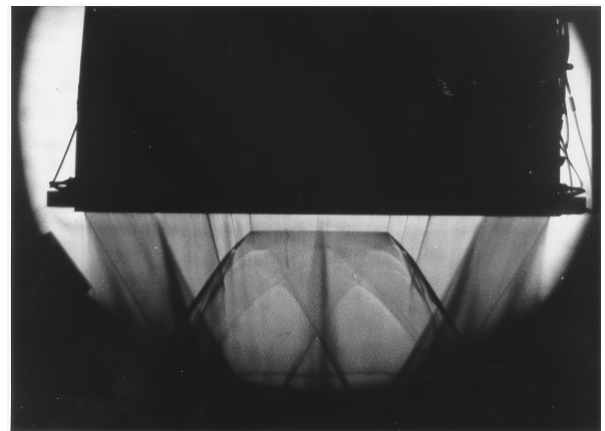
Figure 16 : Schlieren picture: Polygon nozzle exit at full-flowing conditions

The objective of the design was to have a side load reduction of the first side load peak, stemming from the transition between free-and restricted-shock separation. This is the critical side load for Vulcain-type nozzles. The goal was achieved conclusively after 10 tests, as both the mean, the median and the maximum side load was reduced with around 30%. This is the first actual side load reduction demonstration with an FSC concept in a rig test.

Dual-Bell nozzle tests

Another very interesting FSC concept is the Dual-Bell. This is a well-known nozzle type since several decades.. Actual testing with separation has however been very limited. In the testing described in /7/, for instance, separation and start transients are described, but no side load measurements were mentioned. The contour of the Volvo sub-scale Dual-Bell is equal to the reference in the first upstream section. This constitutes the first bell. The dual-bell contour used for this nozzle is then designed according to the principle of positive pressure-gradient in the second bell. This means that the separation front in theory will travel directly from the start of the second bell out to the exit during the start

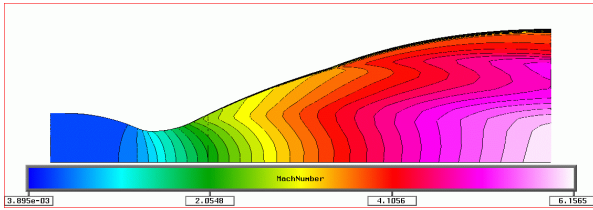transient. Below is shown a CFD-simulation of the nozzle flow

Figure 17 : Internal Mach number in Dual-Bell nozzle.

A shock emanating from the start of the second bell can be noted, although it is quite weak. The angle deviation from the first to the second bell is only about 5 deg. This was enough to assure a considerable pressure drop.
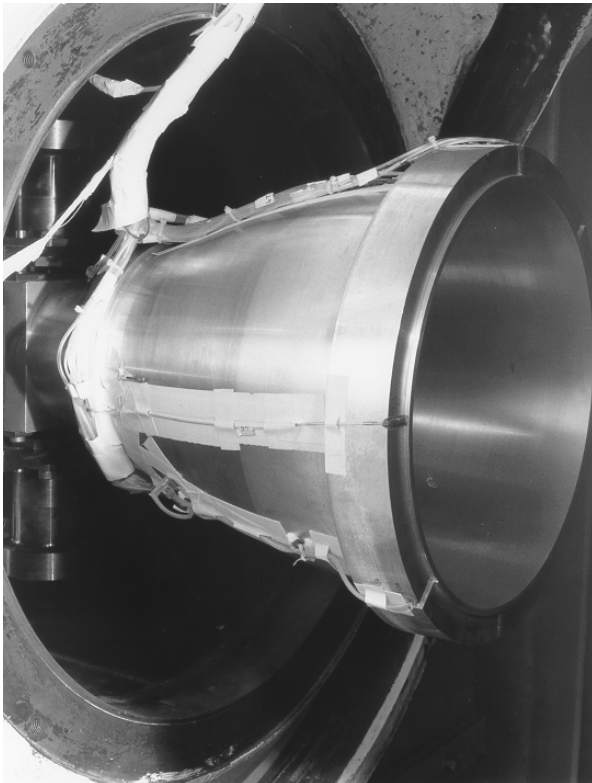

Figure 18 : Dual-Bell nozzle installed in rig (second bell starts at beginning of darker section)

A test campaign of 12 tests were run at FFA with the Dual-Bell nozzle in April 1999. The dual-bell operation functioned according to prediction as can be seen in the figure below. The positive pressure-gradient on the second bell has been achieved.
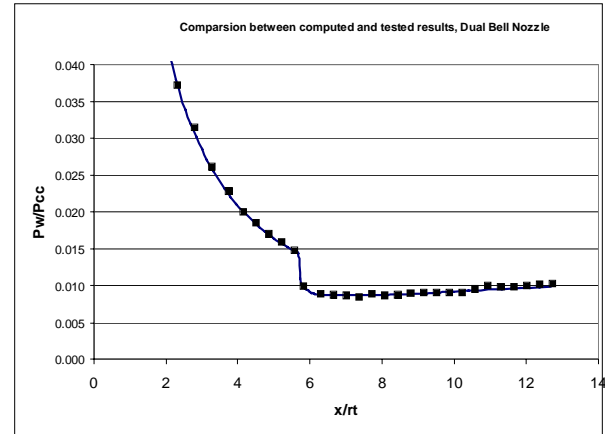
Figure 19 : Analytical and measured pressure profiles, dual-bell nozzle.

The flow pattern is very interesting. In the figure below, the complex pattern downstream of the nozzle during full-flowing operation can be seen.

Figure 20 : Schlieren picture at exit for full-flowing conditions, dual-bell nozzle.

The transition during start-up from the first to the second bell was very rapid. The jump was made in about 5% of the total transient time. The end-effect was almost completely extinguished at the start-up. The side loads corresponding to the separation pattern at the start-up were about 30 % smaller than the separation pattern transition side loads for the Reference nozzle. The end-effect side load at the shut-down stands for the highest torque level. The restricted shock separation is only stable for the shut-down.
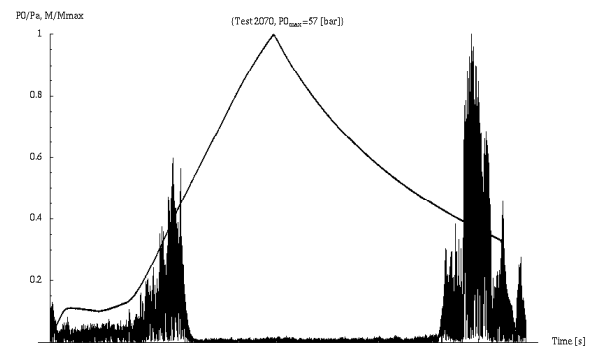

Figure 21 : Side load torques measured in test with Dual-Bell nozzle

7

The testing performed so far is summarised in the table below:

Campaign	Performed
GSTP 1 /1/	1997
GSTP / Polygon inserts /1/	1997
VolvoS1 / GSTP w. cardan	1998
VolvoS2 / GSTP w. extension.	1998
VolvoS3 / V2+ Ref.	1998
VolvoS4 / V2+ Polygon	1998
VolvoS5 / V2+ Dual-Bell	1999

Table 1 : Sub-scale testing in FSC program

Analytical model, aero-elastic coupling

The study of the closed-loop effects of jet separation has not been attacked vigorously due to the complexities involved in generating accurate asymmetric dynamic models of the nozzle-engine support system, the jet boundary layer separation, and interaction at the boundary of the two subsystems. A technique for handling these difficult coupling problems has been developed by Pekkari, /2/. The model is very useful for checking whether aero-elastic instability is present in the case of separated nozzle flow coupled to bending or pendulum modes. By simplifying the relations described in /2/ the following relation can be derived for the aero-elastic coupling :

$$\left(\frac{\Omega}{\omega}\right)^2 = 1 - \frac{(P_a - P_{sep})\rho_\infty \cdot u_\infty^2}{-\left(\frac{\partial P_\infty}{\partial x}\right)\sqrt{M_\infty^2 - 1}} \cdot \frac{r\pi(x \cdot Cos\tau + rSin\tau)}{K_m m L^2 \omega^2}\Bigg]_{x_{sep0}}$$

There is stability if the second term of the right hand side in the equation is lower than unity. If the contrary is the case, the equation will have a non-zero imaginary part in the solution, and there will be instability. The theory was applied to the GSTP nozzle case. The different spring cases were compared for the bending mode. The only spring that was unstable in the model was the "super-weak" one. This was also found to correspond to the actual behaviour in the tests.
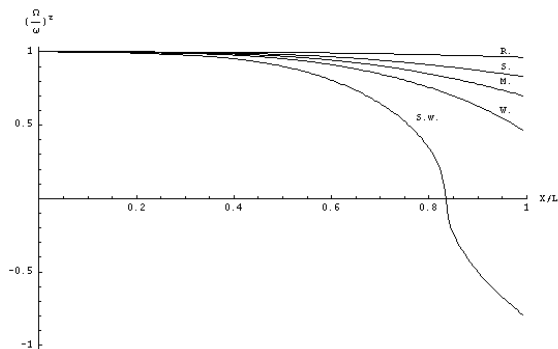

Figure 22 : Analytical aeroelastic stability for the different spring setups, S.W. =Super Weak, W. = Weak, M.=Medium, S.=Stiff and R.=Rigid spring respectively

Analytical model, separation transition

In parallel to the experimental investigations, an analytical model to predict separation transition has been created. The eventual objective is to create at Volvo an engineering model that can be used for accurate side load predictions. So far, in Europe, the Schmucker model /5/ has been used for predictions for sea-level nozzles. This model has however its shortcomings, as it does not take into account all the phenomena involved, as the separation transition. In the frame of the FSCD group, Volvo and DLR have been working with analytical models for predictions of side load transitions based on internal flow parameters.

The first aim of the Volvo model was to correctly predict when the transition from Free Shock Separation to Restricted Shock Separation takes place. It is important to know for which chamber pressure this side load peak will occur. This is interesting as this value tends to vary quite little, as opposed to the side load magnitude which has a considerable scatter.

Investigation made with sophisticated CFD tools and various turbulence models applied to Navier-Stokes calculations showed that it was difficult to find a general model that would give good agreement for many different cases. The present model is therefore based on inviscid 2D flow field calculations. By studying the internal flow field and the momentum balance, it has been possible to set an exact criterion for when the transition will take place.

The first step has been to make refined predictions of separation pressure, both for free- and restricted shock separation. These separation criteria come from both experimental and analytical work /1/. It is well known that the separation pressure for the restricted shock separation at a given chamber pressure will be below the one for free shock separation. This means that the restricted shock separation front will be located further downstream. The separation lines for the free- and restricted shock separation can then be plotted as chamber pressure versus axial position to follow them travelling downstream. By including the normal-shock position for the nozzle centreline, the occurrence of transition can be simulated when comparing the positions. Although this model is quite rough and in an early stage of development, it can still give a good measure of the momentum balance. The chamber pressure for transition from free to restricted shock separation is assumed to be proportional to the chamber pressure when the restricted shock separation is at the same position as the normal shock on the centreline.
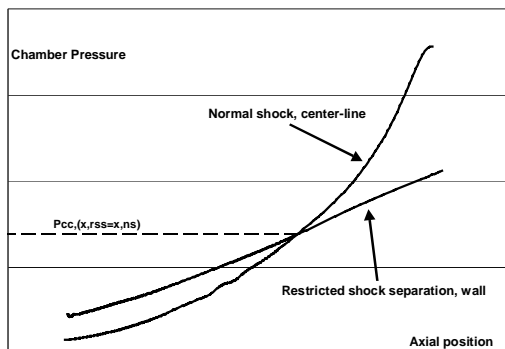
$Pcc,_{transition} = K \; Pcc,_{(x,rss=x,ns)}$

Figure 23 : Principle, transition model

After the transition has taken place, the back-pressure starts to increase again for the separation. This means that the separation position starts to move again towards the free shock separation position. When it approaches the same curve as for free shock separation , there is an actual transition again to free shock, and the second side load peak occurs, the end-effect.

The model can also take injected secondary film into account, as is used in the ANE demonstrator or Vulcain 2 NE. The Volvo film-cooling model /3 / is here used to calculate the separation characteristics which are influenced by the film-injection. The first version of this model has been tested for a number of cases with very good results:

Case	Pcc for transition: predicted / actual
Vulcain NE	0.88
ANE Demo	0.87
GSTP	0.97
V2+ Ref.	0.90
V2+ Polygon	1.00
V2+ Dual-Bell	0.92
J2s sub-scale	0.90
SSME	0.94
LEA Subscale parabolic contour /6/	1.00

Table 2 : Volvo-model for predicting at which Pcc there is an FSS to RSS transition.

One interesting feature is that the model also correctly predicts the absence of transition to Restricted Shock Separation. This will be the case when an Ideal Contour is used, as with, for instance, the Viking or the Russian RD-0120 nozzle.

Presently, the model is being extended to also be able to predict the magnitude of the side loads, taking also the mechanical characteristics into account.

Future plans

The studies of FSC and side-load reductions will continue with the following goals:

- Demonstration of further side load reduction experimentally

- Continued development of engineering side load model

- Studies of the physical nature of different types of separation and the origin of the side loads

- Application of theories to design of sea-level nozzles

Conclusions

The side loads are among the dimensioning loads for the sea-level rocket engine nozzles. To understand these loads is a central theme when designing optimised nozzles. The investigations at Volvo of side loads have lead to a number of interesting results:

- One side load peak for thrust-optimised nozzles stems from the transition from free to restricted shock separation

- This side load can be reduced by Flow Separation Control or side-load reduction devices. Two types, Polygon and Dual-bell have been tested with positive results.

- There are impacts on the side loads from the degrees of freedom, the pressure gradients and the stiffness of the nozzle.

- There can be both aerodynamic and aero-elastic drivers for the side loads

- The occurrence of the separation transition can be predicted by analytical means

Acknowledgements

References

/1/ A Sub-scale Test Program on Investigation of Flow Separation and Side Loads in Rocket Nozzles J.Mattsson et.al, ESA-SP-426, Dec 1998

/2/ Aeroelastic Analysis of Side Loads in Supersonic Nozzles with Separated Flow L.O.Pekkari AIAA 94-3377

/3/ Technology for the Film-Cooled Nozzle of the
Vulcain 2 Engine
M.Bigert et al. IAF-98-S.3.05

/4/ Nozzle and Turbine Impact on Launcher
Performance
M Bigert, AIAA 94-3380

/5/ Status of Separation Prediction in Liquid Propellant
Rocket Nozzles
R.H.Schmucker NASA TM X-68490

/6/ Measurements of side loads in an overexpanded
parabolic nozzle,
S.Girard, T.Alziary de Roquefort, Laboratoires d'Etudes
Aérodynamiques, Université de Poitiers, UMR CNRS
6609.

/7/ Dual-Bell Altitude Compensating Nozzles
M.Horn,S.Fischer Rocketdyne, NASA 94-23057

/8/ Status of Flow Separation Prediction in Rocket
Nozzles
M.Frey, G.Hagemann, AIAA 98-3619

Paper 3

AIAA 99–2583

ASSESSMENT OF TURBULENCE MODELS IN OVEREXPANDED ROCKET NOZZLE FLOW SIMULATIONS

Jan Östlund
Volvo Aero Corporation, SE-46181, Trollhättan, Sweden
Mattias Jaran
The Aeronautical Research Institute of Sweden,
Box 11021, SE-16111 Bromma, Sweden
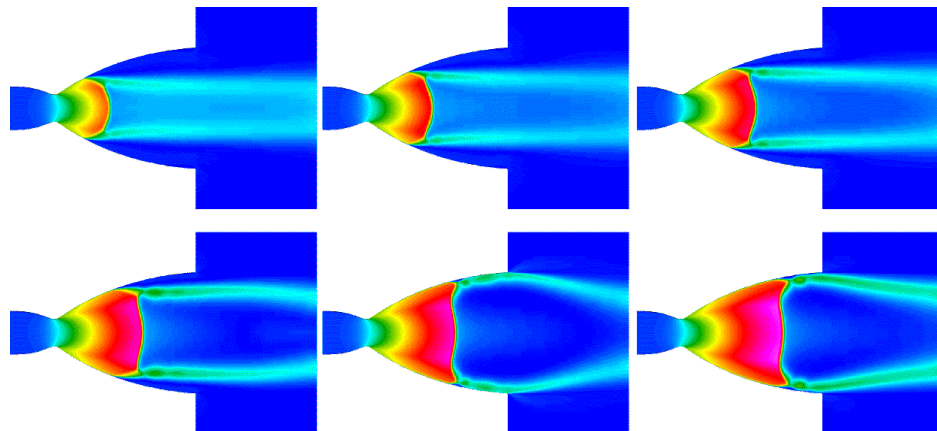
35th AIAA/ASME/SAE/ASEE
Joint Propulsion Conference & Exhibit
June 20-23, 1999/Los Angeles, CA

ASSESSMENT OF TURBULENCE MODELS IN OVEREXPANDED ROCKET NOZZLE FLOW SIMULATIONS

Jan Östlund[*]

Volvo Aero Corporation, SE-46181, Trollhättan, Sweden

Mattias Jaran[†]

The Aeronautical Research Institute of Sweden, Box 11021, SE-16111 Bromma, Sweden

A report is given on the initial validation of Navier-Stokes predictions of turbulent, separated flow in an overexpanded bell nozzle. The CFD predictions are compared to sub-scale wind tunnel test data using a scaled Vulcain nozzle. The test chamber pressure has been varied to simulate the shock hysteresis region of start-up and shut-down. The suitable choice of turbulence model, boundary conditions and CFD solution procedure is investigated by comparison to measured wall pressure data. The details of the turbulent fields of the four investigated turbulence models are compared, as well as its effect on the boundary layers, shocks and separation locations.

Nomenclature

M	Mach number
P	Pressure, Pa
T	Temperature, K
x, y, z	Cartesian axes, m
u, v, w	Velocity in x,y,z, m/s
V	Velocity m/s
k	Turbulent kinetic energy, m^2/s^2
ρ	Density, kg/m^3
ω	Specific dissipation rate, 1/s
μ_t	Eddy-viscosity, kg/ms^3
P_k	Production of turb. kin. en.
D_k	Dissipation of turb. kin. en.
EVM	Eddy viscosity model
SST	Menter shear stress transport model
BSL	Menter base line model
KWL	Wilcox k-ω model with limiter
KWS	Standard Wilcox k-ω model
FSS	Free shock separation
RSS	Restricted shock separation

Subscripts

w	Wall
amb	Ambient condition
s	Stagnation condition

Introduction

Background

SOME rocket engines suffer severe dynamic loads during operation at chamber pressures below the design pressure. This operational condition typically occurs during the start up and throttle down process of the rocket motor at sea level. These loads can sometimes be of such a magnitude that they present life limiting constraints on thrust chamber components as well as on the thrust vector control system. The source of these loads is generally attributed to the in stationary nature of the partially detached and partially attached flow that occurs during operation of the thrust chamber at overexpanded conditions.

The most well known of these dynamic loads that have received attention in the literature is the so called side load.[1][2] Side loads have been observed during start up of overexpanded sea level liquid propellant rocket engines as well as during ignition and the staging of a multi stage solid propellant rockets.[3][45] Due to the severe complications experienced with high levels of side loads, it is one of the most important features in sea level nozzle design. It has e.g. been taken into account for the contour definition for the Vulcain 2 nozzle extension.[6]

The traditional design approach for bell type nozzles is to design the nozzle contour and area ratio such that attached flow and low levels of side-loads are guaranteed at nominal operation at high ambient pressure, sea level conditions. Further, the structure is designed robust enough to withstand the side loads during the throttling up and down process. The reduced performance under vacuum ambient condition and the corresponding weight penalty with a robust design, is accepted with this design approach. Increasing demands for improved launcher performance, however, push the development of new concepts. One possible solution is to adapt the nozzle contour during flight to the changes of ambient and chamber pressure. At-

---

[*]Aero Design Engineer, Space Propulsion Division. Jan Östlund changed his name from Mattsson in Jan 1999.

[†]Research Scientist, Computational Aerodynamics Department.

tempts in this direction, however, have so far not been successful due to the weight and mechanical complexities of such devices. By introducing so called Flow Separation Control Devices (FSCD), high area ratio nozzles can be operated at separated condition at sea level without severe loads, and an improved overall performance is obtained. The feasibility of such devices is under demonstration. The main reason why such devices do not yet exist in full scale is that several basic questions regarding the nature of separation phenomena and the corresponding side loads remain to be answered.

Within the Flow Separation Control (FSC) program at Volvo Aero Corporation (VAC) the flow separation phenomenon in sea level rocket nozzles with corresponding side load features have been investigated. In the course of the work, detailed aerodynamic and aeroelastic sub scale testing have been performed in the modified hyper sonic wind tunnel HYP500 at the Aeronautical Research Institute of Sweden (FFA), under a contract with the European Space Agency (ESA) and the Swedish National Space Board (SNSB).[78] Steady state axisymmetric CFD analyses of the sub scale tests were performed in parallel with the experimental investigations. The analysis revealed a significant change of flow separation pattern at specific pressure ratios in close relation to the points where unsteady side loads were found in the experiments. The change in flow pattern in the calculations showed considerable hysteresis with regard to the pressure at which it occurred, and when increasing or decreasing the driving pressure, see illustrating figure (1). This was in accordance with the experimental findings.

Separated Nozzle Flow Physics

The flow in an overexpanded nozzle is of mixed supersonic/subsonic type with shocks interacting with the nozzle wall boundary layers and a nearly inviscid core flow. The internal shock structures and shock wave/boundary layer interactions produce strong adverse pressure gradients which may give rise to separated, recirculating flow. As reported by Mattsson[7] the two main flow field types found in the present over expanded nozzle feature separation from the wall without reattachment at lower driving pressures, labeled free shock separation (FSS), or with reattachment at higher driving pressures, labeled restricted shock separation (RSS). The solution with free shock separation remains to higher driving pressures during the start up phase and the restricted shock separation solution tend to remain when the driving pressure is lowered. This accounts for the hysteresis effect found in the experiments as well as in the computations, see figure (1).

When starting the nozzle and increasing the chamber pressure (P_s), at first the flow is separated in the free shock separation mode. In the free shock sep-
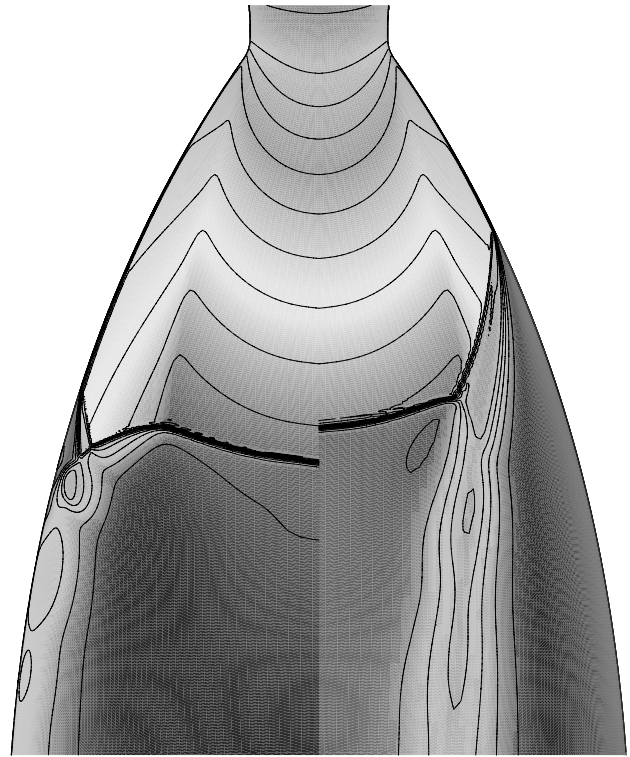

Fig. 1   Illustration of free shock separation (right) and restricted shock separation (left) in the hysteresis region, at a pressure ratio (P_s/P_{amb}) of twelve.

aration regime the flow separates from the wall and the wall pressure rises to a plateau pressure, close to the ambient pressure. The source of this rise is due to the oblique shock originating from the separation point. Downstream the steep pressure gradient region, in the open recirculating zone, the wall pressure increases slowly to almost ambient pressure. As P_s is increased, the hysteresis region is entered, and the flow stays in the free shock separation mode. At the limit were the hysteresis region is exited, the separation pattern changes to restricted shock separation and a closed recirculation zone is formed. The plateau pressure in this closed recirculation bubble is lower than the plateau pressure in the open recirculating zone in the free shock separation case, and a jump of the separation point in the downstream direction occurs. Due to the reattachment of the flow, the wall pressure features an oscillating behavior with values above the ambient pressure. This irregular behavior is caused by the expansion and compression waves, which interacts with the supersonic jet boundaries to match the ambient air. The sudden change of the separation pattern from free to restricted shock separation is connected to significant side loads for the nozzle.

The restricted separation mode itself is stable until the reattachment point reaches the nozzle exit, where a second peak in side load has been found, due to an unsteady phenomena named the end effect. The end effect takes place as the recirculating zone open up and

the plateau pressure behind the separation shock is suddenly increased, as ambient air is sucked in to the nozzle. This pressure increase forces the separation point to move upstream with a subsequent closing of the recirculating zone, again. This procedure repeats its self until the triple point between the separation shock and the internal oblique shock has been transported out of the nozzle.

When decreasing P_s, the same phenomena can be observed but in reversed order. However, the flow stays in restricted separation mode until the lower limit of the hysteresis region is encountered where the transition from restricted to free shock separation takes place.

This entire phenomena have been found in both full scale and cold flow sub scale rocket nozzles of Rao-type.[7] The existence of two different separation topologies is thus a consequence of the chosen contouring method, and not the nozzle size or the working gas.

In the present investigations, an emphasis has been placed on the role of the turbulence modeling in simulating separated nozzle flows as described above. An in depth investigation has been performed to assess the influence of inflow turbulence levels, in the free stream and in the shock regions. Also, a comparison to experimental data for three different driving pressures, in and outside the hysteresis region, is presented.

Numerical Method

The Solver

The simulations have been performed using the EURANUS[9] code developed under contract by the European Space Agency, by FFA, VUB in Brussels and other cooperation partners. EURANUS is a finite volume code for the Reynolds-averaged Navier-Stokes equations. At present the code incorporates a number of turbulence models. Emphasis has been put on the improvement and validation of the code for computing flows including turbulent separation. A number of different schemes may be selected for the spatial discretization. For the present calculations second order central differences were used for the main equations and a second order upwind scheme for the turbulent equations. Solutions to the steady state problems are usually obtained with Runge-Kutta time stepping, with local time stepping, multigrid and residual implicit smoothing used to accelerate convergence.

Turbulence Modeling

Different turbulence models have been tested, all Eddy Viscosity Models (EVM) based on the Boussinesq hypothesis, which is used to close the Reynolds averaged Navier-Stokes equations. Eddy viscosity models are the industrial standard models, today. Many models have been proposed and a few have become widely accepted. We have focussed on the k-ω class of models because of their known ability to predict pressure gradient flows and the success of some of its variants, notably the Menter SST model, to predict flow separation in other cases.

Since the purpose was to test different models, with different turbulence modeling, the following models were selected. As a reference, and for being very well known, the Wilcox[10] k-ω model. The k-ω model was also used together with a limiter on the production for the turbulent kinetic energy, see equation (2) to try to assess the influence of that type of limiter, see figure (2) for an illustration. Furthermore, two models developed by Menter[11] were added. His BSL and SST models differ by the boundary layer treatment. The SST model includes a limiter on the ratio of production to dissipation (P_k/D_k) in the boundary layer. This makes the boundary layer more likely to separate, since it can take less strain. Both models include the so called cross diffusion term that should make the boundary layer insensitive to the free stream ω. Both models also include a limiter on the production of the turbulent kinetic energy in the free stream.

Turbulent Production Limiter

Different codes have different limiters on the production of turbulent kinetic energy. One common type of limiter, that is also specified in the two Menter models,[11] is to limit the production (P_k) by the dissipation (D_k). Menter's models have

$$P_k = \min(P_k, 20 \cdot D_k). \qquad (1)$$

As discussed above, the Wilcox k-ω model has been used in these simulations together with a limiter on P_k. The limiter was proposed by Wallin,[12] and worked well for this type of problem.

$P_k = \min(P^{EVM}, P^{LIM})$, where

$$P^{LIM} = \rho K \sqrt{\frac{P^{EVM}}{\mu_t}}. \qquad (2)$$

For the Wilcox k-ω model, this limiter is not active for $P^{EVM} < \epsilon/C_\mu$, which implies that the limit would not be active for $P_k/D_k < 10$, and hence not interfere with the prediction capability of the model in general.

Geometry

If the nozzle length,[6] from throat to exit is used as a scaling factor and set to unity, then the dimensions of the computational geometry is as follows. The length of the inlet channel is about 4, and the purpose of it is to isolate the nozzle from the inflow boundary condition. At the nozzle exit, the height of the expansion chamber is three times the height of the nozzle. The upper boundary of the expansion chamber has a thirty degree positive angle with the symmetry axis, this is so that an inflow boundary condition can be used with a small velocity in the x direction only. The expansion chamber length is at about 10 in the units defined above.
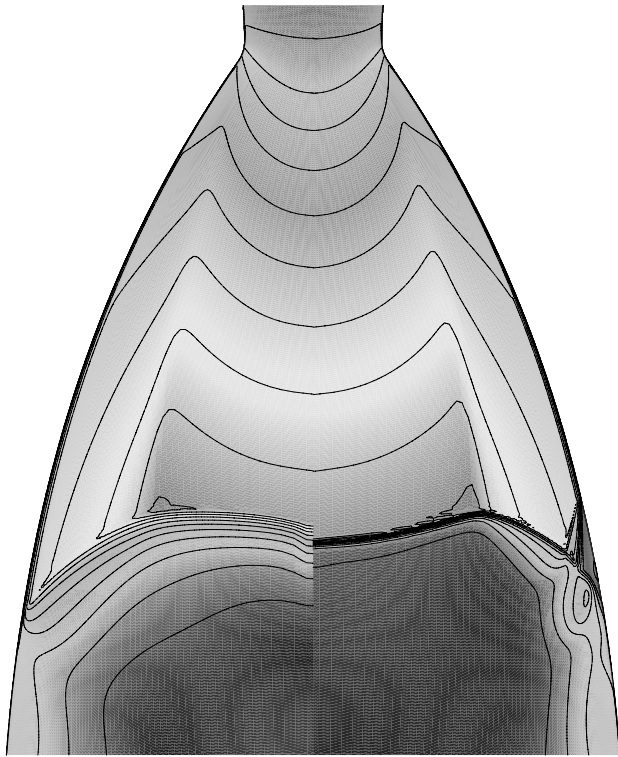
Fig. 2   Illustration of restricted shock separation, with (right) and without (left) turbulent production limiter, at a pressure ratio (P_s/P_{amb}) of 16.2.

Boundary Conditions

In this paper the atmospheric conditions were 290 K, and 0.10 MPa. The stagnation conditions in the nozzle were 500 K, and 0.60, 1.20, and 1.62 Mpa. The turbulence level at the inlet were varied as in table (1), and for the comparison to the experimental data, k=0.01, and ω=500, was selected. Air was used as the driving gas, as in the wind tunnel experiments, for all simulations.

The simulations are treated as axisymmetric, with a three degree opening angle. Symmetry boundary conditions are used at the symmetry planes. A singular polar line is used at the symmetry axis, which imposes the flow direction to be along the symmetry axis. Stagnation conditions are used at the nozzle inlet, where the direction of the flow is imposed and the turbulent quantities are not allowed to fluctuate. An adiabatic wall is used at the channel wall, leading to the nozzle inlet, where the nozzle wall also is treated as adiabatic. The nozzle wall thickness, at the nozzle exit, is modeled as an adiabatic wall with a wall thickness of about one fifth of the nozzle throat radius. The external inflow boundary condition is of the Riemann invariant type, with atmospheric conditions and about 50 m/s in inflow velocity. At the outflow, an extrapolation boundary condition is used. The reason for not using a lower inflow velocity is strictly practical from a numerical point of view. During the start up sequence, the flow could get reversed at the outlet, since

an extrapolation boundary condition was used there. There should be no influence on the nozzle flow by this procedure, so the simulations are as if the nozzle was stationary.

Results & Discussion

Grid Convergence

Three grids were studied for the purpose of showing grid convergence. The grids are multigrid multiples of each other, and have the resolution 101·37, 201·73, and 401·145 in the nozzle. Outside the nozzle about the same amount of nodes are spent additionally.

The grids were designed so that even the coarsest grid would be able to resolve the relevant flow structure. Only very minor differences exist between the medium and fine grid solutions. Still, it turned out that a three level multigrid solution method on the fine grid used about the same computer time as a single grid method on the medium grid, where a three level multigrid method did not converge well.

Since no additional computer cost permitted runs at a finer grid level, it was decided to do so. Hence, all quantitative simulations have been performed on the fine grid with a three level multigrid method.

Sensitivity to Turbulent Inflow Conditions

A series of simulations were conducted to investigate the sensitivity to, and establish, reasonable turbulent inflow conditions. A test matrix was set up, and ran at free separation conditions with a pressure ratio (P_s/P_{amb}) of six.

Table 1   Test matrix to determine correct turbulent inflow conditions.

Std k-ω	Limited k-ω	Menter SST
k=0.01, ω=500	k=0.01, ω=500	k=0.01, ω=500
k=0.10, ω=500	k=0.10, ω=500	k=0.10, ω=500
k=1.00, ω=500	k=1.00, ω=500	k=1.00, ω=500

It was decided to check the inflow conditions at a station half way between the start of the converging section of the nozzle and the nozzle throat, on a grid line from the symmetry axis to the nozzle wall. At this location, a turbulent boundary layer has been established and the flow is accelerating towards the throat. Also, the nozzle inlet was extended far upstream, so that the nozzle was well isolated from the inflow boundary condition.

In general, the influence of the free stream turbulence level was small, for the pressure ratio investigated. No significant influence was found, except for the levels of μ_t in the free stream, see figure (7a). These are high due to the higher levels of turbulent kinetic energy, specified in table (1), which is shown in figure (7e).

Other global measures, such as the velocity profiles in figure (7d) or the turbulent variables in figures (7b - 7c) showed little or no scattering between cases. For example, the main difference in the peak turbulent kinetic energy (k) over all tested models and inflow conditions was about ten percent. The dissipation rate (ω) showed very little difference between cases as seen in figure (7c).

It has been reported[13] that the standard k-ω model suffers from an unphysical free stream sensitivity when it comes to ω. From the results in the present simulations, no significant influence is found physical or not, see figure (7c). Simply, in a complex flow like this, the downstream development of ω cannot be controlled by a realistic variation of the inflow boundary condition.

For the quantitative comparison to experimental data, the lowest values of the turbulent intensity were chosen, since they produce the most physically correct looking eddy viscosity distribution, see figure (7a).

Sensitivity to Shock Modeling

For the test cases in table (1), the modeling over the shock waves were investigated. The results were established by looking at the variation along the center line of the nozzle.

From figure (8c), it is seen that the turbulent kinetic energy grows dramatically over the shock for the standard Wilcox k-ω model, which has no turbulent production limiter. Behind the shock, a turbulent fluctuation $u' \sim \sqrt{k}$ is of the same order of magnitude as the main flow u velocity, which is unrealistic.

As a consequence, the eddy viscosity (μ_t) in figure (8b) also grow to high levels. The eddy viscosity stays at a high level in the nozzle, behind the shock. Outside the nozzle the levels of μ_t increase again. From figure (2) it is seen what happens inside the nozzle for the very high level of μ_t, present in the simulations with no production limiter. The shock is smeared out and the flow behind it has no real structure, since the μ_t levels do not drop, as mentioned.

Finally, it is seen in figure (8a), that the point of separation from the nozzle wall is influenced by the production limiter. The two models based on the Wilcox k-ω model, separate at different locations. The model with the limiter separates just upstream of the one without. For this driving pressure, the separation is of free shock separation type for all models, as it should be, and the difference most likely lies in the way the shock and the back pressure is resolved. For the restricted separation type, the flow field is different and it is more obvious from figure (2) why the separation is late.

The present results clearly show the importance of a limited production of turbulent kinetic energy over the shock. From a simple analysis[12] it can be shown that the turbulent production over a shock for an EVM is almost unlimited and grid dependent. As shown by the behavior of the models incorporating a limiter, a more realistic result is feasible. Also, a strong shock is just the place were a turbulent production limiter will have an influence, and hence the actual limit of the highest possible production makes a difference. The actual values of the limiters have not been investigated here, but obviously a limiter is needed to produce reasonable results.

Comparison to Experimental Data

A complete engine cycle has been simulated. Hence, the driving pressure was increased from a low starting level to the level where a full flowing nozzle is achieved. Then, the driving pressure was decreased as during a shut down. This ramping was made in small steps, and the solution was fully converged for each pressure level. Inflow turbulent conditions are specified as the lowest turbulence intensity in table (1), and the fine grid is used.

Results are shown for three different driving pressures in figures (3 - 6). In figures (4 - 5), the hysteresis phenomenon is shown with two different flow fields at one driving pressure. As the figures show, only the Menter SST model was able to capture the correct separation type during the pressure increase and decrease. Still, the pressure in the supersonic jet, downstream of the separation, show some difference compared to the experimental data, meaning that the model only give qualitatively correct results.

All of the other models fail to predict the free shock separation mode at Ps/P_{amb}=12. Ordering the models in a descending order, the BSL model performed second best, followed by the Wilcox k-ω model with the turbulent production limiter, and last the standard Wilcox k-ω model. The BSL model generally separates before the k-ω models, see figure (3), and therefore is closer to the experiments. The reason for the earlier separation is not clear at the present. The limited k-ω model performs reasonable to, in the sense that it can reproduce the details of the flow, to some degree. The standard k-ω model should not be used in simulations with shocks.

In general, the free and restricted shock separation modes are set up by the respective location of the point of separation and the location of the main normal shock.[8] The influences on the location of the main, almost normal, shock are the surrounding pressure, and if any, the pressure in the closed recirculation area behind the shock. These pressure levels are generally modeled almost the same by different models. What does differ more, is the location of the point of separation. As have been pointed out in this paper, relatively small changes to an existing model can improve the ability to predict separation. Improved separation prediction has also proven effective for predicting the correct separation type in the present nozzle.
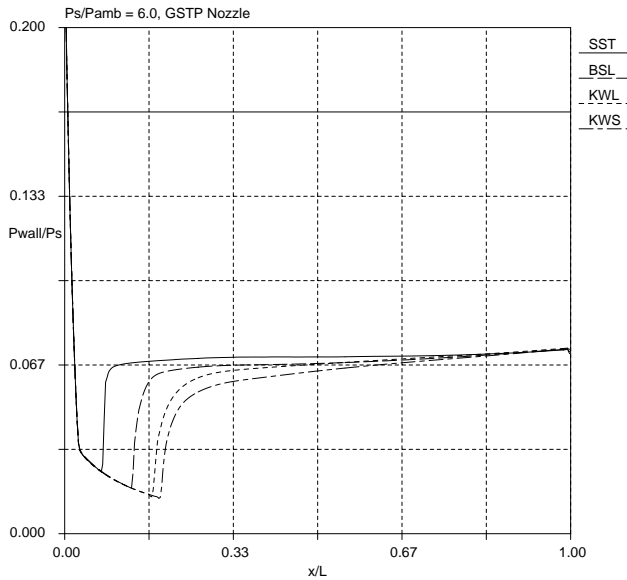
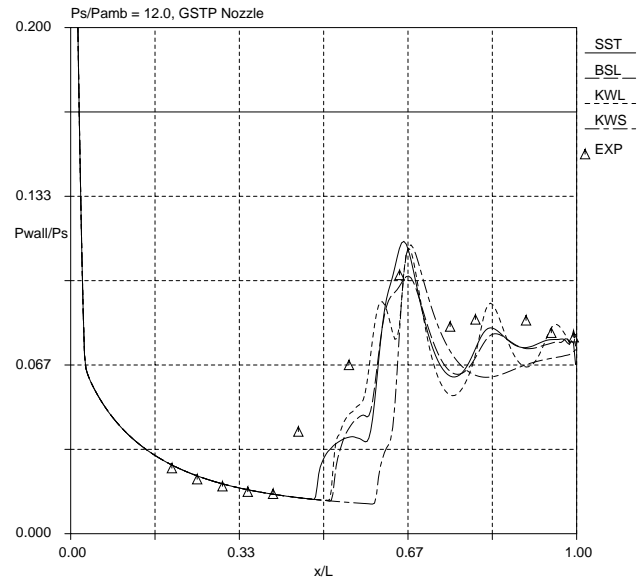**Fig. 3 Free shock separation for a pressure ratio (P_s/P_{amb}) of 6.**

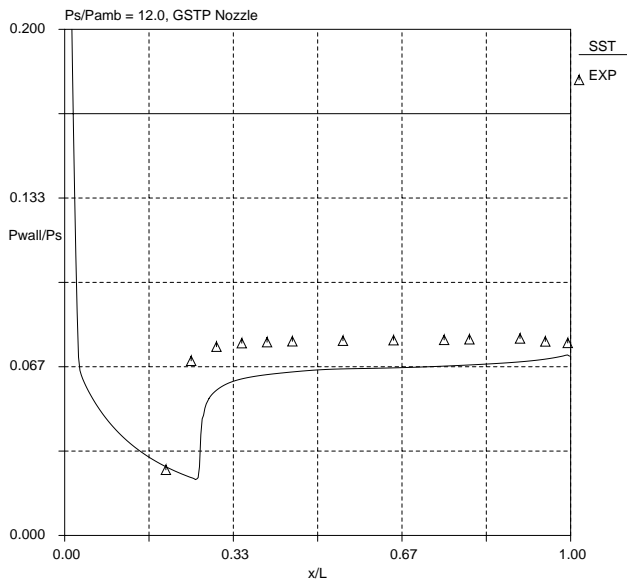**Fig. 5 Restricted shock separation for a pressure ratio (P_s/P_{amb}) of 12.**

Fig. 4 Free shock separation for a pressure ratio (P_s/P_{amb}) of 12.
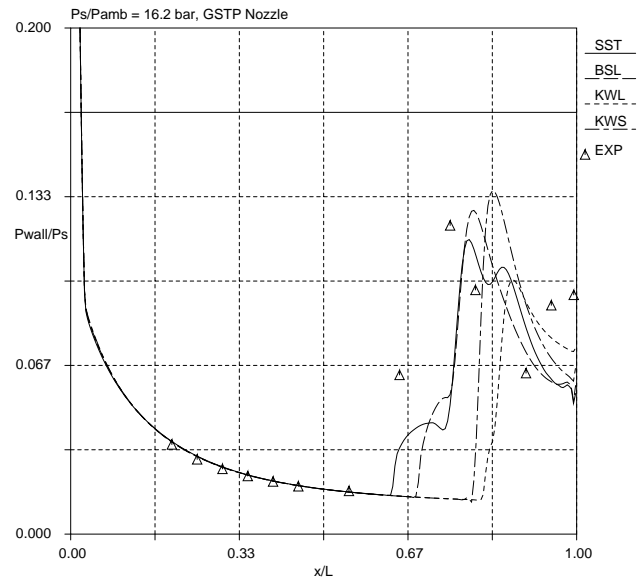

Fig. 6 Restricted shock separation for a pressure ratio (P_s/P_{amb}) of 16.2.

Conclusions

The results in this paper show that it is possible to predict the separation pattern in the present rocket nozzle, reasonably well, as it is started and closed, using standard two equation turbulence models and steady state methodology.

Most important is to have a physical limiter on the production of turbulent kinetic energy over the shocks. Without the limiter, the turbulent fluctuations behind the shock will contain as much energy as the main flow. This generates high levels of the eddy viscosity which will destroy the flow structure behind the shock.

The inflow conditions did not have an influence on the global variables, like the velocity profiles, the turbulent kinetic energy (in the boundary layer), or the turbulent dissipation rate (in the boundary layer). Also, no influence on the point of separation or on the locations of the shocks were found. Hence, the inflow conditions are not of primary importance.

It is shown, together with the references, that key to getting the correct results is the point of separation from the nozzle wall. It is most likely the point of separation that determines the structure of the flow, and hence a model with good separation qualities should be preferred.

Acknowledgment

References

[1] Schmucker, R. H., "Flow processes in overexpanded chemical rocket nozzles, Part 1: Flow separation," NASA TM–77396.

[2] Nave, L. H. and Coffey, G. A., "Sea level side loads in high area ratio rocket engines," AIAA Paper 73–1284, 1973.

[3] Bowyer, J. M., K. G. W. and E., P. R., "An investigation of the Side Force that is Sometimes Observed in Rocket Motor Start-Up," AIAA Paper 78-1045, 1978.

[4] Luke, G. D. and Adams, D. E., "Use of Nozzle Trip Rings to Reduce Nozzle Separation Side Loads During Staging," AIAA Paper 92-3617, 1992.

[5] Romine, G. L., "Nozzle Flow Separation," *AIAA Journal*, Vol. 36, No. 9, 1998.

[6] Bigert, M. Stenholm, T. and Sätmark, T., "Technology for the Film-Cooled Nozzle of the Vulcain Engine," IAF-98-S.3.05.

[7] Mattsson, J. Torngren, L. and Högman, U., "A Sub Scale Test programme on investigation of flow separation and side loads in rocket nozzles," *Third European Symposium on Aerothermodynamics for Space Vehicles*, ESTEC, Nordwijk, The Netherlands, Nov. 1998.

[8] Östlund, J. and M., B., "A Sub Scale Investigation on Side Loads in Sea Level Rocket Engines," AIAA Paper 99–2479, Jun. 1999.

[9] Rizzi, A., Eliasson, P., Lindblad, I., Hirsch, C., Lacor, C., and Hauser, J., "The Engineering of Multiblock/Multigrid Software for Navier-Stokes Flows on Structured Meshes," *Computers Fluids*, Vol. 31, 1993, pp. 341–367.

[10] Wilcox, D. C., *Turbulence Modeling for CFD*, No. ISBN 0–9636051–0–0, DCW Industries Inc, 1993.

[11] Menter, F. R., "Zonal Two Equation k-ω Turbulence Models for Aerodynamic Flows," AIAA Paper 93–2906, Jul. 1993.

[12] Wallin, S., "Personal communication, to be published in," *AVTAC/DEL/FFA/D3.2C3*, May 1999, pp. 13–14.

[13] Menter, F. R., "Influence of Freestream Values on k-ω Turbulence Model Predictions," *AIAA Journal*, Vol. 30, No. 6, 1993, pp. 1657–59.
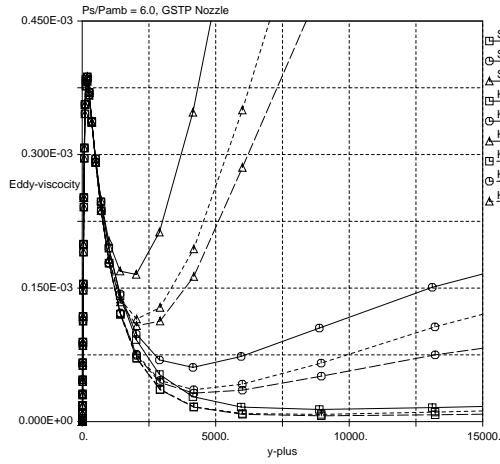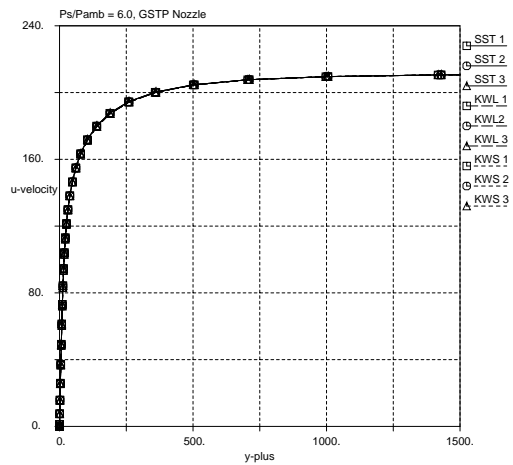
a) Eddy viscosity (μ_t). Turbulence levels as defined in table (1) and models as defined in the Nomenclature.
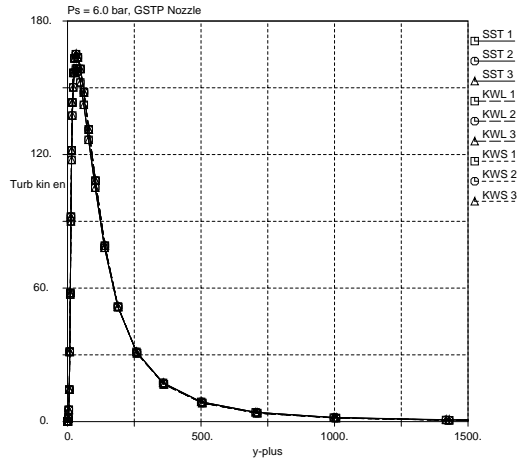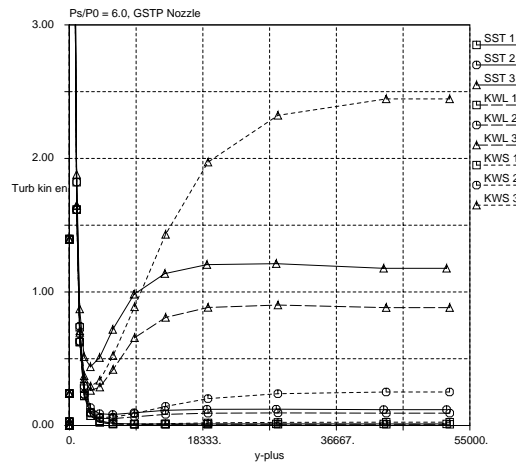

b) Turbulent kinetic energy (k). Turbulence levels as defined in table (1) and models as defined in the Nomenclature.
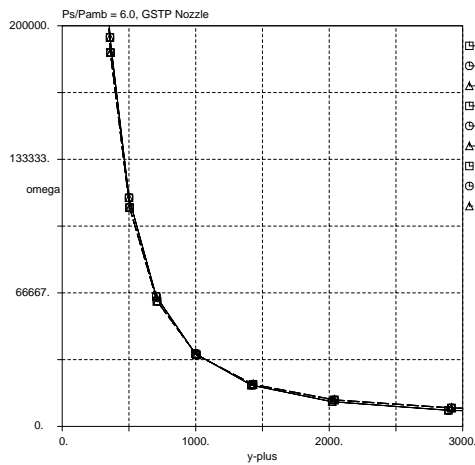
c) Turbulent dissipation rate (ω). Turbulence levels as defined in table (1) and models as defined in the Nomenclature.
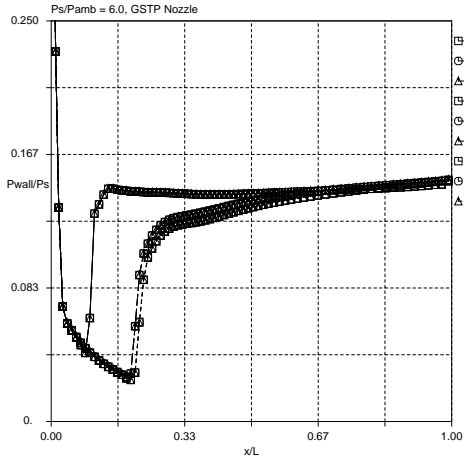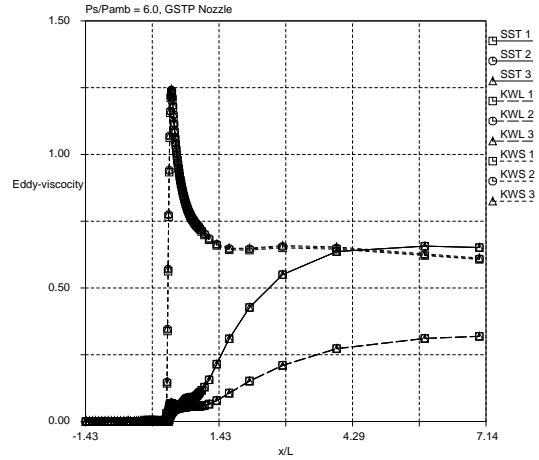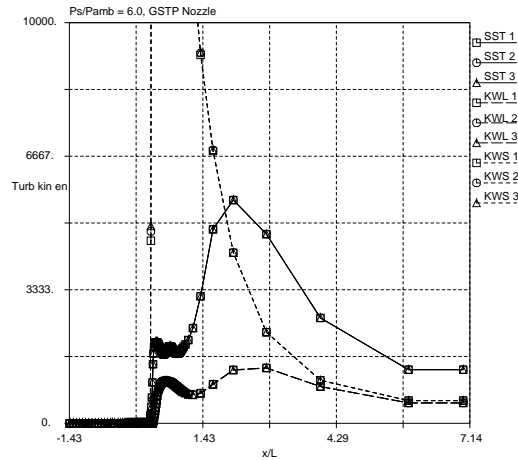

d) U velocity profiles. Turbulence levels as defined in table (1) and models as defined in the Nomenclature.

e) Turbulent kinetic energy (k). Turbulence levels as defined in table (1) and models as defined in the Nomenclature.

Fig. 7   Evaluation of different turbulent inlet conditions.

a) Wall pressure, indication point of separation. Turbulence levels as defined in table (1) and models as defined in the Nomenclature.

b) Eddy viscosity (μ_t) on centerline. Turbulence levels as defined in table (1) and models as defined in the Nomenclature.

c) Turbulent kinetic energy (k) on centerline. Turbulence levels as defined in table (1) and models as defined in the Nomenclature.

Fig. 8   Evaluation of turbulent variables over the shock on the centerline.

Paper 4

AIAA-2001-3684

SIDE-LOAD PHENOMENA IN HIGHLY OVEREXPANDED ROCKET NOZZLES

J. Östlund

T. Damgaard

M. Frey

Space Propulsion

Volvo Aero Corporation

S-461 81 Trollhättan, Sweden

**37th AIAA/ASME/SAE/ASEE
Joint Propulsion Conference & Exhibit
July 8-11, 2001 / Salt Lake City, UT**

SIDE-LOAD PHENOMENA IN HIGHLY OVEREXPANDED ROCKET NOZZLES

J. Östlund[1], T. Damgaard[2], M. Frey[3]

[1]Volvo Aero Corporation, S-461 81 Trollhättan, Sweden, Phone: +46 520 93735, Fax: +46 520 98578,

Department of Mechanics, Royal Institute of Technology (KTH), S-144 00 Stockholm, Sweden,

jan.ostlund@volvo.com

[2]Volvo Aero Corporation, S-461 81 Trollhättan, Sweden, Phone: +46 520 93644, Fax: +46 520 98578,

tomas.damgaard@volvo.com

[3]Volvo Aero Corporation, S-461 81 Trollhättan, Sweden, Phone: +46 520 94278, Fax: +46 520 98578,

manuel.frey@volvo.com

Abstract

The off-design operation of rocket engines in the overexpanded region, e. g. with the ambient pressure being considerably higher than the nozzle wall pressure, can result in dangerous lateral loads acting on the nozzle. These loads only occur if the boundary layer separates from the nozzle wall and the pressure distribution deviates from its usual axisymmetric shape. Different aerodynamical or even coupled aerodynamic/structural mechanic reasons can cause an asymmetric pressure distribution. In Volvo Aero's sub-scale tests, three potential origins of side-loads were observed and investigated - namely the pressure fluctuations in the separation and recirculation zone due to the unsteadiness of the separation location, the transition of separation pattern between free shock separation (FSS) and restricted shock separation (RSS) and the aeroelastic coupling, which indeed cannot cause, but amplify existing side-loads to significant levels in case of instability. All three mechanisms are described in detail and methods are presented to calculate their magnitude and pressure ratio of occurrence.

Nomenclature

Abbreviations

FSC	Flow Separation Control
FSCD	Flow Separation Control Device
FSS	Free Shock Separation
HPG	High Pressure Gradient
PR	Stagnation Chamber to Ambient Pressure Ratio
SSME	Space Shuttle Main Engine
SPT	Small Perturbation Theory
SRS	Shock Response Spectrum
RSS	Restricted Shock Separation
TIC	Truncated Ideal Contour
TOP	Thrust Optimised Parabolic Contour

Symbols

B'	Normalised Pressure Shift Coefficient
C	Separation Point Shift Coefficient
F'	Differential Force
F	Force
J	Mass of Inertia
k	Stiffness
L, l	Length
M	Mach Number or Torque

$\vec{n}$	Wall Normal Vector
P, p	Pressure
r	Radius
S	Surface
s	Arc Length
t	Time
t_1	Pulse Duration Time
u, v	Velocity
$\vec{w}$	Wall Displacement
x	Axial Position
$\vec{x}$	Vector of Location
y	Horizontal Position
z	Vertical Position

Greek letters

δ	Boundary Layer
δ^*	Displacement Thickness
ε	Area Ratio
γ	Specific Heat Ratio
φ	Azimuth
θ	Tilt Angle
ρ	Density
τ	Period Time, Friction or Wall Angle
ω, Ω	Angular Frequency
ψ	Pressure Shift Coefficient

Subscripts

∞	Main Jet Flow State at the Edge of the Boundary Layer
a	Aerodynamic or Ambient
c	Calculated
cc	Combustion Chamber
e	Exit
i	Interaction
m	Measured or Mechanical
max	Maximum
n	Natural
p	Plateau
r	Recirculating
s, sep	Separation
t	Throat
w	Wall
y	Horizontal
0	Undisturbed flow state or Stagnation Condition

Introduction

The performance of a rocket engine is strongly influenced by the characteristics and function of the nozzle extension. The characteristics of a conventional

1

nozzle under vacuum conditions are well understood and under this condition, design tools are available. However, during operation at chamber pressures below design pressure, the rocket nozzle will be subjected to severe dynamic loads. These loads can sometimes be of such a magnitude that they present life-limiting constraints on thrust chamber components as well as on the thrust vectoring control system.

The increasing demand for higher performance in rocket launchers promotes the development of nozzles with higher performance and hence larger area ratio. In a high area ratio nozzle, the flow will not be fully attached, but separated, during testing at sea level condition or during the first phase of the actual flight. In a nozzle which is not under full-flowing conditions, the separation line will move towards the vicinity of the nozzle exit when the chamber pressure increases or when the ambient pressure decreases. Different kinds of dynamic loads occur in the nozzle when the flow is separated. The most well-known of these dynamic loads that have received attention in the literature is the so called side-load. In order to avoid damages by these loads, a deeper understanding of the involved phenomena is needed. Building of knowledge regarding flow separation and side-loads has been a continuous process at Volvo Aero Corporation (VAC) since 1993, when the Flow separation control working (FSC) group was formed with CNES, Snecma and Astrium.

VAC performed focused studies on the topic within the GSTP/FSC program[1], 1996-1999, under a contract with the European Space Agency (ESA) and the Swedish National Space Board (SNSB). Sub-scale testing of rocket nozzles was performed at the modified hypersonic wind tunnel HYP500 at the Aeronautical Research Institute of Sweden (FFA)[*] in order to investigate the aerodynamic and aeroelastic behaviour of a parabolic contour with and without polygon inserts.

In the subsequent FSCD-program since 1998, under contract with Swedish National Space Board (SNSB) and Centre National d'Études Spatiales (CNES), flow separation and side-loads have been studied analytically and by an impressive amount of sub scale testing[2]. This work was performed in co-operation with CNES, Snecma, ONERA, LEA, DLR and Astrium[3].

In the frame of the FSCD-program, VAC performed sub-scale nozzle tests again at FFA's test facility in Stockholm. The tested sub-scale models consist mainly of two parts; one fixed part mounted to the downstream flange of the wind tunnel and one flexible hinged part, Figure 1. The flexible hinged part is suspended by a cardan permitting the nozzle to move in two directions, Figure 2. The side-load torque is measured around the nozzle throat in the cardan by strain gauges located on the torsion springs and this motion simulates the throat-

---

[*] is now a part of the Swedish Defence Research Agency (FOI)

---

bending mode of an real rocket nozzle. Each of the different nozzle concepts tested is equipped with a stiffener ring at the nozzle exit in order to receive approximately the same eigenfrequency in all of the nozzle concepts. In the FSC program VAC has tested eight different nozzle concepts, see Table 1. Note that all experimental data presented in this paper refer to this table.
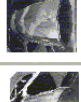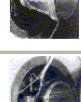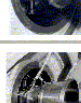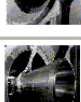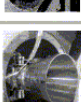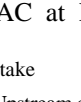
Nozzle	Base Contour	Area Ratio	Nozzle Picture
VolvoS1	Parabolic contour	20	
VolvoS2	Parabolic contour	20,75	
VolvoS3	Parabolic contour	18,2	
VolvoS4	Parabolic Polygon	18,2	
VolvoS5	Parabolic contour (VolvoS3) + Positive pressure gradient on the second bell	18,2	
VolvoS6 short	Truncated Ideal Contour (TIC), same contour as VolvoS6	13,9	
VolvoS6	Truncated Ideal Contour (TIC)	20,7	
VolvoS7	High Pressure Gradient (HPG)	24,6	
VolvoS7 short	High Pressure Gradient (HPG)	20,3	
VolvoS8	HPG with film injection	22,1	

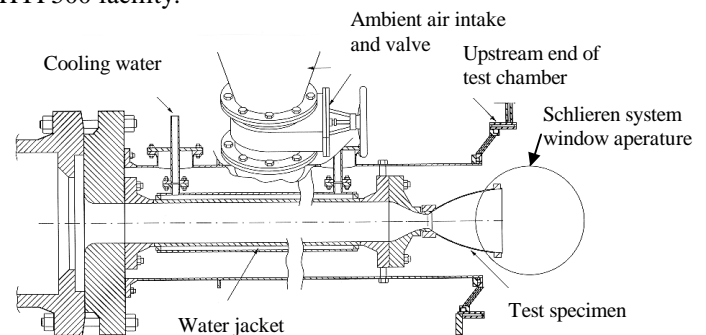Table 1. Sub scale nozzles tested by VAC at FFA's HYP500 facility.

Figure 1. Schematic side view of the cardan hinged test nozzle in FFA tunnel HYP 500.
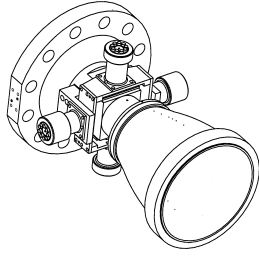
Figure 2. Test nozzle with cardan suspension.

In these test campaigns three main types of side-loads have been observed due to:

1. Random pressure fluctuation

2. Transition of separation pattern

3. Aeroelastic coupling

All these three types are described and exemplified by test results together with analysis in this paper. A fourth type of side-loads, which is due to the influence of the external flow, is not addressed here.

Side-loads created by random pressure fluctuations

Flow separation in supersonic flows is of course not limited to the field of rocket nozzles. When a supersonic flow meets a forward-facing step, a ramp or an incident shock, the pressure rise in the boundary layer can be strong enough to cause flow separation. From basic experiments with exactly these configurations, we know quite well that the boundary layer separation in turbulent supersonic flows is not a stationary process, even if the main flow is stationary[4,5]. Instead, the separation line and the shock which results from the deflection of the flow show a highly instationary behaviour, which seems to be triggered by the major scales of turbulence and also influences the recirculation region downstream[6].

In rocket nozzles, basically the same phenomena can be observed, although the separation location is not fixed by geometrical properties of the test configuration as in the above cases, but results mainly from the pressure ratio between nozzle flow and ambience.
As an example, static wall pressure measurements of a tested truncated ideal nozzle, S6, are shown in Figure 3. As expected, the separation point moves out of the nozzle with growing total pressure ratio.
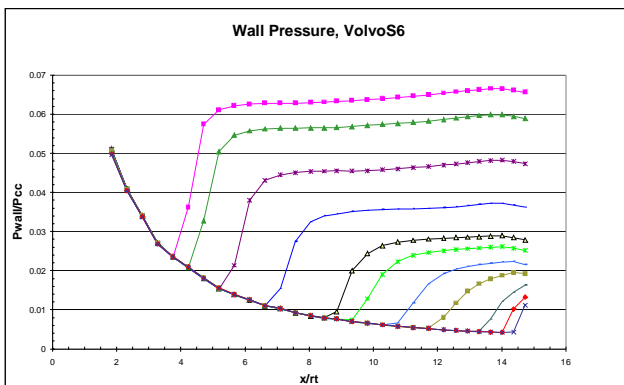

Figure 3. Static wall pressure measurements in the S6 nozzle for different pressure ratios.

Based on the static wall pressure development, the flow can be divided in three regions, see Figure 4: Upstream of the point of minimum static wall pressure (usually indexed "*sep*", although the physical separation occurs later), the boundary layer is attached and its behaviour corresponds to a full-flowing nozzle. The following region of steep pressure rise, which is ended as soon as a certain "plateau" (often indexed "*p*") is reached, is usually referred to as separation zone. In this region, the whole separation process, e. g. thickening of boundary layer and physical flow separation (here indexed "*s*") at the zero wall friction point, $\tau_w=0$, takes place. The last portion of the nozzle, where the flow is fully separated and which is referred to as recirculation zone, shows a weak pressure rise until a wall pressure slightly below the ambient pressure is reached in the nozzle exit plane.
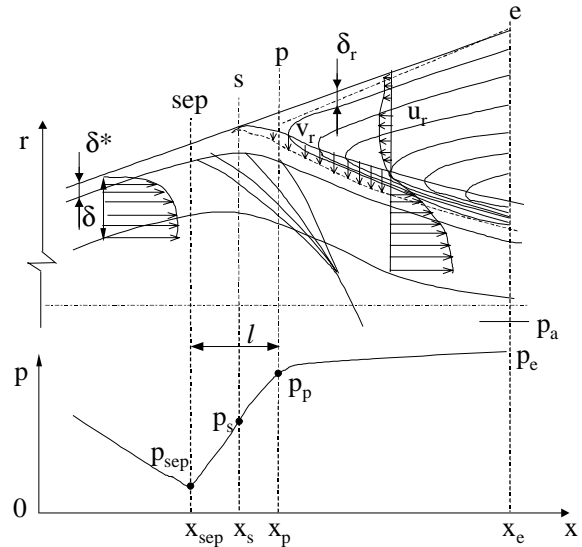

Figure 4. Schematic sketch of Free Shock Separation.

To get a closer insight into the flow structure, the flow in this nozzle was simulated using VolSol[7], an in–house developed Navier-Stokes CFD tool, and the Menter-SST turbulence model[8]. The resulting Mach number distribution is shown in Figure 5 for a specific pressure ratio.
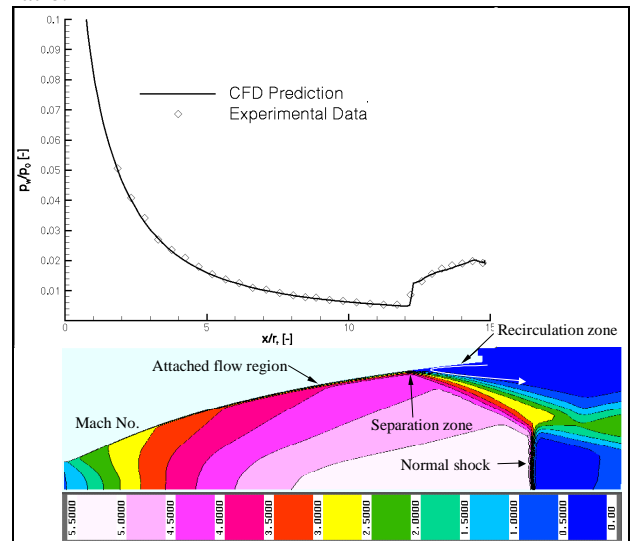

Figure 5. Static pressure distribution and flow structure in the Volvo S6 nozzle.

Looking at the dynamic behaviour of the wall pressure rather than at the static one, interesting features of the flow can be observed. In the region of attached flow, only very small pressure fluctuations exist, which are in fact the pulsations of the attached turbulent boundary layer. As an example, the wall pressure in the above-mentioned truncated ideal nozzle is given at an axial location of $x/r_t \approx 8.5$ and $p_{cc}/p_a = 75$ in Figure 6, bottom. In contrast to this, the pressure pulsations are much greater in the separation zone due to the oscillation of the separation location, as can be seen from Figure 6, centre (same location, but $p_{cc}/p_a = 30$). The measured wall pressure quickly oscillates between two levels – one of them corresponding to the pressure upstream of the separation shock, p_{sep}, the other one corresponding to the pressure at the beginning of the recirculation zone, p_p, merely depending on the position of the separation shock with respect to the pressure sensor. This implies that an instantaneous wall pressure distribution in the separation zone looks very different from the static pressure measurements shown in Figure 3. The pressure rise will be even steeper, only damped by the boundary layer. Downstream of the separation zone, the pressure fluctuations decrease considerably, but are still much higher than in the case of an attached boundary layer, see Figure 6 for the S6 nozzle at $p_{cc}/p_a = 10$. The instationary behaviour of the pressure in this region is mainly generated by the noise from the shear layer of the separated free jet and therefore also depends on the oscillations of the separation point.
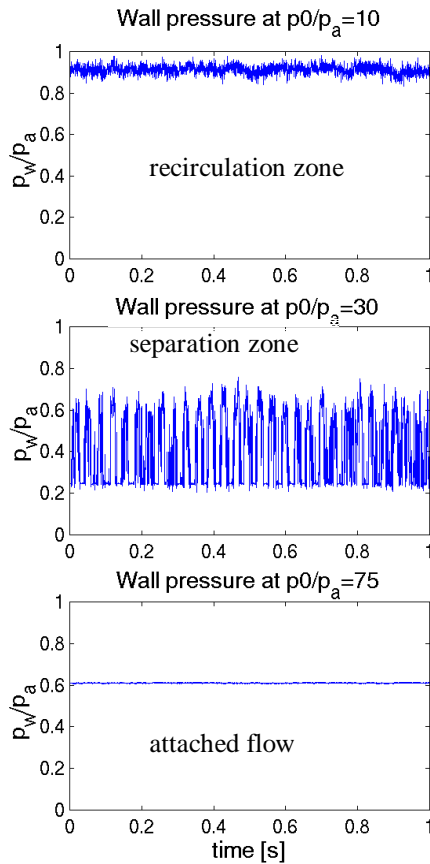
The pressure fluctuations have a random character, but show a clear correlation both in space and time. Therefore, they cause deviations from the axisymmetric flow and hence can produce forces perpendicular to the nozzle axis. Figure 7 shows those forces as a function of test time and pressure ratio for the Volvo S6 nozzle. Dumnov[9] presented a methodology to calculate the size of such forces based on the measurement of correlations both in time and space. This method is well suited to predict side-loads in conical or truncated ideal nozzles. At Volvo Aero, a similar model is under development to calculate side-loads[10]. Figure 8 shows a comparison between a first prediction with this model and experimental side-load data for the S7 nozzle. As can be seen, the general trend of side-load is captured well, whereas there are some deviations in the prediction of its magnitude.
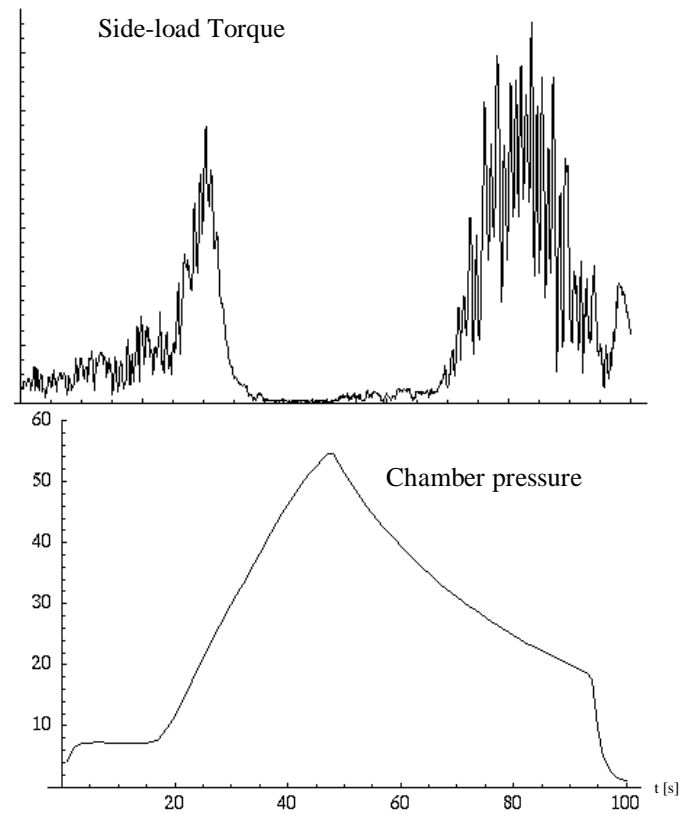

Figure 7. Side-loads created in a nozzle with random pressure pulsation.
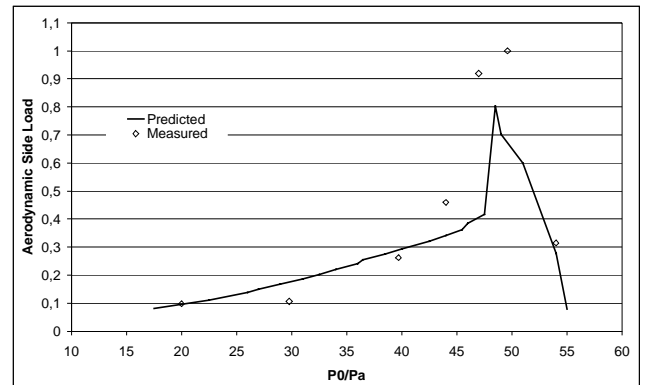

Figure 6. Pressure as function of time.

Figure 8. Side-loads in the S7 nozzle, comparison between prediction and experiment

It is important to note that the above described side-load which results from random pressure fluctuations, is an aerodynamic force which acts on the dynamic system of nozzle or engine. To calculate the system response, i. e. strains, deformations and movements, it is necessary to solve a forced-response problem. The same holds true if the aerodynamic side-load should be extracted from measurements: Since only the system response can be measured, a recalculation of the aerodynamic force is necessary, which requires the precise knowledge of the system's dynamic behaviour. One possibility to do this is to determine the system's transfer function[11]. This procedure was also used to calculate the aerodynamic side-loads from test data recorded at the HYP500 rig.

<u>Side-loads created by transition of separation pattern</u>

In nozzles with an internal shock that yields a cap shock pattern[3] e.g. compressed truncated ideal contours, parabolic contours and direct optimised nozzles, a transition between two distinct separation patterns may occur creating two distinct side-load peaks, see Figure 9 and Figure 10. Two well-known full-scale nozzles with cap shock pattern and a transition in separation pattern are the parabolic Vulcain and the SSME nozzle.
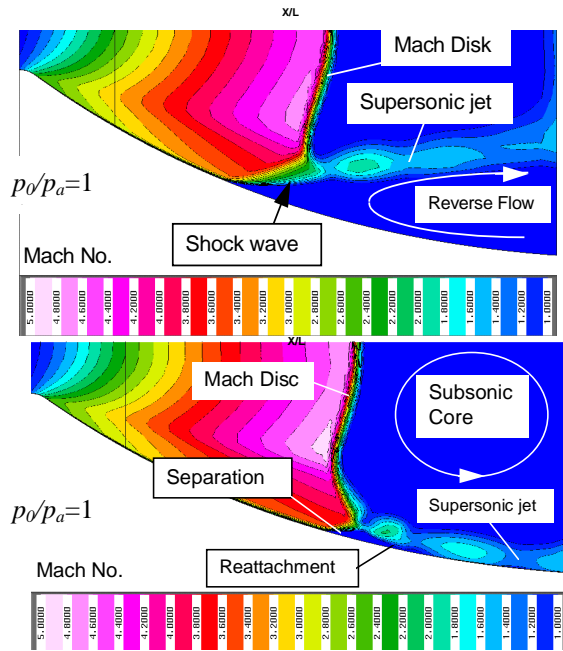

Figure 9. Free Shock Separation (top) and Restricted Shock Separation (bottom) in the S1 nozzle at start-up.

During the start up transient the separation pattern is first Free Shock Separation (FSS) and at a certain chamber pressure a transition occurs and the separation pattern is transformed into a Restricted Shock Separation type (RSS), see Figure 9.

This rapid unsymmetrical transition creates a side-load impulse acting on the nozzle structure. Due to the short duration of the aerodynamic side-load the pulse excitation theory[11] can be used when evaluating the mechanical load.
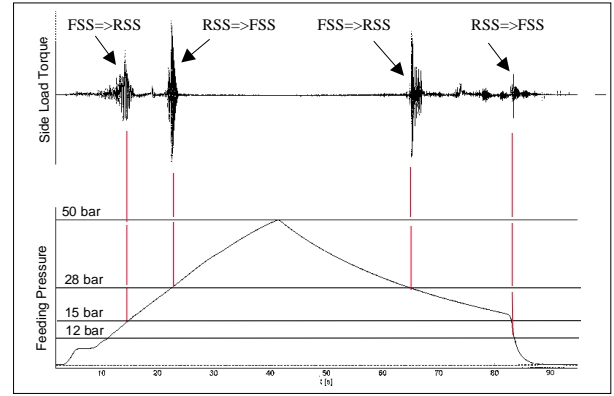

Figure 10. Side-loads created in the parabolic S1 nozzle due to transition in separation pattern.

With this theory the dynamic response factor, i.e. the amplification of the applied load due to the dynamic system, is less than two for any single pulse. The most critical pulse is the single square wave, since it contains the highest energy that any single pulse can have, see Figure 11.
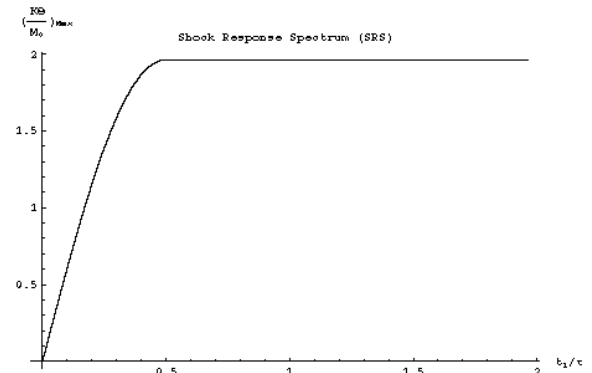

Figure 11. Shock response spectrum (SRS) for a single square wave, t_1=pulse duration time, τ=period time.
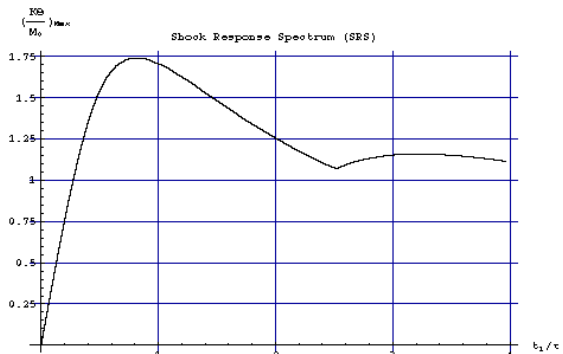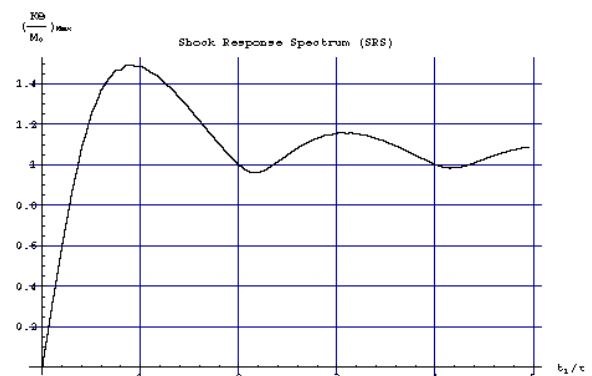

Figure 12. SRS for half sine wave.

Figure 13. SRS for a triangular wave.

5

A further example of waves is the half-sine wave with its SRS depicted in Figure 12. The half-sine and the triangular pulse, see Figure 13, are often good approximations to actual pulse shapes, hence the pulse creating the side-load when the separation pattern is changed from FSS to RSS.

The second side-load peak is created by the transition from RSS to FSS. As the pressure ratio is increased, the reattachment point reaches the nozzle exit and the flow becomes highly unstable. The closed re-circulation bubble opens and the separation point moves upstream and downstream in a cyclic manner until the increase of feeding pressure is enough to move the reattachment shock completely out of the nozzle. Compared to the pulse excitation side-load producing the first side-load peak the second peak is more of a steady state forced response phenomena. If mechanical frequencies of the system are close to the aerodynamic side-load frequency it can lead to severe side-load amplification and thus fatigue of mechanical components. The cause of the failure of the SSME fuel feed line was explained by this phenomenon[12].

In the VAC sub scale testing these kinds of side-loads are detected in the parabolic nozzles e.g. VolvoS1 and VolvoS3 and the measured side-load behaviour is depicted in Figure 10 for the S1 nozzle.

During the sub scale test campaigns VAC developed a side-load model which predicts the aerodynamic side-load prevailing in nozzles with two types of separation pattern. Predictions with the VAC model[2,3] of the transition point and corresponding side-load have been performed on several nozzles, both sub scale and full scale, with excellent agreement, see Table 2. Other models available to predict this transition and side-load is a model developed by DLR/Astrium[3] in parallel with the VAC model.

Nozzle	$P0_m/P0_c$	M_m/M_c
VolvoS1	0.94	1.01
VolvoS3	1.0	1.02
Vulcain	1.05	1.05

Table 2. Comparison between VAC simulated and measured transition feeding pressure and aerodynamic torque.

Aeroelastic stability

From side-load point of view the aeroelastic behaviour of the bending mode is the most relevant one. In highly aeroelastic cases significant side-loads are created by aeroelastic instability of the bending mode but more often an already existing side-load is amplified by aeroelastic coupling. The study of the closed-loop effect between jet separation and displacement of the wall has not been attacked vigorously in the past due to the complexities involved in generating accurate asymmetric

dynamic models of the nozzle engine support system, the jet boundary layer separation, and interaction at the boundary between the two systems. A technique for handling these difficult coupling problems has however been proposed by Pekkari[13-14]. With the model, the aeroelastic eigenfrequencies, the stability as well as the transient aeroelastic behaviour of the nozzle can be evaluated for all nozzle eigenmodes. In the subsequent paragraphs a modified version of the Pekkari model is outlined, applied and compared with experimental data.

Analysis geometry

In order to study the interaction of the flow detachment and the displacement of the nozzle wall we turn our attention to the flow conditions in the vicinity of the wall.

We consider the geometry for the flow and the nozzle wall motion as indicated in Figure 14.
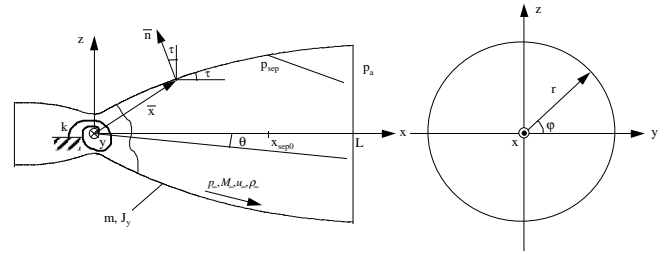

Figure 14. Nozzle and flow separation geometry.

In the model nozzles tested, the first bending mode has been simplified as a pure bending around a flexible joint or cardan with stiffness k located at the throat. θ is the tilt angle between the nozzle centre line and the combustion chamber centre line. L is the length (from the throat to the exit), m is the mass, J_y is the mass of inertia around the y-axis, τ is the local contour angle, and r is the local radius of the nozzle. $\vec{w}$ is the displacement of the nozzle wall.

Equation of motion

The system is considered as quasi static with respect to the flow, i.e. the characteristic time scales of the flow are considered to be an order of magnitude faster than the characteristic time scales of the mechanical system.

The equation of motion for the bending of the nozzle with an angle θ is:

$$J_y \ddot{\theta} = M_m(\theta) + M_a(\theta, Pcc)\big|_y \qquad (1)$$

Here M_m and M_a are the mechanical and aerodynamical torque respectively, which will be discussed in detail below. The equilibrium is given by:

$$M_m(\theta) + M_a(\theta, Pcc)\big|_y = 0 \qquad (2)$$

<u>Mechanical torque</u>

The mechanical torque considered is the restoring torque of the spring in the nozzle suspension, which for small displacements is:

$$M_m(\theta) = -k\theta \qquad (3)$$

<u>Aerodynamical torque</u>

The aerodynamical torque considered is the torque induced by the pressure load onto the nozzle wall, i.e.:

$$M_a(\theta, P_{cc}) = \oiint \vec{x} \times [p_\infty(\vec{w}(\theta), x, P_{cc}) - p_a] \cdot \vec{n}\, dS \quad (4)$$

Where $\vec{n}$ is the wall surface normal vector facing the flow and $\vec{x}$ is the corresponding vector of location:

$$\vec{n} = \{-Sin\tau, Cos\varphi \cdot Cos\tau, Sin\varphi \cdot Cos\tau\} \qquad (5)$$

$$\vec{x} = \{x, r(x)Cos\varphi, r(x)Sin\varphi\} \qquad (6)$$

Upstream of the separation point, x_{sep}, the pressure is the free stream pressure, p_∞. Downstream of the separation point a pressure recovery occurs and the pressure approaches gradually the ambient pressure. We do however here for simplicity and clarity choose a pressure downstream of the separation that is equal to the ambient pressure, p_a.

$$p_\infty(\vec{w}, \vec{x}, P_{cc}) = \begin{cases} P_{cc}\left[\dfrac{p_{\infty,o}(x)}{P_{cc}} + \Psi(\vec{w}, \vec{x})\right] & ; x \le x_{sep} \\ p_a & ; x > x_{sep} \end{cases} \quad (7)$$

Here $p_{\infty 0}(x)$ denotes the vacuum pressure profile in the undeflected nozzle. The second term in the pressure upstream of the separation line is the normalised distortion of the free stream pressure due to a small wall displacement i.e.:

$$\Psi(\vec{w}, \vec{x}) = \frac{p_\infty(\vec{w}, \vec{x}, P_{cc}) - p_{\infty,0}(x)}{P_{cc}} \qquad (8)$$

The location of the separation point is considered to be given by a separation pressure, p_{sep}:

$$p(x_{sep}) = p_{sep} \qquad (9)$$

In the original work by Pekkari, the pressure shift, ψ, was calculated with the use of the small perturbation theory (SPT), i.e.:

$$\Psi(\vec{w}, \vec{x}) = \frac{\rho_{\infty,0} u_{\infty,0}^2}{P_{cc}\sqrt{M_{\infty,0}^2 - 1}} \frac{\partial w}{\partial s} = B'\frac{\partial w}{\partial s}$$

$$(10)$$

Here $w = \vec{w} \cdot \vec{n}$ denotes the normal displacement of the nozzle wall surface facing the flow and s is the arclength along the wall in the axial direction. B' is the normalised pressure shift coefficient and gives the normalised pressure shift due to a unit shift of the wall slope.

However, experience has showed that SPT tends to over predict the pressure shift in cases where 3D effects are significant. A modified approach is therefore used in this article where the normalised pressure shift coefficient B' is extracted from 3D Euler simulations i.e.:

$$B'(x) = \frac{\Psi(\vec{w}, \vec{x})}{\partial w/\partial s} = \frac{p_\infty(\vec{w}, \vec{x}, P_{cc}) - p_{\infty,0}(x)}{P_{cc}\, \partial w/\partial s} \quad (11)$$

In Figure 15 the measured and the calculated wall pressure profile are shown for the undeflected and deflected (1 degree) S1 nozzle, respectively. As can be seen in the figure it is a good agreement between the CFD prediction and the measured wall pressure whereas SPT over predicts the pressure shift. This effect is more visible in Figure 16, which shows the corresponding normalised pressure shift coefficient B'. As indicated in the figure the SPT method overpredicts the pressure shift coefficient by approximately a factor 4 for this case. The CFD predictions on the other hand show close agreement with the experimental data and thus validate the use of Euler simulations for calculating the pressure shift coefficient.
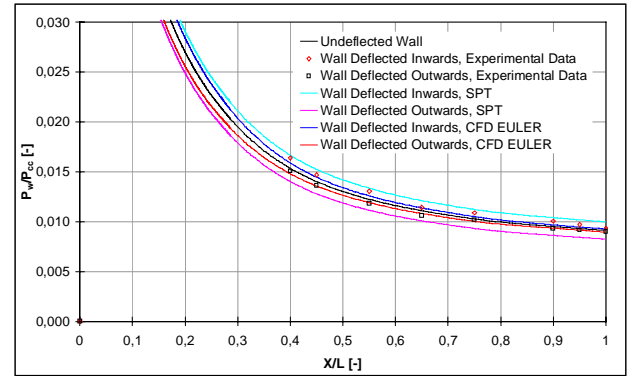

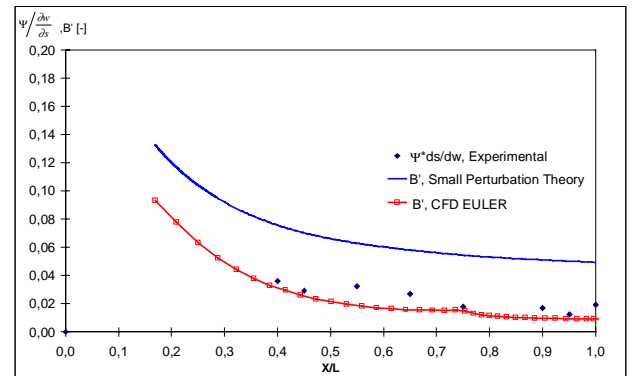Figure 15. Measured and calculated wall pressure in the S1 nozzle static deflected 1 degree.

Figure 16. Comparison between calculated and measured normalised pressure shift coefficient B' in the S1 nozzle.

It must be emphasised that the deviation of the wall pressure due to bending around the throat is highly dependent on the nozzle contour itself. As shown in refs. 15-16, the secondary flow effects due to the uneven flow distribution around the circumference in a conical nozzle are so strong that the pressure deviation trend even reverses itself: On the side with higher flow angles,

where more expansion is expected, the wall pressure is in some portions of the nozzle even higher than on the opposite side. This finding has been confirmed by own numerical simulations and underlines the necessity of case-sensitive methods, see Figure 17 (notice the negative value of B').
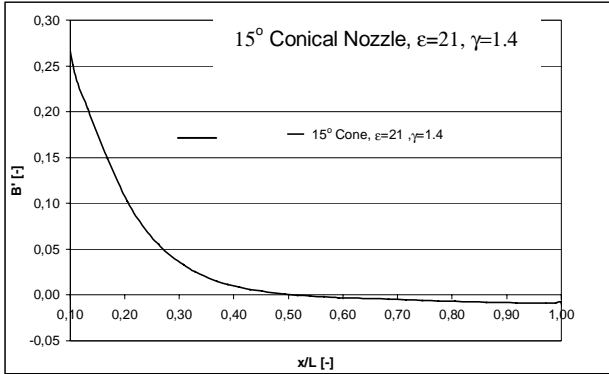

Figure 17. Normalised pressure shift coefficient in conical nozzle.

In order to do an aeroelastic stability analysis we next expand the free stream pressure around the initial location of the separation line, x_{sep0},

$$p_{\infty,0}(x_{sep}) = p_{\infty,0}(x_{sep0}) + \frac{dp_{\infty,o}}{dx}(x_{sep} - x_{sep0}) + .. \quad (12)$$

Equation (8) written at the axial station x_{sep} is:

$$p_{\infty}(\vec{w}, \vec{x}, P_{cc}) = p_{\infty,0}(x) + P_{cc}B'\frac{\partial w}{\partial s} ; x = x_{sep} \quad (13)$$

The separation pressure p_{∞}, at $x=x_{sep}$, approximated for the deformed wall contour by equation (13) will be the same as the separation pressure $p_{\infty0}(x_{sep0})$ for the undeformed wall contour included in equation (12) which can be written as:

$p_{\infty0}(x_{sep0}) = p_{\infty} at \ x=x_{sep}$
(14)

Identity (14) with equation (13) and (12) gives:

$$x_{sep0} - x_{sep} = \frac{P_{cc}B'}{-\dfrac{dp_{\infty,o}}{dx}}\frac{\partial w}{\partial s}\Big|_{x=x_{sep0}} = C\frac{\partial w}{\partial s}\Big|_{x=x_{sep0}} \quad (15)$$

Where $C(x_{sep0})$ gives the shift of the separation point given by unit shift of the nozzle wall slope.

The differential aerodynamic pressure force due to a small wall displacement, may be written as:

$$F_a'(\vec{w}) = \vec{n}(p_a - p_{sep})(x_{sep} - x_{sep0}) =$$

$$= \vec{n}(p_a - p_{sep})C(x_{sep0})\frac{\partial w}{\partial s}$$

(16)

By integrating the differential force around the separation line the aerodynamic pressure force is:

$$F_a(\vec{w}) = \oint_{lsep} F_a' dy = (p_a - p_{sep})\oint_{lsep} \vec{n}C\frac{\partial w}{\partial s}dy\Big|_{x_{sep0}} \quad (17)$$

The corresponding aerodynamic torque is:

$$M_a(\vec{w}) = \oint_{lsep} \vec{x} \times F_a' dy =$$

$$= (p_a - p_{sep})\oint_{lsep} \vec{x} \times \vec{n}C\frac{\partial w}{\partial s}dy\Big|_{x_{sep0}}$$

(18)

The change of the nozzle wall slope at different azimuthal locations, φ, due to a small tilt angle, θ, of the nozzle can be expressed as:

$$\frac{\partial w}{\partial s} = \theta Sin\varphi$$

(19)

Using this and

$$\oint_{l_{sep}} ..dy \approx \int_0^{2\pi} ...r(x_{sep0})d\varphi$$

(20)

for small wall displacements, the aerodynamic torque can be expressed as:

$$M_a(\theta, x_{sep0}) =$$

$$= (p_{sep} - p_a)C r\pi(xCos\tau + rSin\tau)\theta\begin{pmatrix} 0 \\ 1 \\ 0 \end{pmatrix}_{x=x_{sep0}} \quad (21)$$

Eigenfrequency

The equation of motion for the mechanical system alone is derived by putting the considered harmonic amplitude motion solution:

$$\theta \sim e^{i\omega t}$$
(22)

into equation (1), leaving out the aerodynamical torque $M_a(\theta, Pcc)\Big|_y$.

$$-J_y\omega^2\theta = -k\theta$$
(23)

From equation (23), the eigenfrequency is found as:

$$\omega^2 = \frac{k}{J_y}$$

(24)

8

The aeroelastic stability of the complete system

Consider the nozzle displaced when subjected to mechanical and aerodynamical loads and assume the motion to be purely harmonic, i.e.:

$$\theta \sim e^{i\Omega t}$$
(25)

Introducing equation (24) and (25) in (1) and rearranging gives:

$$\left(\frac{\Omega}{\omega}\right)^2 = 1 - \frac{M_a(\theta, P_{cc})\big|_y}{k\theta}$$
(26)

Inspection of equation (26) shows that if:

1. $M_a(\theta, P_{cc})\big|_y < 0$ the aeroelastic torque acts to restore the nozzle to its nominal position, i.e. the system becomes stiffer than the mechanical structure itself and the frequency of the eigenmode is shifted to a higher frequency. This is for instance the case in a full flowing Vulcain nozzle.

2. $M_a(\theta, P_{cc})\big|_y \in [0, k\theta]$ the aeroelastic torque acts in the same direction as the displacement of the nozzle wall, i.e. the system becomes weaker than the mechanical structure itself and the frequency of the eigenmode is shifted to a lower frequency.

3. $M_a(\theta, P_{cc})\big|_y > k\theta$ the unconditionally stable eigenmode becomes aeroelastic unstable.

The aeroelastic stability of the system can also be investigated for small displacements by substituting the linearised aerodynamic torque, equation (21), in (26), which gives:

$$\left(\frac{\Omega}{\omega}\right)^2 = 1 - \frac{(p_{sep} - p_a)C r \pi (x Cos\tau + r Sin\tau)}{k}\bigg|_{x=x_{sep0}}$$
(27)

Aeroelastic analysis

Within the GSTP FSC test programme, the influence of structural response and aeroelastic coupling on the side-load generated in the Volvo S1 nozzle were investigated. This was done by changing the natural eigenfrequency of the bending mode, with the use of exchangeable torsion springs. The resulting natural oscillating frequencies of the bending mode are listed in Table 3 for the different spring set-ups used. The frequencies were determined by performing a ping test on the model set up. A more detailed description of the test programme is presented in ref. 1.

Spring name	Super weak	Weak	Medium	Stiff	Rigid
Natural frequency [Hz]	25,2	36,3	45,0	57,5	120

Table 3. Resulting natural oscillating frequencies of the bending mode for the different spring set-ups with the Volvo S1 nozzle.

With the use of equation (27), the aeroelastic stability of the S1 nozzle can be calculated for the different spring set-ups. Such a calculation is presented in Figure 18 with $p_{sep}/p_a=0.3$ and B' from an Euler calculation according to figure 3. From the figure we can conclude that the only areoelastic unstable system is the S1 nozzle with the super weak spring, whereas the other systems are aeroelastic stable.

The aeroelastic stable system will almost behave like a regular forced response system, i.e. the closer the mechanical egienfreqencies are to the frequencies of the aerodynamic load the higher generated loads. The exception is that a small shift of the system eigenfreqency and a corresponding small amplification of the forced response load will occur. The frequency shift and the size of the aeroelastic side-load amplification depend on the degree of coupling. For the weak, medium, stiff and rigid spring set-ups considered here the coupling is considered to be weak and the aeroelastic effect can almost be neglected.
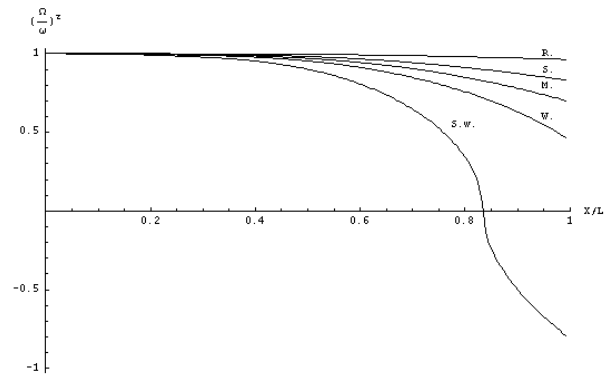

Figure 18. Aeroelastic stability of the S1 nozzle for the different spring setups, S.W. =Super Weak, W. = Weak, M.=Medium, S.=Stiff and R.=Rigid spring respectively.

For the aeroelastic unstable system, on the other hand, we would expect a significantly higher side-load magnitude compared to the classical forced response theory due to the aeroelastic instability. When the separation enters the section of the nozzle that is unstable, the displacement of the nozzle will start to grow exponentially. At the same time the separation line will be displaced accordingly. The non-linear growth of the nozzle displacement will eventually saturate as parts of the separation line start to move out of the nozzle when the displacement becomes sufficiently high. This can be seen in the non-linear stability relation, equation (26), displayed in Figure 19 for tilt angles $\theta=0.1^o$ and $\theta=2.6^o$ respectively. As the mode saturates, the amplitude will eventually drop and the process will be repeated in a cyclic way.

If we study the non-linear stability relation for the S1 nozzle more carefully, Figure 19, we can see that the aeroelastic instability occurs at a pressure ratio of $p_0/p_a=26-28$. When the pressure ratio is increased

further, the nozzle will eventually become full flowing at $p_0/p_a \approx 30$, and the system becomes stiffer than the mechanical structure itself, i.e. $(\Omega/\omega)^2 > 1$, since the aerodynamic torque now acts to stabilise the nozzle.
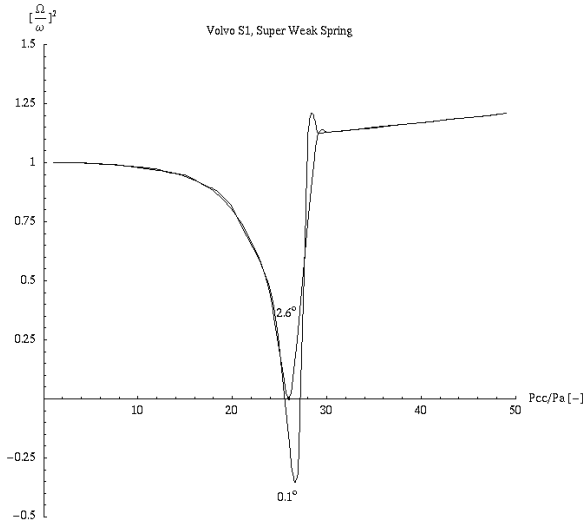

Figure 19. Non-linear stability relation for the S1 nozzle flexible hinged with the super weak spring.

Spring	$\dfrac{\omega}{\omega_n}$ †	No. of tests	$\dfrac{M}{M_{max}}$
Rigid	0.8	2	0.66
Stiff	1.7	10	0.63
Medium	2.2	10	0.48
Weak	2.8	10	0.45
Super Weak	3.9	5	1

Table 4. Measured side-load magnitude versus frequency ratio between the exiting load and the mechanical system, peak at PR=28.

Next we compare the model result with experimental data. For the side-load peak at PR= 28, Table 4, we can see that the test data correlates well with the aeroelastic predictions made above, see Figure 18 and Figure 19. The aeroelastic system, i.e. super weak spring set-up, gives the highest loads (M/M_{max}) and interrupts the trend obtained for the aeroelastically stable systems. The systematic behavior of decreasing response load with decreasing spring stiffness for the rigid to the weak spring can be explained with classical forced response theory. The side-load peak at PR=28 is caused by the separation shock system pulsating with a frequency of about 100 Hz at the exit. Forming the frequency ratio between the aerodynamical force and the mechanical systems, Table 4, we can see the above stated fact. The highest response load is obtained for the rigid spring, which has the frequency ratio closest to unity and the

response decreases with increased distance from the resonance value. The conclusion is thus that the aeroelastic theory is capable of predicting the obtained side-load features.

Finally, we compare the predictions of the aeroelastic stability for the S6 nozzle with experimental data, see Figure 20. The experimental frequency shift of the eigenmode has been determined by applying the Welch method[17] for power spectral analysis on the measured steady state side-load at different constant pressure ratios. The sampling time was at least 8 seconds for each case in order to achieve a sufficient frequency resolution. The linearised aeroelastic stability relation, equation (27), for the S6 nozzle has been calculated with p_{sep}/p_a=0.3 and B' extracted from an Euler calculation. In the figure the linear stability relation based on small perturbation theory is also shown in order to visualise the effect of the over-prediction of the pressure shift this theory causes.
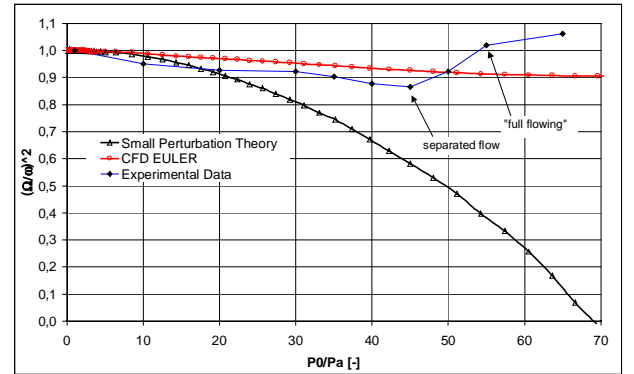

Figure 20. Comparison between measured and calculated frequency shift for the S6 nozzle.

As indicated in the figure the linearised stability theory predicts the same trend of the frequency shift of the mode frequency of the nozzle with separated flow as the ones observed in experiments. The deviation is mainly due to the fact that both structure as well as gasdynamic damping is neglected in the model. Including damping in the model would increase the frequency shift and the model prediction would thus become closer to experimental data. However, the influence of the damping is only significant during steady state operation whereas during short transient phases, such as a rocket engine start up, the damping plays a minor role and the model assumptions will thus become more valid.

The increased system frequency observed in the experimental data when the nozzle is full flowing can not be captured with the linearised stability relation. However, as indicated in Figure 19, this effect can be captured with the non-linear relation.

To summarise, we have seen that the modified aeroelastic model is capable to predict the aeroelastic behaviour experienced in the tests. Further, the necessity of a case-sensitive method to determine the normalised pressure shift coefficient B' has been pointed out.

---

† ω=100*2π [s^{-1}] is the frequency of aerodynamical load, from Schlieren video and pressure measurements. ω_n natural frequency of mechanical system.

Conclusions

The side-load phenomena in highly overexpanded rocket nozzles, has been investigated with the help of extensive sub scale testing at FFA. Three main types of side-loads have been observed in the tests. Side-loads generated by:

1. Random pressure fluctuations
2. Transition of separation pattern
3. Aeroelastic coupling

For all three types of side-loads, prediction models have been developed by VAC. The results presented in the paper show a good agreement with test data.

Acknowledgements

References

/1/ Mattsson J. (Östlund since 1999) et al., "A Sub-scale Test Program on Investigation of Flow Separation and Side Loads in Rocket Nozzles", ESA-SP-426, Dec 1998

/2/ Östlund J., Bigert M., "A Subscale Investigation on Side-Loads in Sea Level Rocket Nozzles", AIAA 99-2759, June 1999

/3/ Hagemann G., Terhardt M., Frey M., Reijasse P, Onofri M, Nasuti F., Östlund J., "Flow Separation and Side-Loads in Rocket Nozzles",4th International Symposium on Liquid Space Propulsion, March 12-15, 2000, DLR Lampoldshausen

/4/ Kistler A., "Fluctuating wall pressure under a separated supersonic flow", Journal of the acoustical Society of America, Vol. 36, No. 3, March 1964, pp 543-550

/5/ Coe C., Chyu W., Dods J., "Pressure fluctuations underlying attached and separated supersonic turbulent boundary layers and shock waves", AIAA 73-996, Seattle, October 1973

/6/ Adams N. A., 2000, "Direct simulation of the turbulent boundary layer along a compression ramp at M=3 and Re=1685", J. Fluid Mech. 420:47-83

/7/ Rydén R., Groth P., "Volsol V2.6 user's Guide", VAC Report 9970-1857, Volvo Aero Corporation Internal Report

/8/ Menter F. R., "Zonal Two Equation k-ω Turbulence Models for Aerodynamic Flows", AIAA 93-2906, July 1993

/9/ Dumnov, G. E., "Unsteady Side-Loads acting on the Nozzle with Developed Separation Zone'', AIAA 96-3220, 1996

/10/ Boman A., "Pressure Fluctuation Based Free Shock Separation Side Load Model, VAC Report SV NT 114 00DR E2009, Volvo Aero Corporation Internal Report, September 2000

/11/ Harris C. M., Crede C. E., "Shock and Vibration Handbook", McGraw-Hill, Inc., ISBN 0-07-026799-5, 1976

/12/ Larson E. W. et al., "Structural Response of the SSME Fuel Feedline to Unsteady Shock Oscillations", 52nd Shock and Vibration Symposium, New Orleans, Louisiana 21-29 October 1981.

/13/ Pekkari, L.-O., "Aeroelastic Stability of Supersonic Nozzles with Separated Flow'', AIAA 93-2588, June 1993

/14/ Pekkari, L.-O., "Aeroelastic Analysis of Side-Loads in Supersonic Nozzles with Separated Flow", AIAA 94-3377, June 1994

/15/ Frey M., "Behandlung von Strömungsproblemen in Raketendüsen bei Überexpansion", PhD thesis, http://elib.uni-stuttgart.de/opus/volltexte/2001/800, ISBN 3-8265-8806-1

/16/ Kwan W., "Aeroelastic effects on a bended conical nozzle", DLR-IB 645-2001-06, DLR Internal Report, 2001

/17/ Welch P. D., "The Use of Fast Fourier Transform for the Estimation of Power Spectra: A Method Based on Time Avaraging Over Short, Modified Periodograms", IEEE Trans. Audio Electroacoust., Vol. AU-15, June 1967, pp.70-73.